Cranfield University

Zenghai Lu

Interferometric filter based planar Doppler velocimetry

Engineering Photonics Centre
School of Engineering

PhD Thesis

Cranfield University

School of Engineering

PhD Thesis

2008

Zenghai Lu

Interferometric filter based planar Doppler velocimetry

Supervisor: Prof. Ralph P. Tatam

Academic Year 2004 to 2007

This thesis is submitted in partial fulfilment of the requirements for the degree of Doctor of Philosophy

ABSTRACT

This thesis describes the development of a Mach-Zehnder interferometric filter based planar Doppler velocimetry (MZI-PDV) flow measurement technique. The technique uses an entirely new optical system, an unbalanced MZI incorporating glass blocks for wavefront-matching, to replace the iodine cell currently used in conventional PDV. The free spectral range of the interferometric filter can be selected by adjusting the optical path difference of the MZI. This allows the velocity measurement range, sensitivity and resolution to be varied. This system offers no restricts to the choice of laser wavelength of operation which is not the case with most techniques. Two techniques to process the interference fringe images are presented. The first uses the shift of the fringe pattern to determine the Doppler frequency shift along profiles. The second provides a full-field measurement by normalising the received light intensity at each pixel in the image. With the single camera MZI-PDV scheme, exact alignment of the two output images on the active area of the camera is automatic. This eliminates the pixel-matching problem in conventional two camera PDV systems. The technique allows the measurement of up to three components of the flow velocity across a plane defined by a laser light sheet.

The construction of a single velocity component MZI-PDV system that incorporates a phase-locking system designed to stabilise the filter is described. Measurements are made on the velocity field of a rotating disc with maximum velocities of ~±70ms^{-1} and an axis-symmetric air jet (with a nozzle diameter of 20mm) with an exit velocity of ~85ms^{-1}. Standard deviations in the measured velocities were found to be about 2.9 and 2ms^{-1} for the two processing methods respectively. The system was then modified to make 3-component velocity measurements using imaging fibre bundles to port multiple views to a single detector head, and the standard deviation of the velocity error is around ±3ms^{-1} for a maximum velocity of ~±30ms^{-1} in the field of view.

The factors that will affect the quality of the interference fringe image are investigated including polarisation sensitivity of the two beam splitters and flatness of the optical components. The inclination angle and the optical path deviation have little effect on the contrast of the interference fringes since collimated light beams, rather than divergent ones, are used in the interferometer.

Keywords:
PDV, Mach-Zehnder interferometer, flow measurement, phase control, coherent fibre bundles

ACKNOWLEDGEMENTS

I would like to thank Ralph Tatam (academic supervisor), Helen Ford and Thomas Charrett (support supervisors) for continued support and advice during my studies.

I would like especially to thank Stephen Staines for his invaluable designs and constructions, Edmond Chehura for his assistance, and the present members of the Engineering Photonics group.

I acknowledge the Overseas Research Scholarship (ORS) award from the Committee of Vice Chancellors and Principals, UK. This work was carried out with the support of the Paul Instrument Fund grant from the Royal Society, UK.

TABLE OF CONTENTS

TABLE OF FIGURES

TABLE OF TABLES

TABLE OF EQUATIONS

GLOSSARY OF SYMBOLS

Doppler equation and geometry

$\hat{o}$	Observation vector
$\hat{i}$	Illumination vector
$(\hat{o}-\hat{i})$	Measured velocity component (sensitivity vector)
Δv	Doppler frequency shift
c	Free space speed of light
v	Frequency of illumination light
λ	Wavelength of illumination light
ϕ	Scattering angle (angle between $\hat{o}$ and $\hat{i}$)
$\hat{V}$	Velocity of scattering object
V_ϕ	Velocity component in the direction of $(\hat{o}-\hat{i})$
U_n	Velocity component along sensitivity vector
U, V, W	Orthogonal velocity components, horizontal, vertical and out-of-plane

Mach-Zehnder interferometer

MZI	Mach-Zehnder interferometer
BS	'Non-polarising' beam splitter
PBS	polarisation beam splitter
Δl	Optical path difference between the two arms
$\Delta\varphi$	Optical phase between the two arms
$l1, l2$	Physical path lengths in the two arms
n	Refractive index
R, T	Reflectance and transmittance of beam splitters
T_{GB}	Transmittance of the glass block
C	Contrast of the interference fringes
S	Interference fringe spacing
FSR	Free spectral range
I_0	Input light intensity
I_1, I_2	Complementary outputs of the interferometer
I_N	Normalised intensity of the interferometer
α	Absorption coefficient decided by the media properties
L	Transmission path

Phase locking system

PID	Proportional-integral-derivative
K	Gain
T_i	Integral time
T_d	Derivative time

1 Introduction

1.1 Planar Doppler velocimetry

Velocity determination in fluid mechanics is fundamental in order to have a better knowledge of the flow behaviour. Maps of the flow velocity field help determine the flow structure and turbulence properties.

The reliability of computational fluid dynamics (CFD) depends on validation with proper experimental data in order to be accepted. Modern computer technology has developed the theoretical simulations of all kinds of flows to a level beyond experimental data, increasing the need to provide validation data [1].

Experimental techniques to measure the fluid flow velocity can be generally classified as intrusive and non-intrusive. Intrusive techniques require that a mechanical probe must be introduced into the flow, while non-intrusive techniques are those where the measurement devices are outside the flow; it does not disturb the flow field. Intrusive techniques have been used to measure the flow properties, such as pressure, temperature, density and local velocity. Traditional techniques such as pitot-static tubes and hot wire anemometers, although cost-effective where high accuracy is not required, perturb the flow under investigation and can not be mounted where they would be damaged by motion of the test piece, for example, in the rotor in gas turbine compressors. Their performance is compromised by the high temperatures and vibration often associated with the measurement environment.

Non-intrusive point and planar optical techniques are therefore being developed to overcome these problems. These either measure transit time of a particle between two locations such as laser two focus (L2F) [2] and particle image velocimetry (PIV) [3], or monitor the optical Doppler shift in frequency experienced by monochromic light scattered from seed particles entrained in the flow such as laser Doppler velocimetry (LDV) [4] and planar Doppler velocimetry (PDV) [5]. The point technique of LDV, also called laser Doppler anemometry (LDA), is well established and very accurate, but to build a three-component velocity vector map with good spatial resolution over an extended region requires a large number of individual measurements and can be very time-consuming. There is therefore great interest in planar techniques, which provide velocity information over a two-dimensional region from a single measurement. Illumination of the flow now uses a laser beam that is either scanned or expanded to generate a light sheet.

The relatively recently-developed technique of planar Doppler velocimetry (PDV) [6-8], also called Doppler global velocimetry (DGV) [9,10], is a Doppler-based planar technique measuring frequency shifts of laser light scattered by moving particles or molecules in a flow, from which the velocity is determined using the Doppler equation.

$$\Delta v = \frac{v_L(\hat{o} - \hat{i}) \cdot \hat{\mathrm{V}}}{c} \qquad \textbf{Equation 1-1}$$

where $\Delta v = v - v_L$ is the difference between the scattered light frequency, v, and the original laser light frequency, v_L. $\hat{\mathrm{V}}$ is the velocity vector associated with the scattering particles and c the free space speed of light. $\hat{o}$ and $\hat{\imath}$ are unit vectors in the observation and illumination directions respectively (Figure 1-1). The maximum Doppler frequency shift is $2\hat{\mathrm{V}} \cdot v_L / c$ when $\hat{o}$, $\hat{\imath}$, and $\hat{\mathrm{V}}$ are all aligned and $\hat{o}$ and $\hat{\imath}$ are in opposite directions. For other geometries the sensitivity of the system depends on $(\hat{o} - \hat{\imath})$.

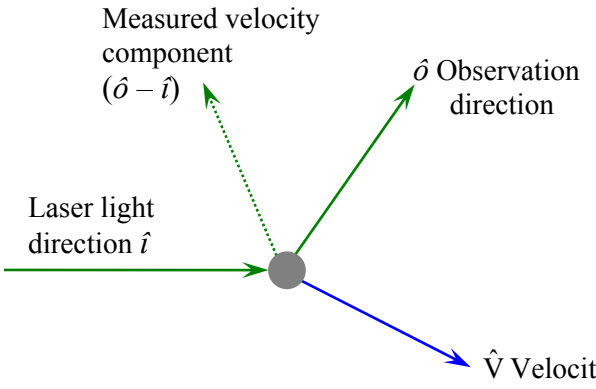

Figure 1-1 Diagram of illumination and observation directions for light scattering from a moving particle.

For a laser wavelength of 514.5nm and velocities in the range of about ±100ms^{-1}, the Doppler frequency shift is about ±200MHz. This suggested to the originators of the PDV technique the use of an atomic or molecular absorption line as a frequency-to-intensity converter [11]. In practical terms, the Doppler frequency shift is determined by imaging a flow region illuminated by a laser light sheet through a glass cell containing an atomic or molecular vapour onto the active area of a CCD camera. The laser frequency is tuned close to a value resulting in 50% absorption, so that the Doppler frequency shift registers in the camera image as a spatial variation of intensity depending on the degree of absorption of light scattered from any particular particle in the flow. Figure 1-2 shows the absorption spectrum centered around 514.5nm calculated using Forkey's model [12] for a typical iodine cell and the frequency-to-intensity conversion relationship.

A typical configuration is shown in Figure 1-3. The laser beam is formed into a light sheet to illuminate the flow region of interest. The scattered light is collected and divided into two parts of equal intensity by a beam splitter. One image is captured by the signal camera after passing through an iodine cell. The other image is recorded by a reference camera. From the cameras, the transmission through the cell is obtained by dividing the intensities of the signal and reference cameras at corresponding pixels after proper calibration. The Doppler frequency shift can be found using the frequency function of the filter providing the laser frequency is known. This process is repeated at each pixel and the velocity is then calculated at each camera pixel using the measured Doppler frequency shift (Equation 1-1). The result is either a time-averaged or instantaneous velocity map depending on the type of the laser used (continuous wave or pulsed). The second and the third velocity components are obtained by measuring different values of $(\hat{o} - \hat{\imath})$.

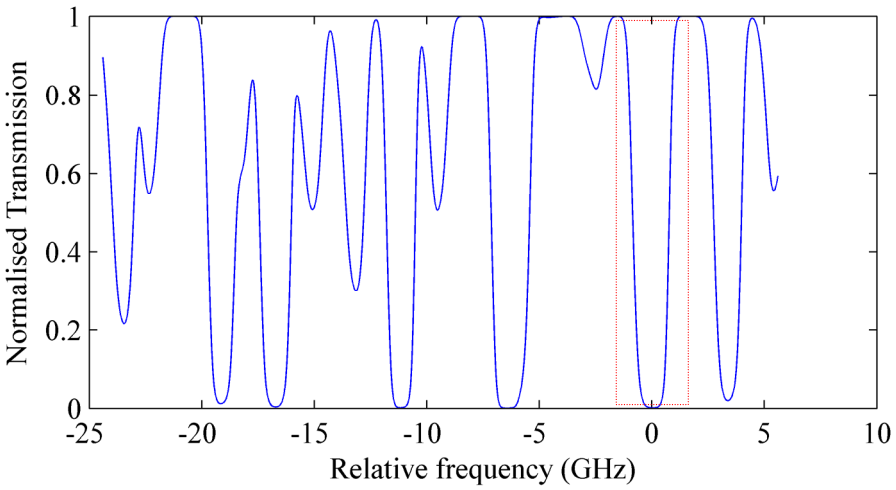

(a)

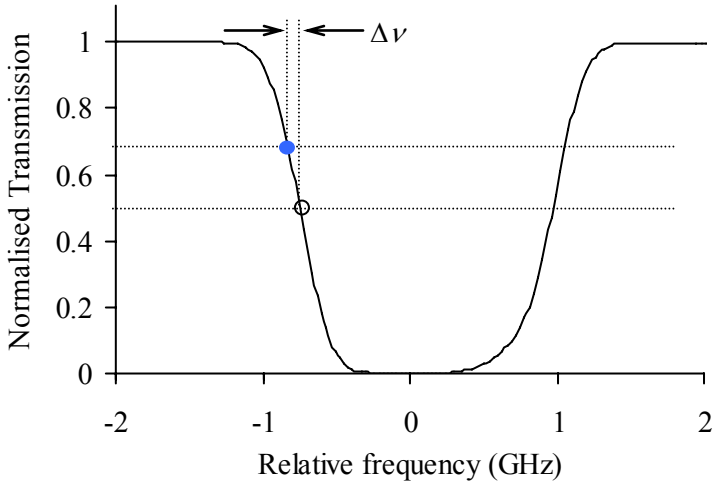

(b)

Figure 1-2 (a) Example of the iodine absorption spectrum centered around 514.5nm, calculated using Forkey's model [12]. (b) A graph showing line marked in 1-2(a) used for a measurement.

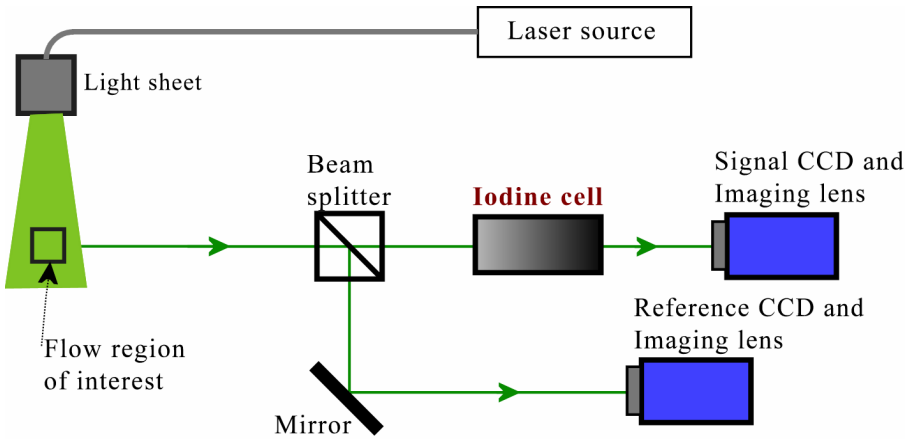

Figure 1-3 A typical PDV arrangement for single component measurement.

However, the use of molecular gas cells has several disadvantages. The first is that the choice of lasers is limited by the requirement to tune onto an appropriate absorption line of the filter. The second is that the transmission function is determined by the form of the gas absorption line and therefore the sensitivity given by the gradient of the transmission function can not be increased, although it is possible to broaden the spectral feature, thus reducing the sensitivity whilst increasing the range, by the addition of buffer gases [13].

Optical interferometry, another technique for frequency-to-intensity conversion, also allows the visualisation of a velocity field [14]. The Doppler frequency shifted light scattered from a flow leads to a change of the light intensity distribution in an interference pattern which directly relates to the flow velocity. This thesis involves the use of a Mach-Zehnder interferometric filter in a novel planar Doppler velocimetry (PDV) system, to measure fluid flow velocity fields over a plane defined by a laser light sheet. The technique is described more completely in chapter 4 of the thesis.

1.2 Optical interferometry – frequency discrimination

Optical interferometers are optical instruments that use optical coherent interferometry to measure wavelength, very small distances and thicknesses as a frequency discriminator. A very common interferometer is Michelson, whose basic configuration includes a monochromatic light source, a beam splitter and two mirrors shown in Figure 1-4(a). Another common two-beam interferometer is Mach-Zehnder interferometer. The difference from Michelson interferometer is that it has two beam splitters for input beam division and combination respectively providing two complementary outputs shown in Figure 1-4(b). This makes it a much more versatile instrument because each of the widely separated beam paths is travelled only once, which improves its sensitivity in contrast to the Michelson interferometer under the same conditions. On the contrary, this makes it more sensitive to changes in the surrounding environment than Michelson interferometer because of its larger setup.

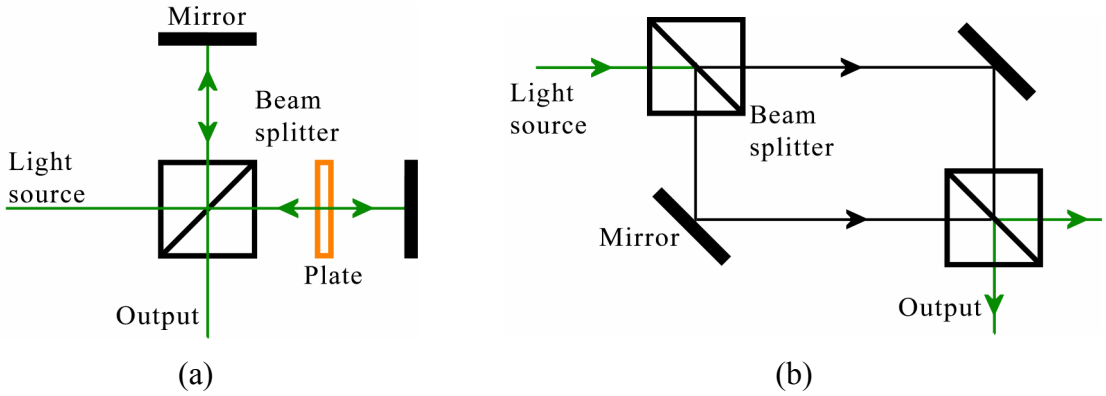

Figure 1-4 Basic interferometer configurations. (a) Michelson. (b) Mach-Zehnder.

For unbalanced Michelson and Mach-Zehnder interferometers, in which the optical paths travelled by the beams are of unequal length, the phase difference $\Delta\varphi$ between beams transmitted via each of the two interferometer paths is dependent on the optical frequency Δv.

$$\Delta\varphi = \frac{2\pi\left(\int_{l1} n(l)dl - \int_{l2} n(l)dl\right)\Delta v}{c}$$ **Equation 1-2**

where $n(l)$ is the refractive index at any position l in each of the two paths $l1$ and $l2$. The output intensity follows the usual cosinusoidal dependence on phase difference, as shown in Figure 1-5, thus interference at the interferometer output results in a cosinusoidal dependence of intensity on Doppler frequency shift. It can be inferred from Equation 1-2 that the frequency sensitivity can be adjusted by using different optical path differences in the interferometer. This will be discussed further in chapter 4.

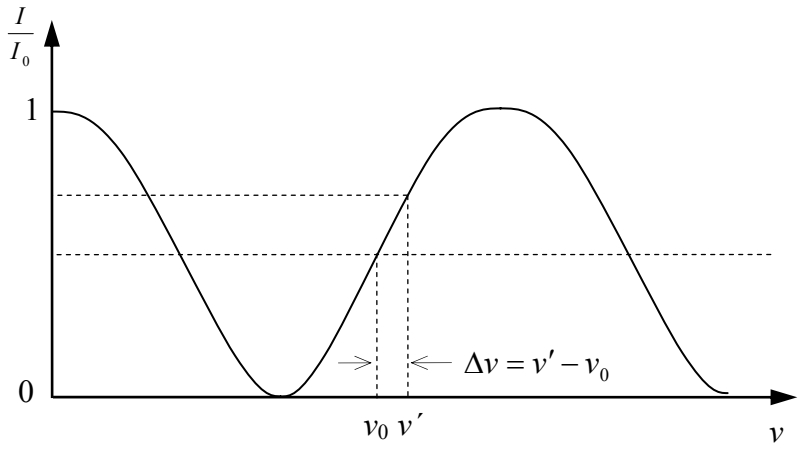

Figure 1-5 Normalised intensity, I/I_0, dependence on optical frequency, v, in an interferometer. I_0: original intensity. The Doppler frequency shift is measured as a change in normalised intensity. $\Delta v = v' - v_0$ is the difference between the Doppler shifted frequency (v') and the frequency of the light source (v_0).

In 1971 [15] an optical scheme employing a Fabry-Perot interferometer as the frequency discriminator was developed to make a velocity measurement at a point defined by a focused laser beam. For planar velocity measurements Michelson interferometer configurations have previously been used [16,17]. They offer large optical path differences in a compact instrument, which also helps reduce sensitivity to environmental perturbations such as temperature variations and mechanical vibrations. However, because only one output can be accessed [17], additional optical parts are necessary to obtain a normalised signal to correct for variations in input light intensity.

In this thesis, a Mach-Zehnder interferometric filter is used as a frequency-to-intensity converter in a PDV system, instead of the molecular filter commonly used. As a Mach-Zehnder provides two complementary outputs, the input light intensity can be normalised without introducing auxiliary optical components. As both outputs of the interferometric filter are sensitive to the Doppler frequency shift, and are in antiphase, normalisation is achieved by taking the difference of the two outputs divided by the sum. This also makes the visibility of the transfer function (normalised light intensity against frequency) twice as large as for a Michelson interferometer under the same conditions, improving both the potential measurement accuracy and resolution.

Another potentially significant advantage over a conventional PDV system is the ability to vary the frequency (and velocity) sensitivity of the filter that is more limited to the molecular absorption line shape. This will be further discussed in chapter 4.

1.3 Contents of thesis

Chapter 2 contains an overview of optical flow velocity measurement techniques. The chapter introduces the development of optical methods to measure flow velocity and their basic principles. Advantages and disadvantages of these techniques are presented and comparisons between them are made.

Chapter 3 is a review of planar Doppler velocimetry. Current developments in the state of the technique are summarised. The two methods of frequency-to-intensity conversion for PDV, molecular absorption filters and optical interferometers, are described and compared. Finally, the main components, the procedures and error sources in PDV systems are reviewed.

Chapter 4 introduces the Mach-Zehnder interferometric filter based PDV (MZI-PDV) technique, with a description of the working principle and theoretical characterisation such as polarisation sensitivity of the beam splitters, Fabry-Perot effect of the glass block, and flatness effect of the optical components. Its advantages and disadvantages are analysed along with comparisons to other techniques.

Chapter 5 reports the development of a single velocity component MZI-PDV system. The chapter includes the details of the laser system, light sheet generator and the imaging head. A modified infinity-corrected microscope optical system was investigated experimentally for constructing the MZI. A phase-locking system designed to stabilise the interferometric filter is also described. The chapter describes two methods of calculating the velocity from the interference fringe pattern; the first uses the shift of the fringe pattern minima to determine the Doppler frequency shift along profiles. The second provides a measurement of the Doppler frequency shift at every pixel in the images by normalising the receiving light intensity using the two outputs of the interferometer. The factors that will affect the uncertainty in MZI-PDV measurements are investigated including the number of the interference fringes and the image processing methods. The factors that will affect the quality of the interference fringe image are also investigated including the inclination angle and the optical path difference deviation in the MZI.

The transmission profile (normalised intensity) of the interferometric filter was investigated by scanning the frequency the laser or modulating the interferometer optical path difference and monitoring the complementary outputs. Results for measurements on a rotating disc with maximum velocities of $\sim\pm 70 ms^{-1}$ at the edge, and measurements on a seeded air jet flow with a nozzle diameter of 20mm and an exit velocity of $\sim 85 ms^{-1}$ are presented. The measured velocity values for the disc are then compared with the calculated ones from an optical tachometer measurement. The measured velocities for the air jet flow are compared with the expected velocities calculated using empirical equations to describe the jet.

Chapter 6 describes a three-component MZI-PDV system by introducing an imaging fibre bundle with multiple channels to port multiple views to a single imaging head. The chapter presents measurement results on a rotating disc and a seeded air jet flow.

Chapter 7 gives the thesis conclusion with a discussion of the main points studied and suggests directions for future work and investigation.

1.4 References

[1] Schodl, R., Willert, C., Roehle, I., Heinze, J., Foerster, W., Fischer, M. and Beversdorff M. (2002), "Optical diagnostic techniques in turbomachinery", *22nd AIAA Aerodynamic Measurement Technology and Ground Testing Conference,* St. Louis, Missouri, AIAA Paper 2002-3038.

[2] Kost, F. and Kapteijn, C. (1997), "Application of laser-two-focus velocimetry to transonic turbine flows", *7th International Conference on Laser Anemometry—Advances and Applications,* University of Karlsruhe, Germany.

[3] Adrian, R.J. (2005), "Twenty years of particle image velocimetry", *Experiments in Fluids,* Vol. 39, No. 2, pp. 159-69.

[4] Yeh, Y. and Cummins, H.Z. (1964), "Localised fluid flow measurement with a He-Ne laser spectrometer", *Applied Physics Letters,* Vol. 4, No. 10, pp. 176-78.

[5] Komine, H., Brosnan, S.J., Litton, A.B. and Stappaers, E.A. (1991), "Real-time Doppler global velocimetry", *29th AIAA Aerospace Sciences Meeting,* Reno, NV, AIAA Paper 91-0337.

[6] Smith, M.W., Northam, G.B. and Drummond, J.P. (1996), "Application of absorption filter planar Doppler velocimetry to sonic and supersonic jets: Aerodynamic measurement technology", *AIAA Journal,* Vol. 34, No. 3, pp. 434-41.

[7] Charrett, T.O.H. and Tatam, R.P. (2006), "Single camera three component planar velocity measurements using two-frequency planar Doppler velocimetry (2*v*-PDV)", *Measurement Science and Technology,* Vol. 17, No. 5, pp. 1194-206.

[8] Arnette, S.A., Samimy, M. and Elliott, G.S. (1998), "Two-component planar Doppler velocimetry in the compressible turbulent boundary layer", *Experiments in Fluids,* Vol. 24, No. 4, pp. 323-32.

[9] Meyers, J.F. (1995), "Development of Doppler global velocimetry as a flow diagnostics tool", *Measurement Science & Technology,* Vol. 6, No. 6, pp. 769-83.

[10] Ainsworth, R.W., Horpe, S.J. and Anners, R.J. (1997), "New approach to flow-field measurement - a view of Doppler global velocimetry techniques", *International Journal of Heat and Fluid Flow,* Vol. 18, No. 1, pp. 116-30.

[11] Komine, H. and Torrance, C. (1990), "System for measuring velocity field of fluid

flow utilizing a laser-Doppler spectral image converter", *United States Patent*, No.4, 919, 536.

[12] Forkey, J.N., Finkelstein, N.D., Lempert, W.R. and Miles, R.B. (1996), "Demonstration and characterization of filtered Rayleigh scattering for planar velocity measurements", *AIAA Journal,* Vol. 34, No. 3, pp. 442-8.

[13] Chan, V.S.S., Heyes, A.L., Robinson, D.I. and Turner, J.T. (1995), "Iodine absorption filters for Doppler global velocimetry", *Measurement Science and Technology,* Vol. 6, No. 6, pp. 784-94.

[14] Seiler, F. and Oertel, H. (1985), "Visualization of velocity fields with Doppler-pictures", *Flow Visualization III, Proceedings of the Third International Symposium on Flow Visualization,* Ann Arbor, MI, pp. 454-9.

[15] Tatam, R.P. (1999), "Speckle interferometry: Optoelectronic developments and applications", *Proceedings of the Interferometry: Applications, Proceedings of SPIE*, Pultusk, Pol, Vol. 3745, 114-33.

[16] Smeets, G. and George, A. (1981), "Michelson spectrometer for instantaneous Doppler velocity measurements", *Journal of Physics E (Scientific Instruments),* Vol. 14, No. 7, pp. 838-45.

[17] Seiler, F., George, A., Leopold, F., Srulijes, J. and Smeets, G. (1999), "Flow velocities visualization using Doppler picture interference velocimetry", *18th International Congress on Instrumentation in Aerospace Simulation Facilities (ICIASF 99), IEEE*, Toulouse, France, 11.1-8.

2 Overview of optical flow velocity measurement techniques

2.1 Introduction

This chapter contains an overview of optical flow velocity measurement techniques, including non-intrusive point, such as LDV and L2F, and planar, such as PIV and PDV, optical methods. The advantages and disadvantages of the techniques are discussed and compared.

2.2 Laser Doppler velocimetry

Laser Doppler velocimetry (LDV), also referred to as laser Doppler anemometry (LDA), is a technique measuring the flow velocity by sensing the Doppler frequency shift of laser light scattered by small particles moving in the flow field. Since its discovery by Yeh and Cummins in 1964 [1], it has become one of the most established local velocity measurement methods in flow measurement. Here only the basic principles of a typical LDV system and some components and techniques widely used are reviewed, although many LDV configurations have been developed [2].

2.2.1 Doppler frequency shift of light scattered by small particles

The fundamental phenomenon in LDV is the Doppler frequency shift of light that is scattered from small particles (typically 0.1 to 10μm in diameter). Consider a monochromatic collimated laser beam of an optical frequency v and wavelength λ illuminating a flow field containing small particles, whose sizes are in the order of λ and move with velocity $\hat{\mathrm{V}}$ (Figure 2-1). The scattered laser light is received by a detector, and its frequency $v + \Delta v$ is different from the incident beam frequency v. The difference Δv is called the Doppler frequency shift. This phenomenon is called the Doppler Effect. The Doppler frequency shift Δv depends only on the speed of the particle, the incident light wavelength, and the scattering angle ϕ:

$$\Delta v = \frac{\hat{\mathrm{V}} \cdot (\hat{o} - \hat{i})}{\lambda} = \frac{2\sin(\phi/2)}{\lambda}\mathrm{V}_{\phi} \qquad \textbf{Equation 2-1}$$

where $\hat{i}$ and $\hat{o}$ are respectively, the unit vectors parallel to the incident and scattered light beams and V_{ϕ} is the component of the particle velocity vector in the direction of $(\hat{o} - \hat{i})$ which is normal to the bisector of the angle ϕ.

In theory, the velocity component V_{ϕ} can therefore be obtained from a known Doppler frequency shift Δv given the parameters λ and ϕ without any calibration. In practice, moving particles slower than several hundred meters per second cause Doppler frequency shifts that are relatively small compared to the incident laser frequency. For this reason, although possible, direct Doppler frequency measurement is limited by practical problems unless the flow velocity is extremely high. This is because that there is no instrument to provide such a large electronic bandwidth to measure the frequency of the laser. Therefore, indirect measurement methods have been developed to

overcome these problems of measuring the Doppler frequency. Most workable laser Doppler measurement configurations therefore make use of the techniques of optical beating [1], interference [3] and molecular filtering [4], in which case the Doppler frequency shift be measured accurately.

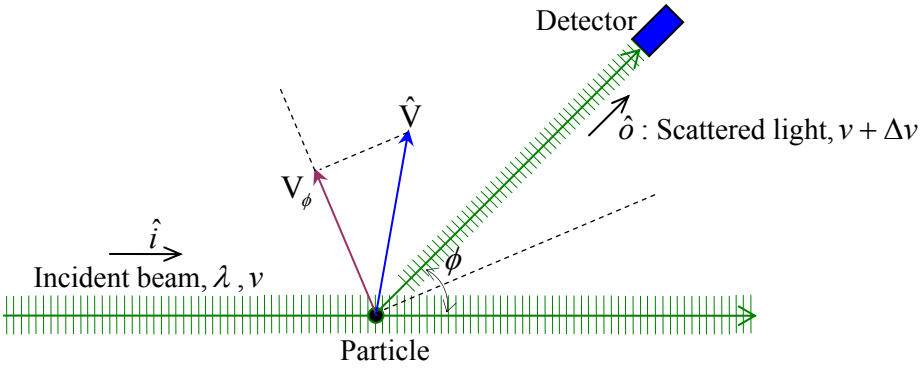

Figure 2-1 Diagram of laser beam light scattered by a moving particle.

An LDV system will be sensitive to tracer particle motion in a particular direction and hence for the measurement of only one component of the velocity vector. The measurement velocity range is from ~0ms^{-1} to supersonic depending on the experimental ability to measure the frequency. It is possible to determine the direction of the measured velocity component by using the direction of the frequency shifting relative to the un-shifted laser light frequency. A widely used and commercially available configuration in LDV is the dual-beam technique described below. Other configurations that have been used are the reference [1], one beam [5], spectrometer [3,6] and molecular filtering [4] methods.

2.2.2 Dual-beam LDV

A typical single component dual-beam LDV is shown in Figure 2-2. A collimated light beam from a monochromic laser, usually He-Ne or argon-ion, is divided into two beams of equal intensity by a beam splitter. With the help of one mirror and focussing lens, the two parallel beams intersect in the focal plane of the lens at an angle θ, where they interfere to produce fringes. These fringes are equidistant and are alternating dark and bright planes. When a small particle moves across these fringes with a velocity $\hat{V}$, the amplitude of the scattered light from the fringe area (measuring volume) is modulated at a frequency v_D determined by the ratio of the velocity component V_θ perpendicular to the fringes and the fringe space d:

$$v_D = \frac{V_\theta}{d} \qquad \textbf{Equation 2-2}$$

where $d = \lambda/(2\sin(\theta/2))$. The velocity can then be easily calculated using frequency v_D, which is independent of the observation direction. v_D can be measured from the output photocurrent generated by the photodetector by using optical heterodyne detection. When two light waves mix and interfere on the surface of a photodetector, a signal that oscillates at the frequency difference is produced, which can be detected if it lies within the frequency bandwidth of the detector.

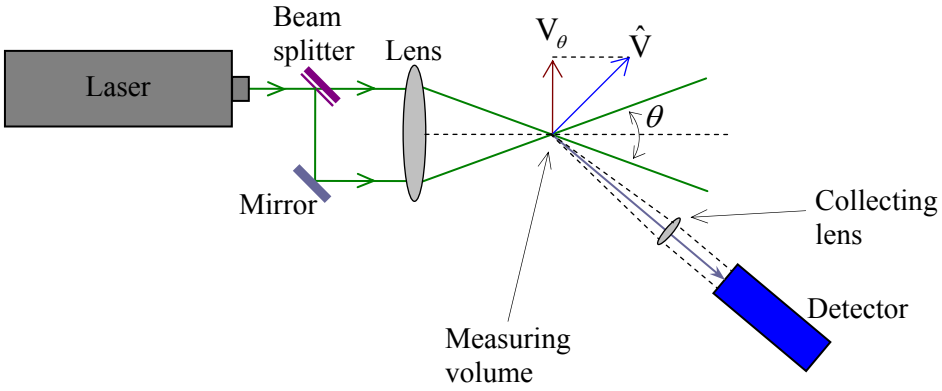

Figure 2-2 Diagram of a dual-beam laser Doppler velocimetry configuration.

It follows from Equation 2-2 that the relationship is linear when the fringe space d is determined. There are some errors and uncertainty in LDV measurements. The first is the fringe divergence uncertainty. The interference fringes in the measuring volume will not be equidistant when the beams do not overlap at their waists leading to measurement errors. Ideal equidistant line fringes are thus required in practical experimental arrangements. The second is the velocity bias: the measured average velocity value will be biased to higher values compared with the real local average velocity, because more particles with faster velocities would be recorded than slower ones in the measuring volume. This bias is worse for turbulent flows where particles are irregularly distributed in the stream. To correct for this bias, a commonly used method is the transit time weighting correction [7,8], where the particle transit time would be used as a weighting function to correct for this. The mean measured velocity without bias correction is,

$$\overline{V}_{unweighted} = \frac{\sum V_i}{N_0} \qquad \textbf{Equation 2-3}$$

where V_i is instantaneous velocity measured by the i-th particle and N_0 total measured particle number. The mean velocity corrected by the transit time weighing method is,

$$\overline{V}_{weighted} = \frac{\sum V_i dt_i}{\sum dt_i} \qquad \textbf{Equation 2-4}$$

where dt_i is the transit time of the i-th particle. The transit time is defined as the time required for the particle to cross the LDV measuring volume.

Another error source in LDV is Doppler ambiguity: the frequency spread in the power spectrum generated by the photodetector will lead to an ambiguity in the measurement of the Doppler frequency. This can be considered in terms of the fringe model in the LDV measuring volume [9]. Suppose that there are N fringes of spacing d. For a particle travelling with speed V, the Doppler frequency is obtained using Equation 2-2 and lasts for a time $\Delta t = Nd/V$. The Doppler signal has a frequency spread of $2V/Nd$ because it lasts for a finite time. Therefore, the width of the frequency spectrum divided by the centre frequency is $2/N$. It can be seen that the more fringes there are, the narrower the Doppler frequency spectrum leading to a smaller Doppler ambiguity.

The basic dual-beam LDV system described above can only measure one velocity component, which is normal to the bisector of the angle between the two illumination laser beams. By using multiple two-beam laser systems, each system having a different laser frequency, two or three-component velocities can be achieved since multiple fringe patterns would be formed in the same flow measuring volume, each allowing one velocity component to be measured. This arrangement is called a two or three-colour LDV system [10,11]. Optical band-pass filters are used in front of each photodetector to make sure that only light from a single fringe pattern is recorded by each detector. In theory, the system can use two or three lasers providing different wavelengths, however, it is more common in practice to use only one laser with multiple wavelength lines. For example, an argon-ion laser is suitable for this purpose because it has three powerful lines (λ = 514.5nm, λ = 488nm and λ = 476.5nm [12]. The disadvantages of the technique are the high cost and the complex laser alignment involved, although it can make instantaneous measurements and the flow is not disturbed.

The reference beam [1] and one beam [5] LDV experimental configurations extract the velocity information by measuring optical Doppler frequency beating between the illumination laser beam and a reference beam or between two scattered beams in two observation directions. The former shown in Figure 2-3(a) is useful when the velocity component along the reference beam direction is wanted, while the latter shown in Figure 2-3(b) is simple and easy to set up because only one laser light beam at one frequency is employed to focus on the flow field.

However, the wavefronts of the interfering beams in the two configurations must be well matched onto the photodetector, leading to limited collection angle, which also causes a poor signal-to-noise ratio. The scattered light intensity is required to be as large as possible to improve the signal-to-noise ratio of the photodetector. For 3-component velocity measurements, a combined dual-beam and reference beam LDV system [13,14] can be used, where the dual-beam subsystem is to measure two in-plane velocity components while the reference beam one is for the third out-of-plane component measurement.

Spectrometer based LDV detects the frequency change directly by using a spectrometer. As a spectrometer, the Fabry-Perot [3,15] and Michelson interferometers [6] are well developed and have been used to measure the local fluid flow velocity. This technique is especially used in high velocity flow situations where a large Doppler frequency shift may be obtained. Molecular filter based LDV uses a molecular filter, for example an iodine vapour, as an optical frequency-to-intensity converter to detect the frequency change. This technique has being well developed and expanded to planar flow measurements in PDV. This will be further discussed in chapter 3.

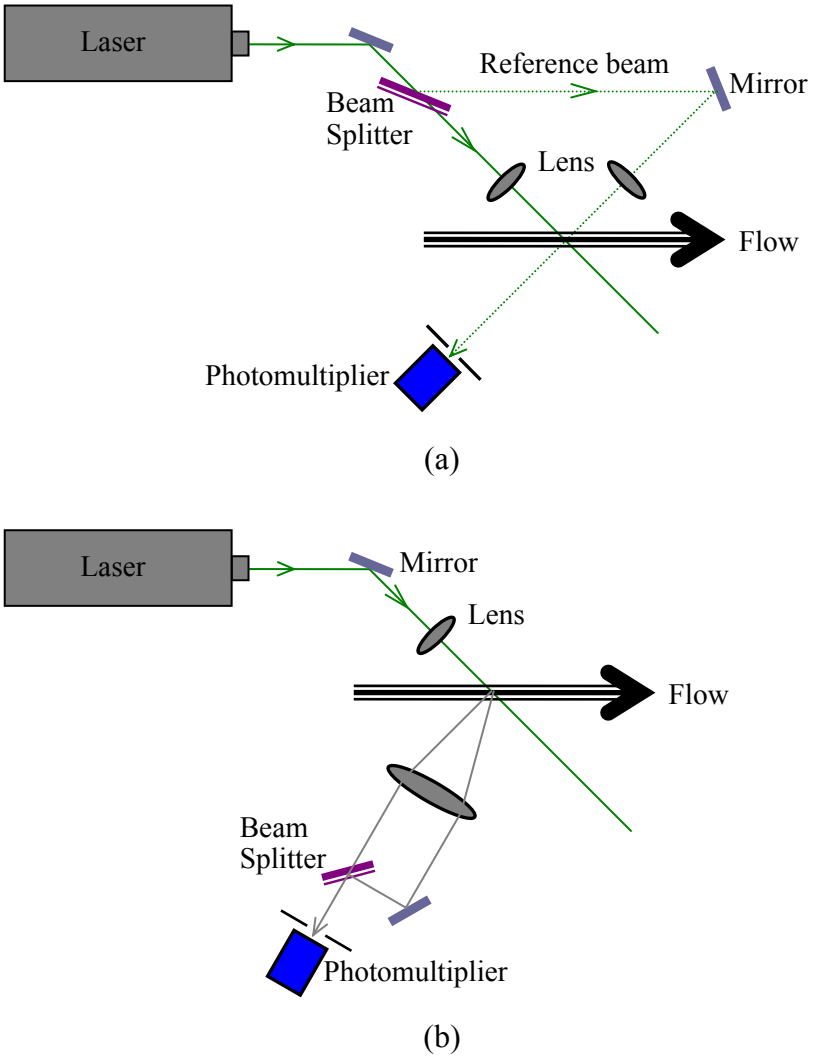

Figure 2-3 (a) Diagram of a reference beam LDV configuration. (b) Diagram of a one beam LDV configuration.

A summary and comparison of possible LDV configurations is shown in Table 2-1. LDV, one of the most widely used flow velocity measurement technique, has many advantages. It is a non-intrusive method providing instantaneous accurate velocity information. The standard LDV system is sensitive to one velocity component, and it can be extended to two or three components. It is particularly suitable for high velocity flow measurements. However, it is very difficult to make measurements in a large area as it is a point measurement technique. Area measurements can be made by scanning across the flow field, which can be very time-consuming and high running costs in experimental facilities.

Table 2-1 A summary and comparison of possible LDV configurations.

LDV configuration	Principles/Advantages	Disadvantages
Reference beam	Doppler effect and optical heterodyne detection Selectable measured component (along reference beam)	Limited coherent aperture Low signal-to-noise ratio, although increased by increasing the reference beam power Single-component point measurement
One beam	Doppler effect and optical heterodyne detection Simple and easy to set up	Limited coherent aperture Low signal, no further development Difficult to measure the Doppler frequency shift directly
Dual-beam	Doppler effect and optical heterodyne detection Unlimited collection aperture Independent of the observation direction Two or three-component measurements	Fringe divergence uncertainty Velocity bias Doppler ambiguity Point measurement
Spectrometer-based	Doppler effect and interference Suitable for high velocity flows	Single-component point measurement Limited for low velocity flows
Molecular filter-based	Atomic or molecular absorption lines Well developed for planar measurements	Limited choice of lasers Measurement range and sensitivity fixed the form of the absorption lines.

2.3 Particle displacement methods

The common measuring principle in particle displacement methods is that fluid velocities are measured by recording the displacement of particles in a flow in a known time interval or by recording the time taken by particles to move a known displacement. These methods are non-intrusive and they can provide two or three-component velocity measurements.

Laser two focus (L2F) velocimetry is a single point technique. It measures the time of flight of particles crossing two fixed laser beams in a measuring volume. It has been well developed because of its easy optical access to the flow field since it uses a back-scattering technique with a confocal optical path beam. It also can detect very small particles, typically 0.2μm in diameter [16]. The technique can be used to make 3-component measurements combined with a Doppler global velocimeter [17], where the L2F subsystem provides two components of the velocity while the PDV measures the in-line velocity component [17].

Whole-field velocimetry techniques based on particle tracking methods include Laser speckle velocimetry (LSV), particle image velocimetry (PIV), particle tracking velocimetry (PTV) and molecular tagging velocimetry (MTV). These techniques provide simultaneous visualisation of the two-component velocity field over an entire plane in steady/unsteady flows in a single measurement.

2.3.1 Particle tracking velocimetry

Particle tracking velocimety (PTV) determines the local velocity by measuring the distance between positions of individual particles entrained in a flow at a known time interval

$$V_m = \lim_{\Delta t \to 0} \frac{\Delta x}{\Delta t} \qquad \textbf{Equation 2-5}$$

where Δx is the distance determined by the movement of a seeded particle in time Δt. For a fixed Δt, the measured velocity can be calculated by accurately measuring Δx. Two well-established PTV algorithms are the four-frame in-line tracking method [18], which uses four sequential images of the tracked particle, and the binary image cross-correlation method [19], which uses only two sequential images.

The advantage of the PTV technique over PIV for some flow fields is that PIV is not suitable to track the movement of individual particles in time, while PTV can follow the motion of a single particle but with lower spatial resolution. The technique is therefore suitable for flows where the particles are well defined in the images and the field is sparsely seeded.

The disadvantage is that PTV becomes inefficient when individual particles overlap and therefore velocities can not be properly extracted. In PTV, 2 or 3-compoent velocity measurements can be made by using two or three camera arrangements [20,21]. A technique called hybrid particle image velocimetry [22], a combination of PTV and

PIV, was developed to investigate how the motion of a single particle was influenced by its size, shape and deformation.

2.3.2 Laser speckle velocimetry

Laser speckle vleocimetry (LSV) measures the velocity field by analysing successive recorded images of speckles generated by the interference of scattered light from each particle inside a flow [23]. The speckle patterns will move with the particles that generate them. In order to generate speckle, the concentration of particles in the flow must be high so that their images overlap and interfere, which is not easily obtained for certain flows. The LSV technique is therefore limited to special flow conditions. The technique when used with a low particle concentration is called particle image velocimetry (PIV).

2.3.3 Particle image velocimetry

Particle image velocity (PIV) is a well developed planar flow velocity measurement technique that measures the velocity of groups of particles across the plane of a laser light sheet [24,25].

In PIV for gas phase flow measurements, a pulsed laser beam is formed into a light sheet to illuminate the particles seeded in a flow (Figure 2-4). The scattered light from these particles is then imaged on a recording media which are widely based on digital image recording. Therefore, PIV is more often termed digital particle image velocimetry (DPIV). The technique requires two sequential images to be recorded with a known time interval between them. In the most popular method, a Nd:YAG laser is used to illuminate the flow area with two sequential laser pulses, a CCD camera is then used to record the two images. Generally there are two operation modes in image recording; one is to record two images in the same frame (multi-exposures/single frame); the other is to record each image in a separate frame (double exposures/double frames).

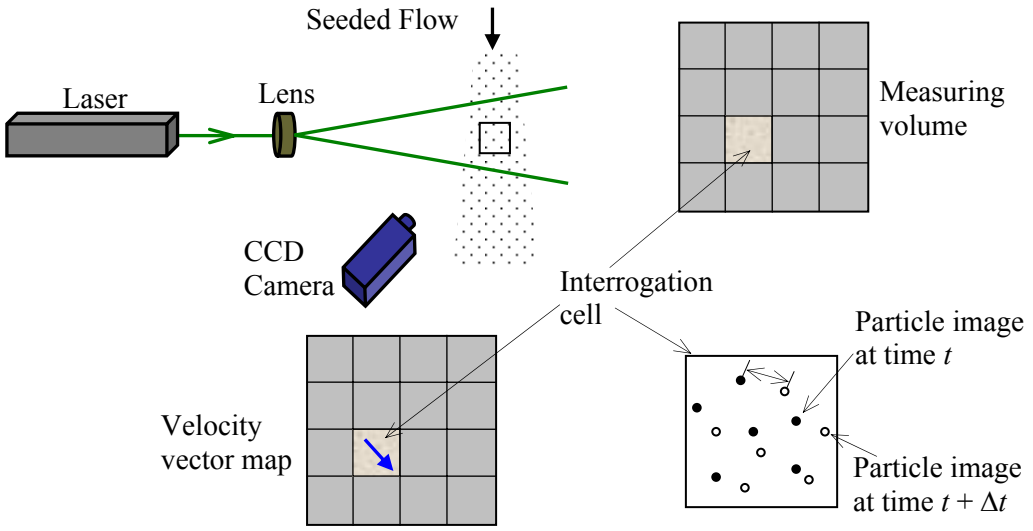

Figure 2-4 Principle of operation of a typical PIV.

Its difference from LSV is that the concentration of particles in PIV is low enough for the images of small groups of particles to be captured and not to interfere with each other. Its difference from PTV is that subdivisions of the images, called interrogation cells, are used to calculate the local flow velocity while PTV is based on a single particle. With modern developments in high-speed computers and digital image recording techniques, PIV has been rapidly developed and is still in the development. Standard PIV systems are now commercially available typically including a 2,000×2,000 pixel CCD camera, a double-pulsed Nd:YAG laser and a software package.

The standard PIV method gives only two in-plane velocity components. The use of a stereo-camera arrangement allows the third out-of-plane component to be measured where the flow in the illuminated plane is viewed from two different directions simultaneously. The most widely used method is stereoscopic PIV [26] and its two basic configurations are shown in Figure 2-5. In the translation method, the image plane is translated parallel to the object plane. The optical axes of the cameras are perpendicular to the object plane. The advantage of this method is that the magnification of the two cameras is the same, so that a fixed displacement in the object plane always corresponds to the same displacement in the image plane. However, the disadvantage is that it is not possible to use large viewing angles, because the off-axis distance increases as the viewing angle increases, leading to worse image quality as a result of lens aberrations. In the angular displacement method, the optical axis of each camera is rotated with respect to the object and image planes. An advantage is that the lenses are used with small viewing angles reducing the lens aberrations. However, the image magnification of the two cameras is no longer the same, which makes it difficult to compute the in-plane displacement.

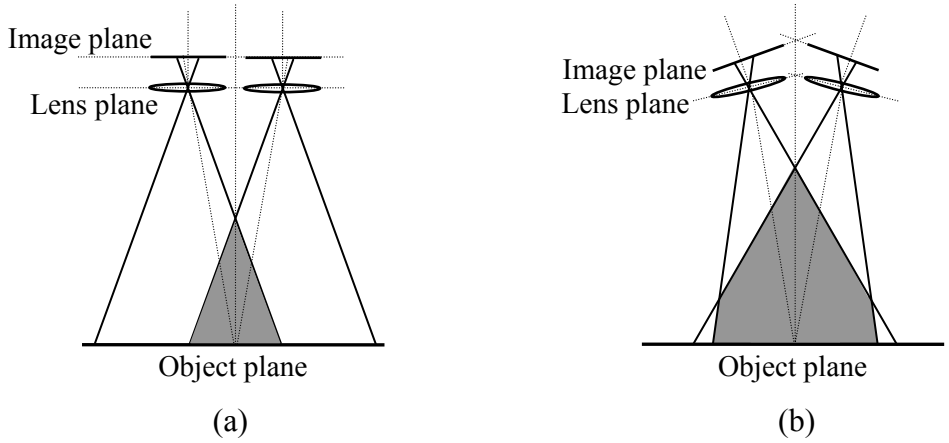

Figure 2-5 The 3-component stereoscopic PIV optical configurations. (a) Translation method. (b) Angular displacement method [26].

Another technique for three-component velocity measurements is holographic digital particle image velocimetry (HDPIV) [27-29]. Generally holography is a method to store the amplitude and the phase of a light wave by recording the interference pattern that occurs when mixed with a reference light wave. The recorded hologram is used to rebuild the original light wave field by illuminating it with the original reference light wave. In HDPIV, the scattered laser light from particles in a flow is combined with the

reference laser light from the same illumination laser to generate the hologram. A real image of the particle field in space can be reconstructed when the recorded hologram is illuminated with the complex conjugate of the original reference light. With a CCD camera, a plane anywhere through the field can therefore be examined for particles. A good feature in HDPIV is the almost unrestricted recording depth of holography.

However, in PIV the measurement dynamic range depends on the modern pulsed laser technology and high-speed CCD camera development. In addition, PIV requires high-quality images of individual particles or groups of particles limiting the measurement area because it correlates images of particles on two successive camera images in the flow.

2.3.4 Molecular tagging velocimetry

Molecular tagging vleocimetry (MTV) [30,31], also called flow tagging velocimetry [32] and planar laser-induced fluorescence velocimetry (PLIF) [33], is a whole-field optical diagnostics technique measuring flow velocity by tracking the motion of photosensitive molecules in a flow. Typically a pulsed laser beam illuminates and excites molecules seeded in a flow field, and those tagged molecules are interrogated with two successive images taken by a CCD camera in a known time interval. Compared with seed particle based LDV, PDV and particle displacement methods, MTV does not require seed particles, but it requires special photosensitive materials that fluoresce when excited in the flow field.

A summary and comparison of the velocimetry techniques based on measuring particle displacement is shown in Table 2-2. Among these techniques, PIV is more useful in industry applications because it is easily operated and has commercially available hardware and software packages. Other techniques are currently in the laboratory research stage, where they are being further advanced. In addition, a successful marriage of PIV and PLIF has been developed to make instantaneous velocity and temperature measurements in turbulent flows [34-36]. In this technique, fluorescent materials and particles were seeded in the flow and two CCD cameras were used to record the fluorescence and particle images simultaneously in two illumination laser pulses.

Table 2-2 A summary and comparison of techniques based on measuring particle displacement.

Technique	Principles/Advantages	Disadvantages	Velocity range
L2F	Time of flight Easy optical access to flows 1 or 3-component	Not suitable for planar measurements	~1 - 2000ms^{-1} [37]
LSV	Time of flight 1 or 3-component planar measurements	Requiring high concentration of particles	Velocity range from zero to supersonic
PTV	Time of flight Motion of single particle 1 or 3-component planar measurements	Low spatial resolution	Velocity range from zero to supersonic
PIV	Time of flight commercially available 1 or 3-component planar measurements	Requiring high-quality images of individual particles More uncertainty for high speed flows	Velocity range from zero to supersonic
MTV	Time of flight No seeding requirement 1 or 3-component velocity and planar measurements	Requiring special photosensitive materials in flow fields	Velocity range from zero to hypersonic [38].

2.4 Planar Doppler velocimetry

The Doppler based LDV technique is well developed and commercially available, but it is difficult to provide global velocity information as it is a point measurement technique. There is therefore great interest in the planar techniques, which provide velocity information over a two-dimensional region with a single measurement. Illumination of the flow now uses a laser beam expanded into a light sheet. PDV techniques are based on two basic operation principles; one uses a molecular absorption filter and the other is optical interference.

PDV can provide 3-component flow velocity field measurements by using three or four imaging heads [39] or a combination of single imaging head with an imaging fibre bundle with multiple channels [40].

A review on the basic principles of operation of the technique and the most important components is presented in chapter 3.

PDV provides velocity maps in a flow field as PIV does, however, the way the velocity information is obtained and processed are different. Advantages and drawbacks of PDV compared to PIV are listed in Table 2-3.

Table 2-3 A general comparison of PIV and PDV.

	PIV	PDV
Physical principle	Time of flight (particle tracking)	Doppler phenomena
Laser source	Pulsed (Nd:YAG) for gas phase flow measurements	Pulsed (Nd:YAG) or continuous wave (Argon ion)
Particle image requirement	Requiring high-quality images of individual particles (cross-correlation of two successive images)	No need for images of individual particles (intensity-based)
Spatial resolution	Limited by the size of the interrogation cell used in the cross-correlation process	High (limited to the area imaged onto a single pixel)
Velocity range	Zero to supersonic	Velocities greater than ~2ms^{-1} unsuitable for low speed flows (small Doppler frequency shifts are not easily resolved as PDV relies upon measuring changes in image intensity)
Dynamic range of measurements	~80 (an interrogation cell size of 8 pixels with a noise floor of 0.1 pixels [41])	~ 44 (a velocity range of ~260ms^{-1} with an error of ~6ms^{-1} [42])
3-component measurement	Two-camera stereo viewing	3 or 4 viewing directions required
Data processing	In minutes	In tens of seconds
Flowing seeding	Low seeding concentration with particle size of ~0.3 - 1μm	High seeding concentrations with particle size of ~0.1λ – λ (λ illumination laser wavelength)
Hardware	Most hardware and software commercially available	Custom designed, relatively complex hardware.

In some applications, there is a successful combination of PIV and PDV. One example is that rapid large area measurements can be made using PDV, while PIV is better used for small areas of interest. For example, in wind tunnel measurements where long running times are expensive, PDV can be used for a quick large flow field investigation and only smaller regions use PIV measurements for higher accuracy.

Another situation is that where 3-component velocity measurements are almost impossible using PIV or PDV because of limited optical access window. In order to solve this problem, planar particle image Doppler velocimetry (PPIDV) [43-47] has been developed to measure 3-component flow velocity in a planar area through a single optical access window. This combines components from PIV and PDV into a single imaging head to measure in- plane velocities using PIV and out-of-plane velocities using PDV.

2.5 Summary

A variety of configurations and related components and accessories have been developed for each experimental measurement of local flow velocity. Here only the basic description and the advantages/disadvantages of the techniques have been presented. A summery of the properties of the techniques is shown in Table 2-4.

Table 2-4 Summary of the properties of the optical flow velocity measurement techniques.

Technique	Summary
Hot wire anemometry	Intrusive, point measurement technique
	High accuracy and resolution
	Wide velocity range (~cms^{-1} - supersonic)
	Real-time 1 or 3-component measurements
	Low cost and easy to use
LDV	Non-intrusive, point measurement technique
	High accuracy and resolution
	Wide velocity range (0ms^{-1} - supersonic)
	Real-time and time-averaged 1 or 3-component measurements
	Commercially available
Particle displacement methods (L2F, LSV, DPIV and MTV)	Non-intrusive, point (L2F)/planar measurement technique
	Wide velocity range (0ms^{-1}- supersonic)
	Real-time and time-averaged 1 or 3 component measurements
Doppler based planar techniques (PDV)	Non-intrusive, planar measurement technique
	Velocity range (> ~2ms^{-1})
	Real-time and time-averaged 1 or 3 component measurements.

2.6 References

[1] Yeh, Y. and Cummins, H.Z. (1964), "Localised fluid flow measurement with a He-Ne laser spectrometer", *Applied Physics Letters,* Vol. 4, No. 10, pp. 176-78.

[2] Hassel, E.P. and Linow, S. (2000), "Laser diagnostics for studies of turbulent combustion", *Measurement Science and Technology,* Vol. 11, No. 2, pp. 37-57.

[3] Jackson, D.A. and Paul, D.M. (1971), "Measurement of supersonic velocity and turbulence by laser anemometry", *Journal of Physics E (Scientific Instruments),* Vol. 4, No. 3, pp. 173-7.

[4] Komine, H., Brosnan, S.J., Litton, A.B. and Stappaers, E.A. (1991), "Real-time Doppler global velocimetry", *29th AIAA Aerospace Sciences Meeting,* Reno, NV,

AIAA Paper 91-0337.

[5] Boutier A. (2000), "Laser Doppler velocimetry", *Optical Velocity Measurements-Von Karman Institute for Fluid Dynamics Lecture Series,* Rhode Saint Genese, Belgium.

[6] Smeets, G. and George, A. (1981), "Michelson spectrometer for instantaneous Doppler velocity measurements", *Journal of Physics E (Scientific Instruments),* Vol. 14, No. 7, pp. 838-45.

[7] Petrie, H.L., Samimy, M. and Addy, A.L. (1988), "Laser Doppler velocity bias in separated turbulent flows", *Experiments in Fluids,* Vol. 6, No. 2, pp. 80-8.

[8] Rinoie, K., Hata, K., Shirai, Y. and Sunada, Y. (1999), "Velocity bias corrections of laser Doppler anemometry for separated flow measurements", *Transactions of the Japan Society for Aeronautical and Space Sciences,* Vol. 42, No. 137, pp. 147-9.

[9] Watrasiewicz, B. M. and Rudd, M. J. (1976), "Laser Doppler Measurements", Butterworths Group, London Boston.

[10] Butefisch, K.A. (1989), "Three component laser Doppler anemometry in large wind tunnels", *Progress in Aerospace Sciences,* Vol. 26, No. 1, pp. 79-113.

[11] Mityushin, A.I. (2003), "A superheterodyne three-component laser Doppler anemometer", *Instruments and Experimental Techniques,* Vol. 46, No. 2, pp. 246-51.

[12] Seelhorst, U., Butefisch, K.A. and Sauerland, K.H. (1993), "Three component laser-Doppler-velocimeter development for large wind tunnel", *International Congress on Instrumentation in Aerospace Simulation Facilities,* 33.1-7.

[13] Ross, M.M. (1997), "Combined differential and reference beam LDV for 3D velocity measurement: Optical Flow Measurement: Recent Advances and Applications", *Optics and Lasers in Engineering,* Vol. 27, No. 6, pp. 587-619.

[14] James, S.W., Lockey, R.A., Egan, D.A., Tatam, R.P. and Elder, R.L. (1996), "3D fiber optic laser Doppler velocimetry", *Fiber Optic and Laser Sensors XIV, SPIE*, Denver, CO, USA, Vol. 2839, 323-34.

[15] Chehura, E. (2002), ″In-line using fibre-optic laser Doppler velocimeter using Bragg grating interferometric filters as frequency to intensity transducers", *PhD thesis,* Cranfield University, Cranfield, UK.

[16] Schodl, R. (1998), "Laser-Two-Focus velocimetry: two and three dimensional techniques", *VKI Lecture Series on Advanced Measurement Techniques,* Belgium, Vol. 1.

[17] Roehle, I., Karpinsky, G. and Schodl, R. (1999), "3-component-Doppler-laser-2-focus: a new kind of three component velocimeter", *International Congress on*

Instrumentation in Aerospace Simulation Facilities, IEEE, Toulouse, France, 13-1.

[18] Hassan, Y.A. and Canaan, R.E. (1991), "Full-field bubbly flow velocity measurements using a multiframe particle tracking technique", *Experiments in Fluids,* Vol. 12, No. 1-2, pp. 49-60.

[19] Hassan, Y.A., Blanchat, T.K. and Seeley, C.H.J. (1992), "PIV flow visualisation using particle tracking techniques", *Measurement Science and Technology,* Vol. 3, No. 7, pp. 633-42.

[20] Kasagi, N. and Nishino, K. (1991), "Probing turbulence with three-dimensional particle-tracking velocimetry", *Experimental Heat Transfer,* Vol. 4, No. 5, pp. 601-612.

[21] Ramadan, A. (2007), "Qualitative assessment of 3D flows using a flow visualisation technique", *Measurement* (In Press).

[22] Choi, H.M., Kurihara, T., Monji, H. and Matsui, G. (2001), "Measurement of particle/bubble motion and turbulence around it by hybrid PIV", *Flow Measurement and Instrumentation,* Vol. 12, No. 5-6, pp. 421-8.

[23] Kowalczyk, M. (1996), "Laser speckle velocimetry", *Optical Velocimetry, Proc. SPIE*, Warsaw, Poland, Vol. 2729, pp. 139-45.

[24] Prasad, A.K. (2000), "Particle image velocimetry", *Current Science,* Vol. 79, No. 1, pp. 51-60.

[25] Adrian, R.J. (2005), "Twenty years of particle image velocimetry", *Experiments in Fluids,* Vol. 39, No. 2, pp. 159-69.

[26] Hinsch, K.D. (1995), "Three-dimensional particle velocimetry", *Measurement Science and Technology,* Vol. 6, No. 6, pp. 742-53.

[27] Barnhart, D.H., Adrian, R.J. and Papen, G.C. (1994), "Phase-conjugate holographic system for high-resolution particle-image velocimetry", *Applied Optics,* Vol. 33, No. 30, pp. 7159-70.

[28] Hinsch, K.D. (2002), "Holographic particle image velocimetry", *Measurement Science and Technology,* Vol. 13, No. 7, pp. 61-72.

[29] Coupland, J.M., Garner, C.P., Alcock, R.D. and Halliwell, N.A. (2006), "Holographic particle image velocimetry and its application in engine development", *Journal of Physics: Conference Series,* Vol. 45, No. 1, pp. 29-37.

[30] Lempert, W.R., Jiang, N. and Samimy, M. (2002), "Development of molecular tagging velocimetry for high speed flow in micro systems", *40th AIAA Aerospace Sciences Meeting and Exhibit,* Reno, NV, AIAA-2002-0296.

[31] Hu, H. and Koochesfahani, M.M. (2006), "Molecular tagging velocimetry and

thermometry and its application to the wake of a heated circular cylinder", *Measurement Science and Technology,* Vol. 17, No. 6, pp. 1269-1281.

[32] Krueger, S. and Gruenefeld, G. (1999), "Stereoscopic flow-tagging velocimetry", *Proceedings of the 1999 Spring Meeting of the Quantum Optics Section of the German Physical Society: Applied Physics B: Lasers and Optics,* Vol. 69, No. 5-6, pp. 509-12.

[33] Cessou, A., Meier, U. and Stepowski, D. (2000), "Applications of planar laser induced fluorescence in turbulent reacting flows", *Measurement Science and Technology,* Vol. 11, No. 7, pp. 887-901.

[34] Law, A.W.K. and Wang, H. (2000), "Measurement of mixing processes with combined digital particle image velocimetry and planar laser induced fluorescence", *Experimental Thermal and Fluid Science,* Vol. 22, No. 3, pp. 213-29.

[35] Hishida, K. and Sakakibara, J. (2000), "Combined planar laser-induced fluorescence-particle image velocimetry technique for velocity and temperature fields", *Experiments in Fluids,* Vol. 29, No. 7, pp. 129-40.

[36] Lindken, R. and Merzkirch, W. (2002), "A novel PIV technique for measurements in multiphase flows and its application to two-phase bubbly flows", *Experiments in Fluids,* Vol. 33, No. 6, pp. 814-25.

[37] Bach, F.W., Laarmann, A. and Wenz, T. (2006), " Modern Surface Technology", Wiley-VCH, Weinheim, Germany.

[38] Ribarov, L.A., Wehrmeyer, J.A., Pitz, R.W. and Yetter, R.A. (2002), "Hydroxyl tagging velocimetry (HTV) in experimental air flows", *Applied Physics B (Lasers and Optics),* Vol. B74, No. 2, pp. 175-83.

[39] Elliott, G.S., Crafton, J., Baust, H.D., Beutner, T.J., Carter, C.D. and Tyler, C. (2005), "Evaluation and optimization of a multi-component planar Doppler velocimetry system", *43rd AIAA Aerospace Sciences Meeting and Exhibit,* Reno, NV, AIAA-2005-35.

[40] Meyers, J.F., Lee, J.W., Fletcher, M.T., Cavone, A.A. and Viramontes, J.A.G. (2006), "Supersonic flow field investigation using a fiber-optic based Doppler global velocimeter", *13th International Symposium on Applications of Laser Techniques to Fluid Mechanics,* Lisbon, Portugal, Paper 1019.

[41] Schodl, R. (1999), "Capabilities of optical point measurement techniques with respect to aero engine application", *Planar Optical Measurement Methods for Gas Turbine Components, RTO Lecture Series 217,* Cranfield, UK/Cleveland, USA.

[42] Elliott, G.S. and Beutner, T.J. (1999), "Molecular filter based planar Doppler velocimetry", *Progress in Aerospace Sciences,* Vol. 35, No. 8, pp. 799-845.

[43] Boemmels, R. and Roesgen, T. (2001), "Development of a planar three-component

velocimeter using Doppler global velocimetry (DGV) and PIV", *19th International Congress on Instrumentation in Aerospace Simulation Facilities (ICIASF 2001) , IEEE*, Cleveland, OH, pp. 211-8.

[44] Wernet, M.P. (2004), "Planar particle imaging Doppler velocimetry, a 3-component velocity measurement technique", *42nd AIAA Aerospace Sciences Meeting and Exhibit,* Reno, NV, pp. 4566-77.

[45] Wernet, M.P. (2004), "Planar particle imaging Doppler velocimetry: a hybrid PIV/DGV technique for three-component velocity measurements", *Measurement Science and Technology,* Vol. 15, No. 10, pp. 2011-28.

[46] Wernet, M.P. and Opalski, A.B. (2005), "Application of the planar particle imaging Doppler velocimetry (PPIDV) technique in a chevron nozzle flow", *43rd AIAA Aerospace Sciences Meeting and Exhibit,* Reno, NV, 1769-85.

[47] Willert, C., Hassa, C., Stockhausen, G., Jarius, M., Voges, M. and Klinner, J. (2006), "Combined PIV and DGV applied to a pressurized gas turbine combustion facility", *Measurement Science and Technology,* Vol. 17, No. 7, pp. 1670-79.

3 Review of planar Doppler velocimetry

3.1 Introduction

Over the last sixteen years, planar Doppler velocimetry (PDV) has been developed by a number of research groups. The original work was done by Komine and Brosnan [1,2], who first introduced an optical frequency-to-intensity converter, typically molecular filters, to aerodynamic flow velocity measurement.

3.2 Review of some main developments in PDV

PDV can be operated in various schemes of velocimetry. Here we will look at the current development directions to illuminate the current state-of-art. Later sections in this chapter will be devoted to the review of the main components, the processing schemes, and the error sources in PDV systems.

- **Michelson interferometer based PDV**

  A PDV system, called Doppler picture velocimetry (DPV) by Seiler *et al* [3-8], has been developed for planar velocity measurements, where an unbalanced Michelson interferometer was designed as the optical frequency-to-intensity converter rather than an iodine cell. Similar work also was performed by Nikiforov [9]. The technique can provide instantaneous and time-averaged measurements by introducing auxiliary optical components and polarised laser light [4]. However, the crosstalk between the polarised reference and signal laser beams whose polarisation directions are perpendicular would cause measurement errors. The configuration is also more complicated because of the introduced auxiliary optical components [4]. In addition, the technique currently provides only single velocity component measurements.

- **Vibration-immunity PDV**

  In the conventional 1 or 3-component PDV, the sensitivity of the laser emission frequency to environmental fluctuations (temperature and mechanical vibrations) can lead to large errors in the measured velocity in certain flow conditions. Therefore, another iodine cell is used to calibrate the illumination laser frequency along with two photodectectors [10]. In PDV using a multiple-channel imaging fibre bundle for 3-component flow velocity measurements [11], one channel can be used to realise this purpose instead of the additional iodine cell.

- **Single-camera PDV**

  A single camera PDV system [12] has been developed which reduces the equipment costs compared with the conventional two-camera PDV system [13]. Here reference and signal images are captured by each half of the active area of the CCD camera respectively. The main drawback of the technique is the loss of half of the spatial resolution under the same conditions because of the use of a

single camera, compared with the whole camera for a conventional PDV system. In addition, the interference between reference and signal beams would further limit the field of view [12].

- **Two-colour PDV**

  A two-colour PDV system was developed by Arnette *et al* [14] in order to remove the problems caused by inaccurate superposition of signal and reference images and polarisation sensitivity in the spilt ratio of the 'non-polarising' beam splitter used. These are typical error sources in a conventional PDV system and will be discussed further in section 3.8. In the technique, a colour CCD camera is used to capture the two images from a flow illuminated with two colours (red + green) at the same time using the red and green pixels on the colour CCD. The two output signals from the camera are used as reference and signal to normalise the scattered light.

  However, one problem is that the scattering intensity is dependent on the illumination wavelength especially when the scattering particle size is larger than wavelength/10 in Mie scattering [15]. This means that the red/green scattering intensity will be significantly different leading to errors in the velocity determination. Also red and green pixels are not at same spatial location since a data point was made up from the signal from a group of three pixels, one each measuring red, blue and green colours in the visible spectrum in a single chip mosaic CCD camera [14].

- **Three-component PDV with imaging fibre bundles**

  A PDV technique has been developed by Nobes *et al* [11] at Cranfield University, to make instantaneous or time-averaged 3-component flow velocity measurements using a single imaging head (one pair of signal and reference cameras) and an imaging fibre bundle. This imports multiple views into the imaging head from each of four separate bundles joined at the imaging head end. Each view occupied ¼ of the CCD image. More recently a similar system was also constructed and used by NASA [16]. The advantage is the fibre flexibility to access optical windows and the system simplification and cost reduction by using only one imaging head. However, the spatial resolution will reduce compared with the conventional 3-component PDV system containing three pairs of image heads because multiple views share a single CCD chip.

- **Two-frequency PDV**

  A two-frequency PDV system with a single camera has been developed by Charrett *et al* [17] to make time-averaged 1 and 3-component measurement with the aid of an imaging fibre bundle with multiple channels. In the technique, the signal and reference images are taken sequentially by a single CCD camera using two different illumination frequencies; one frequency is located on a 100% transmission region of the iodine transfer function as the reference image source, and the other on about 50% point of the transfer function as the signal image source. The two illumination frequencies are obtained from the same laser by using a combination of two acousto-optical modulators [18]. The alignment of

both images is thus automatic eliminating the effect of inaccurate superposition of the two images in the conventional two-camera PDV technique. In addition, the technique removes the polarisation sensitivity of the split ratio of the beam splitter used in the conventional PDV. This work was extended to allow instantaneous velocity measurements to be made using two independently seeded Nd:YAG lasers to illuminate the flow with the two frequencies of light required [19].

- **Hybrid PIV/PDV technique**

  A hybrid measurement technique has been developing, called planar particle Doppler velocimetry (PPIDV) [20-22], in order to make planar 3-component velocity measurements in a fluid flow field using only a single optical access window for viewing the flow. In this technique PIV and PDV are combined into a single imaging head where PIV provides the two in-plane velocity components of a defined plane in the flow field while PDV measures the third out-of-plane velocity component. Measurements on a rotating wheel were successfully made with a measurement error of ~1.6ms^{-1} [21]. More recently, Wernet [22] reports a demonstration of such a system on the measurement of a pressurised generic combustor with the measurement uncertainty of ~3ms^{-1} for a single PIV recording and 1.5ms^{-1} for DGV measurements.

3.3 Light sources

In PDV systems, the laser system used should have a frequency which overlaps with the absorption lines of the molecular filter, have a narrow linewidth, be frequency tunable, be easily integrated with other system components and be readily available [15]. Both the argon-ion laser and the frequency-doubled Nd:YAG laser meet these considerations, and thus have been widely used in PDV systems based on the molecular filter. More details can be found in the review papers by Elliott [15] and Samimy [23].

3.3.1 Argon ion laser

The argon-ion laser operates in continuous-wave (CW) mode, and the 514.5nm single wavelength line is used in PDV as this coincides with iodine absorption lines. They have a power output of up to 10W and a narrow linewidth of around 10MHz when operating with an etalon in the laser cavity [24]. The spectral linewidth characterises the width of a spectral line and is quantified by the full width at half maximum (FWHM). In a PDV system the linewidth of ~10MHz corresponds to a velocity of ~5ms^{-1}. The exact velocity value depends on the observation direction relative to the illumination direction.

The laser system can only be used for measuring slowly changing flow fields, i.e. time-averaged measurement, because the collected scattered laser light is integrated over the exposure time of the camera. However, one benefit of this mode of operation is that it reduces speckle effects in the image because the speckle pattern will be averaged out during the exposure time.

The laser is tuneable in frequency by either heating or tilting the etalon located in the laser cavity to change its transmission function, but mode hops should be avoided. Typical mode hope frequencies are around 70 to 130MHz [24], which can cause trouble when the transfer function of the iodine molecular filter is to be obtained by tuning the laser frequency through the absorption line, because the scanning frequency values are missed where mode hops happen. This problem can be corrected by curve fitting to the theoretical iodine absorption model using the code developed by Forkey [25]. Another issue is the laser frequency drift that will be discussed in section 3.3.2 together with the Nd:YAG laser system.

3.3.2 Nd:YAG laser

The Q-switched frequency-doubled, injection-seeded Nd:YAG laser is another popular laser system used in PDV. In this laser system, a CW seed laser, typically a YAG laser, with a narrow linewidth of approximately 10KHz is directed through a Nd:YAG crystal and amplified to emit the 1064nm light with a linewidth of about 50MHz. This emission light is then frequency doubled through a nonlinear KDP crystal to 532nm with a pulse width of about 10ns and a pulse energy of around 200-300mJ [24]. The pulse repetition rate is typically around 10-30Hz [24]. The flow field can therefore be 'frozen' when the pulsed laser light illuminates the flow. This makes it possible to make instantaneous measurements of the flow field velocity.

The Nd:YAG laser is tuneable in emission frequency over a range of about 30GHz since its injection seed laser provides this tunability by controlling the temperature of the seeder [24]. However, the laser system has a long term drift and also pulse-to-pulse variations in frequency on the order of 20MHz and power fluctuations of ~5% [15] due to the laser cavity mirror dither used to lock the cavity to the seed laser frequency. To overcome this problem, a reference frequency monitoring system was developed by Mosedale *et al* [26] and Beutner *et al* [27] to monitor or control the stability of the Nd:YAG laser system. A small amount of the laser power is split into two parts of equal power; one part enters one photodiode through another iodine filter; the other part enters the second photodiode directly. The ratio of the output signals from the two photodiodes provides the transmission of the filter, which is used to modulate the bias voltage of the laser system to stabilise the frequency. With this monitoring and controlling system, the Nd:YAG laser frequency variation has been reported to be ~2MHz [23].

3.3.3 Laser light sheet forming

Normally the laser beam is formed into a light sheet by using cylindrical lenses to illuminate the flow of interest. However, the resulting light sheet will show the same Gaussian intensity distribution as the source beam. To overcome this problem, a prism-scanning device has been developed by DLR [28] to provide a more uniform light sheet. The device gives an intensity profile of the generated light sheet with an ideal 'top-hat' intensity profile. The uniform intensity distribution across the light sheet is important to detect the scattered light by illuminating the measurement area evenly.

3.4 Flow seeding

PDV, like LDV and PIV, is a particle-based velocimetry technique. Considerations should be given to the seed particles including:

(1) the availability, and ease of introducing into the flow.
(2) the response of the particles to the dynamics of the flow [29].
(3) the spatial resolution.

As Melling [29] states that the criteria for the maximum size of seeding particles to ensure acceptable flow tracking demands particle diameters of about 1μm or smaller for most seeding materials in typical turbulent or high speed gas flows. A larger maximum particle size and hence a larger scattering cross section is feasible by using hollowing or porous particles with a lower density ratio.

Particle scattering can be either Mie or Rayleigh scattering [30] depending on the size of the particles relative to the illumination wavelength. Mie scattering is defined as scattering from particles which are greater than one tenth of the incident light wavelength and Rayleigh scattering is defined as scattering from particles whose size is smaller than one tenth of the incident light wavelength [15]. The intensity profiles of the two kinds of scattering are shown in Figure 3-1. In the Mie region, the scattering has a strong forward direction, and nonuniform 'lobed' scattering towards the sides, as shown in Figure 3-1(a). In the Rayleigh scattering, the scattering pattern will show a toroidal shape when the incident light polarisation direction oriented through the centre as shown Figure 3-1(b). Since these scattering distributions will depend on the particle size, incident light wavelength, and polarisation, when collecting the scattered light in PDV measurement system, the size of the seeded particles and all of the above factors should be considered in order that the collected scattered light is as high as possible with the proper system sensitivity.

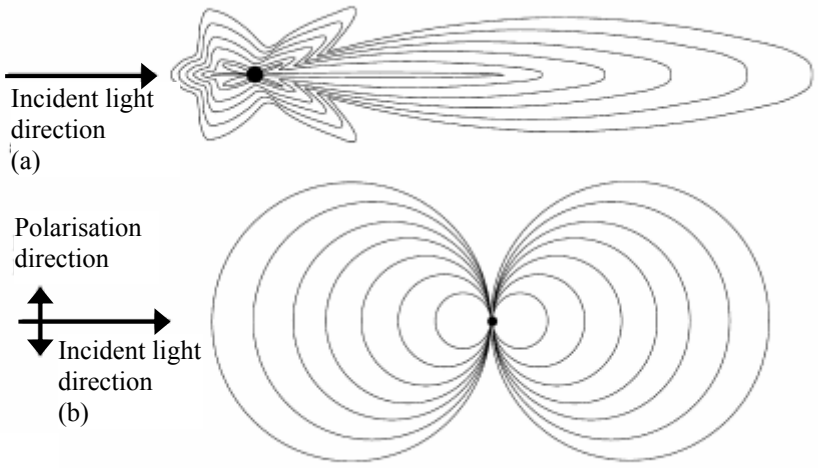

Figure 3-1 Scattering intensity profiles [15]. (a) Mie scattering. (b) Rayleigh scattering.

In PDV, because the signal collected by the CCD camera from moving particles in the measuring volume is cumulative, a high particle density with small particles can be used in the system while keeping the response of the particles to the dynamics of the flow for higher scattering intensity, which is very important for CCD cameras' operation.

3.5 CCD camera and receiving optics

A conventional PDV system [1] is shown in Figure 3-2. It includes a beam splitter, a mirror, and two CCD cameras (reference and signal). Two cameras are used to obtain a normalised signal to correct for variations in scattered light intensity resulting from uneven seeding levels, light sheet power distribution variations, and optical distortions in the imaging optics. In some work [15], a neutral density filter is introduced into the optical reference path in order to balance the signal intensity into the two cameras. Another approach is to use a beam splitter with an unbalanced split ratio. In addition, a polariser may be placed in front of the beam splitter to eliminate the polarisation sensitivity of the split ratio, but the received intensity will reduce. The PDV configuration (Figure 3-2) can be simplified to use a single camera to capture both reference and signal images as described in section 3.2. These are shown in Figure 3-3.

Similar camera and receiving optics configurations are used in a Michelson interferometer based PDV [8], where two- and three-camera configurations (Figure 3-4) are used. This will be discussed further in section 3.6.2.

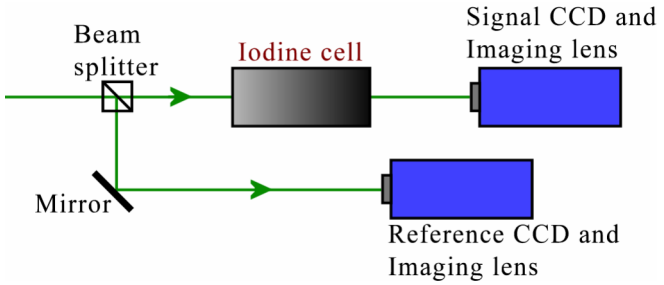

Figure 3-2 A typical camera and receiving optics for PDV.

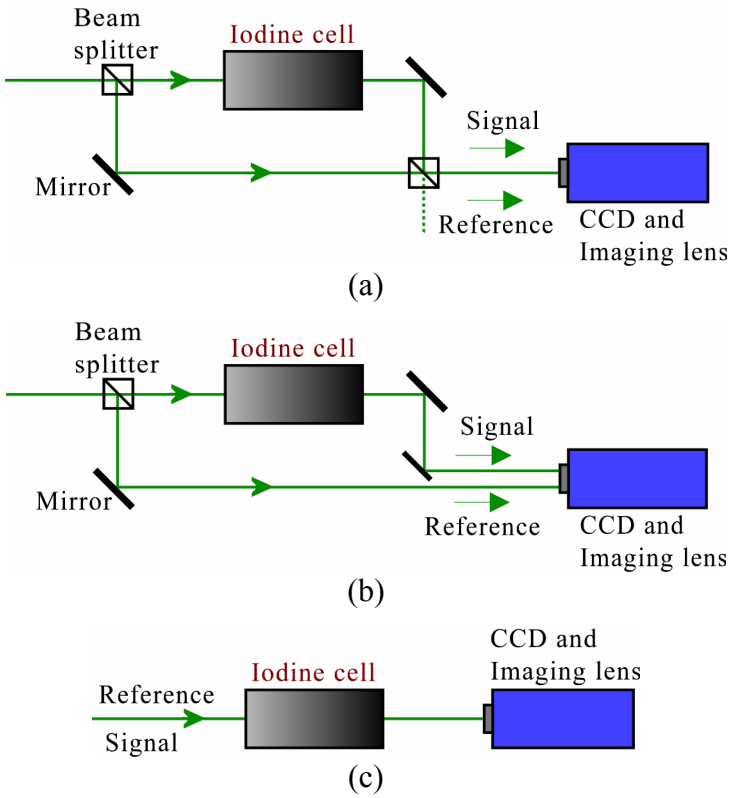

Figure 3-3 Single camera configuration. (a) With a beam splitter [13,31]. (b) With a mirror [12,32]. (c) Two colour configuration [17].

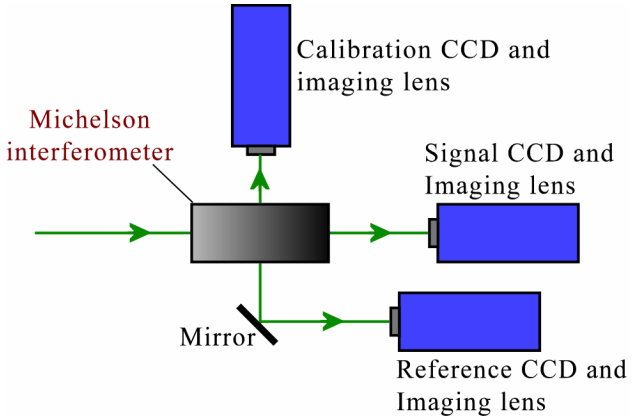

Figure 3-4 Three-camera configuration using a Michelson interferometer [8]. More details about the Michelson interferometer can be found in Figure 3-12.

3.6 Frequency to intensity conversion techniques

In PDV, a key component is the frequency-to-intensity converter (Figure 1-3). Until now, the most common method has been to use a molecular absorption filter, and PDV systems based on this approach have been developed in the last sixteen years since it was pioneered by Komine [1]. Another filter developed for PDV in the last several years is the path length unbalanced Michelson interferometer. Here the properties of both methods are discussed and compared for the PDV application.

3.6.1 Molecular absorption filter

Molecular absorption lines are generally selected as the filter for PDV since they have several attractive characteristics. Currently the most popular molecular filter uses iodine molecules. It has absorption lines around 514.5nm and 532nm of the two widely used laser sources in PDV and the absorption line has two smooth slopes with a frequency range of about 1GHz each, which matches well with the Doppler frequency shift from the general flow velocities of several hundred meters per second.

The absorption process through a media can be described using Beer's law

$$I = I_0 \cdot \exp(-\alpha \cdot L) \qquad \textbf{Equation 3-1}$$

where I_0 is the input light intensity, I is the transmitted intensity, L is the transmission path, and α the absorption coefficient decided by the media properties.

The characteristics of a molecular absorption line depend on three broadening processes. The first is natural broadening resulting from the finite lifetime of the excited energy state of the molecule. The second is Doppler broadening (also termed as temperature broadening) due to random thermal motion of the molecules as their temperature is increased or as they absorb the incident light. The third is pressure broadening due to collisions with foreign non-absorbing gases. The shape of the absorption line is practically a result of the combination of the three broadening effects.

A filter can be realised by using a sealed gas cell shown in Figure 3-5. The gas cell includes a glass cylinder with optical windows on each end, and the diameter and the length of the cell are on the order of centimetres, typically 7.5cm in diameter and 10-20cm in length, although there are no standard cell dimensions.

A vacuum pump port is used to evacuate the cell and introduce other types of gas into the cell when needed. A side arm is used to control the partial pressure in the cell by adjusting the iodine number density, which is realised by changing the temperature of the side arm where some solid iodine is present. A cold finger is used to cause some iodine vapour to become crystalline in order that other types of gas are able to be introduced into the cell. The cell is controlled to a temperature T_{cell} around the cell by a temperature controller. This temperature is high enough to make sure that the iodine vapour will not crystallise in the cell walls and on the two optical windows. The pressure of the cell is controlled by accurately controlling the temperature T_{side} of the side arm, and this temperature is lower than that of the cell.

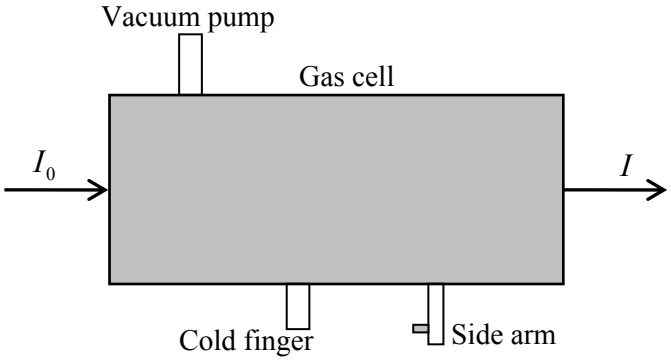

Figure 3-5 A typical iodine cell used in PDV where the diameter and the length of the cell are on the order of several centimetres [32].

Based on the structure in Figure 3-5, two basic operating modes can be considered: saturated and starved modes. In saturated cells there is still solid iodine in the side arm, and the characteristics of the cell are therefore directly related to T_{side}, which controls the iodine number density in the cell. In practice, these are easier to construct. However, saturated cells are more sensitive to variations in environmental conditions, particularly temperature [15].

Starved cells contain iodine vapour in both the body cell and the side arm. The number density of the iodine vapour in the cell is fixed as long as it operates at a higher temperature than that of the point of evaporation of iodine. An inactive gas such as nitrogen [33] may be introduced into the cell to reduce the slope of the absorption profile and stretch the transmission curve over a wider frequency range which may be desirable for some applications where a large velocity range is expected in a flow. This is because that the pressure broadening begins to dominate, resulting in more gradual slopes of the profile, although less sensitivity is obtained.

In practical applications, it is necessary to measure the filter profile experimentally before any flow measurements. This can be realised by scanning the laser frequency across the filter transfer function and recording the transmitted intensity. Forkey [25] has developed a computational model to calculate the absorption lines of iodine, which provides a good guide when designing a filter. The experimental results can also be compared to the theoretical model. Commercial iodine molecular filters are available from companies such as Innovative Scientific Solutions Inc. (ISS) [34].

The Spectra-Physics argon-ion laser used allows the optical frequency to be scanned by applying a voltage ramp to an input that controls the etalon temperature. This process must be carried out slowly to avoid instability and mode hopping. Figure 3-6 shows an example of the absorption lines of an iodine gas cell with a length of 15cm, a diameter of 25mm, and a cell vapour temperature 40ºC that was used in our laboratory, overlaid with the theoretical absorption spectrum, calculated using Forkey's model [25] for the iodine cell. Figure 3-6(a) shows the position of the absorption line being used while Figure 3-6(b) shows the region enlarged. In Figure 3-6(b), the 'hops' in the experimental curve (cross symbol) are due to the laser mode hopping during the scanning.

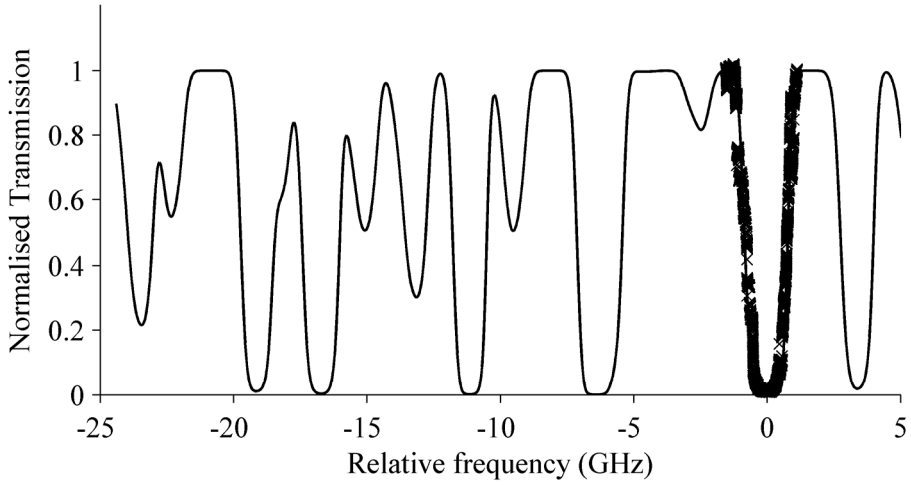

(a)

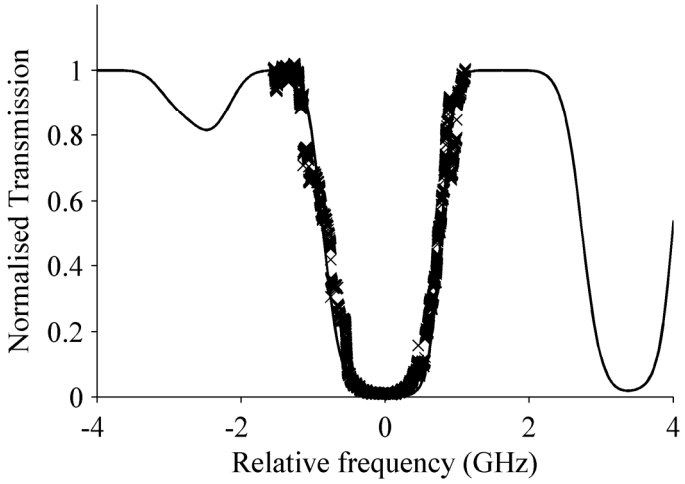

(b)

Figure 3-6 (a) An example of the absorption lines of an iodine filter used at Cranfield University with the theoretical absorption spectrum centered about 514.5nm, calculated using Forkey's model [25]. (b) An enlarged region showing the absorption line marked in Figure 3-6(a).

—— theoretical curve;
×××× experimental curve.

3.6.2 Optical interferometer

Optical interferometry can be used for the visualisation of a velocity field, since the Doppler frequency shifted light scattered from a flow leads to a change of the light intensity distribution in an interference pattern which directly relates to the flow velocity. In addition, it has some attractive characteristics. The first is that the filter profile of an interferometer can be selected in accordance with the expected measurement range by controlling the phase difference between the interfering beams. The second is that the illumination wavelength is no longer restricted to values that correspond to an absorption line of an atomic or molecular gas. Any CW or pulsed laser of sufficient power and narrow linewidth may be used to form into a light sheet. However, one major problem with this filter is the filter phase drift, which can directly introduce measurement errors. A number of optical schemes of interferometers have been previously used for flow velocity measurements. The following is a brief review.

Fabry-Perot interferometer

The Fabry-Perot interferometer (FPI) was the first used for flow velocity measurement [35]. A confocal FPI configuration was used with a free spectral range (FSR) of around 2GHz. The instrument is suitable for high velocities since the FSR is restricted by the separation between the two reflection planes in the filter; larger separation leads to poor light transmission and more instability as well. More recently an all-fibre Bragg grating-based FPI has been reported for in-line velocity measurements [36], where a phase-locking feedback system was designed to actively compensate for phase variations in the filter.

FPIs however are not suitable for whole-field measurements as they are a point technique, although for single point measurements an all-fibre structure makes a compact instrument that also provides good measurement resolution of about $0.2ms^{-1}$ [36].

Phase-stabilised Michelson interferometer

A phase-stabilised Michelson interferometer was designed by Smeets [3] as a sensitive spectrometer to measure the local flow velocity. The technique provides instantaneous measurements by stabilising the phase in the interferometer. This is realised by using an additional electro-optical system to generate a continuously varying electrical signal, which is proportional to the Doppler frequency shifts of the scattered laser frequency. The additional system consists of a Pockels cell, polarisation beam splitter (PBS), two detectors and a phase stabiliser.

Figure 3-7 shows the experimental arrangement. The scattered laser light from a point defined by a focused argon-ion laser beam is collected into a single mode fibre. The output of the fibre is linearly polarised by a polariser, and then enters the Michelson interferometer after passing through a Pockels cell. The cell is used to induce birefringence under the influence of an applied voltage. The interferometer includes a polarisation beam splitter (PBS1), one mirror and one glass block with one end coated as a reflector. The recombined two beams out of the interferometer pass through a

second polarisation beam splitter (PBS2) which is aligned at 45° with respect to PBS1. In this way, the two beams show complementary interference outputs I_1 and I_2 after passing through PBS2.

$$I_1 = I_0 \cdot \cos^2(\frac{\pi \Delta l}{c} v)$$

$$I_2 = I_0 \cdot \sin^2(\frac{\pi \Delta l}{c} v)$$

Equation 3-2

where I_0 is the original intensity. Δl is the optical path difference of the two beams and v the laser frequency.

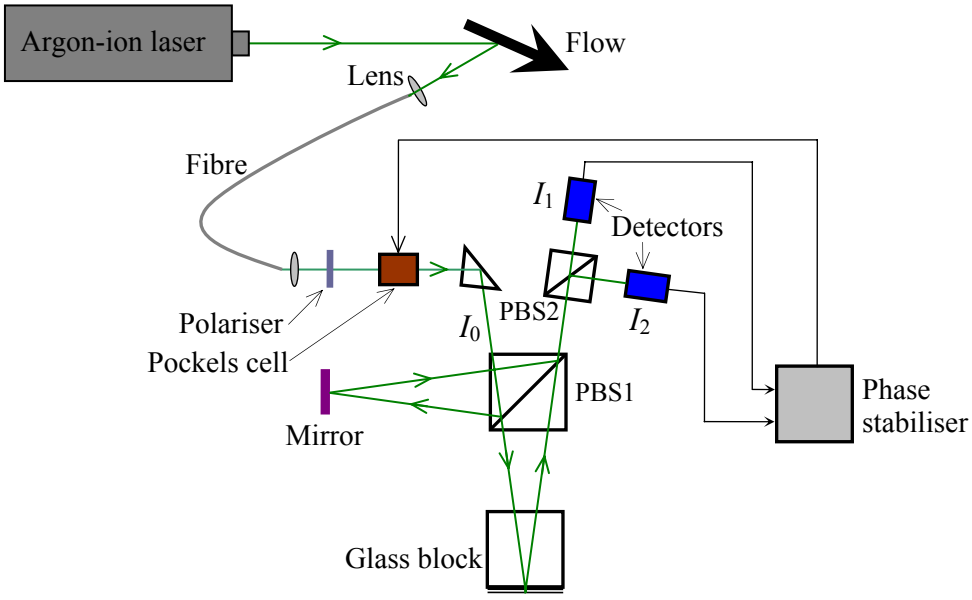

Figure 3-7 Arrangement of a phase-stabilised Michelson spectrometer [3].

The two perpendicularly polarised beams in the interferometer are phase shifted in the Pockels cell, which generates a small distribution $d\Delta l$ proportional to the applied voltage. A dynamic phase stabilisation can therefore be realised in the interferometer. The phase $\pi\Delta l \cdot v/c$ can be kept constant. A Doppler frequency shift Δv of the scattered light can be automatically compensated by a $d\Delta l$ in the Pockels cell. The Doppler frequency shift can be calculated from $d\Delta l$ and then the velocity. The function of the glass block is to generate different optical path differences of the interferometer leading to expected wavelength sensitivity. This will be discussed further in chapter 4.

The technique is suitable for high velocities, but not for low velocities because of the interferometer phase instability and the laser frequency fluctuations. The interferometer phase drift will directly add measurement errors. To overcome this problem, an additional phase stabilisation subsystem is introduced by Smeets [3] into the interferometer to compensate for the phase drift, as shown in Figure 3-8. Part of the original collimated laser beam was polarised and sent into the Michelson interferometer from the right hand side. The output from this same side entered into a third polarisation beam splitter PBS3 and then two photodetectors. Thus a second phase stabilisation

system was obtained to act on a piezoelectric element modulating either the mirror in the Michelson interferometer or one of the laser cavity mirrors.

A disadvantage of this technique is that it can not provide whole-field measurements as it is a point technique. Also there has to be sufficient intensity of the scattered light with a polarisation parallel to that of the polariser used before the Pockels cell.

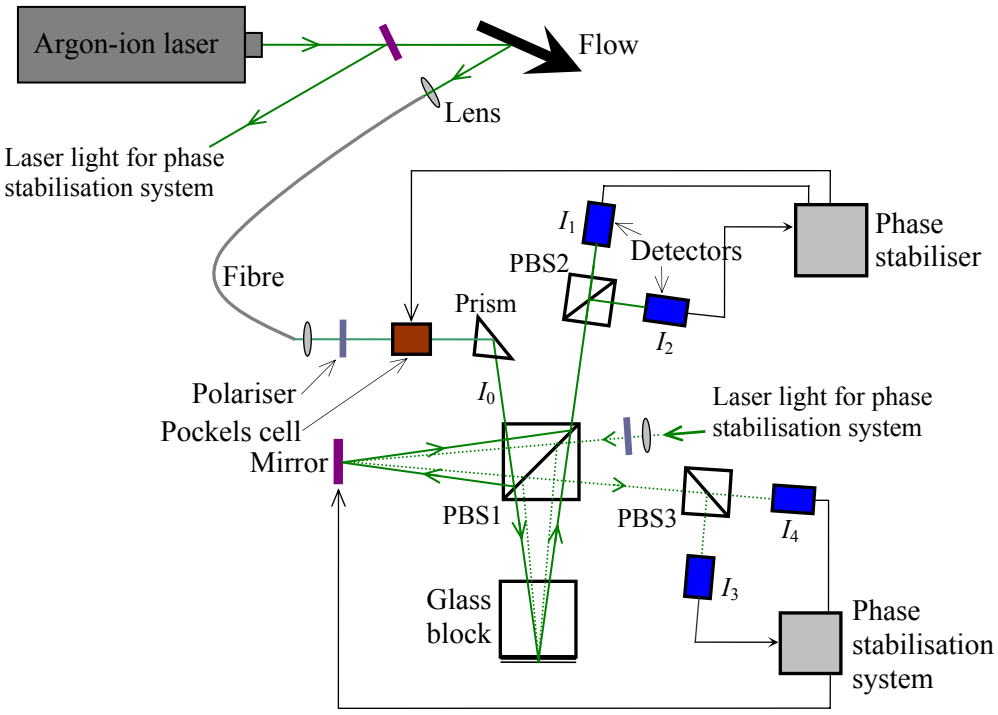

Figure 3-8 Arrangement of a phase-stabilised Michelson spectrometer with a second phase-stabilisation system to compensate for the interferometer phase drift [3].

Single-camera Michelson interferometer

An unbalanced Michelson interferometer was first used as a full-field flow velocity visualisation technique by Seiler *et al* [37] with a single CCD camera. The technique directly converts the Doppler frequency shifts into a shift of the interference pattern through the inteferometric filter. The output of a Michelson interferometer can be expressed as

$$I = I_0 \cos^2(\frac{\Delta\varphi}{2}),$$

$$normalised: \frac{I}{I_0} = \cos^2(\frac{\Delta\varphi}{2}) \; with \; 0 \le \frac{I}{I_0} \le 1 \qquad \textbf{Equation 3-3}$$

where I_0 is the input light intensity, I is the output intensity, and $\Delta\varphi$ the phase difference between the two arms. The output intensity of a Michelson is thus determined by its optical phase difference and original light intensity. The intensity is approximately zero for a phase shift of π, 3π…. At these points it generates equidistant lines in the interference pattern. This makes the output intensity located at dark lines independent of

the original scattered light intensity. A pair of interference pattern images is required to detect the fringe shift. One image is taken with the flow off, and it provides a reference measurement of the fringe locations. The other is taken with the flow field on, and it provides the velocity information. The fringe shift is then determined by locating the minimum-intensity lines in both images, as well as the fringe space distances in the reference image. From the fringe shift, the Doppler frequency shift can therefore be evaluated and then the velocity can be calculated using the Doppler equation (Equation 2-1).

A typical configuration is shown in Figure 3-9. The scattered light from a flow, defined by a laser light sheet, was collected by lens L1, which collimated the light through the Michelson interferometer and imaged it onto a CCD camera by a second lens, L2. The function of the glass block is to correct for the difference in magnification and focal distance in the two arms and provide a large optical path difference of the interferometer.

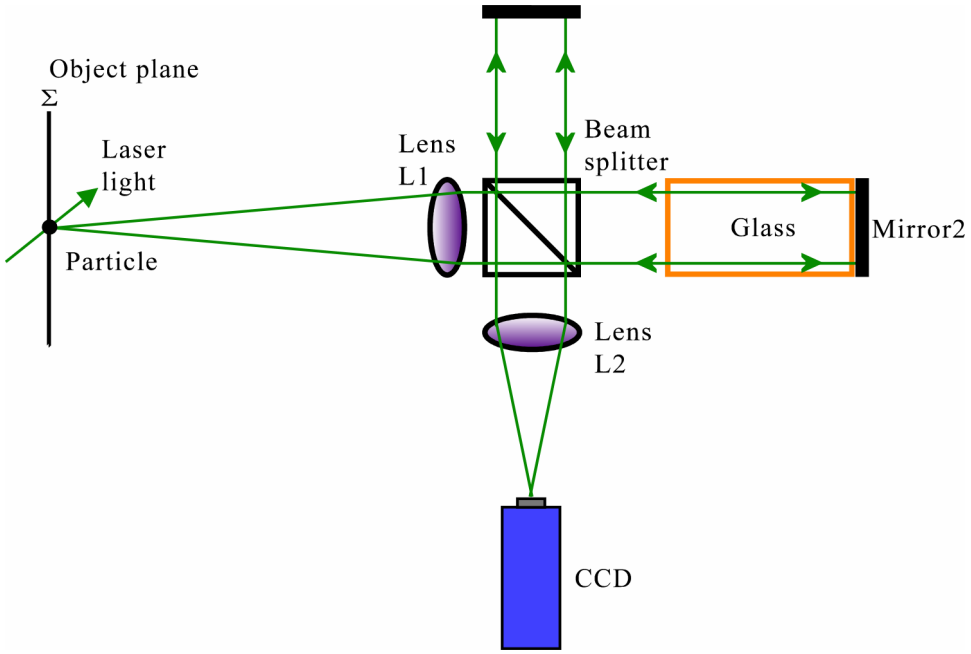

Figure 3-9 A typical Michelson interferometer configuration with a single CCD camera for velocity measurements [37].

The glass block is replaced with an ideal thin lens in the work of Nikiforov [9] to provide a large optical path difference as shown in Figure 3-10. This makes the configuration compact and convenient as well as to select the expected measurement range by employing a lens of different focal lengths. For example, a two meter path difference was obtained from a lens with a 25cm focal length, and measurements with an accuracy of about 5% were made on a flow at the velocity of around 100ms^{-1} [9]. However, the disadvantage is that large-dimension thin lens (L3) is required since the scattered light passed through L3 two times in separation space. For example, a dimension of ~45×25mm is required while the thickness of the lens must satisfy the approximate condition as a real thin lens if a beam size of ~20mm is used.

The technique however is limited to high velocity flows as a result of the interferometer phase drift, although the measurement range can be selected by introducing different lengths of the glass block and the frequency sensitivity can be increased by tilting the mirror in the Michelson interferometer, although the spatial resolution will reduce. In addition, the technique only provides velocity profiles through the measurement region since only dark lines are used, thus it can not measure the whole velocity field distribution of interest.

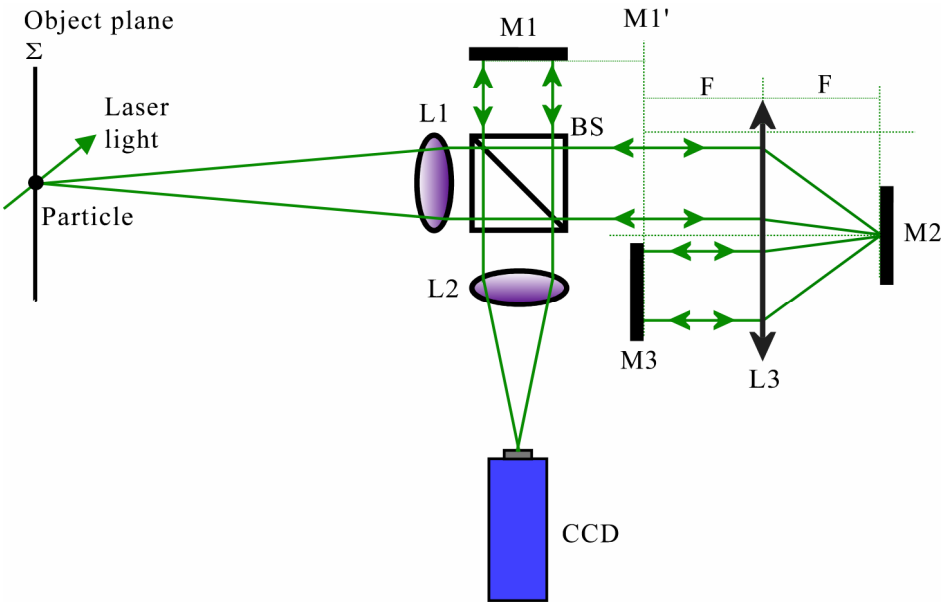

Figure 3-10 A typical Michelson interferometer configuration with an ideal thin lens for velocity measurements [9]. L1, 2: lenses; L3: ideal thin lens; M1, 2, 3: mirrors; BS: 'non-polarising' beam splitter; F: focal length of L3; M1': front focal plane of L3.

Two-camera Michelson interferometer

An improved technique is therefore reported by Seiler *et al* [8] to normalise the scattered light with the actual light distribution captured by using another reference CCD camera. It can provide full-field velocity information by processing each pixel in the image. Similar to single-camera Michelson interferometer, a pair of interference pattern images is required to detect the Doppler frequency shift. One image is taken with the flow off, and it provides a zero-velocity reference. The other is taken with the flow field on, and it provides the velocity information. A typical configuration is shown in Figure 3-11. It uses an additional CCD camera to record original light intensity distribution with the help of a beam splitter, compared with the single camera Michelson interferometer configuration (Equation 3-3).

A significant disadvantage in the technique is the interferometer phase drift because images for flow on and off are taken at different moments, not simultaneously. This makes it difficult to make instantaneous measurements. To overcome this problem, a three-camera Michelson interferometer configuration has been developed by Seiler *et al* [6].

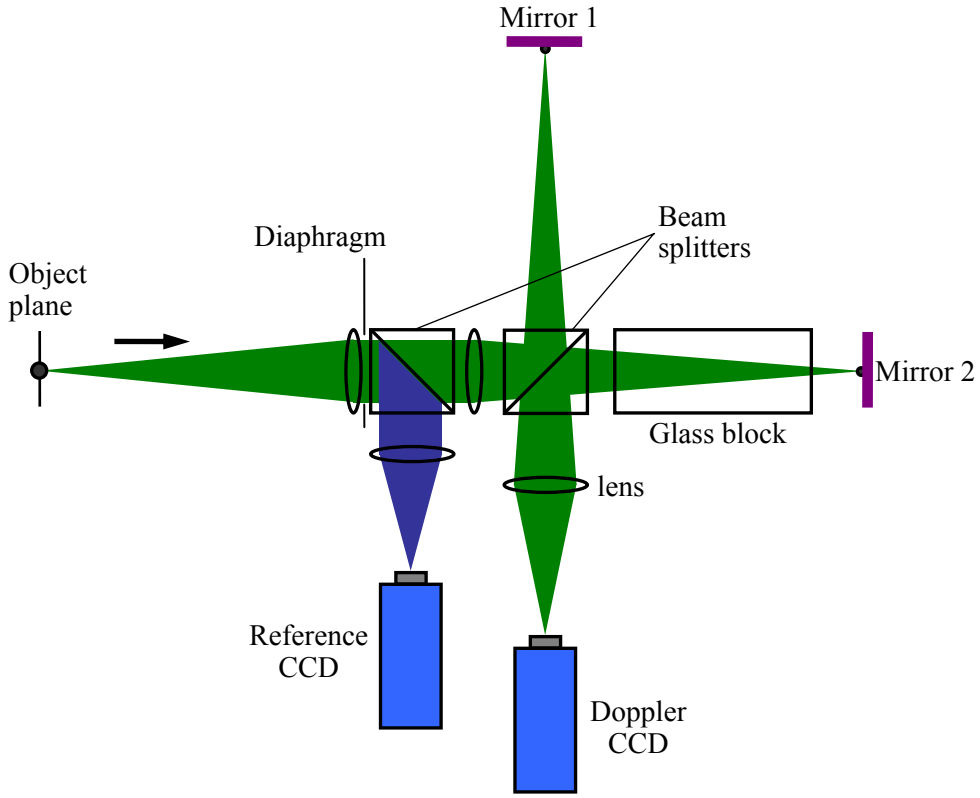

Figure 3-11 A typical Michelson interferometer configuration with two CCD cameras for velocity measurements [8]. Green beam: the scattered light from the object plane into the interferometer; blue beam: the reference light used to normalise the image taken by Doppler CCD.

Three-camera Michelson interferometer

A three-camera Michelson interferometer [6] is shown in Figure 3-12. CCD1 is used for recording the interference fringes resulting from Doppler frequency shifted laser scattered light, CCD2 for recording the reference picture resulting from the un-shifted laser light scattered from a motionless dispersion screen, and CCD3 for recording the intensity distribution of the scattered light from the investigated flow area.

The laser beam is divided into two parts by a beam splitter, the main part for the flow illuminating light and the other to illuminate a motionless dispersion screen. The scattered light from flow particles is polarised as horizontal linear polarisation light and enters the interferometer and its interference image (Doppler shifted) is captured by CCD1. This is normalised by the intensity image taken by CCD3 simultaneously.

The scattered light from the screen is polarised as vertical linear polarisation light and enters the interferometer and its interference image is captured by CCD2. This is used as a zero-velocity calibration. The velocity can then be calculated using these images.

The technique has increased system complexity and reduced cost efficiency compared with conventional two-camera PDV systems since three cameras were required, and additional data processing work was introduced. Another problem was the ‘cross-talk’ between reference and flow scattered light beams since light polarisation is sensitive to

birefringence of optical components such as beam splitters and glass block, and this was previously observed [6]. It is also difficult to measure polarisation sensitivity resulting from flow scattering because it only collects one polarisation state of the scattered light.

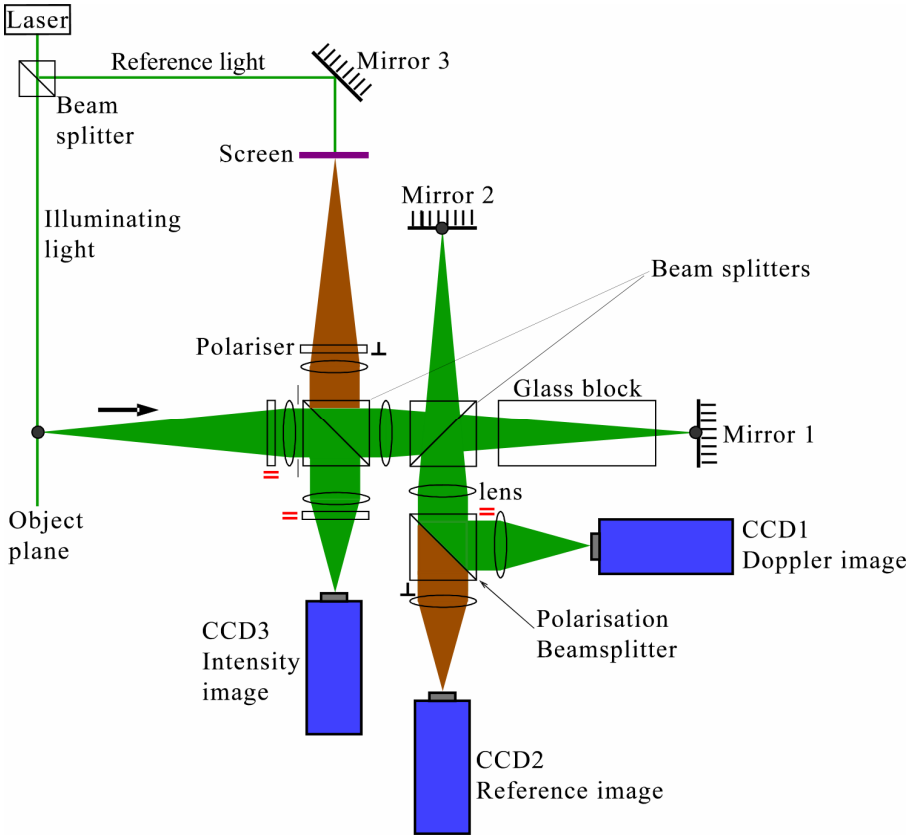

Figure 3-12 A typical Michelson configuration with three cameras for velocity measurements [6]. Green beam: the scattered light from the object plane; brown beam: the reference light used to calibrate the zero-velocity.

More recently the technique was modified to evaluate the velocity information by using a linear interpolation method, which removed the need for CCD3 for intensity distribution recording along with the image lens and polariser used in Figure 3-12. However, it did not really provide the actual velocity information at each pixel because the local phase values were estimated at locations between dark lines in the images [4].

3.6.3 Summary/comparison of frequency-to-intensity conversion techniques

A summary and comparison of the optical configurations of interferometers used for flow measurement is shown in Table 3-1. The most popular interferometer configuration for planar velocity measurement is the Michelson interferometer due to its compact structure and easy building. It offers the free spectral range that corresponds to the expected measurement range and sensitivity. However, because only one output can be accessed [4], additional optical parts are necessary to obtain a normalised signal to correct for variations in scattered light intensity. Table 3-2 shows a general comparison of iodine molecular absorption lines and interferometers as frequency-to-intensity converters for PDV application.

Table 3-1 A summary of optical configurations of interferometers for flow measurements.

Optical configurations	Principles/Advantages	Disadvantages	Ref.
FP	Direct frequency measurement Suitable for high velocity flows	Phase drift Point technique	1971 [35]
Phase-stabilised Michelson	Direct frequency measurement Suitable for high velocity flows (>100ms^{-1})	Phase drift Point technique Glass block required	1981 [3]
Single-camera Michelson	Direct frequency measurement Simplicity and compact Suitable for high velocity flows (>100ms^{-1})	Phase drift Glass block required Only dark fringes can be processed	1985 [37] 2000 [9]
Two-camera Michelson	Direct frequency measurement Full-field measurement Suitable for velocities (>100ms^{-1})	Phase drift Limited for unsteady flows Glass block required	1999 [8]
Three-camera Michelson	Direct frequency measurement In-time absolute measurement Eliminate effects of phase drift and laser frequency fluctuations.	Complexity and low cost efficiency Crosstalk between reference and signal images Polarisation sensitive Glass block required.	2004 [6].

Table 3-2 A general comparison of Iodine molecular filters and interferometers for PDV.

	Iodine cell	Interferometer
Principle	Gas absorption	Optical interference
Transfer function	Fixed to absorption line	Cosinusoidal form
Stability	Typical requirement for saturated cells: <~±0.5˚C [38] Temperature sensitivity for starved cells is smaller (~10 times smaller) than for saturated cells	Temperature and vibration sensitive Requiring phase control subsystems
Light source	Limited to those able to be tuned onto a proper absorption line	Any laser of sufficient power and enough narrow width
Free spectral range	Fixed to absorption line shape (some thermal/pressure broadening)	Selectable
Complexity	Simple	Complex structure
Availability	Commercial (limited)	Custom designed.

3.7 Processing schemes

The basic principle of data processing schemes from the various research groups of PDV is similar. The key system calibration and data-processing steps are summarised by Elliott [39] in Table 3-3. The following five steps are required to obtain velocity images using the PDV data from a test.

Table 3-3 Main processing steps used in PDV data processing.

Data Taken	Processing steps	Results/purpose
Dot card images	Image mapping	Improve CCD image alignment. Dewarp images to normal view
Green card (static or running) Images and background images with laser on and flow seeding off	Determine intensity calibration parameters - Subtract background images - Calculate slope and intercept to calibrate reference image intensity to signal image intensity at each pixel	Correction for pixel sensitivity variations
PDV data images Background images taken with the laser on and flow seeding off at frequency where data was taken	Apply spatial and intensity calibration to PDV data - Subtract background images - Use dewarping coefficients to map image - Apply slope and intercept to calibrate reference and signal images	Calibrate raw data
Filter profiles Laser frequency as determined from a wavemeter	Calculate Doppler frequency shifts - Divide calibrated signal and reference image pairs and determine transmission - Compute Doppler frequency shift from filter profile and laser frequency as determined from wavemeter	Obtain Doppler frequency shifts in the calibrated image
Physical locations of camera and laser coordinates	Calculate Velocity Components - Calculate illumination and observation unit vectors for each PDV component - Calculate sensitivity vectors for each camera component - Calculate velocity components	Velocity values.

(1) Iodine molecular filter calibration

Before collecting the actual PDV images, the transmission function of the iodine cell needs to be measured and stored for final calculation calibration. This is carried out by scanning the laser frequency while measuring the transmission profile of the iodine cell.

(2) Image mapping

Signal and reference images must be aligned on a pixel-to-pixel basis in order to calculate the transmission ratio for light scattered from a point. Both the signal and reference images are mapped to an image plane corresponding to the physical space with equally spaced pixels and all perspective and magnification variations removed.

Normally a dot card is used to provide a spatial reference for each camera. The card with equally-spaced circular dots is placed in the image plane (plane of the laser sheet), so that optical distortions caused by the optical path differences and the viewing angles can be measured. For each pixel location in the mapping image, linear interpolation was used with a weighted average of the surrounding pixels in the data image to determine the appropriate pixel intensity in the mapped image [40]. Since the surrounding environment often changes, so the dot card images need to be taken repeatedly during the experiment.

(3) Determination of intensity calibration parameters

An intensity calibration program is required before calculating the ratio of the signal to reference images. It can remove the intensity difference coming from the beam splitter, mirrors, and camera sensitivities.

A white-card is placed in the image plane. The laser is tuned to a region of the iodine absorption profile where the transmission is near a maximum and shows little dependence on frequency, and illuminates the white card. At first, some background images are acquired with the laser on but with the beam blocked. These images are subtracted from subsequent white-card images removing background light. Then changing the laser light power gradually, a series of white-card images are taken corresponding to different illumination intensities.

After subtracting the background images, these reference and signal images are mapped. Because these images are acquired at the maximum transmission, the ratio of the signal to reference images should be the same. So, the calibration coefficients, slope and intercept are determined from a linear-fitting, which should match the signal and the reference images at each pixel. The linear-fitting is based on the expected linearity of the camera response. Because of the background subtraction, the values of the intercept should be close to zero [39].

(4) Apply spatial and intensity calibration to PDV data

After subtracting background intensity levels, mapping the signal and reference images to a common image plane, the signal images will be divided by the reference images on

a pixel-by-pixel basis, and then a series of images containing the transmission ratio at each pixel for a PDV component are obtained.

(5) Calculate Doppler frequency shift

The transmission ratio images are then converted to frequency through the frequency function of the iodine cell, which is measured in step 1. At the same time, the laser wavelength is also recorded in real-time by a wavemeter or by another iodine cell monitoring the laser wavelength. So the Doppler frequency shift Δv is then obtained at each pixel position as the difference between the measured frequency v_m in the camera system and the real-time laser frequency v_r.

$$\Delta v = v_m - v_r \qquad \textbf{Equation 3-4}$$

(6) Calculate velocity components

The final step in processing PDV images is to determine the velocity component from the Doppler frequency shifts calculated at each pixel position. The unit vectors of the incident laser sheet and the observation directions are determined from the angle relations of the PDV configuration. The velocity component can be calculated from Doppler equation 2-1.

For three component measurements, three pairs of cameras are required to image the flow field from three different views. Similar to the single component case, the Doppler frequency shift can be calculated from the transmission ratio of each reference and signal camera from each view and then the velocity. The Doppler equation 2-1 may be rewritten in the measurement coordinate (x, y, z) as

$$\begin{pmatrix} k_{oi1x} & k_{oi1y} & k_{oi1z} \\ k_{oi2x} & k_{oi2y} & k_{oi2z} \\ k_{oi3x} & k_{oi3y} & k_{oi3z} \end{pmatrix} \begin{pmatrix} V_x \\ V_y \\ V_z \end{pmatrix} = \lambda \begin{pmatrix} \Delta v_1 \\ \Delta v_2 \\ \Delta v_3 \end{pmatrix} \qquad \textbf{Equation 3-5}$$

where k_{oin} is the system sensitivity vector for view n and is the difference between the observation and incident light vectors *(ô-î)*. The velocity vector $\boldsymbol{V}$ can then be solved from Equation 3-5.

3.8 Error sources and analysis

A number of researchers have investigated sources of PDV measurement uncertainty. A summary of the analysis of the potential measurement error sources in PDV can be found in the review papers by Elliott *et al* [15] and Meyers *et al* [41]. The following is a general description of the major sources of uncertainty.

Uncertainty in the wavelength of the incident laser light

As Elliot [15] states, the Doppler equation 2-1 can be rewritten as follows in order to understand the uncertainty sources in PDV measurement,

$$V_\phi = \frac{\lambda}{2\sin(\phi/2)}\left[\zeta(TR) - f_0\right] \qquad \textbf{Equation 3-6}$$

where ϕ is the angle between the incident and observation vectors (also termed the scattering angle), TR is the transmission and $\zeta(TR)$ is the frequency function of the iodine absorption line. The Doppler frequency shift is the difference between $\zeta(TR)$ and f_0, the laser frequency.

For a relative laser wavelength uncertainty $\Delta\lambda/\lambda$, the effect on the measured velocity may be expressed as:

$$\Delta V_\lambda = \frac{\partial V}{\partial \lambda}\Delta\lambda = V\frac{\Delta\lambda}{\lambda}. \qquad \textbf{Equation 3-7}$$

As observed above, the relative uncertainty $\Delta V_\lambda/V$ due to the laser wavelength uncertainty is equal to the relative wavelength uncertainty $\Delta\lambda/\lambda$. This means that the error coming from the uncertainty in λ is negligible for most PDV systems, because a general variation below 0.5GHz (0.00047nm) in λ is required for a laser system used. This results in an error in the measured velocity of less than 0.0001% for an argon-ion laser (514.5nm) or a Nd:YAG laser (532nm) widely used in PDV systems.

Uncertainty in the scattering angle

The uncertainty in the velocity due to the scattering angle ϕ can be written as [15]

$$\Delta V_\phi = \frac{\partial V_\phi}{\partial \phi}\Delta\phi = \frac{-V_\phi}{2\tan(\phi/2)}\Delta\phi \qquad \textbf{Equation 3-8}$$

It shows that the relative uncertainty $\Delta V_\phi/V$ due to the uncertainty $\Delta\phi$ in the angle ϕ is inversely proportional to the angle itself. Figure 3-13 shows the $\Delta V_\phi/V$ plotted against the angle ϕ at different $\Delta\phi$. It can be seen that the maximum and minimum errors are found when ϕ is equal to 0˚ and 180˚ respectively. The relative uncertainty in V_ϕ is proportional to the uncertainty $\Delta\phi$ at a fixed ϕ. For example, the quantity $\Delta V_\phi/V$ increases from about 0.44% to 1.75% when $\Delta\phi$ is increased from 0.5˚ to 2˚ at $\phi = 90$˚.

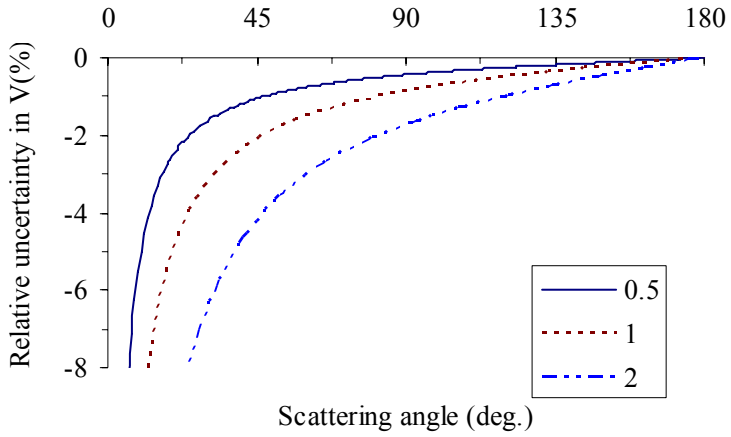

Figure 3-13 The relative uncertainty in V (%) plotted against the scattering angle ϕ at different uncertainty $\Delta\phi$.

Uncertainty in the laser frequency

From Equation 3-6, any change in the laser set point frequency, f_0, will cause the calculated Doppler frequency shift to be inaccurate. Most lasers (i.e. argon-ion and Nd:YAG) are sensitive to the surrounding environment leading to frequency fluctuations and long-term wavelength drift. The laser frequency monitoring system is therefore required for lasers used in PDV systems. For example, the Nd:YAG laser frequency variation has been reported to be a few MHz [23] for both short- and long-term frequency variations.

Uncertainty in characterisation of the filter frequency function

There are two main sources to cause uncertainty in the measured velocity introduced by the frequency function, ζ; the first is the accuracy in measuring the function; the second is the function stability.

In most of PDV systems, the transmission profile is measured by scanning the laser system frequency while monitoring the filtered and unfiltered power of the laser. The laser used has the same frequency linewidth as that used in the experiment. A possible problem arises due to mode hops for an argon-laser system during the scan, leading to jumps in the transmission curve. Therefore, the scan must be carried out slowly to avoid instability and mode hopping. An uninterrupted scan is generally difficult to achieve, so successful scans are compiled to cover the full range. Some researchers used the Doppler frequency shift of a rotating wheel to fill in the transmission profile to obtain the filter frequency function [42]. Using a Nd:YAG laser for measuring the transmission profile usually involves providing a bias voltage to the temperature control circuit on the injection seeder. The scan should be carried out over a time short enough that the laser does not vary in temperature significantly to avoid the laser frequency drift due to temperature variations. Further, the measured transmission profile can be smoothed by fitting the curve to a theoretical absorption line developed by Forkey [25].

The second source of error in the frequency function results from differences in the function during the iodine cell calibration and during the measurement. The surrounding environment can affect the iodine cell operating status such as temperature change and mechanical vibrations. The measurement conditions are normally different from that in the iodine cell calibration. An approach that has been used to reduce this error source s by periodically scanning the cell to avoid the frequency function variation [26,27].

Uncertainty in the measured transmission of the filter after calibration and mapping

The measurement uncertainty due to the transmission, *TR*, comes from three sources: camera nonlinearity and radiometric noise, image alignment and calibration, and laser speckle noise associated with laser light coherence.

The measurement uncertainty is directly related to the camera nonlinearity and radiometric noise used in PDV. They have been analysed in PDV applications in detail by McKenzie [12]. He reports that scientific-grade cameras can have nonlinearities of less than 1% which may be ignored in PDV applications. He also describes radiometric noise comprising three components: the amplified-circuit noise of the detector system (readout noise and dark charge), the inherent photon-statistical noise of the detection process, and the truncation of the signal in the analog to digital conversion.

Error exists in mapping the reference and signal images, although the dot target calibration is performed. Elliot [15] quotes typical values from 30% to less than 10% for the accuracy of image mapping, but this may increase if the signal and reference cameras experience misalignments due to vibrations during the experiment. In image processing, errors can be introduced due to changes in the background signal and misalignment due to camera movement.

Speckle is the result of interference between coherent beams scattering from an irregular surface that is illuminated by a coherent light source. When the surface is moving, the speckle intensity varies in both time and space. Therefore, laser speckle is one main source of random error for a typical application of PDV because it will superimpose on the data field. This can reduce spatial resolution and distorts experimental data. More details can be found in the work of Smith [43] and McKenzie [44,45]. They reported an equation for the speckle noise-to-signal ratio (NSR):

$$NSR = \frac{1.2(1+m)\lambda F}{\Delta x} \qquad \textbf{Equation 3-9}$$

where F is the *f*-number of the optical system (focal length/aperture of lens), m is the magnification ratio (image size/object size), and Δx is the average size of the camera pixels. This equation shows the possibility of reducing the speckle noise by using a large camera aperture (small *f*-number), a small magnification ratio, and large CCD pixels. In addition, Clancy *et al* [46] have reported that random uncertainties in the velocity due to laser speckle can be reduced when spatial smoothing is applied.

3.9 Summary

The purpose of this chapter is to give a review on planar Doppler velocimetry and the current state-of-art. This involves previous work in the PDV technique and the main components used in PDV systems, including

------ light sources and laser light sheet forming optics
------ flow seeding
------ camera and receiving optics
------ frequency-to-intensity conversion techniques.

Finally, the PDV processing procedure has been presented, and the main error sources in PDV applications have been discussed.

3.10 References

[1] Komine, H. and Torrance, C. (1990), "System for measuring velocity field of fluid flow utilizing a laser-Doppler spectral image converter", *United States patent*, No. 4, 919, 536.

[2] Komine, H., Brosnan, S.J., Litton, A.B. and Stappaers, E.A. (1991), "Real-time Doppler global velocimetry", *29th AIAA Aerospace Sciences Meeting,* Reno, NV, AIAA Paper 91-0337.

[3] Smeets, G. and George, A. (1981), "Michelson spectrometer for instantaneous Doppler velocity measurements", *Journal of Physics E (Scientific Instruments),* Vol. 14, No. 7, pp. 838-45.

[4] Seiler, F., George, A., Srulijes, J. and Havermann, M. (2006), "Progress in Doppler picture velocimetry (DPV) Technique", *12th International Symposium of Flow Visualization,* German Aerospace Center (DLR), Germany, pp. 1-10.

[5] Wernert, P., Martinez, B., George, A., Leopold, F. and Seiler, F. (2005), "Development of Doppler based planar velocimetry techniques for high-speed flows at ISL", *8th International Symposium on Fluid Control, Measurement and Visualization (FLUCOME),* Chengdu, CN, Paper 316.1-18.

[6] Seiler, F., George, A., Havermann, M. and Srulijes, J. (2004), "Doppler picture velovimetry (DPV) applied to high-speed shock tunnel flows", *11th International Symposium on Flow Visualization,* Notre Dame, Indiana.

[7] Seiler, F., Havermann, M., George, A., Leopold, F. and Srulijes, J. (2003), "Planar velocity visualization in high-speed wedge flow using Doppler picture velocimetry (DPV) compared with particle image velocimetry (PIV)", *Journal of Visualization,* Vol. 6, No. 3, pp. 253-62.

[8] Seiler, F., George, A., Leopold, F., Srulijes, J. and Smeets, G. (1999), "Flow velocities visualization using Doppler picture interference velocimetry", *18th*

International Congress on Instrumentation in Aerospace Simulation Facilities (ICIASF 99), IEEE, Toulouse, France, 11.1-8.

[9] Nikiforov, S.B., Pavlov, A.A. and Fomichov, V.P. (2000), "The use of field interferometers for panoramic LDA", *9th International Symposium on Flow Visualization, Heriot-Watt University, Edinburgh*, Paper 226.1-6.

[10] Jenkins, T.P. and McKenzie, R.L. (2007), "Planar Doppler velocimetry system with vibration immunity", *45th AIAA Aerospace Sciences Meeting, AIAA,* Reno, NV, Vol. 18, 12777-83.

[11] Nobes, D.S., Ford, H.D. and Tatam, R.P. (2001), "Instantaneous, two camera, three dimensional planar Doppler velocimetry using imaging fiber bundles", *Optical Diagnostics for Fluids, Solids, and Combustion, Proc. SPIE*, San Diego, CA, Vol. 4448, pp. 283-94.

[12] McKenzie, R.L. (1996), "Measurement capabilities of planar Doppler velocimetry using pulsed lasers", *Applied Optics,* Vol. 35, No. 6, pp. 948-64.

[13] Wernert, P., Martinez, B., Gauthier, T. and Guermeur, F. (2004), "Details of image processing procedure for validation of a single camera DGV system", *Journal of Flow Visualization and Image Processing,* Vol. 11, No. 4, pp.335-56.

[14] Arnette, S.A., Elliott, G.S., Mosedale, A.D. and Carter, C.D. (2000), "Two-color planar Doppler velocimetry", *AIAA Journal,* Vol. 38, No. 11, pp. 2001-6.

[15] Elliott, G.S. and Beutner, T.J. (1999), "Molecular filter based planar Doppler velocimetry", *Progress in Aerospace Sciences,* Vol. 35, No. 8, pp. 799-845.

[16] Meyers, J.F., Lee, J.W., Fletcher, M.T., Cavone, A.A. and Viramontes, J.A.G. (2006), "Supersonic flow field investigation using a fiber-optic based Doppler global velocimeter", *13th International Symposium on Applications of Laser Techniques to Fluid Mechanics,* Lisbon, Portugal, Paper 1019.

[17] Charrett, T.O.H., Ford, H.D., Nobes, D.S. and Tatam, R.P. (2004), "Two-frequency planar Doppler velocimetry (2ν-PDV)", *Review of Scientific Instruments,* Vol. 75, No. 11, pp. 4487-96.

[18] Ford, H.D., Nobes, D.S. and Tatam, R.P. (2001), "Acousto-optic frequency switching for single-camera planar Doppler velocimetry", *Optical Diagnostics for Fluids, Solids, and Combustion, Proc. SPIE*, San Diego, CA, Vol. 4448, pp. 272-82.

[19] Charrett, T.O.H. and Tatam, R.P. (2006), "Instantaneous Two-frequency Planar Doppler Velocimetry using pulsed Nd:YAG lasers", *13th International Symposium on Applications of Laser Techniques to Fluid Mechanics*, Lisbon, Portugal, pp. 1-11.

[20] Wernet, M.P. (2000), "Planar particle image Doppler velocimetry system and method", *United States Patent*, No.6, 542, 226, B1.

[21] Wernet, M.P. (2004), "Planar particle imaging Doppler velocimetry: a hybrid PIV/DGV technique for three-component velocity measurements", *Measurement Science and Technology,* Vol. 15, No. 10, pp. 2011-28.

[22] Willert, C., Hassa, C., Stockhausen, G., Jarius, M., Voges, M. and Klinner, J. (2006), "Combined PIV and DGV applied to a pressurized gas turbine combustion facility", *Measurement Science and Technology,* Vol. 17, No. 7, pp. 1670-79.

[23] Samimy, M. and Wernet, M.P. (2000), "Review of planar multiple-component velocimetry in high-speed flows", *AIAA Journal,* Vol. 38, No. 4, pp. 553-74.

[24] Spectra-Physics BeamLok Argon Ion laser, website (2007), www.newport.com.

[25] Forkey, J.N., Finkelstein, N.D., Lempert, W.R. and Miles, R.B. (1996), "Demonstration and characterization of filtered Rayleigh scattering for planar velocity measurements", *AIAA Journal,* Vol. 34, No. 3, pp. 442-8.

[26] Mosedale, A.D., lliott, G.S., Carter, C.D. and Weaver, W.L. (1998), "On the use of planar Doppler velocimetry", *29th Fluid Dynamics Conference,* Albuquerque, NM, AIAA-1998-2809.

[27] Beutner, T.J., Williams G.W., Baust H.D., Elliot G.S., Crafton J. and Carter C.J. (1999), "Characterization and applications of Doppler global velocimetry ", *37th AIAA Aerospace Sciences Meeting and Exhibit,* Reno, NV, AIAA-1999-266.

[28] Willert, C., Stockhausen, G., Klinner, J., Beversdorff, M., Quest, J., Jansen, U. and Raffel, M. (2003), "On the development of Doppler global velocimetry for cryogenic wind tunnels", *20th International Congress on Instrumentation in Aerospace Simulation Facilities, IEEE*, Gottingen, Germany, 2-14.

[29] Melling, A. (1997), "Tracer particles and seeding for particle image velocimetry", *Measurement Science and Technology,* Vol. 8, No.12, pp.1406-16.

[30] Bohren, C. F. and Huffman, D. R. (1998), "Absorption and scattering of light by small particles", John Wiley & Sons, INC., Chichester.

[31] Ainsworth, R.W., Horpe, S.J. and Anners, R.J. (1997), "New approach to flow-field measurement - a view of Doppler global velocimetry techniques", *International Journal of Heat and Fluid Flow,* Vol. 18, No. 1, pp. 116-30.

[32] Chan, V.S.S., Heyes, A.L., Robinson, D.I. and Turner, J.T. (1995), "Iodine absorption filters for Doppler global velocimetry", *Measurement Science and Technology,* Vol. 6, No. 6, pp. 784-94.

[33] Elliott, G.S., Samimy, M. and Arnette, S.A. (1994), "A molecular filter based velocimetry technique for high speed flows", *Experiments in Fluids,* Vol. 18, No. 1-2, pp. 107-118.

[34] Innovative Scientific Solutions, Inc., USA, website, (2007), www.innssi.com.

[35] Jackson, D.A. and Paul, D.M. (1971), "Measurement of supersonic velocity and turbulence by laser anemometry", *Journal of Physics E (Scientific Instruments),* Vol. 4, No. 3, pp. 173-7.

[36] Chehura, E., Ye, C.-C. and Tatam, R.P. (2003), "In-line laser Doppler velocimeter using fibre-optic Bragg grating interferometric filters", *Measurement Science and Technology,* Vol. 14, No. 6, pp. 724-35.

[37] Seiler, F. and Oertel, H. (1985), "Visualization of velocity fields with Doppler-pictures", *Flow Visualization III, Proceedings of the Third International Symposium on Flow Visualization,* Ann Arbor, MI, pp. 454-9.

[38] Forkey, J.N., Finkelstein, N.D., Lempert, W.R. and Miles, R.B. (1995), "Control of experimental uncertainties in filtered Rayleigh scattering measurements", *33rd Aerospace Sciences Meeting and Exhibit,* Reno, NV, AIAA-1995-0298.

[39] Elliott, G.S., Crafton, J., Baust, H.D., Beutner, T.J., Carter, C.D. and Tyler, C. (2005), "Evaluation and optimization of a multi-component planar Doppler velocimetry system", *43rd AIAA Aerospace Sciences Meeting and Exhibit,* Reno, NV, AIAA-2005-35.

[40] Mosedale, A.D., Elliott, G.S., Carter, C.D. and Beutner, T.J. (2000), "Planar Doppler velocimetry in a large-scale facility", *AIAA Journal,* Vol. 38, No. 6, pp. 1010-24.

[41] Meyers, J.F., Lee, J.W. and Schwartz, R.J. (2001), "Characterization of measurement error sources in Doppler global velocimetry", *Measurement Science and Technology,* Vol. 12, No. 4, pp. 357-68.

[42] Meyers, J.F., Lee, J.W., Cavone, A.A. and Suzuki, K.E. (1993), "Investigation of the vortical flow above an F/A-18 using Doppler global velocimetry", *Fifth International Conference on Laser Anemometry,* Veldhoven, Netherlands, Vol. 2052, pp. 633-40.

[43] Smith, M.W. (1998), "The reduction of laser speckle noise in planar Doppler velocimetry systems", *20th Advanced Measurement and Ground Testing Technology Conference,* Albuquerque, NM, AIAA-1998-2607.

[44] McKenzie, R.L. (1997), "Planar Doppler velocimetry performance in low-speed flows", *35th AIAA Aerospace Sciences Meeting and Exhibit, AIAA,* Reno, NV, AIAA-1997-498.

[45] McKenzie, R.L. and Reinath M. S. (2000), "Planar Doppler velocimetry capabilities at low speeds and its application to a full-scale rotor flow", *21st AIAA Aerodynamic Measurement Technology and Ground Testing Conference, AIAA*, Denver, CO, AIAA-1997-498.

[46] Clancy, P.S., Samimy, M. and Erskine, W.R. (1999), "Planar Doppler velocimetry: Three-component velocimetry in supersonic jets", *AIAA Journal,* Vol. 37, No. 6, pp. 700-7.

4 Mach-Zehnder interferometric filter based PDV (MZI-PDV) system

4.1 Introduction

Previous interferometer configurations for PDV have been based on Michelson interferometer configurations. Mach-Zehnder, another two-beam interferometer, can also be used as a frequency discriminator for planar velocity measurements. The obvious advantage over Michelson interferometer is that Mach-Zehnder offers two complementary outputs, which provides a means to normalise the output automatically without introducing auxiliary optical components. As both outputs are sensitive to the Doppler frequency shift, and are in antiphase, normalisation is achieved by taking the difference of the two outputs divided by the sum. This also makes the visibility of the transfer function (normalised intensity against frequency) twice as large as for a Michelson interferometer under the same conditions, improving both the potential measurement accuracy and resolution.

However, a Mach-Zehnder interferometer structure is not as compact as a Michelson interferometer, making it more sensitive to temperature variations and small mechanical vibrations. This problem will be discussed further in chapter 5.

4.2 Theory of Mach-Zehnder PDV interferometer

Figure 4-1 shows the arrangement of an unbalanced Mach-Zehnder PDV interferometer (MZI-PDV). A laser light sheet, of frequency v_L, illuminates the object plane Σ located in the flow. Light scattered from particles seeded in the flow is collected and coupled into the interferometer. Frequency variations caused by the Doppler effect are converted into variations in the recorded intensities on CCD detectors located at Σ', and Σ''.

The scattered light coming from the object plane Σ is collimated by lens L1 and then the collimated light is divided by BS1 (beam splitter, 50:50 split ratio) into two beams of equal intensity, which follow paths l1 and l2. The light in path l1 is turned at mirror M2 and prism P2 before being split by BS2 (beam splitter, 50:50 split ratio) and imaged onto the two detectors located at Σ', and Σ'' using lenses L2 and L3. The second path, l2 passes through a glass block, G, with a length, *l*, and refractive index, *n*. The light is retroreflected by prism P1, making a second pass through the glass block. It is then turned at mirror, M1 and recombined with the light in the first path at BS2.

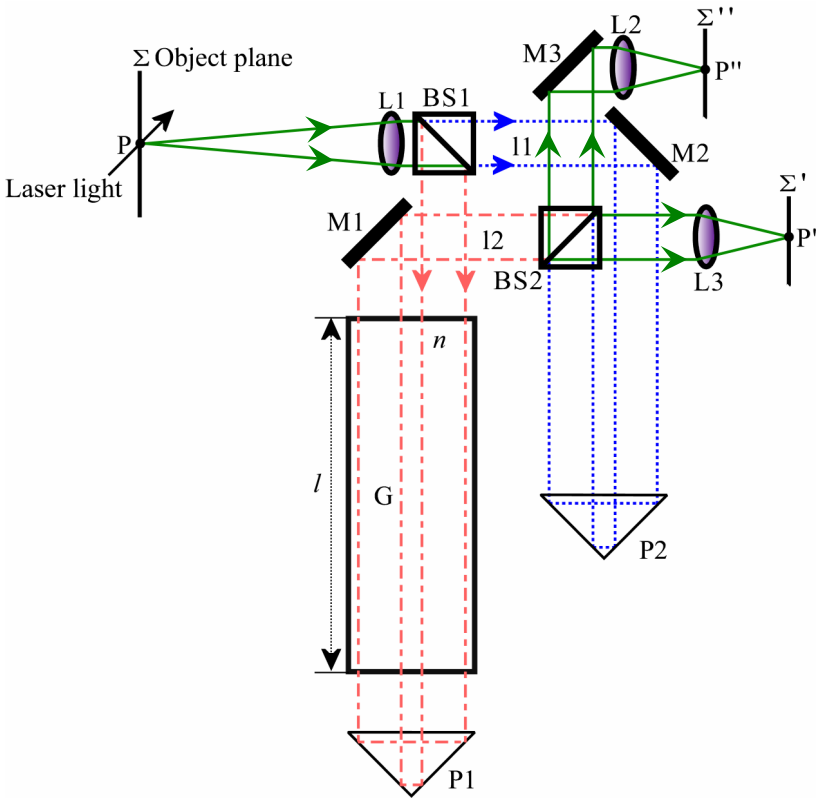

Figure 4-1 An unbalanced Mach-Zehnder interferometer for PDV. The beam paths are shown in different styles and colours: path l1 is dashed (blue), path l2 is dot-dashed (red) and combined path is solid (green).

The intensity at the two outputs of the interferometer will depend on the phase difference $\Delta\varphi$ between the two arms, and can be found from

$$I_1 \propto I_0 \cos^2(\frac{\Delta\varphi}{2})$$

$$I_2 \propto I_0 \sin^2(\frac{\Delta\varphi}{2})$$

$$I_0 \propto I_1 + I_2 \qquad \textbf{Equation 4-1}$$

where I_0 is the input light intensity and I_1 and I_2 are the intensities at each of the outputs. Therefore, for a Mach-Zehnder interferometer, the normalised intensity I_N can be found by taking the difference of the two intensities and dividing by the sum. This can then be expressed as:

$$I_N = \frac{I_1 - I_2}{I_1 + I_2} \propto V \cdot \cos(\Delta\varphi) \qquad \textbf{Equation 4-2}$$

where V is the interference fringe visibility determined by the transmission performance of the whole optical set-up. The normalised intensity, I_N, is a function only of the phase difference $\Delta\varphi$ and is independent of the original input intensity I_0. The phase

difference $\Delta\varphi$ is a function of the optical path difference (Δl) between the two arms, the light source frequency (v_L) and the free space speed of light (c):

$$\frac{\Delta\varphi}{2\pi} = \frac{\Delta l}{c} v_L . \qquad \textbf{Equation 4-3}$$

The optical path difference can be varied by selecting the length of the glass block, with the path difference given by [1]

$$\Delta l = l_2 - l_1 + (n-1)\cdot 2l \qquad \textbf{Equation 4-4}$$

where l_1, l_2 are the physical path lengths in the two arms of the interferometer. The primary purpose of the glass block is to correct for the difference in magnification and focal distance in the two arms of the interferometer that would occur given the path length imbalance. The relation between the block length and the physical path length difference is

$$2l = \frac{n}{n-1}\cdot\left(l_2 - l_1\right). \qquad \textbf{Equation 4-5}$$

Equation 4-4 can therefore be rewritten as

$$\Delta l = (l_2 - l_1)\cdot(n+1) \quad or$$
$$\Delta l = 2l \cdot \frac{n^2 - 1}{n} \qquad \textbf{Equation 4-6}$$

Differentiation of Equation 4-3 leads to the following expression:

$$\Delta\left(\frac{\Delta\varphi}{2\pi}\right) = \frac{\Delta l}{c}\Delta v . \qquad \textbf{Equation 4-7}$$

From Equation 4-7 it can be seen that any Doppler frequency shift of the scattered light will cause a variation in the phase difference between the two arms of the MZI and this in turn will cause a variation of the normalised intensity, I_N, from Equation 4-2.

$$d(I_N) \propto -V \cdot \sin(\Delta\varphi)\cdot d(\Delta\varphi). \qquad \textbf{Equation 4-8}$$

In order to obtain detectable variations in I_N, for typical Doppler frequency shifts found in flows, the optical path difference Δl has to be large enough to allow sufficient variation in the phase difference. This can be accomplished by using different glass blocks, enabling the free spectral range (FSR) of the interferometric filter to be varied. The FSR of an MZI is computed by using the Equation 4-9.

$$FSR = \frac{c}{\Delta l}. \qquad \textbf{Equation 4-9}$$

Figure 4-2 shows the free spectral range (FSR) of an MZI plotted against the length of the block in a range from 5cm to 50cm when made of various optical materials (BK7: n = 1.52, Flint glass: n = 1.76 and TiBr: n = 2.49 at 514.5nm). The FSR of an MZI against other ranges of the length of the glass block can be calculated using Equation 4-9.

From Figure 4-2, it can be seen that the range over which the Doppler frequency shift can be measured, and hence the velocity measurement range, is inversely proportional to the optical path difference Δl. For example, the FSR at 514.5nm reduces from about 7GHz for a 5cm block of BK7 to 0.7GHz when the length is increased to 50cm. This ability to vary the frequency (and velocity) sensitivity of the filter is much more limited in conventional PDV systems that use molecular filters, where it is limited to the molecular absorption line shape.

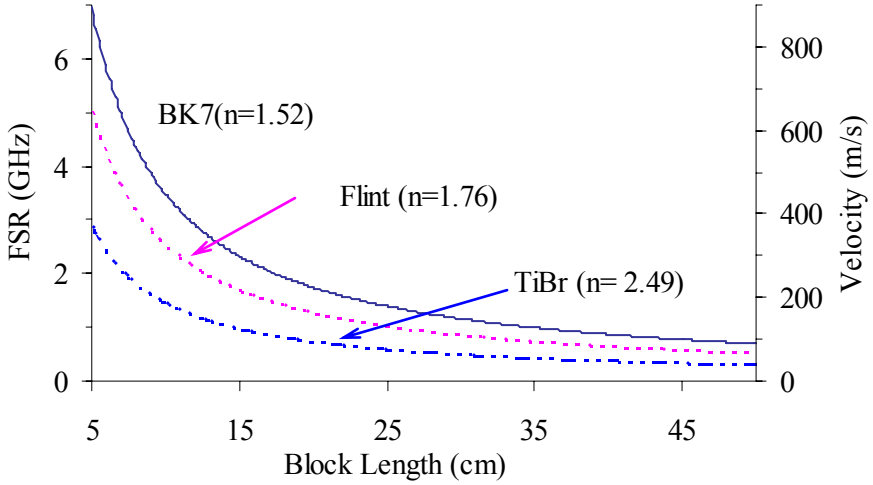

Figure 4-2 Calculated free spectral range (FSR) of a Mach-Zehnder interferometer and maximum measurement velocities for different lengths and materials of the glass/crystal block at a wavelength of 514.5nm.

Thus the use of a glass/crystal block potentially offers a significant advantage over conventional PDV, allowing both lower and higher velocity measurement ranges to be accessed. The technique is limited for low velocities as a long block length is required, leading to optical distortions, phase instabilities and 'vignetting' effects in images. These effects are greater for larger optical path differences. For example an FSR of ~350MHz, giving a velocity range of ~±50ms^{-1}, requires a block length of 100cm. In our work, a 15cm BK7 glass block was used giving a velocity measurement range of ~±150ms^{-1} that was estimated approximately according to the Doppler equation 2-1 and the exact value depends on ($\hat{o}$-$\hat{i}$) as shown in Figure 1-1. This FSR of around 1.16GHz, was used as it is similar to the width of the iodine absorption line (in the order of 1GHz) used in conventional PDV systems and allows comparison with results from PDV systems.

In an MZI-PDV system described above (Figure 4-1), two cameras in the interference fringe planes Σ', and Σ'' are required to record both outputs of the MZI, which are similar to signal and reference cameras in the imaging head arrangement in traditional PDV systems (Figure 1-3).

It is also possible to obtain the two complementary outputs from a single camera using the MZI-PDV system, although precise simultaneity of acquisition will be lost. This technique can be termed single camera MZI-PDV and is shown in Figure 4-3.

The technique requires application of a π phase change to one arm of the interferometer between successive frames. In Figure 4-3 this is achieved by moving prism P2 to change the path length l1. This is readily achieved by adding a constant voltage, synchronised to the camera timing, to the error signal already being used to control the path imbalance for phase locking and control system in the interferometer (described in chapter 5).

The technique has an additional advantage since both images are now captured on the same camera, avoiding the requirement for pixel matching, which avoids errors due to pixel matching in typical two-camera PDV systems. It also reduces complexity and leads to better cost efficiency. However, this technique can only be applied to flows that are stable over the time period required to acquire the two images. Another possible problem is the interferometer phase drift during image acquisition.

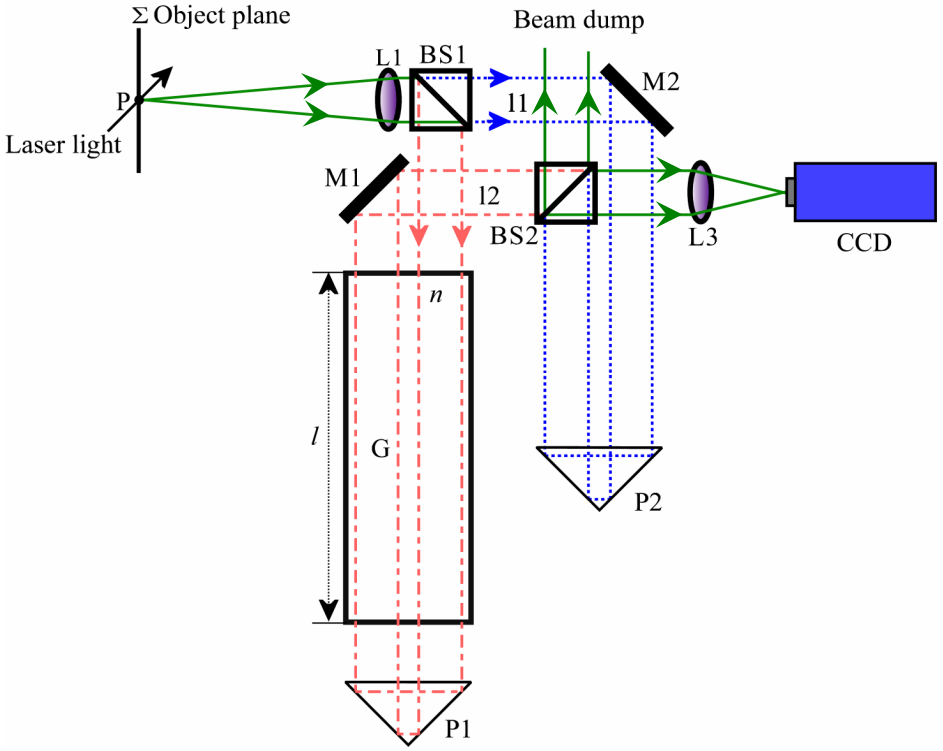

Figure 4-3 A typical single camera PDV system with a Mach-Zehnder interferometer. The beam paths are shown in different styles and colours: path l1 is dashed (blue), path l2 is dot-dashed (red) and combined path is solid (green). BS1, 2: 'non-polarising' beam splitters; M1, 2: mirrors; G: glass block with a length of *l* and a refractive index of *n*; P1, 2: right angle prisms; L1: camera lens; L3: tube lens; P: particle.

4.3 Theoretical characterisation of the Mach-Zehnder PDV interferometer

The form of the transfer function of an MZI is well defined from Equation 4-2 and constant over time. Its amplitude is determined by the visibility of its interference fringes, which mainly depends upon the transmission performance of the whole MZI setup. The transmission performance of the MZI involves polarisation sensitivity, intensity attenuation, scattering, flatness, parallelism and so on. The following is the discussion of the effects of these issues on the transfer function.

In this work, an MZI was designed with a FSR of around 1.16GHz. The key optical components and their performance in the MZI are listed in Table 4-1.

Table 4-1 Components for the MZI.

Components	Dimensions(mm)	Performances
'Non-polarising' Beam Splitter	25.4×25.4×25.4	< +/-3% splitting ratio@488-514.5nm AR coating<= 0.50%@514.5nm 0+/-2 deg Flatness: $\lambda/8$ @633nm; $\left\|T_s - T_p\right\|$ <= 5%
45° Prism (BK7)	38.1×38.1×38.1	Flatness: $\lambda/8$ @633nm AR coating<= 0.50%@514.5nm 0 deg.
Mirror	22.4x31.5×3.5	Flatness: $\lambda/10$ @633nm R>= 90%@514.5nm
Glass Block (BK7)	50×50×150	Fatness: $\lambda/10$ @633nm Refractive Index: 1.52@514.5nm AR coating<= 0.25%@514.5nm 0 deg.

4.3.1 Polarisation sensitivity

In a conventional two-camera PDV system, one important error source is the polarisation sensitivity of the splitting ratio of the beam splitter used which is shown in Figure 1-3. Ideally the beam splitter should split the incoming light 50:50 between the signal and reference cameras with no variation for different polarisations and incoming intensities of light. However, even the 'non-polarising' beam splitters commercially available still have some sensitivity to polarisation, typically ±3% variation in the split ratio for S and P polarised light [2]. This leads to velocity errors of ~±7ms^{-1} [3] in a conventional PDV system. In the MZI-PDV system, two 'non-polarising' beam splitters shown in Table 4-1 were used, so it is necessary to analyse the effect of the polarisation sensitivity on the transmission profile of the interferometric filter.

Considering actual performances of all the optical components in the MZI shown in Figure 4-1, Equation 4-2 can be rewritten as:

$$\frac{I_1}{I_0} \propto R \cdot T \cdot \left(T_{GB} + 1\right) + 2 \cdot R \cdot T \cdot \sqrt{T_{GB}} \cdot \cos(\Delta\varphi)$$

$$\frac{I_2}{I_0} \propto \left(R^2 \cdot T_{GB} + T^2\right) - 2 \cdot R \cdot T \cdot \sqrt{T_{GB}} \cdot \cos(\Delta\varphi)$$

$$I_N = \frac{I_2 - I_1}{I_1 + I_2} \propto \frac{\left[\left(R - T\right) \cdot \left(R \cdot T_{GB} - T\right) - 4 \cdot R \cdot T \cdot \sqrt{T_{GB}} \cdot \cos(\Delta\varphi)\right]}{\left(T_{GB} \cdot R + T\right) \cdot \left(R + T\right)}$$

Equation 4-10

where R and T are reflectance and transmittance of beam splitters BS1 and BS2 respectively. T_{GB} is the transmittance of the glass block. $\Delta\varphi$ is the phase difference between the two arms in the MZI. It is shown from Equation 4-10 that the DC level is different for outputs I_1 and I_2, although the AC variation (fringe amplitude) is the same on each output. This causes the fringes to appear to be asymmetric for both outputs, as well as the normalised intensity I_N. The visibility is different for each output.

In order to investigate the specific effect of the two beam splitters' polarisation sensitivity on the transmission profile of the MZI, all other factors are considered under ideal conditions. The DC, AC components and visibility in outputs I_1, I_2, and I_N against polarisation dependent loss (PDL) are plotted in Figure 4-4. PDL is defined as (R - T) for a beam splitter for convenience.

The calculated DC components are plotted in Figure 4-4(a). The AC components are shown in Figure 4-4(b) and the fringe visibility is in Figure 4-4(c). For I_1, the DC level reduces from 0.5 to 0 when the quantity of PDL is increased from 0 to 1 while it is complementary with I_1 for I_2. This results in the sum of I_1 and I_2 being constant and equal to 1. For I_N, it increases from 0 to 1 when the quantity of PDL is increased from 0 to 1. The AC level of I_1 varies from -0.5 to 0 when the quantity of PDL is increased from 0 to 1, while for I_2 it is equal to I_1 in quantity but in antiphase. The AC level of I_N decreases from 1 to 0 in quantity when PDL is increased from 0 to 1 in quantity.

The fringe visibility for I_2 reduces from 1 to 0 when the quantity of PDL is increased from 0 to 1, while it is always 1 for I_1. It can therefore be indicated that the AC level will reduce with the increase of polarisation dependent loss of the beam splitters, which directly decreases the measurement sensitivity and range.

For example, under ideal conditions, i.e. R = T = 0.5, T_{GB} = 1 and polarisation insensitivity, Equation 4-10 is equivalent to Equation 4-1. The normalised intensity against frequency is shown in Figure 4-5(a). The two normalised outputs, $I_1/(I_1 + I_2)$ and $I_2/(I_1 + I_2)$, are exactly symmetrical in the range from 0 to 1, which means their visibilities are both 1. I_N, which is independent of the original intensity $I_0 = I_1 + I_2$, is also symmetrical from -1 to 1 in one fringe and offers double sensitivity to frequency as only one output.

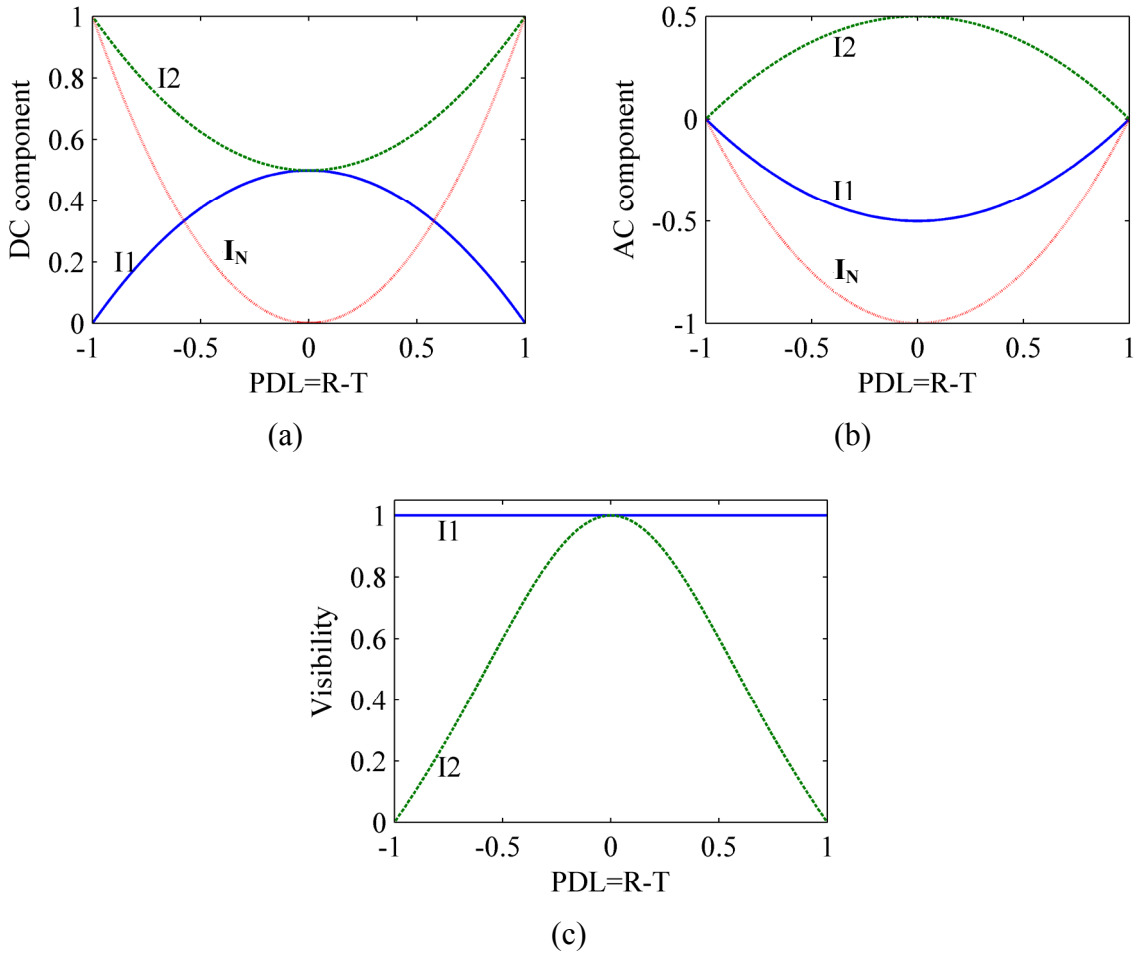

Figure 4-4 DC, AC components and visibility in outputs I_1, I_2, and I_N against polarisation dependence loss (PDL). (a): DC; (b): AC; (c): Visibility.

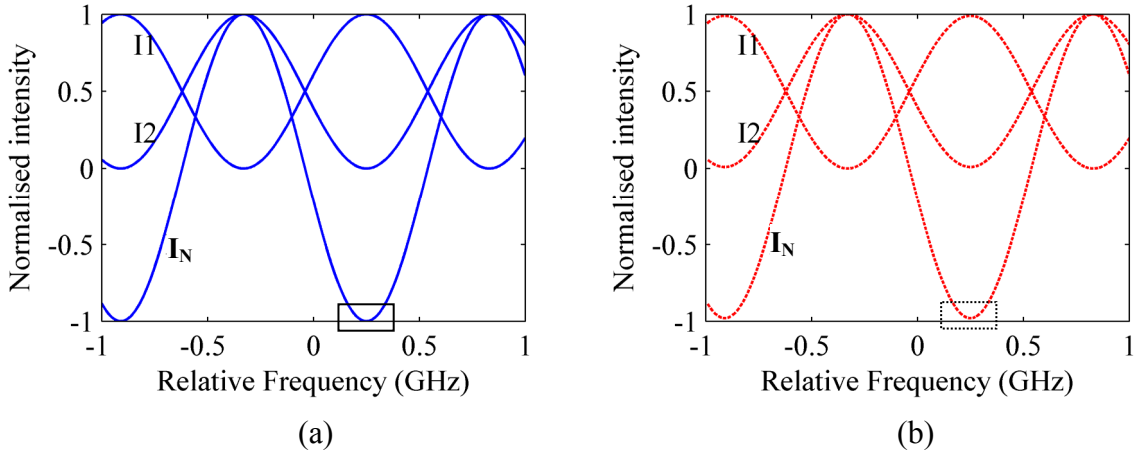

Figure 4-5 Normalised intensity against frequency in an MZI. (a) Under ideal conditions; (b) For ±5% variation in the split ratio for S and P polarised light corresponding to ±0.1 of PDL.

In our setup, the two beam splitters were used with about ±5% variation in the split ratio for S and P polarised light corresponding to a PDL of ±0.1. Equation 4-10 can be rewritten as:

$$I_1/(I_2+I_1) \propto 0.495 + 0.495 \cdot \cos(\Delta\varphi)$$

$$I_2/(I_2+I_1) \propto 0.505 - 0.495 \cdot \cos(\Delta\varphi)$$

$$I_N = \frac{I_2 - I_1}{I_2 + I_1} \propto 0.01 - 0.99 \cdot \cos(\Delta\varphi) \ . \qquad \textbf{Equation 4-11}$$

This assumes the glass block transmittance of unity. The normalised intensity against frequency, I_N, is plotted in Figure 4-5(b). For the two outputs in the MZI, the DC level is 0.495 and 0.505 respectively, although the AC variation (fringe amplitude) is the same 0.495. The visibility is therefore different for the two outputs (1 and 0.98).

For I_N, the gradient of the slope region is around 293[MHz]$^{-1}$ while it is 290[MHz]$^{-1}$ under ideal conditions. For a laser wavelength of 514.5nm and velocities in a range of about ±100ms^{-1}, the Doppler frequency shift is about ±200MHz. Therefore, the frequency error from ±5% polarisation sensitivity of two beam splitters used in the MZI, leads to the maximum velocity error of about 1.5ms^{-1}. This compares with an error of ±7ms^{-1} in a conventional PDV system using a beam splitter with a typical ±3% variation in the split ratio for S and P polarised light [3]. The interferometric filter therefore has the advantage of reducing the uncertainty due to polarisation sensitivity. This is due to the optical interference principle of the MZI as shown in Equation 4-10. In one output I_1 of the interferometer, both the two beams that form interference pass through one reflection and one transmission of the beam splitter (BS1 or BS2), leading to a visibility of 1 in the interference pattern. In the other output I_2, one of the two beams that form interference passes through double reflections of the beam splitter while the other double transmissions, leading to a visibility of ~0.98 in the interference pattern. The normalised intensity calculated from the two outputs is therefore less sensitive to polarisation variations compared to a conventional PDV system where only a single 'non-polarising' beam splitter is used.

4.3.2 Transmittance of glass block

The glass block, inserted in the longer arm of the MZI, will attenuate the optical intensity (Figure 4-1). In order to investigate this effect on the normalised intensity in the MZI, only the block's transmittance is considered in the system while all other factors are considered to operate under ideal conditions. Equation 4-10 can therefore be rewritten as:

$$I_1/(I_2+I_1) \propto 0.25 \cdot (T_{GB}+1) + 0.5 \cdot \sqrt{T_{GB}} \cdot \cos(\Delta\varphi)$$

$$I_2/(I_2+I_1) \propto 0.25 \cdot (T_{GB}+1) - 0.5 \cdot \sqrt{T_{GB}} \cdot \cos(\Delta\varphi)$$

$$I_N = \frac{I_2 - I_1}{I_2 + I_1} \propto \frac{-\sqrt{T_{GB}} \cdot \cos(\Delta\varphi)}{0.5 \cdot (T_{GB}+1)} . \qquad \textbf{Equation 4-12}$$

For both outputs, $I_1/(I_1 + I_2)$ and $I_2/(I_1 + I_2)$, the DC and AC levels are the same, and those quantities will depend on the transmittance of the glass block, T_{GB}. The normalised intensity I_N is completely symmetric around 0 but its amplitude (AC level) depends on T_{GB}. The relationship is plotted in Figure 4-6. The amplitude reduces from 1 to 0 when T_{GB} is decreased from 1 to 0. The most rapid change takes place in the range from T_{GB} = 0 to 0.5, while the amplitude only changes by 0.06 between T_{GB} = 0.5 and 1. This means that the transmittance of the block has little effect on the amplitude of the normalised intensity in the MZI since T_{GB} will be larger than 0.5 for most commercially available glass blocks.

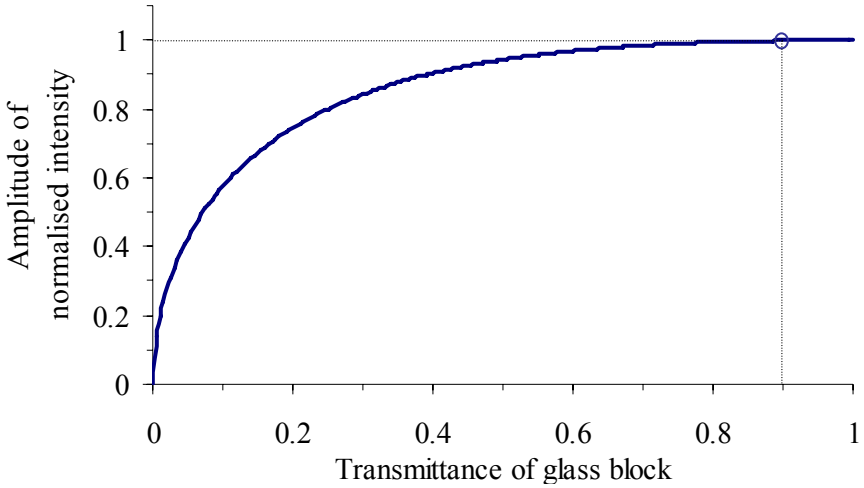

Figure 4-6 Amplitude of I_N against T_{GB}.

In our case, the transmittance is around 0.9 (30cm length of BK7) [4] at 514.5nm leading to an amplitude of 0.998 of the normalised intensity in the MZI. Further examples are shown in Figure 4-7 for values of 1 and 0.5 for the transmittance of the block.

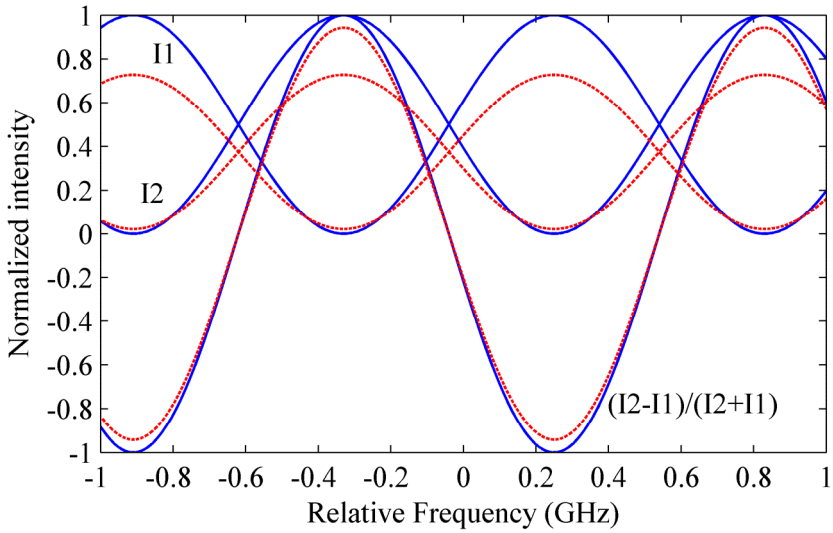

Figure 4-7 Normalised intensity of the MZI against frequency. Solid lines (blue): T_{GB} = 1; Dashed lines (red): T_{GB} = 0.5.

4.3.3 Fabry-Perot (FP) effect of glass block

Between two parallel, partially reflecting surfaces, multiple-beam interference can take place, called the FP effect. Thus the two surfaces of the glass block used in the MZI can result in the FP phenomena, and its length is large enough to produce a free spectral range (FSR) close to that of the MZI. It is therefore worth analysing this effect.

The length of the glass block in our system is 15cm (refractive index: 1.52@514.5nm), generating a 0.66GHz FSR of the FP interference fringes. This is comparable to the 1.16GHz FSR of the MZI. The reflectance for a glass-air interface is calculated to be 4.26% by using Fresnel's Equations [5]. Figure 4-8 shows the effect of the FP interference from the two optical surfaces of the glass block, on the normalised intensity in the MZI. The amplitude of the transmission profile of the glass block is around 0.05. It can be concluded that little effect is imposed on the MZI normalised intensity by the FP effect of the glass block for small reflectances (<5%) on the end surfaces. For example, in our system the reflectance on the two optical surfaces of the glass block was about 0.25% due to the use of anti-reflecting coatings leading to a reduction of ~0.01 in the amplitude of the interference fringes.

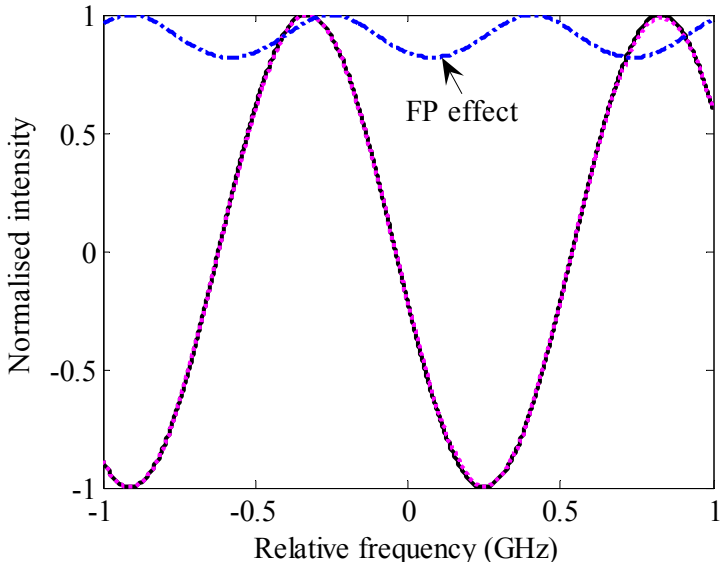

Figure 4-8 Normalised intensity against frequency with the FP effect of the glass block. Solid line (black): no FP effect; Dot dashed line (red): 4.26% reflectance of the glass block end surfaces.

4.3.4 Flatness effect

The flatness of an optical surface is the degree to which it approximates an ideal mathematical plane. This is directly related to the quality of the interference image in the MZI. In order to characterise this relationship, we assume that flatness means one optical surface varies from 0 (ray 1) to +/- flatness (ray n) linearly as shown in Figure 4-9(a) and (c), although the change should be irregular and a more practical case is the wavy change in optical surfaces as shown in Figure 4-9(b). The quality of the interference image can be quantified using the contrast

$$C = \frac{I_{max} - I_{min}}{I_{max}}$$ **Equation 4-13**

where I_{max}, I_{min} are the maximum and minimum interference intensities respectively.

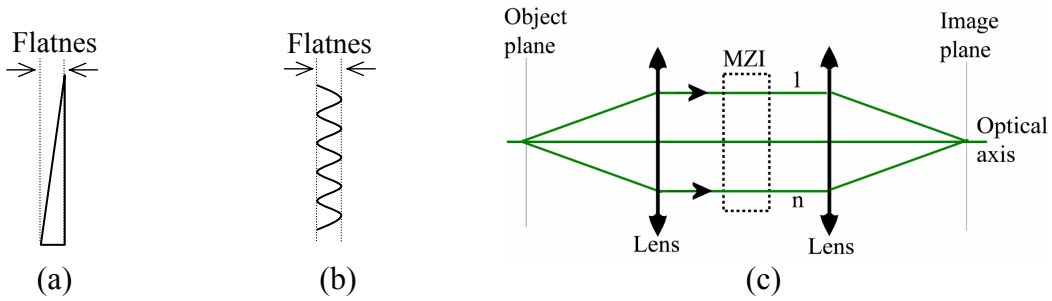

Figure 4-9 A simplified plane in order to investigate flatness effect of optical surfaces on the normalised intensity in the MZI. The fatness linearly increases from 0 to the maximum for optical rays 1…n as shown in (c) like a wedge (a). (b) A more practical case in the optical component surface variations like a wave.

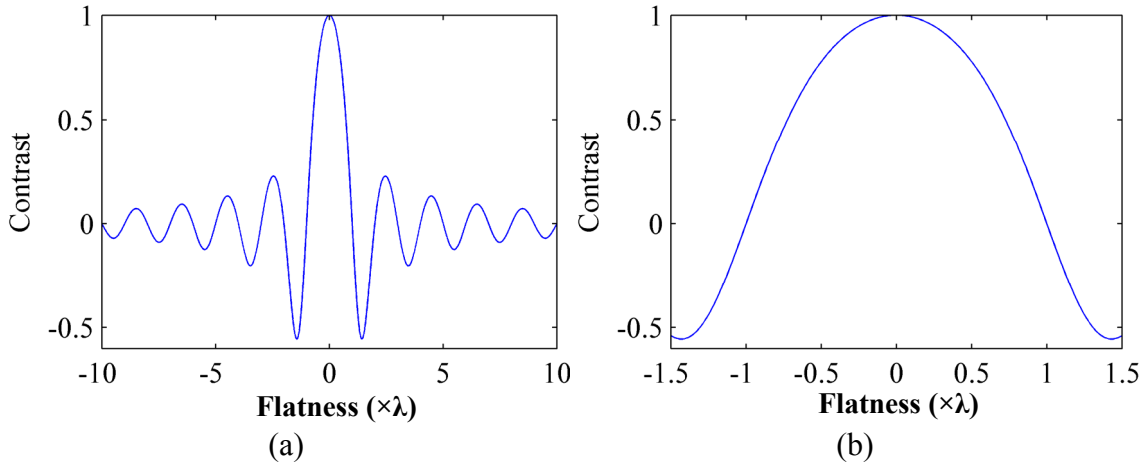

Figure 4-10 Contrast of the interference fringes is plotted against the flatness of the optical components in the MZI.

Figure 4-10(a) shows the contrast C of the interference fringes in the MZI plotted against the combined flatness in the interferometer, which is the integrated value of all the optical surfaces (around 20).

It can be seen that C oscillates periodically with increasing flatness, and the oscillation amplitude decreases as the flatness increases. The oscillation period is ~3λ shown in Figure 4-10(b). The flatness is therefore selected to be as small as possible to increase the interference fringe quality. In this work a flatness of ~λ/2 is evaluated as a representative figure for all of the optical surfaces within the system, which leads to a contrast of 0.78 in the interference fringes. It is worth noting that the theoretical analysis is necessarily a simplified model for the overall system as there are many optical components at different planes in the system. The purpose of the theoretical modelling is used to investigate the likely effect of the flatness on the contrast of the interference fringes. Therefore, the modelling here may be limited for practical conditions.

4.3.5 Detector sensitivity

From Equation 4-2, the normalised intensity I_N of the MZI plotted against the optical frequency has a perfect cosinusoidal form, and its amplitude is determined by the transmission performance of the whole MZI setup. Here the effect of detector sensitivity on the normalised intensity profile is discussed.

A detector can be characterised as

$$Sig_{out} = k \cdot Sig_{in} + Sig_{dark} \qquad \textbf{Equation 4-14}$$

where k is sensitivity coefficient and Sig_{dark} is noise from the detector intrinsic dark current and surrounding environmental factors. The actual calculated I_N in the MZI is directly related to the two used detectors sensitivity coefficients and dark signals.

Effect of detector sensitivity coefficient

First, the effect of the detector sensitivity coefficient will be discussed. Figure 4-11(a) shows the full width at half maximum (FWHM) of the normalised intensity profile in the MZI plotted against the ratio $k2/k1$, providing $Sig_{dark} = 0$, where $k1$, $k2$ are the sensitivity coefficients of the two detectors used to collect the two outputs in the MZI respectively. The FWHM reduces from π to 1.67rad when $k2/k1$ is increased from 1 to 5, leading to a sharper normalised intensity profile shown in Figure 4-11(b). This will distort the normalised intensity dependence on optical frequency resulting in the measurement error. The two detectors' sensitivity coefficients must therefore be calibrated before any measurement.

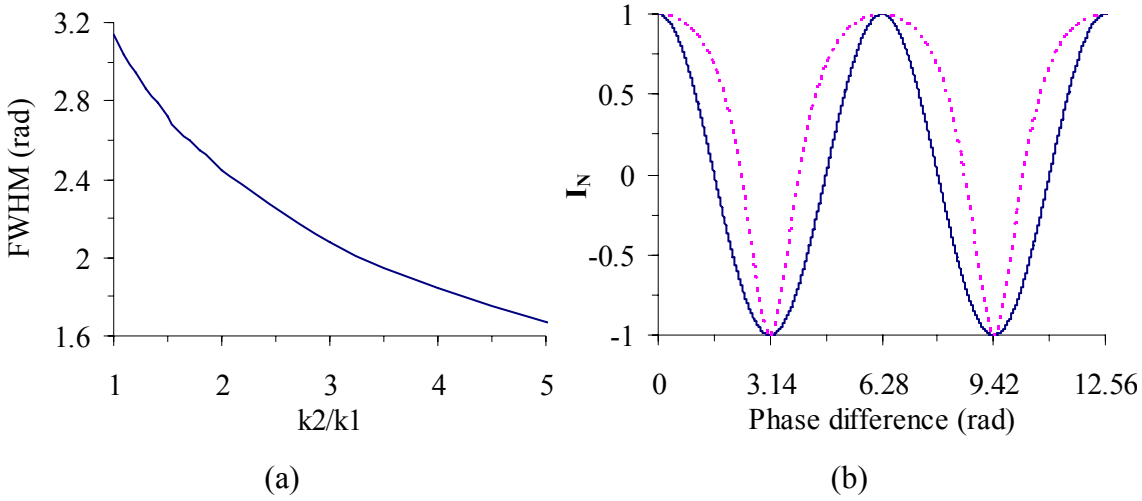

Figure 4-11 Effect on the normalised intensity (I_N) profile in the MZI of different sensitivity coefficients by using theoretical analysis. (a) FWHM against the ratio of two detectors' sensitivity coefficients. (b) Peaks sharpening or broadening in the normalised intensity profile. Solid line (blue): k2/k1=1; Dashed line (red): k2/k1=5.

Effect of detector dark current

The dark current in the detectors will also have an effect on the normalised intensity in the MZI. Figure 4-12 shows the amplitude of the normalised intensity for the MZI plotted for dark noise Sig_{dark} from two detectors with the same sensitivity coefficients (k2=k1). With no dark noise, i.e. Sig_{dark} =0, the amplitude (AC level) is 1 corresponding to the point (0, 0) in Figure 4-12. The amplitude reduces when Sig_{dark} is increased. For example, the amplitude reduces from 0.82 to 0.58 when detector 1's dark noise is increased from 0 to 50% when detector 2's dark noise is 20%.

In order to eliminate this problem, it is necessary to carry out a subtraction of the background noise in the acquired images during the processing of measurements.

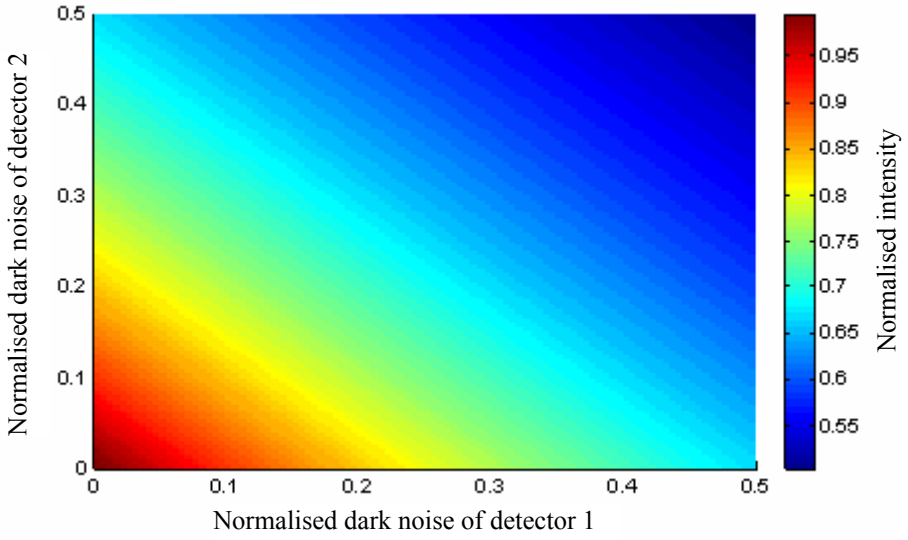

Figure 4-12 Effect of different dark noises from two detectors with the same sensitivity coefficients by using theoretical analysis. Dark noise was expressed as the percent of signal power entering a detector.

4.3.6 Combination of the PDL, FP, glass transmission and flatness effects

The overall effect of the error sources including the polarisation sensitivity of the beam splitters, the effect of the flatness of optical surfaces and the performance of the glass block discussed in section 4.3.1 to 4.3.4 on the performance of the MZI is plotted in Figure 4-13. The performance of the glass block includes the FP effect from the two block end surfaces and the optical attenuation due to the glass material. This figure shows the normalised intensity against frequency in the MZI under ideal conditions (PDL = 0, T_{GB} = 1, 0 flatness (perfectly flat) of optical surfaces and 0 reflectance of the glass block end surfaces) and the specific conditions (PDL = ± 0.1, T_{GB} = 0.9, $\lambda/2$ flatness and 5% reflectance of the glass block end surfaces) at the wavelength of 514.5nm. It can be seen that the amplitude reduces to ~0.75 and ~0.77 for PDL = -0.1 and 0.1 respectively when compared to ideal conditions. This will reduce the measurement sensitivity.

The difference between the two is due to the optical configuration of the MZI in which the glass block is located in the longer beam path (l2 in Figure 4-1) that is reflected by the first beam splitter (BS1 in Figure 4-1). There is more light reflected than transmitted by BS1 when PDL, defined as R-T, is 0.1. This is then attenuated through the glass block (T_{GB} = 0.9), so the light in both paths is closer in intensity compared to the situation at PDL = -0.1 leading to larger interference fringe visibility.

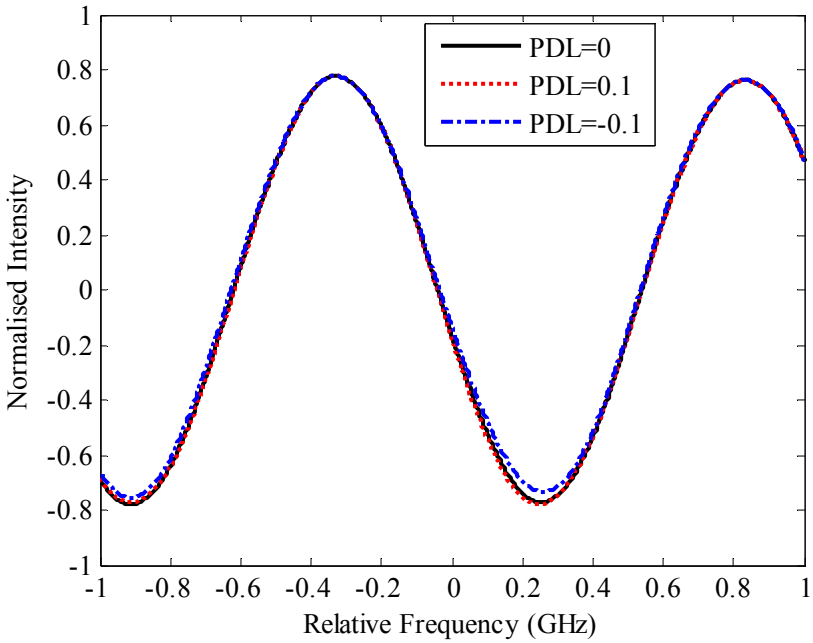

Figure 4-13 Normalised intensity against frequency in the MZI by using theoretical analysis.

4.4 Summary

The basic motivation for this work is the replacement of the iodine cell in current use with an entirely new optical system in the form of an unbalanced MZI as a frequency-to-intensity converter for PDV. The normalised intensity can be automatically obtained from the two complementary outputs of the MZI, which is independent of the original intensity. This eliminates spatial intensity variations caused by effects other than Doppler frequency shifting. The use of an MZI has several advantages over the iodine cell.

- The normalised intensity in an MZI is well defined and constant over time, having the usual cosinusoidal dependence on frequency while the transfer function of the iodine cell can be affected by environmental factors such as temperature variations and mechanical vibrations.

- Proper optical path difference of an MZI can be selected to correspond to the expected measurement range of velocities in a given flow situation by using different glass blocks, which also can correct different magnifications in the two arms to improve the numerical aperture of the system. It is very difficult to realise this for the iodine cell.

- ❖ The illumination light wavelength is no longer restricted to particular values. Any continuous wave (CW) or pulsed laser of sufficient power and enough narrow linewidth can be used to form a light sheet for illuminating the flow.

- ❖ With the single camera MZI-PDV scheme, exact alignment of the two output images on the active area of the camera is automatic. This eliminates the pixel-matching problem in conventional two camera PDV systems. Although one camera PDV system has also been implemented with the use of the iodine cell.

However, all the optical components in an MZI are required to be of very good quality, which is illuminated in section 4.3. For example, the polarisation dependence variation should be smaller than ±5% for beam splitters, the flatness $\lambda/2$. The MZI phase will be sensitive to temperature variations because of the thermal expansion of the optical components and small mechanical vibrations. This can result in measurement errors and some measures to cope with the phase drift must be taken in order to conduct accurate measurements.

4.5 References

[1] Seiler, F. and Oertel, H. (1985), "Visualization of velocity fields with Doppler-pictures", *Flow Visualization III, Proceedings of the Third International Symposium on Flow Visualization,* Ann Arbor, MI, pp. 454-9.

[2] Newport Inc., USA, website, (2007), http://www.newport.com.

[3] Meyers, J.F., Lee, J.W. and Schwartz, R.J. (2001), "Characterization of measurement error sources in Doppler global velocimetry", *Measurement Science and Technology,* Vol. 12, No. 4, pp. 357-68.

[4] Lambda Research Optics, Inc., USA, website, (2007), http://www.lambda.cc.

[5] Fowles, G. R. (1989), "Introduction to modern optics", Dover publications, Inc., New York.

5 A single velocity component MZI-PDV system

5.1 Introduction

A single velocity component MZI-PDV system is presented in this chapter. A detailed description of the equipment and components used in this system, as well as the processing procedure will be presented. A modified and infinity-corrected microscope optical system was used to construct the MZI. A phase-locking system designed to stabilise the filter is also described. The factors that will affect the uncertainty in MZI-PDV measurements were investigated including the quality of the interference fringe image, the number of the interference fringes and the image processing methods. Experimental results are presented for measurements of a rotating disc with maximum velocities of ~±70ms^{-1} at the edge of the disc. Measurements from a seeded air jet with a nozzle diameter of 20mm and an exit velocity of ~85ms^{-1} are also presented.

5.2 Laser illumination system

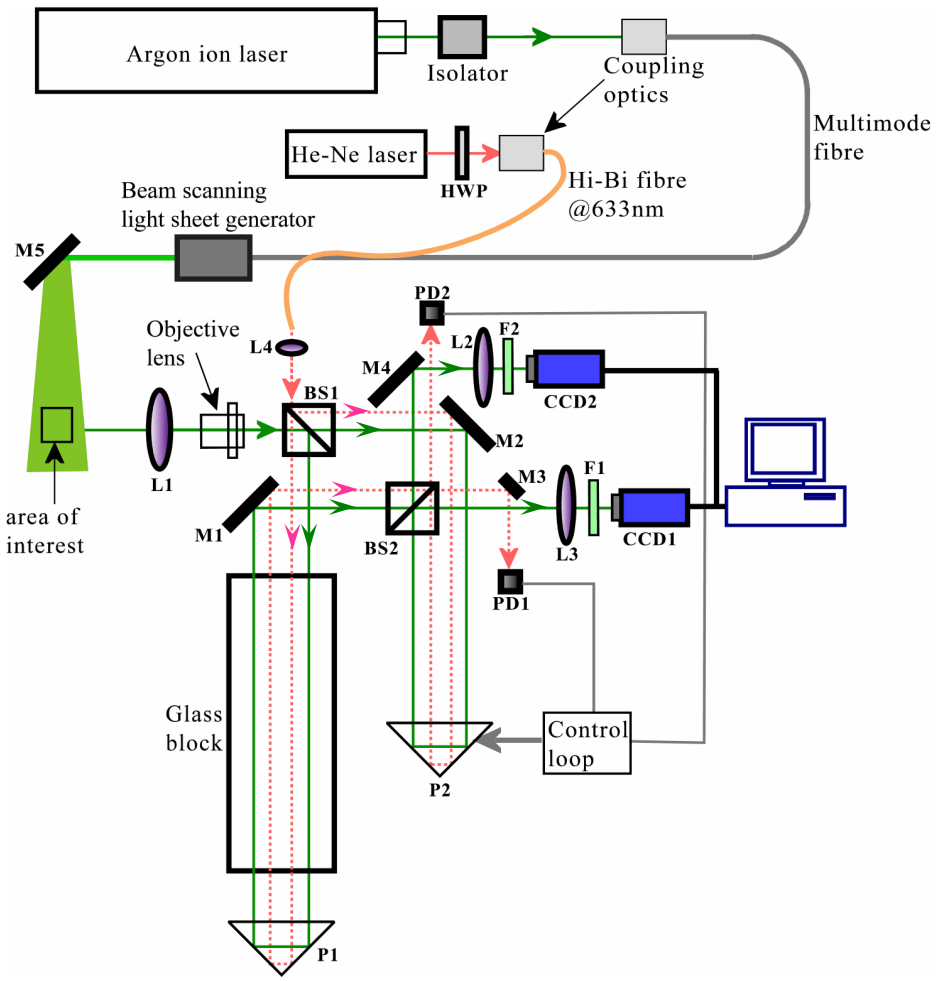

Figure 5-1 The experimental arrangement of the single component MZI-PDV system: HWP: half-wave plate; BS1, 2: 'non-polarising' beam splitters; L1: camera lens; L2, 3: tube lenses; L4: coupling lens; M1-5: mirrors; F1, 2: green filters; P1, 2: prisms. Beam path for measurement shown as solid line (green), beam path for locking system shown as a dotted line (red).

A schematic of the experimental arrangement is shown in Figure 5-1. The illuminating laser was a tuneable argon-ion laser (Spectra Physics Beamlok 2060-7S), incorporating a temperature-stabilised etalon to ensure single-mode operation at 514.5nm. The stabilised laser, after ~30 minute warm up with BeamLok engaged, has a single-mode linewidth of about 3MHz and an overall residual jitter of ~10MHz. The laser frequency drift is about 50MHz/ºC [1].

It is worth noting that the actual wavelength used to calculate the velocity in the Doppler equation 2-1 may not be exactly 514.5nm because of the environmental impact. However, the measurement error introduced to the velocity by this slight uncertainty, typically less than 0.5GHz in the laser wavelength, is negligible according to the error sources analysis in chapter 3.

Light from the laser was coupled into a multi-mode fibre (10μm core diameter, 10m length), through a Faraday isolator to prevent back reflections from entering the laser cavity. The output was formed into a light sheet using a prism-scanning device supplied by DLR [2] in Germany that scanned the beam rapidly across the measurement area. The optical configuration of the generator is shown in Figure 5-2(a).

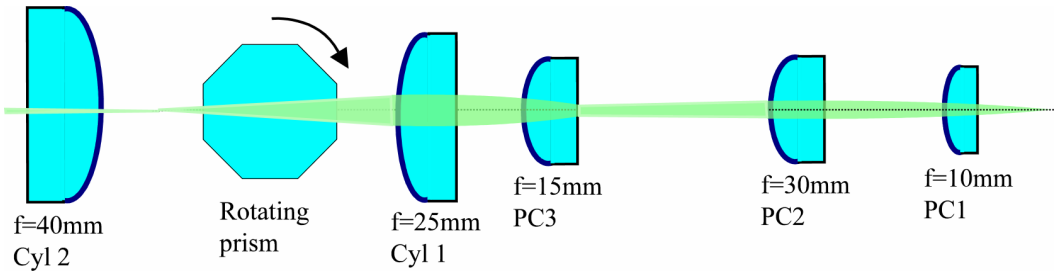

(a)

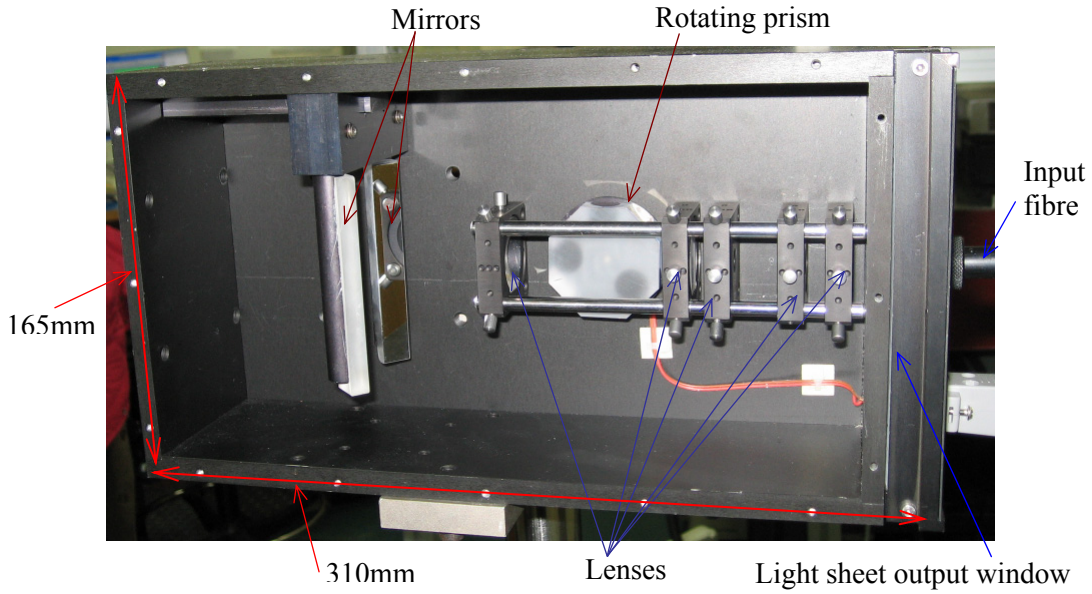

(b)

Figure 5-2 (a) The optical configuration and (b) the photograph of the light sheet generator [2]. PC1, 2, 3: plano-convex lenses; Cyl 1, 2: cylindrical lenses.

The rotating prism displaces the input light beam periodically. A cylindrical lens (Cyl 2) then converts this displacement into an angle deflection creating a light sheet. With the help of the plano-convex lenses PC1, 2 and 3, the focal point of the light beam can be adjusted to obtain the optimal shape for the flow area. The maximum rotation frequency is around 30Hz. This gives an intensity profile of the generated light sheet with an ideal 'top-hat' shape rather than the Gaussian profile formed using cylindrical lenses. The photograph of the device is shown in Figure 5-2(b).

5.3 MZI imaging head arrangement

The image capture system in Figure 5-1 is similar to a traditional PDV imaging head (Figure 3-2) with the MZI replacing the gas cell. However, in this case the two CCD cameras were used to capture the two complementary output images of the MZI. The scattered light from a region in the flow was imaged using a 35mm SLR camera lens. A microscope objective was used to image the image plane of the SLR camera lens as the input to the MZI, constructed using an infinity-corrected microscope optical system. The MZI components were inserted within the infinity space of the imaging system. The glass block was made of BK7 and was 15cm in length. An infinity-space distance of around 600mm was required in which to fit the optical components. The experimental arrangement of the MZI imaging head is shown in Figure 5-3.

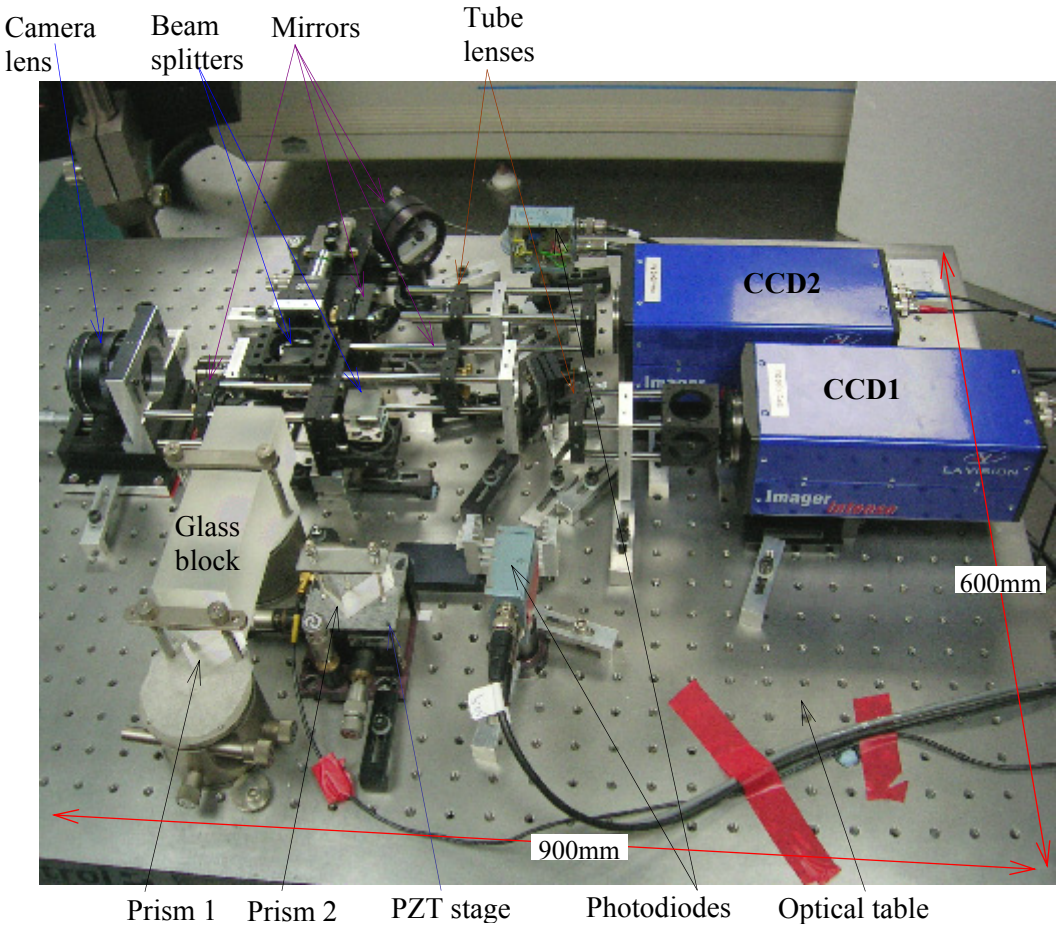

Figure 5-3 A photograph of the experimental arrangement of the MZI used with covers removed. Figure 5-1 is its schematic.

5.3.1 Modified infinity-corrected microscope optical system

In previous work [3,4] an infinity-corrected microscope optical system was built for a conventional PDV system. This had ~270mm infinity-space distance and was built with an objective (Plan Apo 1.25×/0.04) and a tube lens (f=180mm) supplied by Olympus. The specific lens combination was custom specified to the manufacturer. In this infinity-space images of the flow area of interest was transmitted through an iodine cell onto the active area of CCD cameras for detection. In this configuration the iodine cell was located in the imaging space. Therefore an infinity-corrected optical system can also be used for the MZI-PDV. This optical arrangement offers flexible space for auxiliary optical components to be introduced with nearly no image aberration since the light beam is collimated in this space as shown in Figure 5-4.

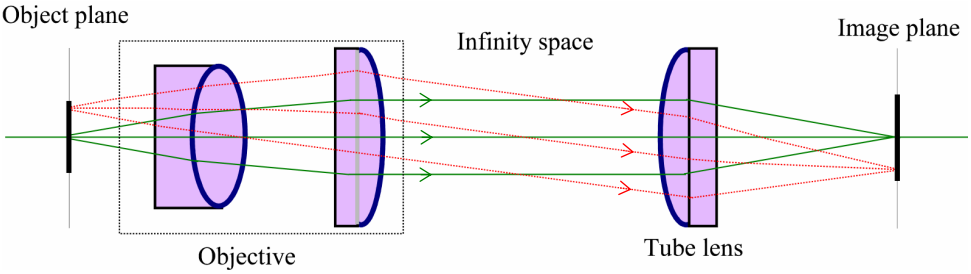

Figure 5-4 The principle of an infinity-corrected microscope optical system. Beam path for the object point located on the optical axis shown as solid line (green), beam path for the object point located on off-axis shown as a dashed line (red).

However, the number of peripheral light waves collected by the tube lens will be reduced with increasing infinity-space distance, which results in darkened and blurred edges in the output image, also called the 'vignetting effect'. The working space distance depends mainly on the required image quality and what optical components are required in the space. As each optical component added into the space will have a detrimental effect on the optical image, then the more that are added, the worse the image will be. Compared with a conventional PDV system [4], an MZI filter consists of more optical components, which requires a longer space distance to be used. It is necessary to investigate and characterise the working performance (image quality) of the infinity-corrected optical system for different infinity-space distances. An experiment was therefore designed to assess this, and is shown in Figure 5-5.

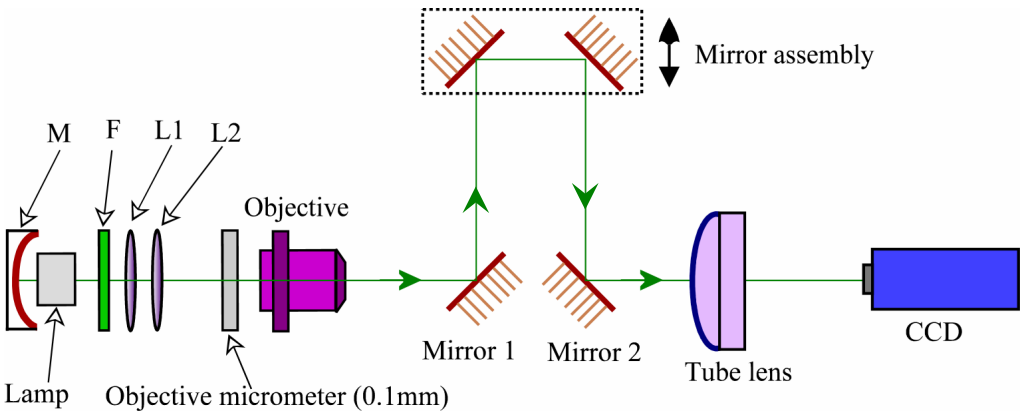

Figure 5-5 An infinity-corrected microscope optical system built with an objective and a tube lens. M: spherical focussing mirror; F: green filter; L1, L2: 18 and 400mm focal length lenses.

The experimental setup was constructed using the microbench system. A tungsten-halogen lamp (~10W) was used as the light source. After a green filter, the light beam was adjusted to form a broad collimated light bundle with the aid of a spherical mirror M and two lenses L1, L2. The green filter allowed the green wavelengths of the lamp light to reach an objective micrometer. The objective micrometer was located exactly in the front focal plane of the objective, and then 0.1×0.1mm grids image was generated in the infinity space after passing through the objective. Through mirrors 1, 2 and a mirror assembly, the collimated light beams were focused by the tube lens onto the active area of a CCD camera.

The camera used for image capture was a 'FlowMaster' supplied by LaVision, which was a digital camera with 12 bit A/D conversion on a Peltier-cooled chip (-15˚C), and a 1280 by 1040 image resolution. The pixel size is 6.7μm by 6.7μm. Image acquisition and processing software (DaVis) was used to control the camera and display the image intensity distribution.

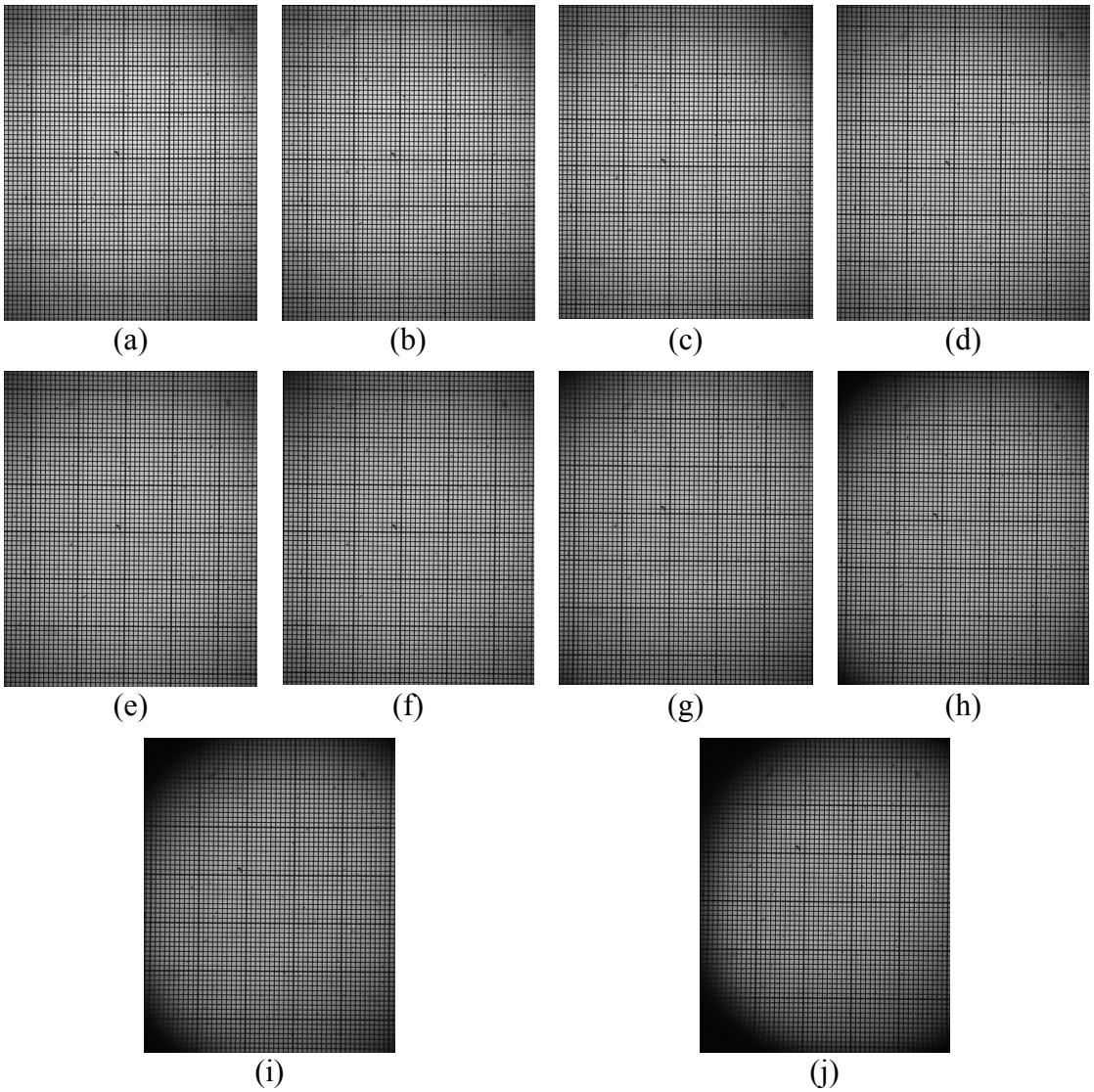

Figure 5-6 The recorded images taken at different infinity-space distances. (a), (b), … (j), at 200, 250, … 650mm.

This infinity space between the objective and the tube lens can be adjusted by moving the mirror assembly along the direction of the light beam with the help of microbench rods, while keeping all other conditions the same. A series of images can then be taken corresponding to different infinity-space distances simultaneously, and thus the image quality can be compared and analysed. Figure 5-6 shows the recorded images taken at different infinity-space distances in the range of 200 to 650mm in steps of 50mm. The integration time of the camera was set to be 0.1s in order to acquire clear images.

It can be clearly seen from Figure 5-6 that the image intensity decreases when the space distance is increased. The relative average and maximum intensities reduce to 63% and 80% respectively from a space distance of 200 to 650mm as shown in Figure 5-7. Their approximate slopes were fitted to be about -0.0047 and -0.0076 in this space range, which may be used to evaluate the relative average and maximum intensities at other space distances than the range used (solid lines in Figure 5-7). The difference between the two losses is due to the variation of the pixel location in the image with the maximum intensity when the infinity space distance was increased. This results from the slight misalignment between the optical axis and the camera chip. Therefore, a more powerful laser source or higher dynamic-range CCD camera will be required when a longer infinity-space distance is used.

In Figure 5-8, the usable image area also reduces when the space distance is increased, leading to the reduction of the flow area of interest. The usable image area is a region where the 0.1×0.1mm grid image can be recognised. The useable area decreases to 62% at the space distance of 650mm compared to 200mm. The approximate slope was fitted to be -0.0085. This effect will directly reduce spatial measurement resolution despite considering a fixed area under investigation.

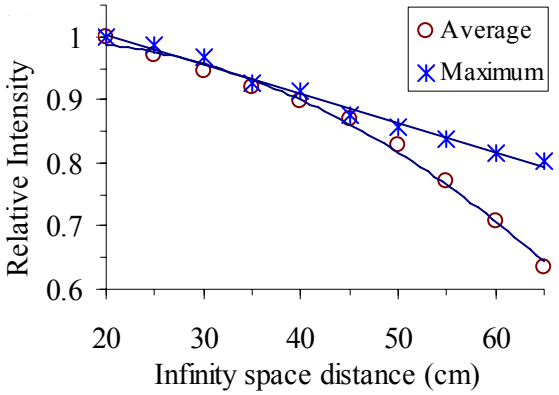

Figure 5-7 Relative average and maximum intensity against infinity space distances.

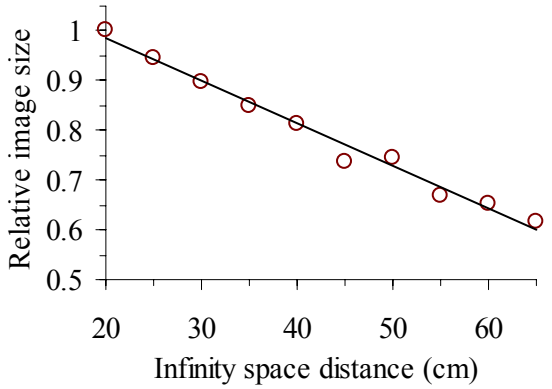

Figure 5-8 Relative useable image size against infinity space distances.

The image magnification was found to vary with increasing space distance. This is shown in Figure 5-9. It is ~1.25 at the space distance of 200mm, which is in accordance with the used objective (1.25×). However, the magnification increases by ~5.4% at 650mm when compared to the space distance of 200mm. This possibly results from the optical distortions due to the imperfections of the optical components used in the setup and the slight beam misalignment. The slope is fitted to be ~0.0015. This effect will reduce the investigated flow area that can be imaged and increase spatial resolution.

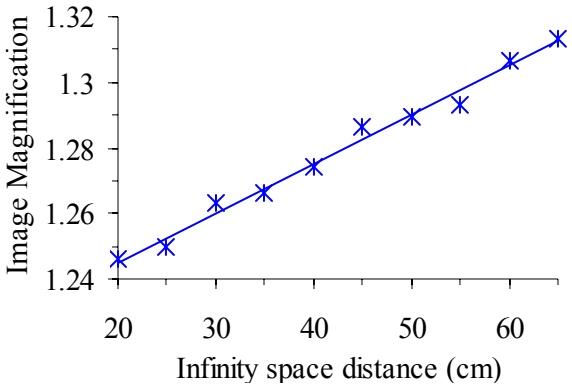

Figure 5-9 Image magnification against infinity space distances.

In the MZI-PDV system designed here, an infinity-space distance of around 600mm was required in which to fit the MZI optical components. This results in a ~35 and 20% reduction in average and maximum image intensities respectively, when compared to a space distance of 200mm. This also results in a 40% reduction in the usable image area. An increase of about 4.5% is caused in the output image magnification.

5.3.2 Camera properties

The cameras used (LaVision Imager Intense) are scientific grade CCDs operating at -15ºC giving low noise performance. Resolution is 1376×1040 pixels with 6.7×6.7µm pixel size and 12-bit digitisation. DaVis imaging software supplied by Lavison GMBH was used to control the cameras, display and process the results. The integration time of the cameras is adjustable from 1ms to 1000s depending on the scattered light intensity. The camera linearity was measured and is shown in Figure 5-10. This indicates that the cameras are linear over 90% of full range, and agrees with measurements taken previously [4].

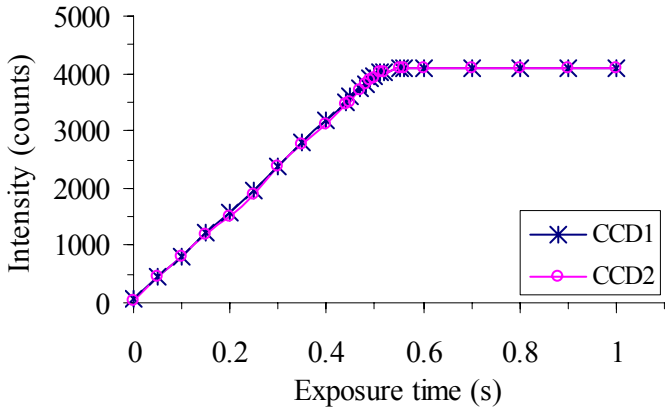

Figure 5-10 A plot showing the results of the investigation into the CCD linearity.

Figure 5-11 shows the dark current of the two cameras when changing the integration time. In theory the dark noise should not vary with changing integration time, however the graph in Figure 5-11 indicates that the dark noise slightly increases for both cameras when the integration time is increased in the range of 0 to 16s. This increase is larger for CCD1 (cross symbol) than for CCD2 (circle symbol).

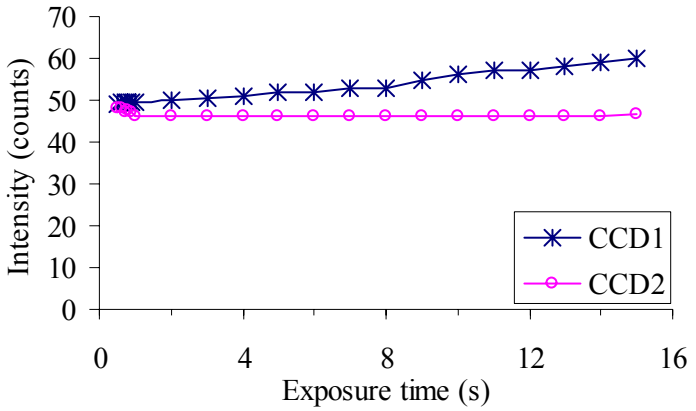

Figure 5-11 A plot showing the results of the investigation into the CCD dark current.

In order to explain this phenomenon, a simple test was made by covering the camera so that no light was collected in the integration time; the dark noise can then be measured for each pixel. Figure 5-12 shows the CCD1 pixel intensity distribution in the image taken at an integration time of 10s; the normalised intensity distribution (left) shows that most of the pixels have typically 50 to 60 counts; the right hand plot shows that a few pixels (~10) have intensities that are over 100 and even up to 880 counts. The dark noise in these pixels was found to increase when the integration time was increased. Figure 5-13(a) shows the averaged dark noise increases from 56 to 800 counts in the pixel that has the maximum intensity (880counts) among these pixels when the integration time is increased from 0.1 to 10s. It is these pixels that cause the dark noise to increase with the integration time for CCD1 in Figure 5-11.

The behaviour of these pixels is due to manufacturing defects called warm or hot pixels that describe a CCD characteristic that can be observed when long integration times are used, typically more than 3s [5]. This effect can be reduced/removed in experiments by using an image background subtraction or by applying a median filter to the image. Median filtering is also known as a 'neighbourhood operation', where each pixel in the processed image is the result of the evaluation of the defined neighbourhood area in the original noisy image. The original pixel value is replaced by the processed pixel value by looking at the pixels in the neighbourhood area and choosing the value that is the closest to the median of all of them.

In normal pixels the dark noise was found to be generally constant, as shown in Figure 5-14(a), but a strange effect was that the dark noise appeared to reduce slightly when the integration time was increased, for example, the average for dark noise reduced from 49 to 44 counts when the integration time was increased from 0.1 to 10s.

CCD2 generally has a similar performance to CCD1. The only difference from CCD1 is that the number of pixels whose intensities are over 100 and even up to 400 counts is less, shown in Figure 5-15. This is why the increase of the camera dark noise for CCD2 is smaller than CCD1 when the integration time is increased as shown in Figure 5-11.

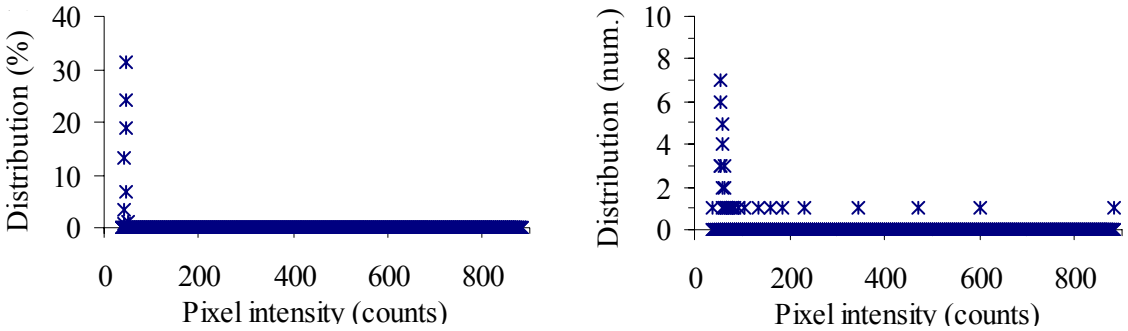

Figure 5-12 CCD1 pixel intensity distribution in the image taken at an integration time of 10s.

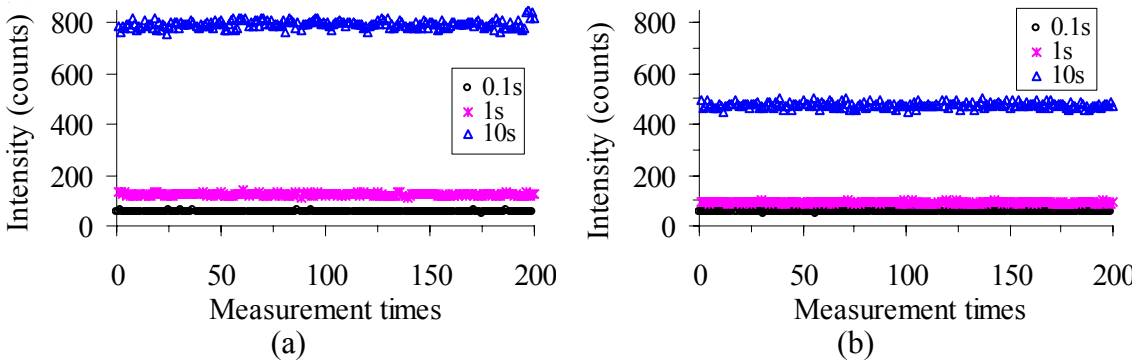

Figure 5-13 Dark noise against the integration time in the pixel that has the maximum intensity in the image taken at an integration time of 10s by CCD1 (a) and CCD2 (b).

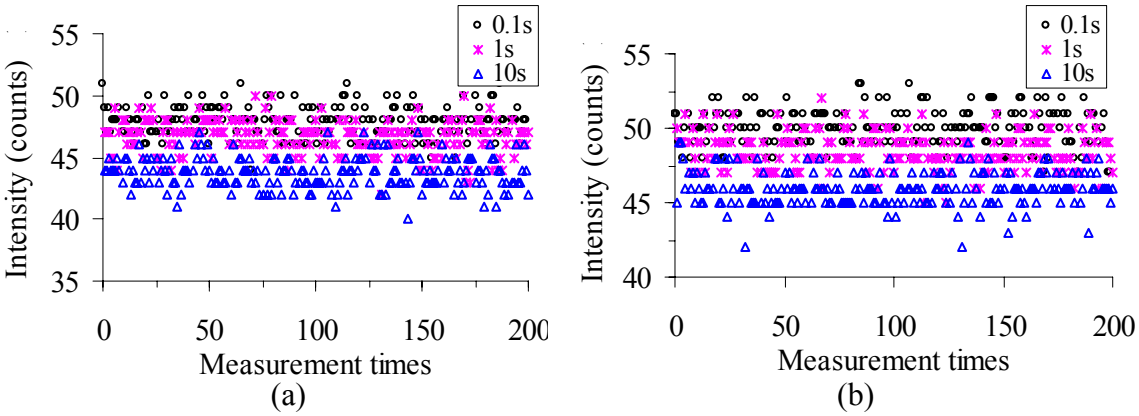

Figure 5-14 Dark noise against the integration time at a normal pixel. (a) CCD1; (b) CCD2.

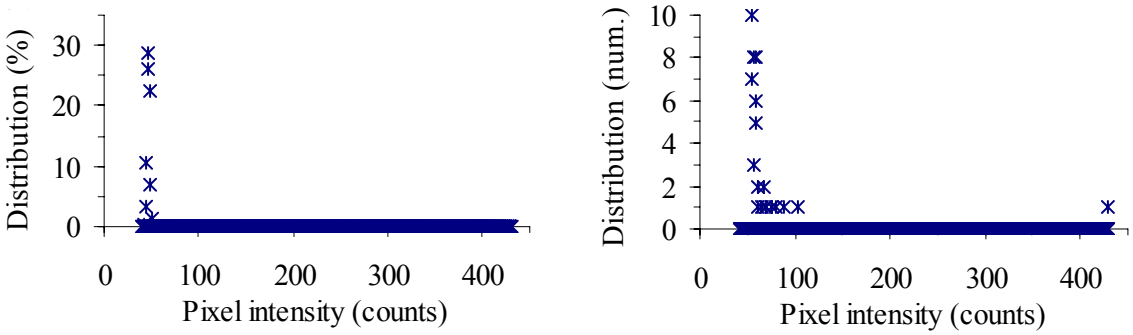

Figure 5-15 CCD2 pixel intensity distribution in the image taken at an integration time of 10s.

5.3.3 MZI filter properties

The Mach-Zehnder interferometer built in this work, as shown in Figure 5-3, operates at a room temperature of ~20ºC. All the components are located in a small optical table of 610×910mm and covered with a polystyrene box. This is supported by a vibration isolator that isolates vibrations from other sources such as the floor.

The transmission profile (normalised intensity) of the interferometric filter was measured using two approaches. The first is to obtain the profile by frequency scanning the laser and monitoring the complementary outputs of the interferometer using the two photodiodes. The Spectra-Physics argon-ion laser used in this work allows the optical frequency to be scanned by applying a voltage ramp to an input that controls the etalon temperature. This voltage ramp is from 2 to 3 volts involving a frequency range of around 6GHz. The scan must be performed slowly to avoid mod hopping. This approach will take a few hours to achieve a successful scan.

The second approach is much faster than the first one. It is by modulating the interferometer optical path difference and monitoring the two outputs using two CCD cameras to determine the profile. The PZT stage supporting the right-angle prism P2 (Figure 5-3) allows the optical path difference to be scanned by applying a voltage to the PZT controller.

Figure 5-16(a) shows the transmission profile in the MZI by using the laser frequency scanning. The laser frequency scanning range is around 6GHz in the form of a triangle wave, leading to five fringes to be detected with the fringe amplitude of about 0.75. This agrees with the designed free spectral range of this interferometric filter of about 1.16GHz. The discontinuousness in the curve, as shown in the rectangle in Figure 5-16(a), comes from the laser mode hops during the scanning.

Figure 5-16(b) shows the transmission profile in the MZI by modulating the optical path difference of the interferometer. The data was from a single pixel in the images recorded by two CCD cameras shown in Figure 5-3. In this approach, the modulation signal was a sinusoidal wave with a frequency of 0.005Hz and amplitude of 0.06V generated from a function generator (Stanford Research Systems DS3345). This signal was applied to the piezo controller (Photon Control MD3-75C) with a voltage gain of 15. The output of the controller was then fed to the PZT material to drive the PZT stage as shown in Figure 5-3. The amplitude of the measured transmission profile is around 0.7 which is in accordance with that obtained in the first approach (~0.75). The resultant profile is nosier than that measured using the first approach possibly due to the MZI interferometer phase drift during the scanning of the optical path difference of the interferometer, which mainly comes from the mechanical vibration of fans inside CCD cameras used. This will be further discussed in section 5.4.

The amplitudes of the measured transmission profile in the MZI achieved by using the two experimental approaches as shown in Figure 5-16 are both smaller compared with the result obtained with the theoretical modelling from Chapter 4 specifically with regard to the flatness term. This is possibly due to the limitation of the theoretical modelling used where a simplified model for the overall system was used to investigate

the approximate effect of the flatness on the transfer function of the MZI as there are many optical components at different planes within the system.

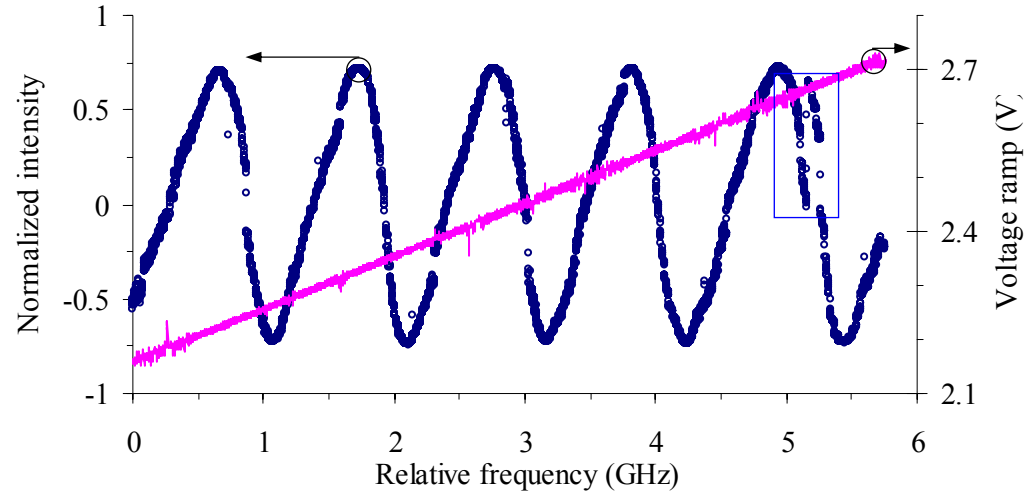

(a)

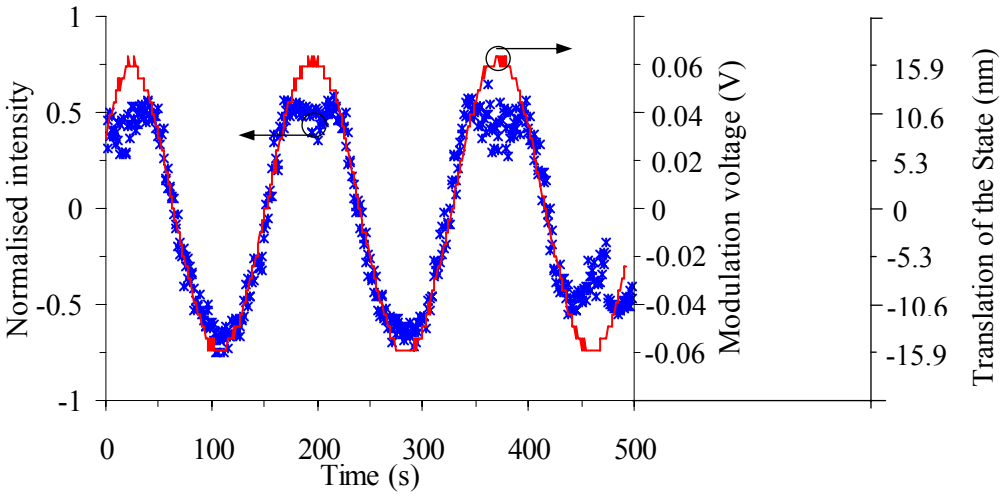

(b)

Figure 5-16 Normalised intensity of the MZI obtained by (a) using laser frequency scanning and (b) modulating the optical path difference of the interferometer.

5.4 Phase stabilisation of the interferometer

The form of the Mach-Zehnder interferometric filter function will be independent of temperature and mechanical vibrations. However, the interferometer phase will be sensitive to these effects. Temperature changes and mechanical vibrations will cause changes in the optical path difference. In practice, the output from the MZI was found to drift over time. This drift was partly removed by covering the whole interferometer with a polystyrene box to act as a shield from air currents and to provide some thermal stabilisation. To further improve the stability of the interferometer a locking system using a feedback loop controller to adjust the phase difference was constructed [6].

5.4.1 Recorded phase drift of the MZI

By monitoring the complementary outputs of the MZI interferometer using the two photodiodes shown in Figure 5-3, the output from the interferometer was found to drift over time due to the phase instability. Figure 5-17 shows the recorded drift in the output from the MZI with two cameras on and off respectively over a period of time using the argon-ion laser as the source. The two cameras are located on the same optical table as the MZI. The results indicate that the drift is slower when the cameras are off than when the cameras are on. This comes from the mechanical vibration of fans inside the cameras used to keep a normal operating temperature for the active chips by cooling them. The frequency of this drift is around 160Hz when the cameras are on.

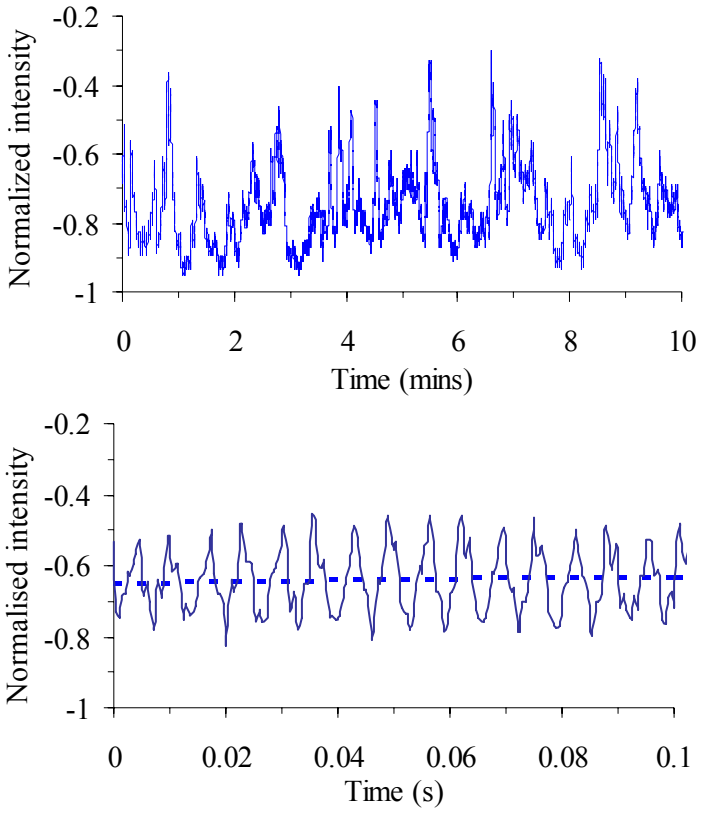

Figure 5-17 Normalised intensity of the MZI with cameras off (top), and on (below) together with the result (blue dashed line) when the cameras were off for comparison, showing the phase drift due to CCD cooling fan vibrations.

5.4.2 Feedback control

The normalised intensity of the MZI can be adjusted by modulating the path difference of the interferometer. Figure 5-18 shows a typical normalised intensity response to the modulation voltage which controls the PZT stage mounting the prism P2 as shown in Figure 5-3. The modulation signal is generated by a function generator (Stanford Research Systems DS345) in the form of sinusoidal wave with an amplitude of 0.06V and a frequency of 0.8Hz. This provides the possibility of actively locking the interferometer phase whenever a phase drift occurs by applying a small voltage signal to the PZT stage to modulate the interferometer's phase difference. A feedback control system [6] was therefore designed to lock the phase of the MZI to the laser wavelength as shown in Figure 5-19(a). It involved a custom designed PID controller for adjusting the PZT stage to change the path difference of the MZI [6].

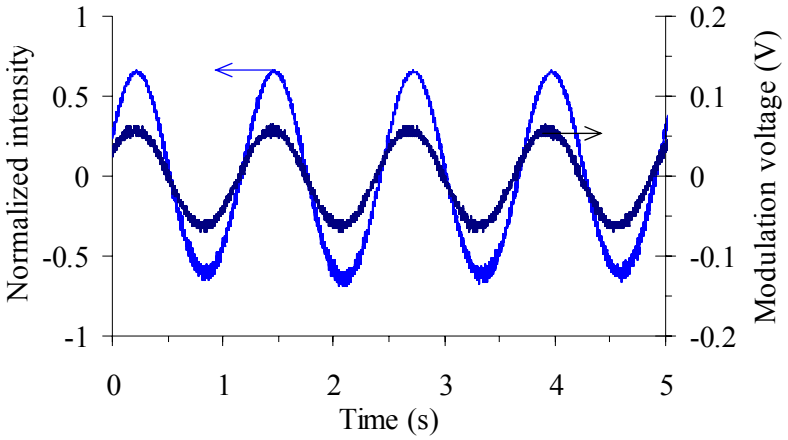

Figure 5-18 Normalised intensity of the MZI by modulating its optical path difference. Modulation signal: sinusoidal wave with amplitude of 0.06V, and frequency of 0.8Hz.

In Figure 5-19(a), a separate, low power, single frequency laser beam was directed from the other side of the beam splitter BS1 through the MZI near the periphery of the image area in order to measure and control the phase of the MZI. Two photodiodes (BPX65) PD1 and PD2 were used to monitor the complementary interferometric outputs using mirror M3. The signals from the two photodiodes were normalised through an electrical circuit comprising sum, subtraction and division units. The circuit is one part of the PID control loop shown in Figure 5-19(b).

Through a low-pass filter, this output was connected to a custom-designed PID electronic circuit. The circuit then generated an error signal relating to the interferometer phase drift. The error voltage was then fed back onto the piezoelectrically controlled stage supporting the right-angle prism P2, to modify the interferometer path difference. A feedback voltage of 60mV would move the MZI through one free spectral range (1.16GHz). The expected phase drift was on the order of 0.4π that was obtained from the experimental results in Figure 5-17 corresponding to a velocity range of ~100ms^{-1}. The exact velocity value depends on $\hat{\imath}$ and $\hat{o}$. An offset voltage on the piezo controller (Photon Control MD3-75C) supplied by a function generator (Stanford Research Systems DS345) was required to tune the interferometric filter to the quadrature position of the transfer function where the sensitivity of locking

system was maximum. The details on the electronic circuit designs and components used are discussed in Appendix A.

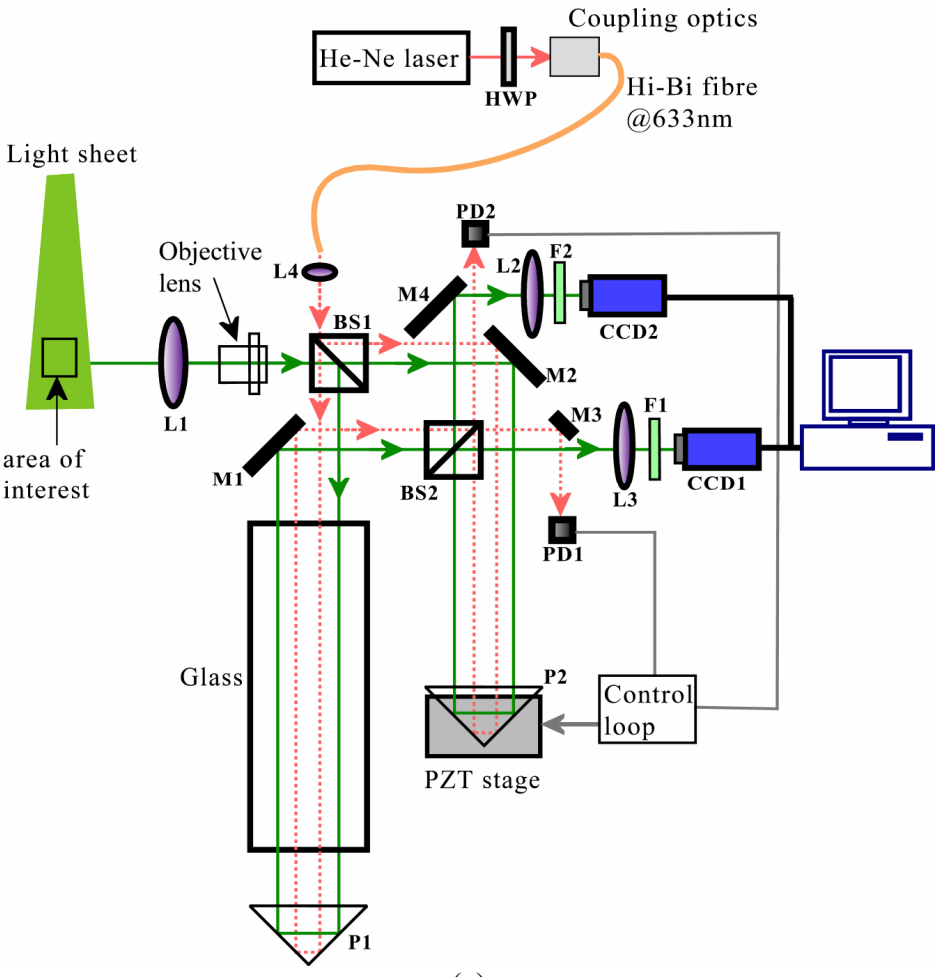

Figure 5-19 (a) The experimental arrangement of the phase locking system in the MZI. Beam path for measurement system shown as solid line (green), beam path for locking system shown as a dotted line (red). (b) The control loop. HWP: half-wave plate; BS1, 2: 'non-polarising' beam splitters; L1: standard camera lens; L2, 3: tube lenses; L4: coupling lens; M1, 2, 3, 4: mirrors; F1, 2: green filters; P1, 2: right angle prisms.

5.4.3 Light source for the phase locking system

Ideally the laser light source for the phase locking system should be at the illumination laser wavelength (argon-ion laser), and then the locking system locks the interferometer to this laser wavelength. This can also effectively remove the remaining small frequency drift of the laser source. Unfortunately, this would result in 'cross-talk' between the flow image and the laser beam used in the locking system.

Figure 5-20 shows the 'cross-talk' captured by the camera CCD1. This possibly results from the laser beam intrinsic transmission performance. According to the theory of light diffraction, the size of any collimated light beam will increase along its transmission path. For example, in our case, the laser beam transmission distance in the phase locking system is about 0.8m and the divergence angle of a collimated beam with a single mode fibre operating at 514.5nm and an objective lens (40/160) is found to be around 0.13º (9/4mrad). The laser beam size will therefore be an additional 2mm in diameter after travelling through the MZI, compared to its original size.

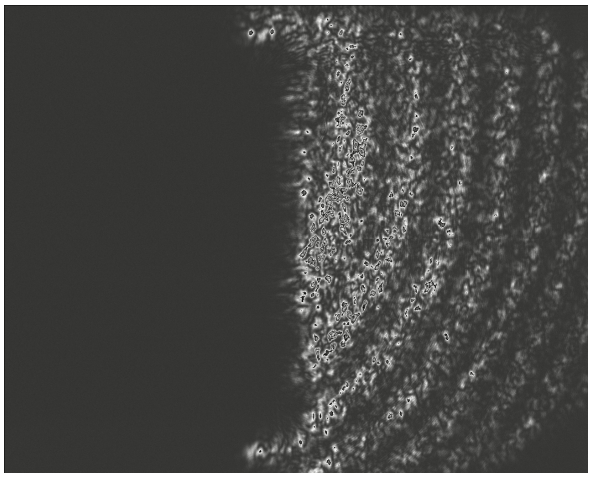

Figure 5-20 'Cross-talk' between a flow image and the laser beam used in the phase locking system in an MZI.

This diffraction fringe pattern can be clearly seen in Figure 5-20 as a result of the laser beam diffracting when it passes through the MZI. In addition, there is large scattering at the edges of the optical components where the quality is not as good as the central region. This results in a larger power distribution area.

This 'cross-talk' can cause errors in measurements because the laser light intensity in the phase locking system varies in real-time. Also, its power (even in ~nw order) may be more than, or appropriately in the same order, as the scattered power from the investigated flow. To solve this, a single frequency-stabilised He-Ne laser (Coherent Model: 200) was employed as the light source for the locking system.

The He-Ne laser light was coupled into one eigen axis of a Hi-Bi fibre with an operating wavelength of 632.8nm, through a Half-wave plate (HWP) to minimise the polarisation sensitivity of the phase locking system due to the laser polarisation drift and environmental variations. The output was directed from the other side of the beam

splitter BS1 through the MZI near the periphery of the image area to measure and control the phase of the MZI as shown in Figure 5-19(a).

Two band-pass filters F1 and F2, with a transmission band of 400-580nm and >85% transmission [7], as shown in Figure 5-21 (blue curve as marked), were placed in front of the two cameras to prevent light from the He-Ne locking laser being detected by the CCD cameras.

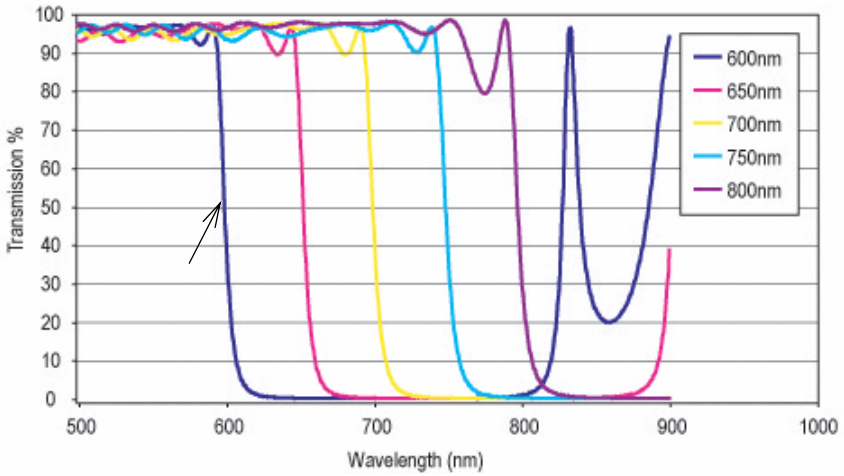

Figure 5-21 Transmission curve (blue curve as marked) of the band-pass filters used [7].

One disadvantage of this approach is that the operational stability depends on the frequency stability of the He-Ne laser (~±2MHz in 1 hour plus 0.5MHz/ºC) corresponding to ~±1ms^{-1} velocity error. The exact velocity value depends on ($\hat{o}$–$\hat{i}$). Any frequency drift from this laser will be recorded as an additional Doppler frequency shift, which will lead directly to measurement errors. Figure 5-22 shows the single frequency profile of the He-Ne laser obtained using a scanning flat plate Fabry-Perot interferometer (TEC OPTICS model FBI-25).

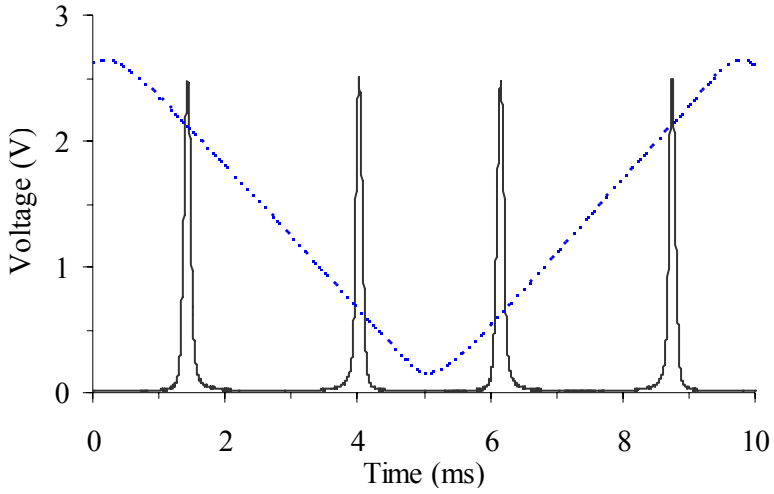

Figure 5-22 Single frequency profile of the He-Ne laser. FSR = 15GHz. Lines (blue): ramp signal sent to the Fabry-Perot interferometer. Lines (black): output of the He-Ne laser.

Another possible problem is a reduced sensitivity in the phase locking system, compared to the original argon-ion laser, as the split ratio of the two beam splitters is 70/30 at 632.8nm. This reduces the fringe amplitude to ~0.8 in the normalised intensity, while it is 1 when the argon-ion laser is used since the beam splitters operate at a design wavelength of 514.5nm. A possible method to remove this problem is to use an optical attenuator in the beam with 70% of the input light power. A comparison of the two laser sources for the locking system is given in Table 5-1.

Table 5-1 A comparison of two laser sources for the phase locking system in an MZI.

Lasers	Advantages	Disadvantages
Argon-ion	No need for a second laser for the locking system, this reduces the cost and simplifies the system. The working point is always kept at the 50:50 point of the transfer function of the filter. This leads to higher sensitivity and a larger measurement range. Removes laser drift effect from the illumination laser.	'Cross-talk' between the two laser beams (one is for the locking system and the other is to illuminate the flow area) will cause measurement errors. Reduces the illuminating power.
He-Ne	Removes the 'cross-talk' phenomena. No need to reduce flow illumination power.	A second laser is required which increases the cost and the system's complexity. Reduces sensitivity and dynamic range of the phase-locking system.

5.4.4 Low-pass filter

The normalised intensity of the MZI is unstable over time, especially when the cameras are turned on (see Figure 5-17), and the frequency variation in the phase drift is around 160Hz, which is difficult to track using the PZT stage that has a resonant frequency of ~200Hz [8].

However, as the particle scattering intensity is generally low, a camera exposure time of several seconds and even up to approximately 10s is required depending upon the flow conditions. Thus, the total effective integrated noise in this exposure time tends to be constant if the DC level of the noise does not drift in that time as the AC component averages out. This provides a possibility of only locking to the slowly drifting level (low frequency component) of the noise, while leaving the high frequency component of the noise. By doing this, the effect of the interferometer phase drift on measurements can be reduced.

A low-pass filter was therefore designed for this purpose and used in the locking system. Figure 5-23 shows the normalised intensity of the MZI before and after the application of a low-pass filter with a cut-off frequency of around 6Hz. Details on the electronic circuit designs and components used are discussed in Appendix B.

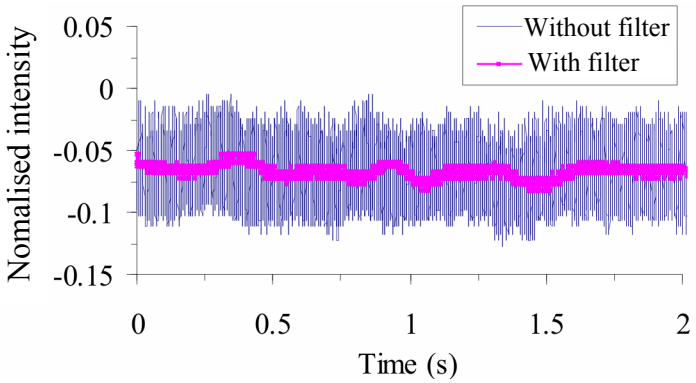

Figure 5-23 Normalised intensity of the MZI before and after the application of a low-pass filter.

5.4.5 Principle of PID

PID stands for proportional-integral-derivative. It is an automatic feedback control system widely used in industry. Figure 5-24 shows the basic PID structure. It compares a measured value V_{sensor} (process variable) from a process with a reference setpoint value $V_{set\text{-}point}$. The difference V_{error} (called error signal) is then used to calculate a feedback signal to impose on the plant to bring the process variable back to its desired setpoint. It can adjust process outputs based on the history and rate of change of V_{error}, which offers accurate and stable control.

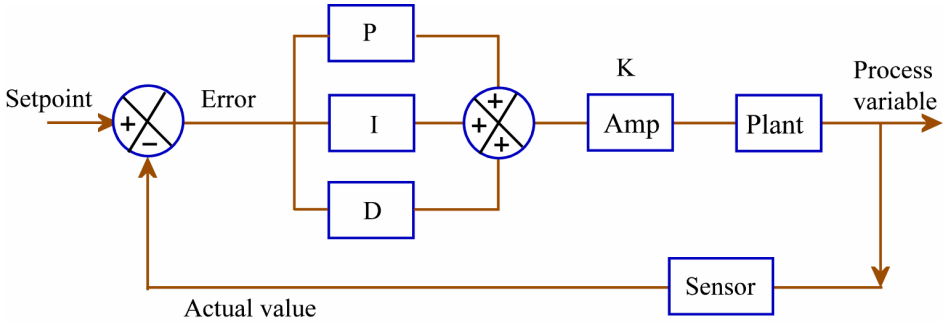

Figure 5-24 PID control for closed loop feedback system.

Proportional control deals with the present. The error V_{error} is multiplied by a negative constant P and added to the controlled quantity. P must be in the band over which a controller's output is proportional to the error of the system.

Integral control deals with the past. V_{error} is integrated over a period time, termed as the integral time T_i, to get an average, which is added to the controlled quantity. This step averages the measured error to calculate the process variable's average error from the setpoint. Since a proportional step can oscillate around the setpoint, integral process can remove the average difference between the process variable and the setpoint. The integration action is increased by reducing T_i, which will cause system instability [9].

Derivative control deals with the future. The derivative of the process variable over time is calculated. The derivative term controls the response to a change in the system. It is characterised by a derivative time T_d and the longer this time is, the more rapidly the controller responds to changes in the process output.

A PID can bring the process variable to its desired value. One such controller was designed for a MZI phase control. In Figure 5-24, the plant represents the MZI. Two photodiodes and the laser source (He-Ne) form the sensor.

The actual value from sensing the process variable is compared with the setpoint value to get the error signal V_{error}. The integral, proportional and derivative actions operate on this error signal and the results are summed up and amplified in gain K. The control algorithm is expressed as [9]:

$$V_{control} = K \cdot \left(P \cdot V_{error} + \frac{1}{T_i} \int V_{error} \cdot dt + T_d \cdot \frac{dV_{sensor}}{dt} \right). \qquad \textbf{Equation 5-1}$$

5.4.6 Circuit Time Constant

The PID controller settings for a full PID system must be determined before the control loop shown in Figure 5-19 can be used. Constants for the proportional band, integral time and derivative time must be set. The 'open loop reaction curve test' was therefore used to decide these parameters, this method is the gentlest of the tuning methods proposed by Cohen and Coon in 1953 [9]. The process reaction curve is identified by doing an open loop step test of the process and identifying process parameters.

The controller output was first adjusted manually to bring the interferometer to near the desired operating point. Then a small manual output step of 0.10V (ΔOP) from a function generator (Stanford Research Systems DS345) was applied to the control loop in open loop mode shown in Figure 5-25(a). This led to a change in the normalised intensity of the MZI or process variable (ΔPV) of about 0.12 shown in Figure 5-25(b).

The process gain K_p is then obtained

$$K_p = \frac{\Delta PV}{\Delta OP}. \qquad \textbf{Equation 5-2}$$

A tangent is drawn to the process variable response curve at the steepest point from which an apparent transit delay T_{delay} and apparent time constant T_c can be inferred. The control loop settings are then calculated by [9]

$$PB = \frac{80 \cdot K_p \cdot T_{delay} \Delta PV}{T_c} \%$$

$$T_i = 2.5 \cdot T_{delay}$$

$$T_d = 0.4 \cdot T_{delay} \qquad \textbf{Equation 5-3}$$

where the parameters PB, T_i and T_d are the proportional band, the integral time and the derivative time constant respectively.

The integral time of this control loop was 0.27s, derivative time 0.04s, and a proportional band 90%.

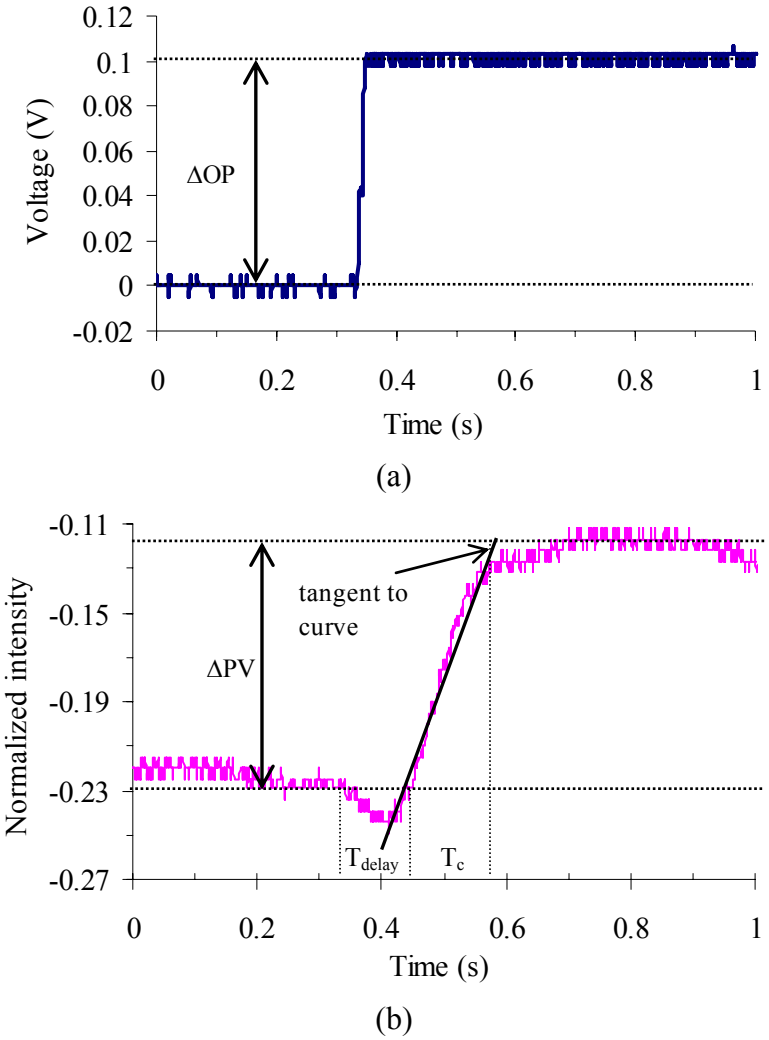

Figure 5-25 The Reaction Curve Test. (a) The small manual step voltage used to drive the system in open loop mode. (b) The process variable response curve.

5.4.7 Control system response

Based on these obtained PID parameters, the control loop still needs further tuning in order to achieve precise and stable control, which is time consuming. Normally, proportional action should be tuned first to get the best status, then integral and derivative actions.

Figure 5-26 is an example of the PID response when the system was used in closed-loop feedback control mode. The system generally took about 0.5s (from 0.25 to 0.75s in the time scale in Figure 5-26) to stabilise to within 30MHz and finally stabilise to within ±5MHz in around 3s corresponding to ~±2.5ms^{-1} velocity error. The actual value of velocity depends on $\hat{o}$ and $\hat{\imath}$. This velocity error is further reduced since the exposure time of the CCD cameras used is several seconds in current measurements. Any frequency drift from the phase locking system will be recorded as an additional Doppler frequency shift, which will lead directly to measurement errors. The normalised intensity is not centred around zero, as the split ratio of the optical components is not 50/50 at 632.8nm, and therefore the two complementary outputs are not equal.

Figure 5-27 shows an example of the PID response programmed in Labview 7.0. The system generally took about 10s to stabilise to within ±5Hz. The performance of this control system mainly depends on the sampling rate, which is decided by the performance of the computer hardware used. In our system, a maximal sampling rate of 100 samples per second (S/s) was used. This is why the PID response speed is slower than the electronic-circuit based PID controller shown in Figure 5-26.

It can be clearly seen from Figures 5-26 and 5-27 that there is an offset between the initial working point within around 0.25s and the setpoint of the phase locking system. This is because that the working point of the phase locking system was located at the arbitrary position on the transfer function of the filter which was not at 50% point of the transfer function before the PID controller was turned on. When the PID controller was turned on, the working point of the locking system was settled down at 50% point of the transfer function providing the largest sensitivity.

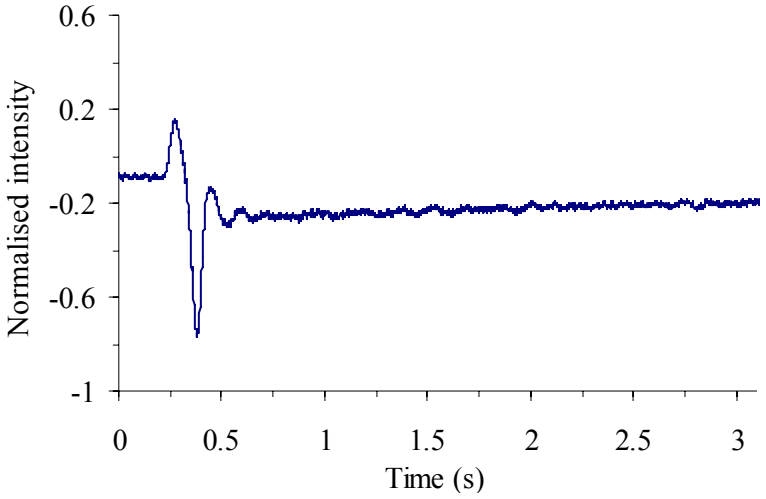

Figure 5-26 PID closed-loop feedback control response signal.

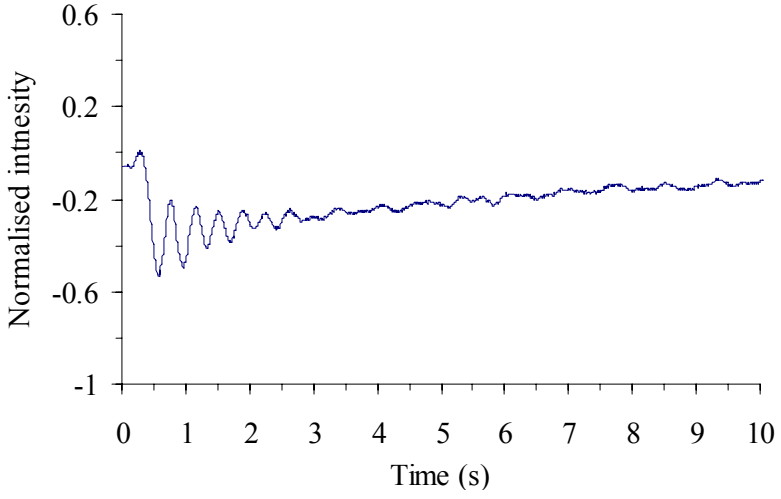

Figure 5-27 PID closed-loop feedback control response signal, programmed in Labview 7.0.

5.5 Data collection and processing procedure

Two methods of calculating the velocity have been investigated. The first uses the shift of the fringe pattern minima to determine the Doppler frequency shift, similar to the method reported by Seiler *et al* [10]. The second provides a measurement of the Doppler frequency shift at every pixel in the images by normalising the received light intensity using the two outputs of the MZI.

5.5.1 Velocity calculation based on the shift of the fringe pattern

The output light intensity of an MZI depends on its optical phase difference and original light intensity profile, having the usual cosinusoidal distribution, given in equation 4-1. It is nearly equal to zero at $\Delta\varphi = \pi, 3\pi, \cdots$ for the first output (CCD1) and $\Delta\varphi = 0, 2\pi, \cdots$ for the second output (CCD2). At these points it generates equidistant dark lines in the interference pattern. This makes the output intensity located at dark lines independent of the original scattered light from a region of interest. The Doppler frequency shift, Δv, can therefore be evaluated from the shift in position, Δs, of these dark lines.

$$\frac{\Delta s}{s} = \frac{\Delta l}{\lambda_L} \cdot \frac{\Delta v}{v_L} \qquad \textbf{Equation 5-4}$$

where s is the un-shifted fringe spacing. Δl is the optical path difference in the interferometer. λ_L and v_L are the wavelength and optical frequency of the illumination laser light. The velocity can be calculated using the Doppler equation 2-1.

A pair of interference pattern images is required to detect the fringe shift. One image is taken with the flow off and provides a reference measurement of the fringe locations. The other is taken with the flow field on and provides the velocity information. The fringe shift is then determined by locating the minimum-intensity lines in both images, as well as the fringe space distances in the reference image. When locating the minimum-intensity lines in the images one problem is the laser speckle noise because it will superimpose on the interference fringe and the speckle intensity varies in both time and space when the test target is moving. To solve this problem, an approach is to apply spatial smoothing to the raw images. This is further discussed in section 5.6.2

This processing technique can only calculate the velocity field along profiles corresponding to fringe minima, not across the whole image plane. Seiler *et al* [11] have reported a similar system using a Michelson interferometer. However, the MZI based approach can provide double the number of profiles under the same measurement conditions due to the availability of two complementary outputs, compared to the single output generally experimentally available from a Michelson interferometer.

5.5.2 Velocity calculation based on the normalised intensity of the fringe pattern

The second processing technique is based on the pixel-by-pixel evaluation of the normalised intensity of the MZI, as described by equation 4-2. From this, the Doppler frequency shift and hence the velocity can be evaluated at every point in the image. The

necessary system calibration and the data processing steps are summarised in Table 5-2 and described in detail in the following paragraphs.

Table 5-2 Processing stages for a single velocity component measurement using the MZI-PDV.

Processing Stage	Processing steps	Results / Purpose
1) Dot card calibration.	Capture images of target (background subtraction).	Improve CCD image alignment. Dewarp images to normal view. Calculate pixel observation vectors and sensitivity vectors.
2) Calculate the zero-shift phase difference.	Capture images under zero velocity conditions (background subtraction, filtering, dewarping).	
	Evaluate phase at each pixel.	Find $\Delta\varphi_0$, the zero-shift phase difference at each pixel.
3) Flow measurements.	Capture images with the flow on (background subtraction, filtering, dewarping).	
	Evaluate phase at each pixel.	Doppler frequency shifted phase difference, $\Delta\varphi_D$, at each pixel.
	Calculate change in phase.	Change in phase difference, $\Delta(\Delta\varphi)$.
	Calculate Doppler frequency shift at each pixel.	Doppler frequency shift, Δv.
	Calculate the measured velocity component using sensitivity vector calculated in step 1.	Velocity component, at each pixel.

Dot card calibration

The first processing stage is to capture images of a target composed of an array of equi-spaced white dots on a black background, aligned in the plane of the laser light sheet. This allows the view of the light sheet to be mapped onto a plane normal to the optical axis.

The observation direction, $\hat{o}$, can also be calculated for each pixel in the image using the results of this dewarping process [12]. This is needed to calculate the sensitivity vector, ($\hat{o}$-$\hat{i}$), and hence the velocity, in the Doppler formula. In order to calculate the normalised intensity, the two complementary output images (CCD1, CCD2) must be aligned on a pixel-to-pixel basis to sub-pixel accuracy. This image mapping process also improves the alignment of the two captured images to each other, removing magnification and distortion variations caused by lens aberrations and imperfections of the beam-splitters, prisms, mirrors and the glass block.

However, this stage is not necessary in a single camera MZI-PDV system (described in chapter 4) since the two complementary outputs from the MZI will be obtained using a single camera in the technique.

Calculation of zero-shift phase difference

In practice, the range of the normalised intensity will not be within $-1 \le I_N \le 1$ across the whole image due to optical distortions in the MZI. To take account of this equation 4-2 can be rewritten for one pixel as:

$$I_N(i,j) = \frac{I_1(i,j) - I_2(i,j)}{I_1(i,j) + I_2(i,j)} = \left(\frac{I_{N\max}(i,j) + I_{N\min}(i,j)}{2}\right) + \left(\frac{I_{N\max}(i,j) - I_{N\min}(i,j)}{2}\right)\cos(\Delta\varphi(i,j))$$

Equation 5-5

where the indices (i,j) give the pixel position in the images. $I_{N\max}$ and $I_{N\min}$ are the maximum and minimum values for the normalised intensity at each pixel, which can be approximately evaluated from the closest maximum and minimum in the fringe pattern. The phase difference, $\Delta\varphi(i,j)$, for each pixel, can then be found by rearranging Equation 5-5.

$$\Delta\varphi(i,j) = \arccos\left(\frac{2 \cdot I_N(i,j) - \left(I_{N\max}(i,j) + I_{N\min}(i,j)\right)}{I_{N\max}(i,j) - I_{N\min}(i,j)}\right) \pm n\pi \qquad n = 0,1,2,3...$$

Equation 5-6

The initial, zero Doppler frequency shift, phase difference will be different for each pixel in the image. Therefore, before measurements can be made from a flow, this must be measured. Images are captured with the flow off and the zero-shift phase difference, $\Delta\varphi_0(i,j)$, calculated for each pixel using Equation 5-6.

Flow measurements

The final stage is to capture images under measurement conditions with the flow on. The Doppler frequency shifted phase difference at each pixel, $\Delta\varphi_D(i,j)$, can be calculated using Equation 5-6 and the new images. The change in the phase difference can then be found

$$\Delta\left(\Delta\varphi(i,j)\right) = \Delta\varphi_D(i,j) - \Delta\varphi_0(i,j).$$ **Equation 5-7**

The Doppler frequency shift is then found from Equation 4-6 and Equation 5-7:

$$\Delta v(i,j) = \frac{c}{2\pi \cdot \Delta l}\Delta\left(\Delta\varphi(i,j)\right).$$ **Equation 5-8**

The final step in the process is to calculate the velocity component from the measured Doppler frequency shift and the sensitivity vector for each pixel using the Doppler formula given in equation 2-1. It is worth noting that, using the normalised intensity processing method, the uncertainty in the calculated velocity will vary due to the cosinusodial form of the filter transfer function. Close to maxima and minima, the velocity sensitivity will be lower than at the quadrature positions where a Doppler frequency shift will cause the greatest variation in measured intensity.

5.6 Uncertainty analysis in MZI-PDV

The general description and analysis of the main sources of measurement errors in the conventional PDV technique has been presented in chapter 3 including the uncertainty in the wavelength of the incident laser light, in the scattering angle, in characterisation of the filter frequency function, and in the measurement of the transmission of the filter. Here the factors that will affect the uncertainty in MZI-PDV measurements have been investigated including the quality of the interference fringe image, the number of the interference fringes and the image processing methods.

5.6.1 Errors from the MZI

Uncertainty due to the large inclination angle and the optical path deviation

The measurement accuracy is directly related to the quality of the interference fringe image, which can be improved in several ways. One way is to reduce the 'wash-out' effect of the fringes, increasing visibility especially in the outer edges of the image. In the MZI of Figure 4-1, the required block length, given by equation 4-6, will in practice be a function of the inclination angle, θ, from the optical axis:

$$2l = \frac{(l_2 - l_1)\cdot\sqrt{n^2 - \sin^2(\theta)}}{\sqrt{n^2 - \sin^2(\theta)} - \cos(\theta)} \qquad \textbf{Equation 5-9}$$

where l and n are the physical length and refractive index of the glass block, G, respectively shown in Figure 4-1. The derivation of the equation is described in Appendix C-1. This means that, ideally, different block lengths are necessary to correct for the different magnifications in the two arms, for different light beam inclination angles. The contrast of the interference images can be expressed as:

$$C = \frac{I_{\max} - I_{\min}}{I_{\max}} = \frac{r_0\cdot(1-\tan(\theta)) - (l_2 - l_1 - 2l)\cdot\tan(\theta) - \dfrac{2l\cdot\sin(\theta)}{\sqrt{n^2 - \sin^2(\theta)}}}{r_0\cdot(1-\tan(\theta)) - \dfrac{1}{2}(l_2 - l_1 - 2l)\cdot\tan(\theta) - \dfrac{2l\cdot\sin(\theta)}{2\cdot\sqrt{n^2 - \sin^2(\theta)}}}$$

Equation 5-10

where $I_{\max}$, $I_{\min}$ are the maximum and minimum intensities respectively; r_0 is the diameter of the transmitted image beam. The derivation of the equation is described in Appendix C-2. In the current experimental arrangement this beam diameter r_0 is ~20mm. Ideally the optical path difference within the MZI should be equal to the effective length of the glass block in order to match the magnifications in each of the two arms. However, in practice this cannot be achieved and the difference between the two can be described by the optical path deviation, Δ:

$$\Delta = \frac{n}{n-1}\cdot 2l - (l_2 - l_1). \qquad \textbf{Equation 5-11}$$

The contrast of the interference fringes is plotted in Figure 5-28 for different values of Δ. This indicates that the inclination angle and the optical path deviation, Δ, have little

effect on the contrast of the interference fringes since collimated light beams, rather than divergent ones, are used in the interferometer.

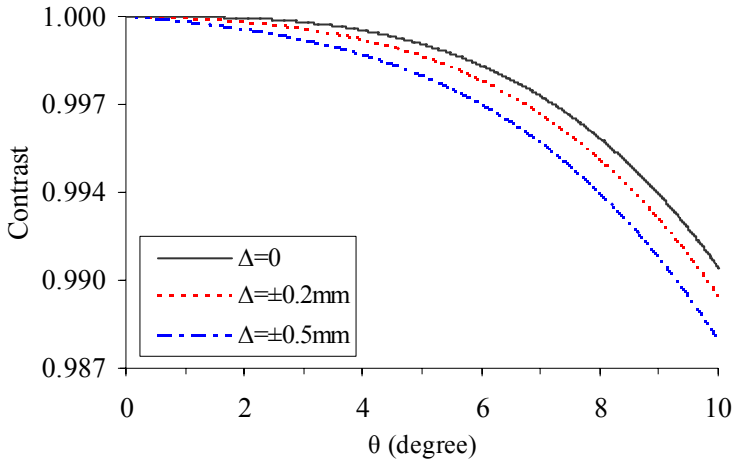

Figure 5-28 Contrast of the interference fringes versus light beam inclination θ for different optical path deviations, Δ.

As mentioned by Seiler *et al* [13], the optical path difference Δl of the interferometer is also a function of the inclination angle and the optical path deviation, Δ. This will lead to non-equidistant fringes, which will increase the measurement error in the processing technique based on the fringe shift. Therefore θ and Δ should be made as small as possible. In our present arrangement the angle is limited to ~2.1° by the diameters of the optical components in the infinity-corrected optical system. Figure 5-29 shows the relation between the relative change $[\Delta l(\theta)-\Delta l(0)]/\lambda$ in optical path difference against the inclination angle θ, for various values of the optical path deviation, Δ.

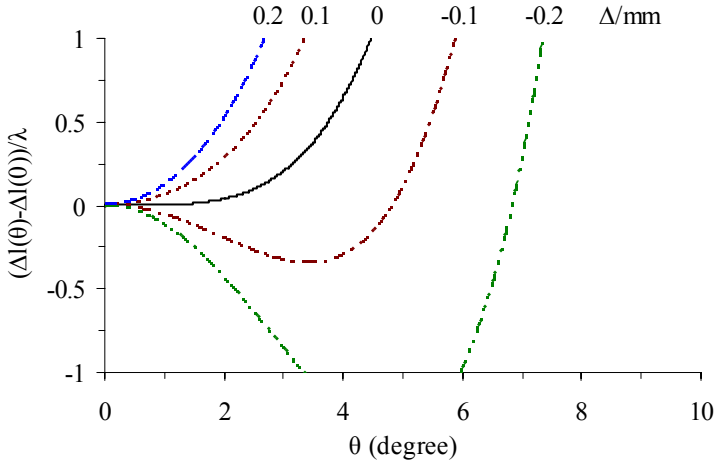

Figure 5-29 Relative change $[\Delta l(\theta)-\Delta l(0)]/\lambda$ in optical path difference against light beam inclination angle θ, for various values of the optical path deviation Δ, at λ = 514.5nm, l = 0.15m and n = 1.52.

In our system, Δ is evaluated to be negligibly small otherwise the clear interference image would not be achieved. Therefore for an inclination angle of ~2.1˚ this will cause a change of ~0.05λ in the optical path difference. The change will introduce a 5% increase in the fringe spacing at the edge region compared with the centre region of the

measurement area. The correction for the fringe space distances in the whole image therefore is required, when the fringe shift processing technique is used.

The contrast of the interference images will also be affected by polarisation sensitivity of the beam splitters, and by the flatness of the optical components within the system (described in chapter 4). Therefore this application requires high quality components.

Uncertainty due to the number of interference fringes in the image

In the processing method based on the shift of the fringe pattern (described in chapter 5.5.1), the prism P1 in Figure 5-30 is tilted a small angle, β, in order to generate equidistant dark lines in the interference fringe pattern. These dark line locations are used to evaluate the Doppler frequency shift because they only depend on the optical frequency and are independent of the varying intensities of the scattering light. The optical path difference, Δl_x, is now added to the optical path difference, Δl, between the two arms in the MZI.

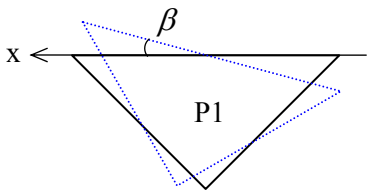

Figure 5-30 Tilt of the prism P1 at an angle of β.

The phase difference is then $\Delta\varphi$ together with $\Delta\varphi_x$. $\Delta\varphi_x$ changes linearly with the coordinate x, and is also proportional to the frequency v:

$$\frac{\Delta\varphi_x}{2\pi} = \frac{\Delta l_x}{\lambda} = v \cdot \frac{\Delta l_x}{c}. \qquad \textbf{Equation 5-12}$$

Differentiation of Equation 5-12 leads to the following expression:

$$\Delta\left(\frac{\Delta\varphi_x}{2\pi}\right) = \frac{\Delta l_x}{\lambda} \cdot \frac{\Delta v}{v}. \qquad \textbf{Equation 5-13}$$

The outputs of the MZI now can be rewritten as

$$I_1 \propto I_0 \cos^2\left(\frac{\Delta\varphi + \Delta\varphi_x}{2}\right)$$

$$I_2 \propto I_0 \sin^2\left(\frac{\Delta\varphi + \Delta\varphi_x}{2}\right)$$

$$I_0 \propto I_1 + I_2 \qquad \textbf{Equation 5-14}$$

where I_0 is the input light intensity, I_1 and I_2 are the intensities at each of the outputs.

At initial frequency v_0, the generated fringe pattern has equidistantly spaced dark lines with a separation of s. The change of the phase difference of the interferometer along the distance $\Delta x = s$ is

$$\Delta\varphi_0 + \Delta\varphi_x = 2\pi\,. \qquad \textbf{Equation 5-15}$$

For any point located at $\Delta x' \neq s$, the phase difference changes as

$$\frac{\Delta(\Delta\varphi_x)}{2\pi} = \frac{\Delta x'}{s}. \qquad \textbf{Equation 5-16}$$

Therefore, if a point in the dark line, where $\Delta\varphi_0 + \Delta\varphi_x$ is equal to π, is shifted by $\Delta x'$ compared to its original location at $v = v_0$, at the shifted point, the phase difference is:

$$\Delta\varphi_0 + \Delta\varphi_x = \pi + \Delta(\Delta\varphi_x)\,. \qquad \textbf{Equation 5-17}$$

If the shifted point is in the dark fringe at $v \neq v_0$, there is

$$\Delta\varphi + \Delta\varphi_x^{'} = \pi\,. \qquad \textbf{Equation 5-18}$$

By combining Equation 5-16, Equation 5-17 and Equation 5-18 with Equation 5-13 and Equation 4-6, the frequency shift $\Delta v = v - v_0$ can be expressed as a function of the fringe shift $\Delta x'$

$$\frac{v - v_0}{v_0} = -\frac{\lambda}{\Delta l + \Delta l_x} \cdot \frac{\Delta x'}{s}. \qquad \textbf{Equation 5-19}$$

The $\Delta v/v$, the frequency sensitivity, is a function of $\lambda/(\Delta l + \Delta l_x)$. This means that the frequency sensitivity can be increased by using large $(\Delta l + \Delta l_x)$. Generally $\Delta l_x << \Delta l$ and therefore is neglected as done by Seiler *et al* [14]. Figure 5-31 shows the relative errors in $\Delta v/v$ caused by making this assumption for various numbers of interference fringes at different optical path differences. When a small optical path difference (<0.01m), and large number of fringes (~50) are used, this error should be considered. These are values typically used for high velocities. In this work, an optical path difference of ~26cm was used. This leads to a relative error of ~0.001% in $\Delta v/v$ at a fringe number of seven, which can obviously be neglected.

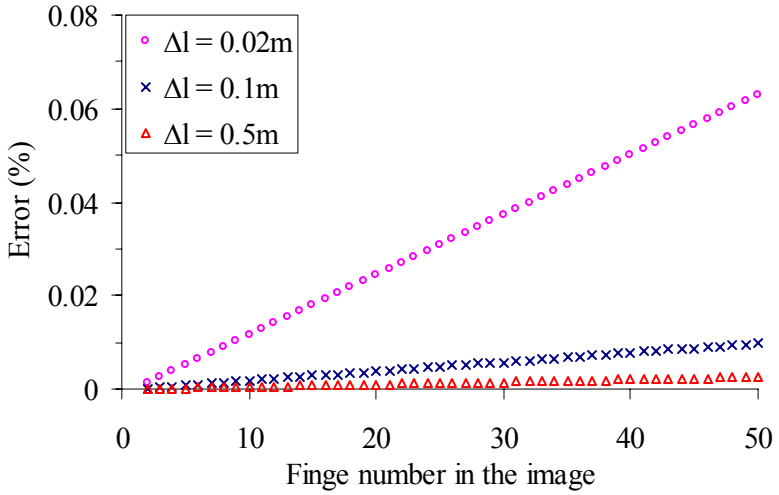

Figure 5-31 Relative errors in $\Delta v/v$ caused by Δl_x against the number of fringes for different optical path differences Δl.

At a fixed optical path difference Δl, the number of the interference fringes may be selected by adjusting the tilting angle β (Figure 5-30) in the image taken by the CCD cameras for a flow region of interest. This will affect the frequency sensitivity since the minimum recognizable fringe shifting distance is one pixel in the interference images. Figure 5-32 shows the simulated minimum measurable frequency shift against the fringe number at a fixed Δl and a fixed pixel number of 1040 across the CCD cameras used. It can be seen that the measurable shift, quantified as the percent of free spectral range (FSR) of the filter, increases when increasing the fringe number in the image leading to a decreased measurement resolution. On the contrary, this will reduce the interferometer phase drift effect on measurements since the phase drift smaller than this measurable shift would be suppressed. Therefore, for a higher measurement resolution, the interferometer phase will be more sensitive requiring higher phase control ability.

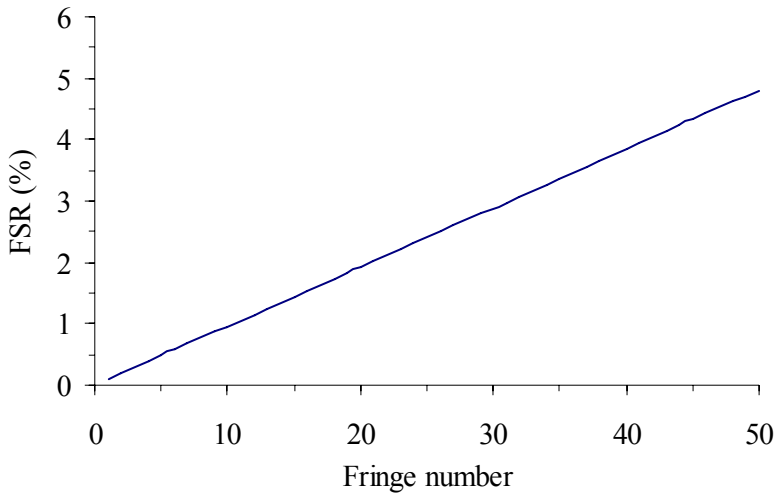

Figure 5-32 Simulated minimum measurable frequency shift against the fringe number at a fixed optical path difference Δl *and a fixed* pixel number of 1040 across the CCD cameras used, in terms of the percentage of FSR of the filter.

5.6.2 Errors from the image processing

Fringe shift method

In the existing image processing method based on the shift of the interference pattern, the key step is to recognise the locations of the dark (minimum intensity) fringes in the images. An algorithm used to identify minima locations in the image is zero-derivate method and the equations are shown in Equation 5-20.

$$\text{For maxima: } (I_{n-1} - I_n) \cdot (I_{n+1} - I_n) > 0,$$
$$\text{For minima: } (I_{n-1} - I_n) \cdot (I_{n+1} - I_n) < 0 \qquad \textbf{Equation 5-20}$$

where I_n is the normalised intensity at the n-th pixel. However, in the interference images some secondary even sub-secondary minima and maxima are generated due to the uneven power distribution in the illumination light sheet and optical distortions in the imaging system. Figure 5-33(a) shows an example of minima found in the raw image taken for a rotating disc. Some false minima can be seen clearly.

In order to locate the real minima, a uniform smoothing filter was used to remove the false minima and this has been applied to this work. Another filter that is also useful is the Gaussian filter which implements a weighting effect to the region of interest. The number of false minima decreases when the application of the smoothing filter is increased. This can be seen clearly from Figure 5-33(b)-(d) where a 3×3 smoothing filter was applied by one, two and eight times respectively. In addition, the application of more powerful filters will remove the false minima with relatively fewer applications, as shown in Figure 5-33(e) and (f) where only two applications of a 5×5 smoothing filter and one application of a 9×9 smoothing filter were employed in order to obtain clear minima locations in the image.

As expected, the application of filtering has nearly no effect on the measured locations of the real minima in the image. This is shown in Figure 5-34, where one profile obtained from a raw interference image taken for a rotating disc including seven dark fringes was filtered using different types of smoothing filters. This figure indicates that the estimated locations of minima in the image profile after the application of filtering approximately are the same compared to the raw image profile. Therefore, the measurement uncertainty using the fringe shift processing method is independent of the application of filtering to the raw images. However, the application of filtering to the raw image affects the measurement accuracy when using the normalised intensity processing method since it changes the fringe amplitude.

Normalised intensity method

Therefore, the effect of filtering in the normalised intensity processing method has been investigated and the results are shown in Figure 5-35. This figure indicates that the computed Doppler frequency shift values after the application of different types of filters were generally the same in profile but a relative bias error was introduced in the measured Doppler frequency shifts. For example, the zero-velocity location of the calculated Doppler frequency shift profile was shifted by ~3 pixels when the application of a 3×3 smoothing filter was used eight times compared to only once. This leads to a maximum error of ~8MHz in the measured Doppler frequency shift. This was also ~3 pixels when the application of a 9×9 smoothing filter was used five times compared to only once. However, there was no shift when the application of a 5×5 smoothing filter was used by five or two times compared to only one time.

The reason for this is that the application of filtering to the raw image changed the amplitude of the normalised intensity (fringes) although the minima and maxima locations of the fringes were not affected. This effect was worse in the regions around minima and maximum leading to larger measurement errors in these regions compared to the quadrature regions.

In order to reduce this uncertainty resulting from the application of filtering, as few applications of filtering as possible should be used. This means that the contrast of the interference fringes must be improved (discussed in section 5.6.1) and CCD cameras with high dynamic ranges are required.

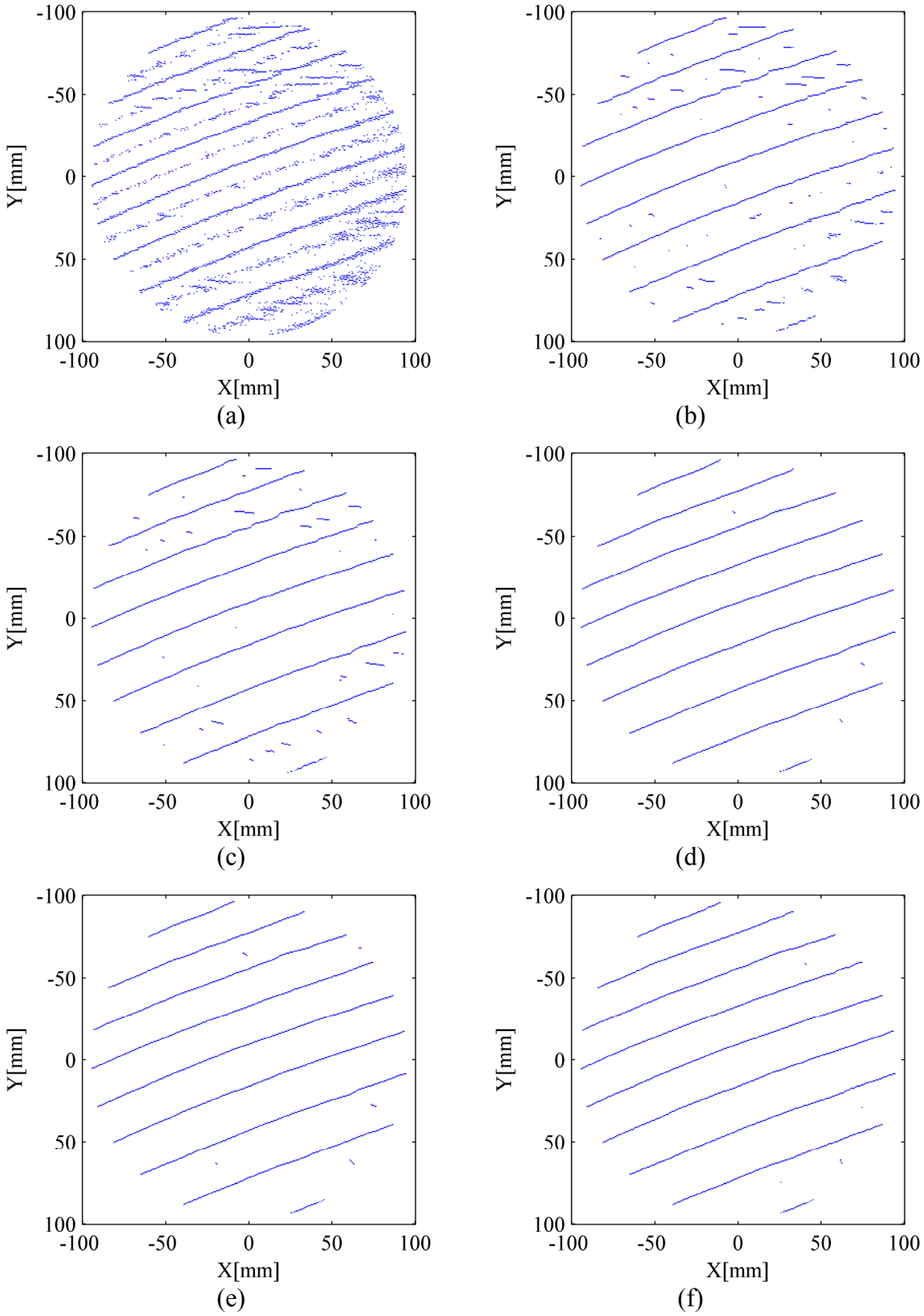

Figure 5-33 Minima locations in the raw image (a) and images after one (b), two (c), eight (d) applications of a 3×3 smoothing filter. (e): after two applications of a 5×5 smoothing filter. (f): after one application of a 9×9 smoothing filter.

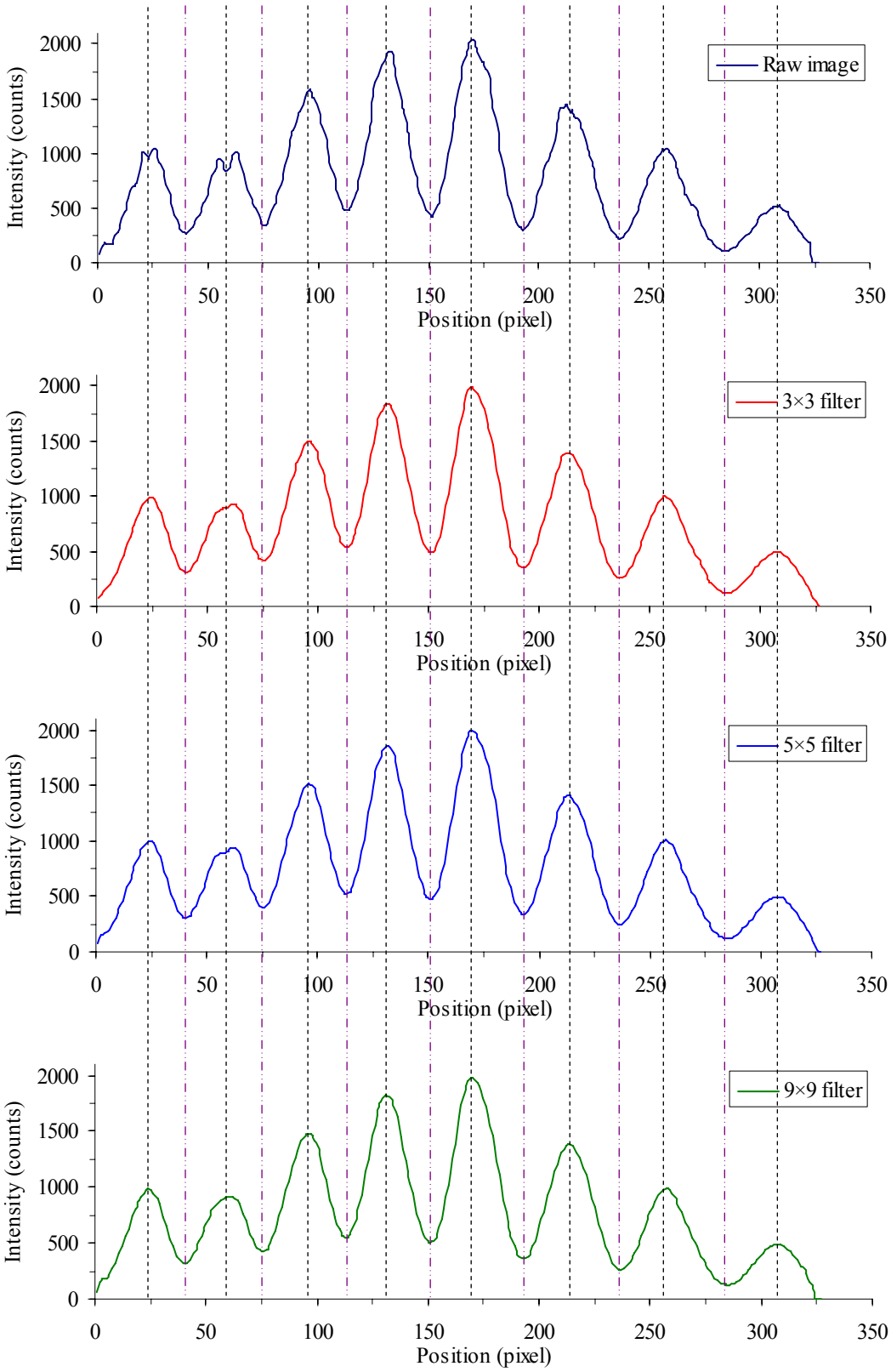

Figure 5-34 Effects of filtering on the recognition of the minima locations in the image.

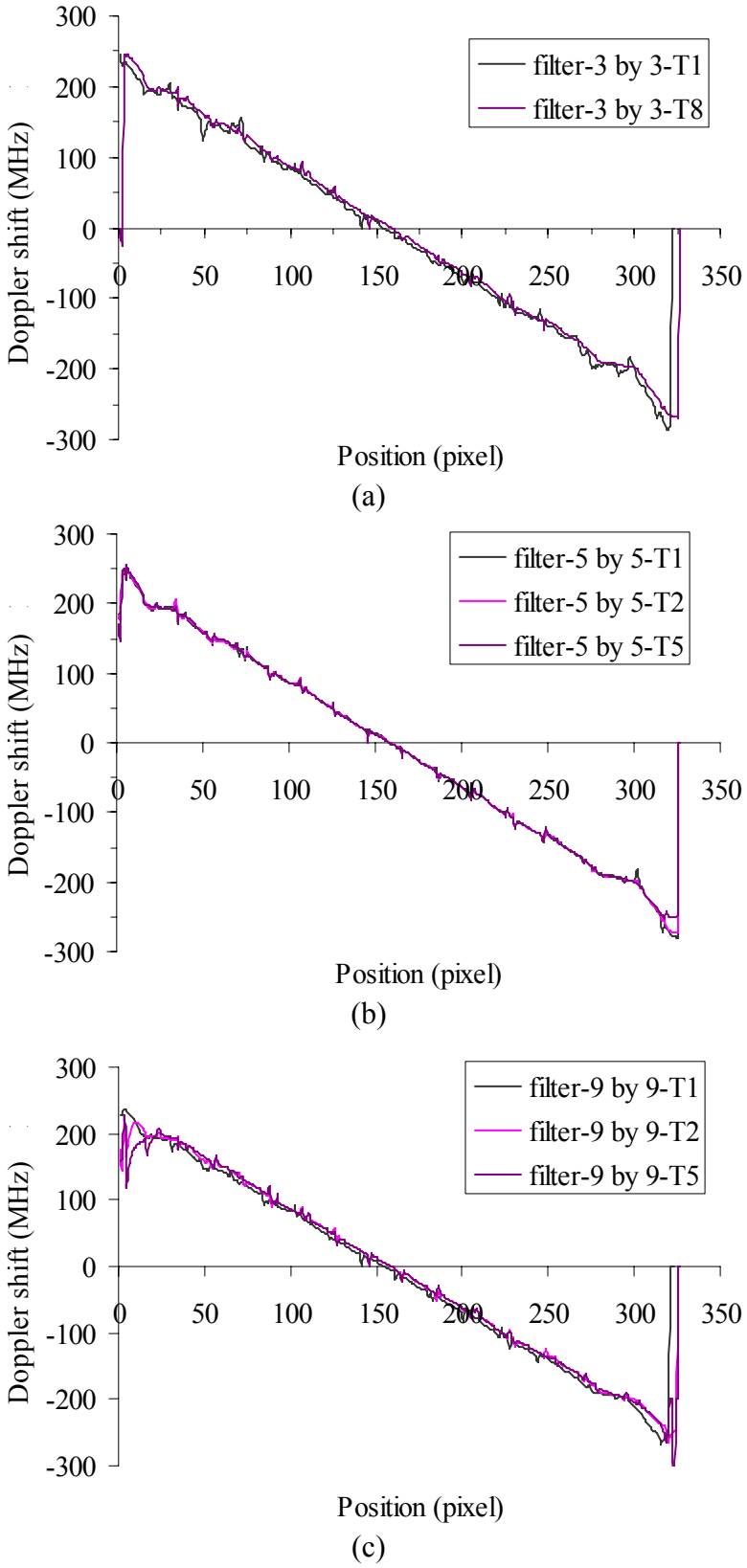

Figure 5-35 Effects of filtering on the Doppler frequency shift measurements using the normalised intensity processing method. (a) 3×3 smoothing filter; (b) 5×5 smoothing filter; (c) 9×9 smoothing filter. T1, 2, 5, 8: the time of the applications of the filter is 1, 2, 5 and 8.

5.7 Validation on a rotating disc

The first test velocity field used to validate the system was a rotating disc. This provides a well-defined velocity field with which to characterise the performance of the system. The disc was 200mm in diameter and coated with white paint in order to enhance the light scattering. The aim of this experiment was to investigate a known velocity field. The maximum circumferential velocity of the disc was ~±70ms^{-1} with a variation of ~±3ms^{-1}, which was measured independently using an optical tachometer.

5.7.1 Experimental arrangement

Figure 5-36 shows the arrangement of the wheel with the illumination and observation directions marked. The observation direction $\hat{o}$ was at an angle of ~18º to the plane of the wheel, measured from the centre of the wheel to the centre of the imaging lens. The illumination direction $\hat{\imath}$ was at an angle of ~14º to the observation direction. The geometry was selected to have a high sensitivity to the horizontal velocity component, which is expected to vary linearly along any vertical line through the disc.

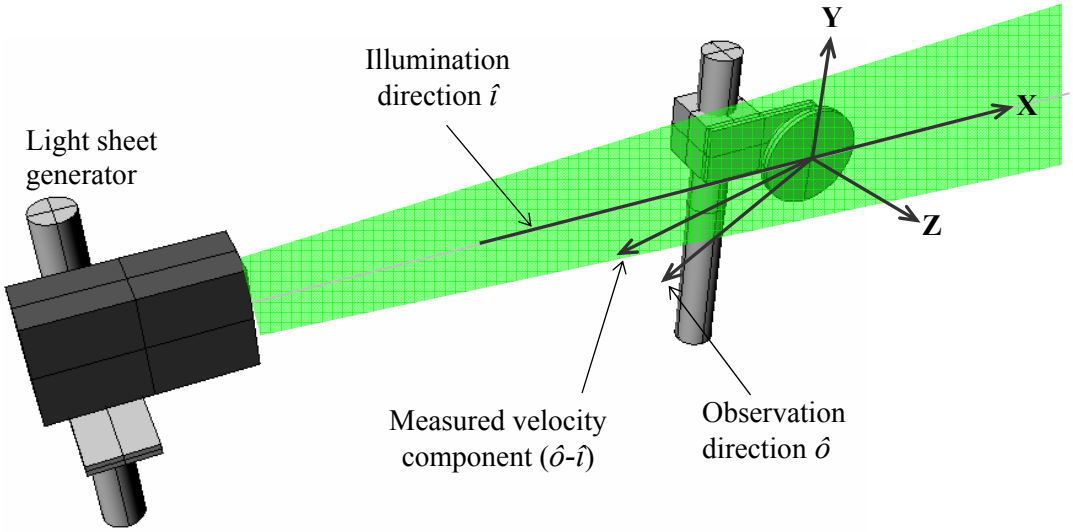

Figure 5-36 Experimental arrangement of the light sheet generator and the rotating disc.

A calibration target shown in Figure 5-37(a) was used to dewarp the two images captured by the two CCD cameras to a normal view. The white dots are 2.5mm in diameter and spaced on a regular grid of 10mm. The white circle lines are used to make the expected measurement area easy to track. Figure 5-37(b) shows an example image of the target in the experimental arrangement, and (c) shows the 'dewarped' view where the two images from the two outputs of the MZI are calibrated onto a normal view by using the de-warping algorithm from Davis.

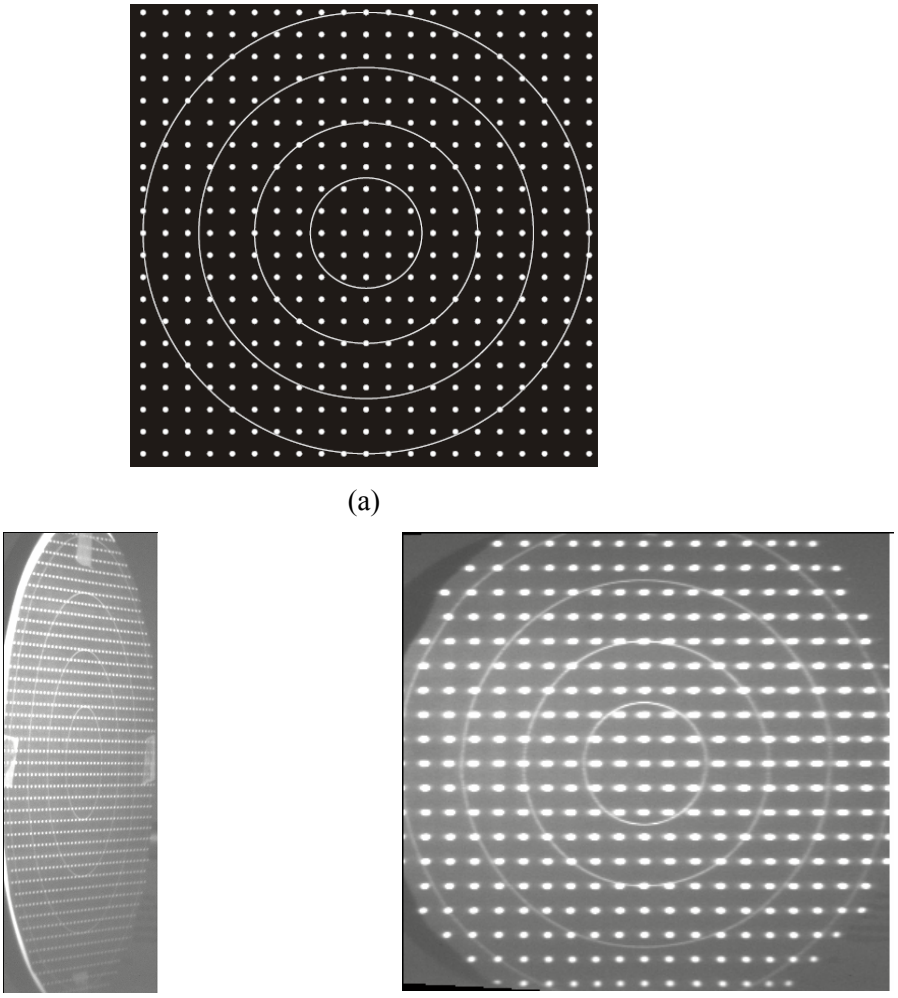

Figure 5-37 (a) A calibration target. (b) An example image of the target and (c) The 'dewarped' view showing two images calibrated onto a normal view.

5.7.2 Results: fringe shift processing method

With the disc motionless a pair of images was captured simultaneously (one on each CCD camera). The disc rotation was started and a second image pair captured. These are shown in Figure 5-38. The images with the wheel stationary exhibit a speckled appearance which is removed for the rotating wheel as the speckle field is averaged over the integration time of the cameras. A camera exposure time of 3 seconds was used to obtain sufficient signal intensity.

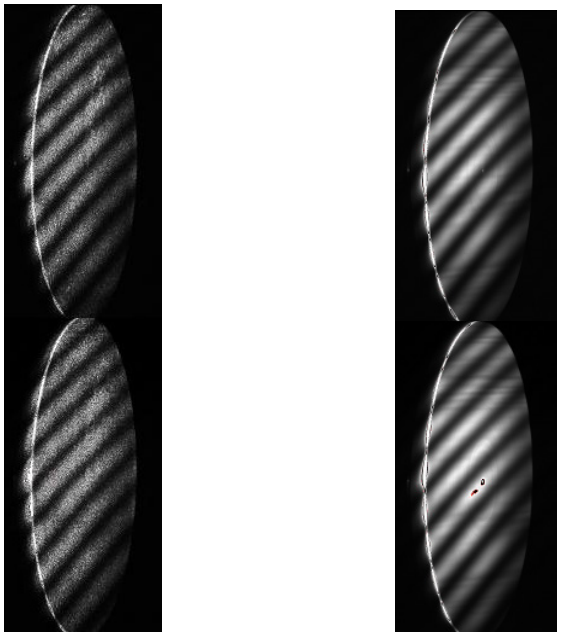

Figure 5-38 Two pairs of fringe images recorded by CCD1 (top) and CCD2 (bottom): for the motionless disc (left) and for the rotating disc (right) in the MZI-PDV system.

These images were then processed using the fringe shift method described in section 5.5.1. Figure 5-39(a) shows the positions of the dark fringes in the images taken by CCD1 for the disc stationary and rotating after two applications of a 5×5 smoothing filter. Here the shift in the fringe locations can be clearly seen. A similar image is obtained using the second CCD2 with the fringes located between those found from CCD1, and is shown in Figure 5-39(b).

The velocity at each point along the fringe was calculated using the procedure described above, and Figure 5-40 shows the computed velocity at points through the centre of the disc. The solid line represents the velocity calculated from the optical tachometer measurements. The standard deviation of the measured velocities is 2.9ms^{-1}. As discussed previously, the use of an MZI allows twice the number of measurement profiles compared to a Michelson interferometer; using a single output the measurement profiles would be spaced at ~40pixels (22mm) apart, but using the two outputs available with the MZI arrangement allows the number of profiles to be doubled giving a spacing of ~20pixels (11mm). This can be seen in Figure 5-40 where values from the two outputs are plotted with different symbols.

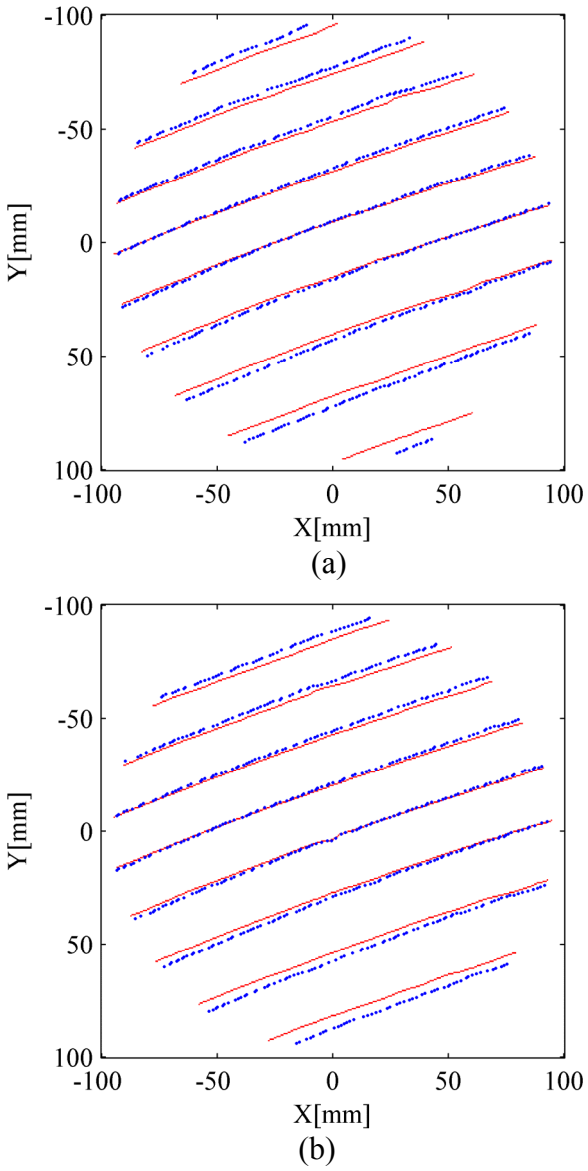

Figure 5-39 Dark fringes in images taken by CCD1 (a) and CCD2 (b) for the disc. Solid (red) lines: disc stationary; Dashed (blue) lines: disc rotating.

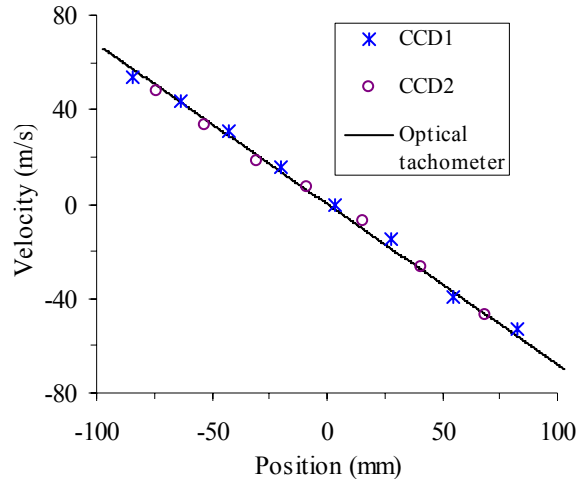

Figure 5-40 Velocity profiles across the centre of the rotating disc using the fringe shift technique.

5.7.3 Results: normalised intensity processing method

The second method, described in section 5.5.2, was then used to process measurements made on the rotating disc. This method allows the velocity to be evaluated at each pixel in the captured images. Figure 5-41 shows the computed velocity component made by calculating the normalised intensity at each pixel after two applications of a 5×5 smoothing filter. Figure 5-42 shows a velocity profile taken through the centre of the disc (vertical line indicated in Figure 5-41). The measured velocities correspond very well with the values calculated from the optical tachometer. The standard deviation of the measured velocities for this technique is 2ms^{-1}.

The measurements towards the edge of the disc vary more from the expected values possibly due to lower interference fringe quality in these regions, and lower signal levels resulting from the 'vignetting effect' in the infinity-corrected optical system. The faint striping that can be seen corresponds to the locations of fringe maxima and minima and is due to the use of the smoothing filter. The deviations from a cosinusoidal form are largest close to maxima/minima resulting from filter smoothing.

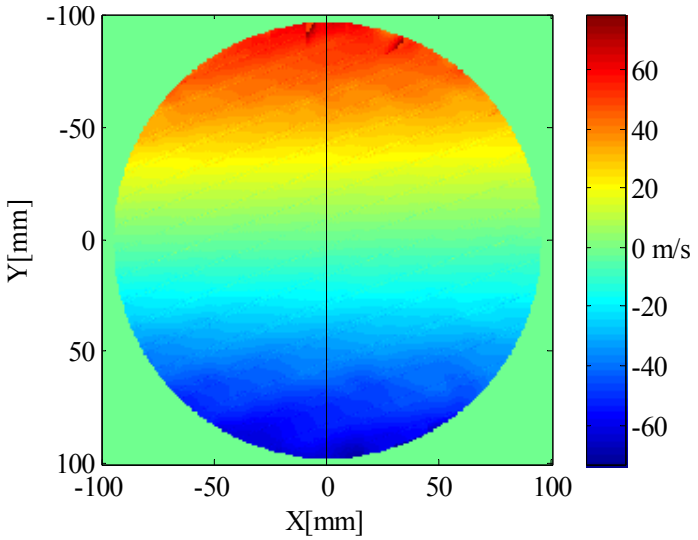

Figure 5-41 Computed velocity component of the rotating disc calculated using the normalised intensity method.

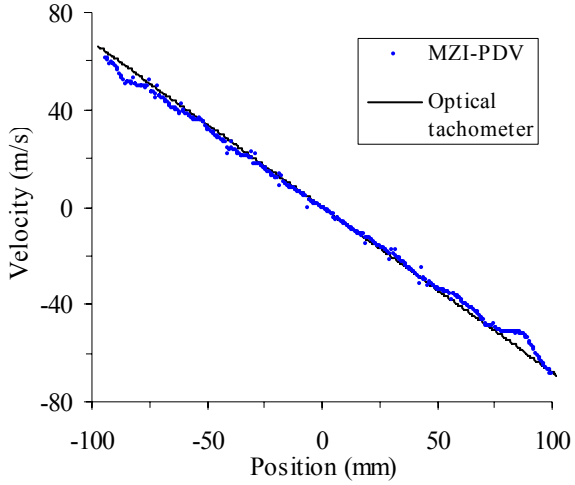

Figure 5-42 Velocity profile taken through the centre of the disc (vertical line indicated in Figure 5-41) using the normalised intensity method.

5.7.4 Results: single camera MZI-PDV

In section 4.2, a single camera system was proposed, where the two complementary outputs will be obtained using a single camera. This requires application of π phase change to one arm of the interferometer between successive frames. This can be achieved by moving prism P2 to change the path length l1 by applying a constant voltage, synchronised to the camera timing, to the PZI stage shown in Figure 4-3. This voltage can be obtained by analysing the shift of the interference fringe pattern in the MZI. In this work, the voltage was found to be 0.06V.

In the single camera technique, the images taken by the CCD camera after the π phase shift correspond to the images taken by CCD2 in the normal MZI-PDV technique. This method was investigated by using only one of the two CCD cameras in the current imaging head.

Velocity calculation based on the shift of the fringe pattern

With the disc motionless a pair of images (one before and the other after the application of the π phase shift) was captured by CCD1. The disc rotation was started and a second image pair captured. These are shown in Figure 5-43. The images with the wheel stationary exhibit a speckled appearance which is removed for the rotating wheel as the speckle field is averaged over the integration time of the camera. A camera exposure time of 3 seconds was used to obtain sufficient signal intensity.

Different fringe patterns were used for the measurements using both cameras and for the single camera measurements. This means that there are more measurement points than in the normal MZI-PDV system results.

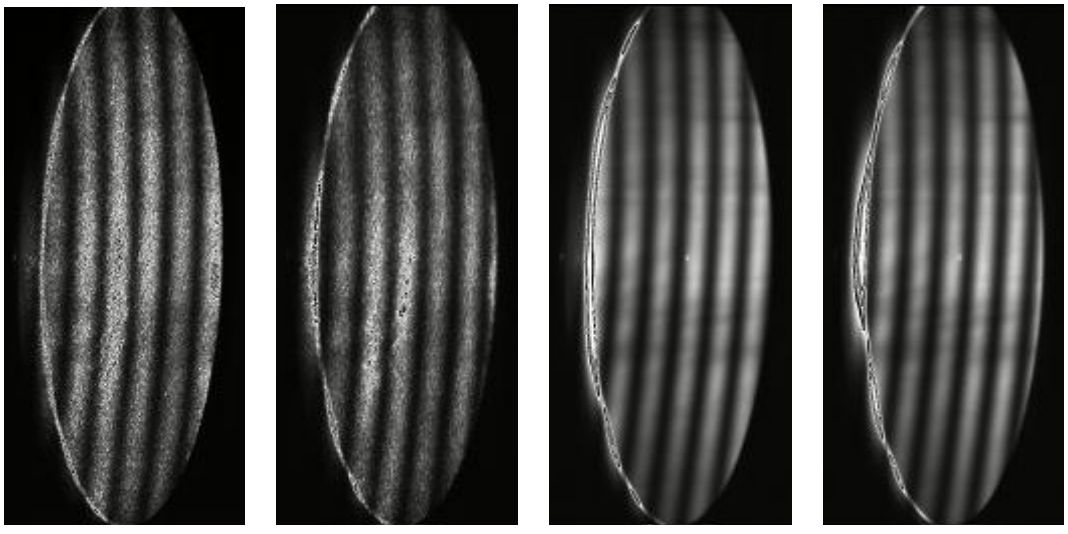

(a) (b) (c) (d)

Figure 5-43 Four fringe images recorded by CCD1 for the motionless disc (a) and (b), before and after the application of the π phase shift; and for the rotating disc (c) and (d) in the single camera MZI-PDV system.

Using the fringe shift processing method, these images were then processed. Figure 5-44(a) shows the positions of the dark fringes in the images taken by CCD1 for the disc stationary (a) and rotating (c) in Figure 5-43 before the application of the π phase shift. Here the shift in the fringe locations can be clearly seen. A similar image is obtained using the two images taken by CCD1 after the application of the π phase shift for the disc stationary (b) and the disc rotating (d) in Figure 5-43. This is shown in Figure 5-44(b) with the fringes located between those found in Figure 5-44(a).

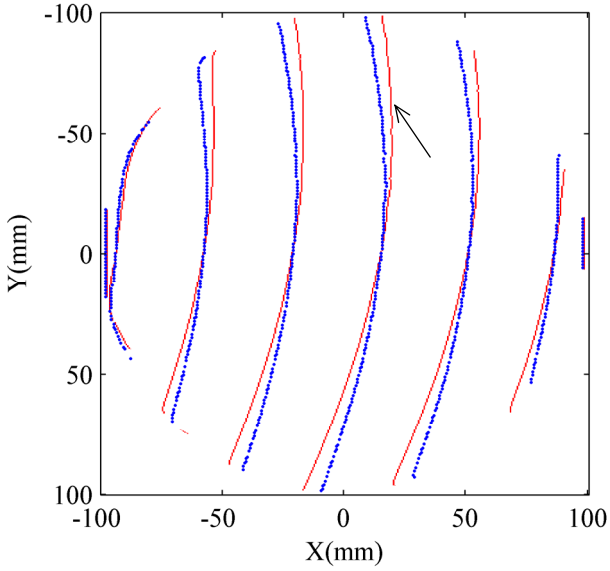

(a)

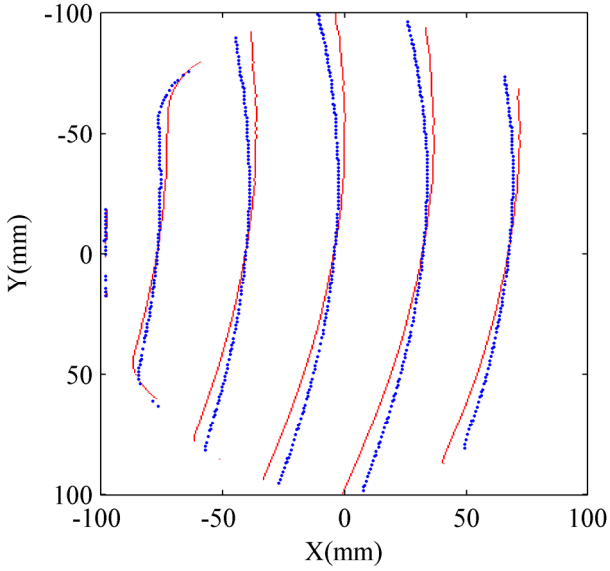

(b)

Figure 5-44 Dark fringes in images taken before (a) and after (b) the application of the π phase shift for the disc. Solid (red) lines: disc stationary; Dashed (blue) lines: disc rotating.

The velocity at each point along the fringe was calculated using the procedure described in section 5.5.1. Figure 5-45 shows the computed velocity at points along the fringe through the centre of the disc (labelled in Figure 5-44(a)). The solid line represents the velocity calculated from the optical tachometer measurements. The standard deviation of the measured velocities is 2.2ms^{-1}. This is lower from that of the normal MZI-PDV technique (2.9ms^{-1}). The difference is possibly due to the measured points located at one dark fringe for the single camera but from several ones for the normal MZI-PDV systems. The measured velocity resolution is around 5ms^{-1} and the steps in Figure 5-45 are due to the processing method where only whole pixel shifts can be measured.

Using the pair of images (a) and (c) in Figure 5-43, the measurement profiles would be spaced at ~64pixels (36mm) apart, but using the two pairs allows the number of profiles to be doubled giving a spacing of ~32pixels (18mm).

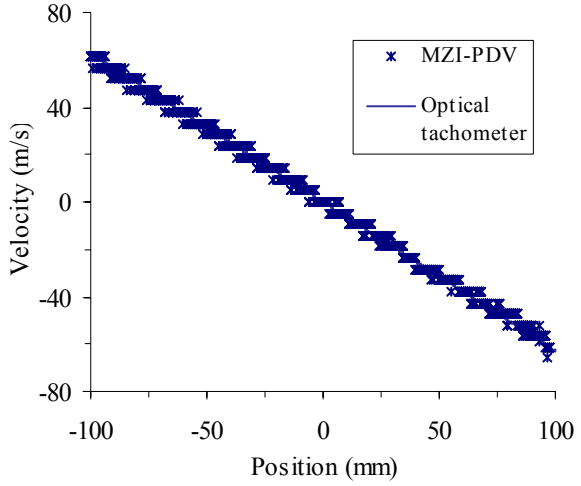

Figure 5-45 Velocity profiles across the centre of the rotating disc using the fringe shift processing technique in the single camera MZI-PDV system.

Velocity calculation based on the normalised intensity method

The normalised intensity processing method was then used to process measurements made on the rotating disc. Figure 5-46 shows the computed velocity component made by calculating the normalised intensity at each pixel after two applications of a 5×5 smoothing filter. Figure 5-47 shows a velocity profile taken through the centre of the disc (vertical line indicated in Figure 5-46). The measured velocities correspond very well with the values calculated from the optical tachometer. The standard deviation of the measured velocities for this technique is 2ms^{-1}.

It is worth noting that a few pixels have been shifted in the images in order to map the maxima in the images taken before the π phase change and the minima in the images taken after the phase change for the disc. This mapping is required in the second processing method. This misalignment between them is due to the interferometer phase drift between successive frames since the phase locking system was turned off during the experiment in order to provide the π phase change to one arm of the interferometer

between successive frames by modulating the PZI stage mounting the prism P2 (Figure 5-3). This is a disadvantage in the technique and will be further discussed in chapter 7.

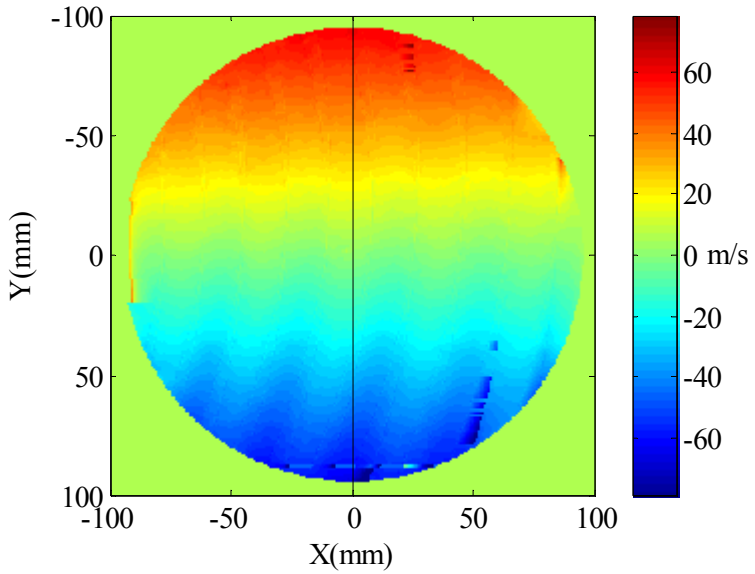

Figure 5-46 Computed velocity component of the rotating disc calculated using the normalised intensity method.

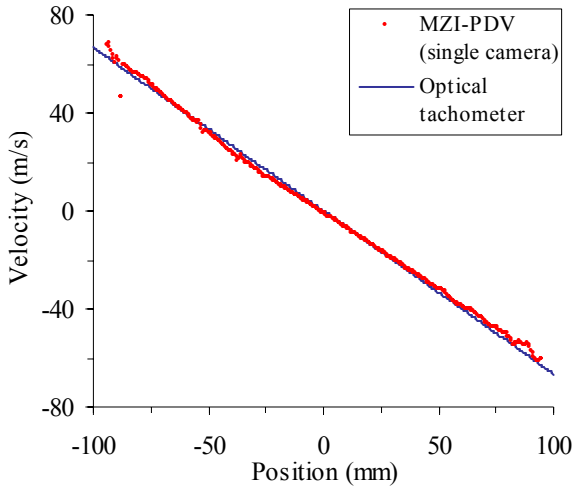

Figure 5-47 Velocity profile taken through the centre of the disc (vertical line indicated in Figure 5-46) using the normalised intensity method.

5.8 Measurements on a seeded air jet

The system was used to make measurements on a seeded air jet, with a 20mm diameter smooth contraction nozzle.

5.8.1 Experimental arrangement

The exit velocity of the jet is ~85ms^{-1}. The air intake to the jet and the surrounding co-flow were seeded using a Concept Engineering ViCount compact smoke generator, which produces particles in the 0.2-0.3µm-diameter range. Figure 5-48 shows the experimental arrangement. The main flow direction is opposite to the laser illumination direction and the observation direction is perpendicular to this. This provides a measured velocity component that is at an angle of ~45º from the main flow direction.

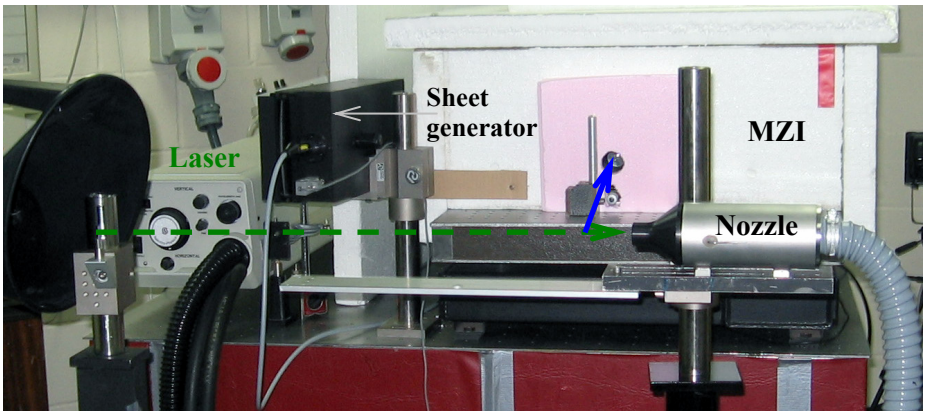

Figure 5-48 Experimental arrangement for the seeded air jet. Laser illumination and observations are shown in dashed (green) and solid (blue) lines respectively.

Figure 5-49 shows an example of the 'dewarped' calibration target view showing the two images from the two outputs of the MZI calibrated onto a normal view. The measured area was approximately 50x50mm and a camera exposure time of 10 seconds was used.

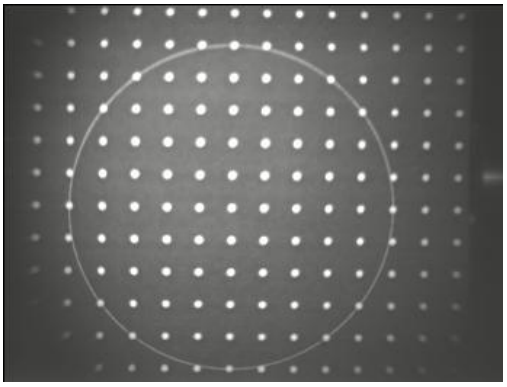

Figure 5-49 An example of the 'dewarped' calibration target view.

5.8.2 Results: fringe shift processing method

Two pairs of images were stored with the jet off and on, and are shown in Figure 5-50 (a) and (b). In order to obtain clear interference fringes when the jet flow was off, a smooth plate was placed in the measurement plane. The ripple in the static flow images comes from the roughness of the smooth plate used and the uneven power distribution in the illumination light sheet. This is due to the scratches on the optical surfaces of the two mirrors used in the light sheet generator as shown in Figure 5-2(b). The ripple in the images for the jet flow is smaller than that in the static flow images because the smooth plate was removed in recording the jet flow image.

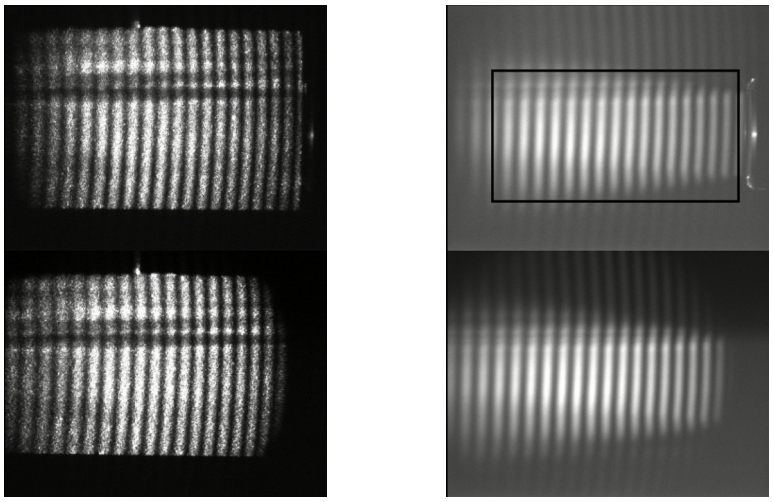

(a) (b)

Figure 5-50 Fringes from each camera recorded for the air jet flow. (a): with a smooth plate when the jet flow was off; (b): jet flow on (plate removed).

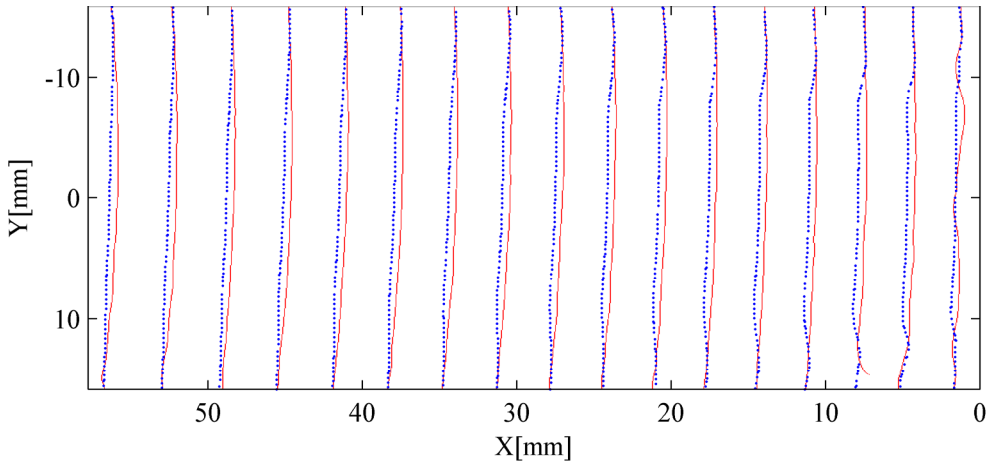

Figure 5-51 Dark fringes in images taken by CCD1 (the area in the rectangle in Figure 5-50). Red (solid lines): flow off; Blue (dashed lines): flow on.

The data was first processed using the fringe shifting method and the results are shown in Figure 5-51 after five applications of a 9×9 smoothing filter in order to locate the positions of minima in the interference images. Figure 5-51 shows the dark fringe locations in the images taken by CCD1. As for the rotating disc measurements, the shift

of the fringe can be clearly identified and the calculated velocity results are presented in Figure 5-53 (cross symbol). This figure shows the computed velocity profiles vertically across the main flow direction and the profiles are located at 0.5, 1, 1.5, 2, and 2.5 diameters downstream from the nozzle exit (x/d).

These computed velocity profiles were compared with the velocity profiles calculated using simple empirical equations to describe the development region of a circular air jet given by Rajaratnam [15] and the empirical equations are:

$$r_1/r_0 = 0.95 - 0.097 \cdot x/r_0 \qquad \textbf{Equation 5-21}$$

$$b/r_0 = 0.10 + 0.111 \cdot x/r_0 \qquad \textbf{Equation 5-22}$$

$$r_2/r_0 = 1.07 - 0.158 \cdot x/r_0 \qquad \textbf{Equation 5-23}$$

$$\frac{u - u_1}{u_0 - u_1} \approx \frac{u}{u_0} = \frac{\left[1 - \cos(\pi \cdot \varsigma)\right]}{2} \qquad \textbf{Equation 5-24}$$

$$\varsigma = \frac{r_1 - r}{r_2 - r_1} \qquad \textbf{Equation 5-25}$$

where

r	Radial distance from centre line
r_0	Radius of nozzle
r_1	Distance from centre line to inner edge of shear layer (outer edge of potential core
r_2	Distance from centre line to outer edge of jet
b	Distance to half initial velocity (u_0) point from the inner edge of shear layer (outer edge of potential core)
u	Magnitude of velocity
u_0	Initial jet velocity
u_1	Magnitude of velocity of fluid
x	Distance along centre line (downstream from nozzle)
x_0	Distance along centre line the potential core extends to

The geometry used in the above equations is shown in Figure 5-52. The potential core is the triangular region extending from the jet nozzle where the jet's velocity remains constant at the exit velocity. As the jet transmits it mixes the surrounding air generating the shear layer across which the velocity varies from u_0 at the inner edge to zero at the outer edge.

The calculated velocity profiles using Equation 5-21 to Equation 5-25, located at the same positions downstream from the nozzle exit (x/d) as the experimental results, are plotted (solid line) along with the MZI-PDV results (cross symbol) in Figure 5-53. It can be seen that there is generally good agreement between the two sets of profiles, in terms of the overall profile of the jet flow. The steps in the measured velocities are due to the processing method whereby only whole pixel shifts can be measured.

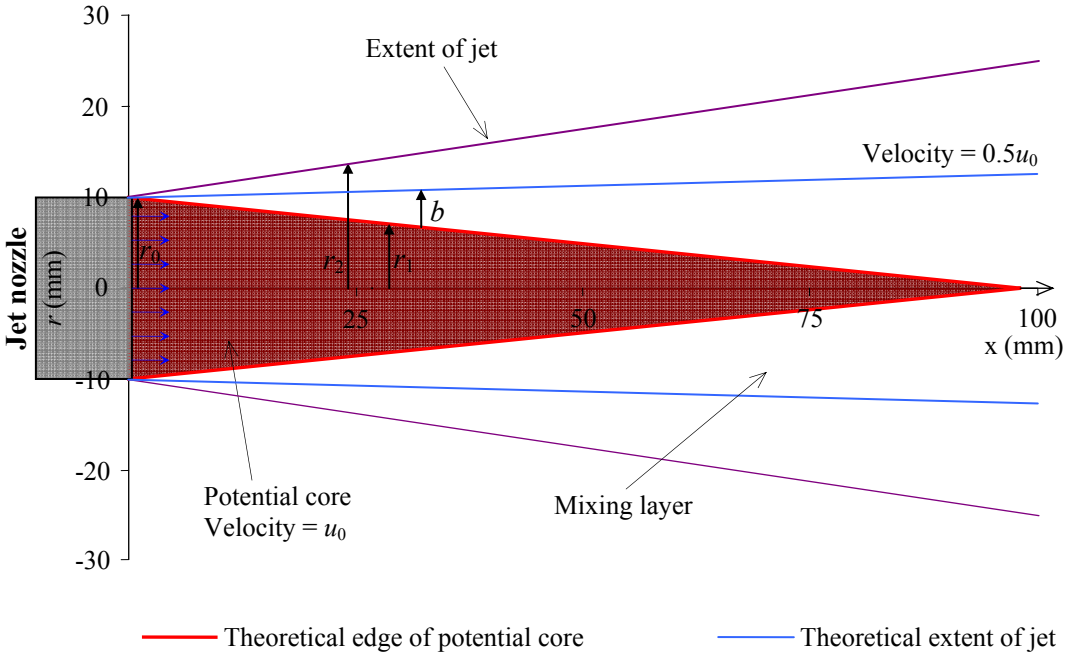

Figure 5-52 Diagram showing the geometry used to calculate the theoretical jet velocity profiles [15].

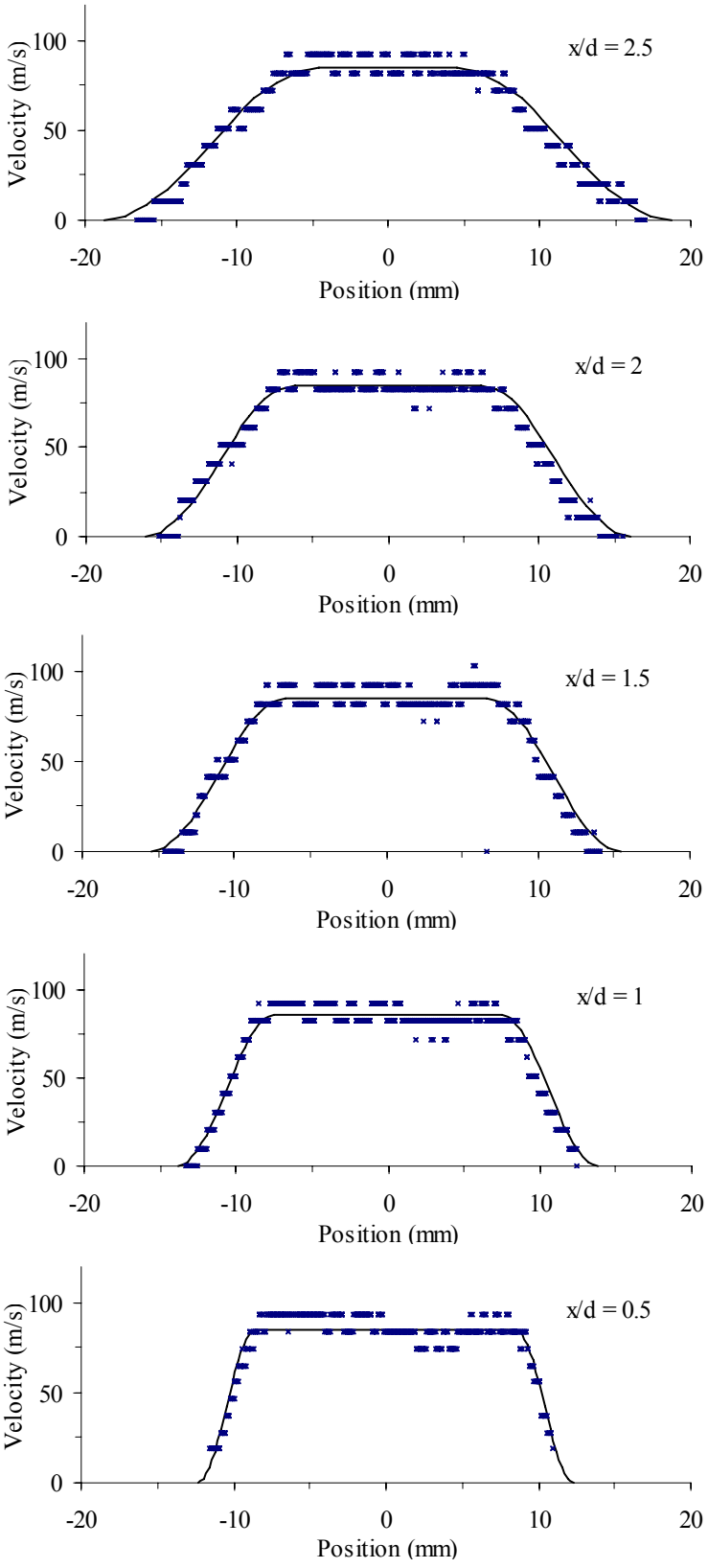

Figure 5-53 A comparison between computed velocity profiles, taken thorough the centre of the air jet at x/d = 0.5, 1, 1.5, 2, and 2.5 diameters downstream from the nozzle using the MZI-PDV system, and the theoretical jet profiles calculated using empirical equations described by Rajaratnam [15]. — Theoretical values; × MZI-PDV.

5.8.3 Results: normalised intensity processing method

Figure 5-54 shows the computed velocity component based on calculating the normalised intensity at each pixel after five applications of a 9×9 smoothing filter. The purpose of the filtering is to remove the false minima and maxima in order to locate the dark and bright fringe positions in the interference images. Figure 5-55 shows the computed velocity component profiles across the main flow direction, along with the theoretical velocity distribution [15]. The profiles are located at 0.5, 1, 1.5, 2, and 2.5 diameters downstream from the nozzle. There is generally good agreement between the two sets of profiles.

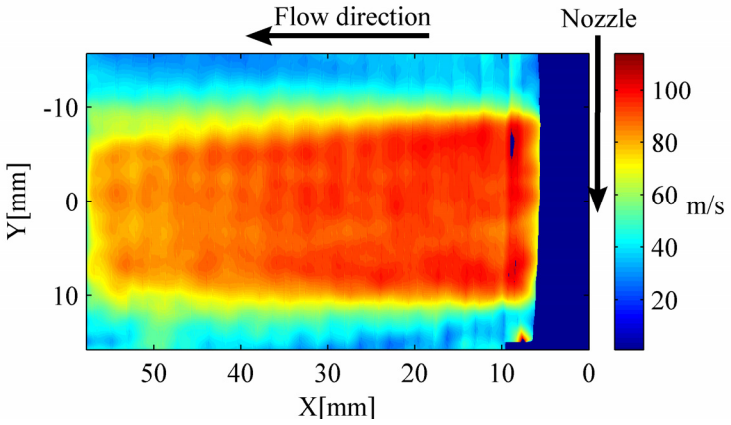

Figure 5-54 The computed velocity component of the air jet flow made using the MZI-PDV system (the area in the rectangle in Figure 5-50).

Because of optical distortions, the fringe amplitude in some region is less than unity. To correct for this, the nearest maximum and minimum are located for each pixel, allowing the local fringe amplitude to be measured. This is used to remove amplitude variations in the fringe pattern.

The 'striping' effect in the image in Figure 5-54 results from the processing method. Close to maxima and minima, the velocity sensitivity is lower than at the quadrature positions. Also, small deviations from a cosinusoidal form, resulting from smoothing, are largest close to maxima/minima and can result in slight velocity errors.

The measurements towards the outside of the jet flow vary more from the expected values possibly due to worse interference fringe quality in these regions, lower signal levels resulting from the 'vignetting effect' in the infinity-corrected optical system and lower seeding levels in these regions as well. The seeding density was low during the measurements because the smoke generator was not adjusted to the optimal operation status during measurements. Additionally, the uneven power distribution in the illumination light sheet results in lower fringe quality here, as seen in Figure 5-50 (a) and (b). This is due to the scratches on the optical surfaces of mirrors used in the light sheet generator as shown in Figure 5-2(b). Although the shape of the theoretical and experimental curves is well matched, the magnitudes differ slightly between the two sets of values. This can be explained by the simple empirical equations used to calculate the theoretical profiles and the possible variations between the flow generated by the jet nozzle and a theoretical jet flow.

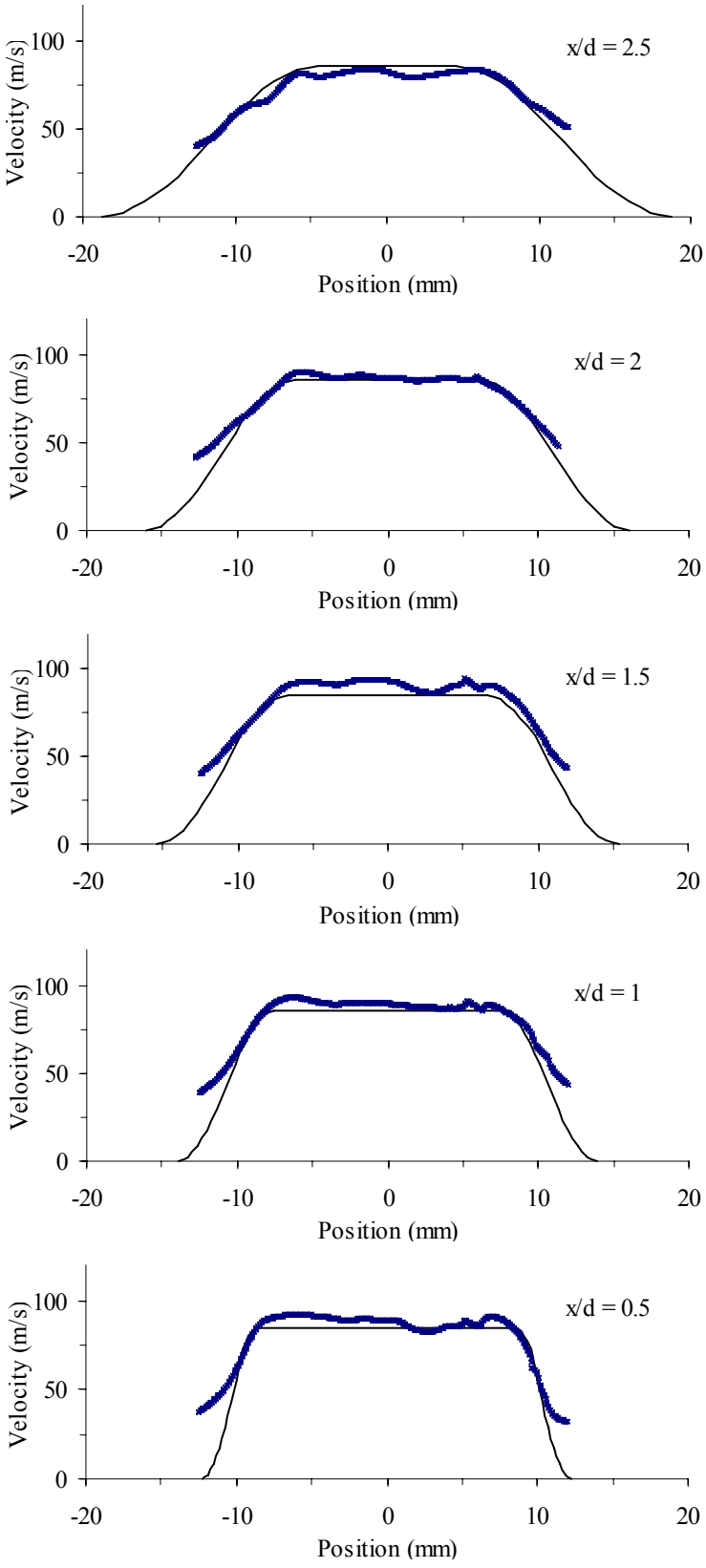

Figure 5-55 A comparison between computed velocity profiles, taken thorough the centre of the air jet at x/d = 0.5, 1, 1.5, 2, and 2.5 diameters downstream from the nozzle using the MZI-PDV system, and the theoretical jet profiles calculated using empirical equations described by Rajaratnam [15]. — Theoretical values; × MZI-PDV.

5.9 Summary

An MZI-PDV system to measure time-averaged, single velocity component has been described. This system can provide profiles or full-field measurements using the shift or the normalised intensity of an interference pattern processing technique.

A modified infinity-corrected microscope optical system was investigated and used to construct the MZI. This imaging system is limited for long infinity-space distances due to the 'vignetting effect'. A phase locking system was designed to stabilise the interferometric filter in order to eliminate the interferometer phase drift. The system efficiency is limited by the frequency stability of the He-Ne laser used. The system sensitivity and dynamic range was also reduced since the operating wavelength of the optical components was at 514.5nm.

The factors that will affect the quality of the interference fringe image are investigated. The inclination angle and the optical path difference deviation have little effect on the contrast of the interference fringes since collimated light beams, rather than divergent ones, are used in the interferometer.

The measurable Doppler frequency shift increases when increasing the interferometer fringe number in the image leading to a decreased measurement resolution, but this reduces measurement uncertainty due to the interferometer phase drift because the phase drift smaller than this measurable shift would be suppressed. Therefore, for a higher measurement resolution, the interferometer phase will be more sensitive requiring accurate phase control ability.

The application of filtering has nearly no effect on measurements using the fringe shift processing method since it does not affect the measured locations of the real minima in the image. However, it introduces a relative bias error in measurements using the normalised intensity processing method because the application of filtering changes the fringe amplitude.

The results of measurements from a rotating disc have been used to validate this system. The standard deviation of the measured velocities was about $2.9ms^{-1}$ using the fringe shifting processing method and $2ms^{-1}$ using the normalised intensity method, for a velocity range of $\sim\pm70ms^{-1}$. This possibly comes from: optical distortions, uneven power distribution in the illumination light sheet and application of the smoothing filter.

Single camera technique also has been validated from measurements on the rotating disc. The technique is being further developed to cope with the interferometer drift during the measurement since the phase locking system was currently turned off for the π phase shift.

Measurements on a seeded air jet with a maximum velocity of around $85ms^{-1}$ were made, demonstrating good agreement with the expected velocities calculated using empirical equations to describe the jet.

5.10 References

[1] Spectra-Physics BeamLok Argon Ion laser, website (2007), www.newport.com.

[2] Roehle, I., Schodl, R., Voigt, P. and Willert, C. (2000), "Recent developments and applications of quantitative laser light sheet measuring techniques in turbomachinery components", *Measurement Science and Technology,* Vol. 11, No. 7, pp. 1023-35.

[3] Nobes, D.S., Ford, H.D. and Tatam, R.P. (2001), "Instantaneous, two camera, three dimensional planar Doppler velocimetry using imaging fiber bundles", *Optical Diagnostics for Fluids, Solids, and Combustion, Proc. SPIE*, San Diego, CA, Vol. 4448, pp. 283-94.

[4] Charrett, T.O.H., Ford, H.D., Nobes, D.S. and Tatam, R.P. (2004), "Two-frequency planar Doppler velocimetry (2ν-PDV)", *Review of Scientific Instruments,* Vol. 75, No. 11, pp. 4487-96.

[5] PCO imaging, website (2007), http://www.pco.de/pco/php/support.

[6] Chehura, E. (2002), ″In-line using fibre-optic laser Doppler velocimeter using Bragg grating interferometric filters as frequency to intensity transducers", *PhD thesis,* Cranfield University, Cranfield, UK.

[7] Edmund Optics (UK) Ltd., website, (2007), www.edmundoptics.com.

[8] Melles Griot Inc., website, (2007), http://www.mellesgriot.com.

[9] Warwick, K. (1996), "An introduction to control systems", World Scientific, Singapore.

[10] Wernert, P., Martinez, B., George, A., Leopold, F. and Seiler, F. (2005), "Development of Doppler based planar velocimetry techniques for high-speed flows at ISL", *8th International Symposium on Fluid Control, Measurement and Visualization (FLUCOME),* Chengdu, CN, Paper 316.1-18.

[11] Seiler, F., George, A., Srulijes, J. and Havermann, M. (2006), "Progress in Doppler picture velocimetry (DPV) Technique", *12th International Symposium of Flow Visualization,* German Aerospace Center (DLR), Göttingen, Germany, pp. 1-10.

[12] Nobes, D.S., Wieneke, B. and Tatam, R.P. (2004), "Determination of view vectors from image warping mapping functions", *Optical Engineering,* Vol. 43, No. 2, pp. 407-14.

[13] Seiler, F. and Srulijes, J. (1986), "Doppler-pictures of velocity fields - An application to fluid mechanics", *3rd International Symposium on Applications of Laser Anemometry to Fluid Mechanics,* Lisbon, Portugal, Paper 19.1.

[14] Seiler, F., George, A., Leopold, F., Srulijes, J. and Smeets, G. (1999), "Flow velocities visualization using Doppler picture interference velocimetry", *18th International Congress on Instrumentation in Aerospace Simulation Facilities (ICIASF 99), IEEE*, Toulouse, France, 11.1-8.

[15] Rajaratnam, N. (1976), "Turbulent jets", Elsevier, Amsterdam, Netherlands.

6 A three-component MZI-PDV system

6.1 Introduction

The aim of the PDV technique is to obtain the velocity vector map of the flow, however, with the MZI-PDV system shown in Figure 5-1, only the component of the velocity in the ($\hat{o}$-$\hat{i}$) direction can be obtained. This chapter describes the development of a time-averaged, 3-component MZI-PDV system.

In the conventional PDV technique, three components of the velocity can be obtained by illuminating the flow from three different directions [1] or collecting the scattering light from three different directions [2]. Roehel *et al* [1,3] used the first option to make 3-component velocity measurements by using 3 orthogonal light sheets to illuminate the same flow area. However, the technique is limited for instantaneous measurements since each component is measured sequentially rather than simultaneously.

The second option is to use three pairs of cameras (reference and signal) to view the light sheet from three different directions, and this has been used by many researchers [4-6]. McKenzie [7] and Arnette *et al* [8] reduced the number of cameras used from 6 to 3 by using single camera to record both reference and signal images. This has some drawbacks. The resolution is reduced by a factor of 2. The use of a single CCD to record both signal and reference images invariably results in some image overlap [7].

More recently an optical imaging-fibre-bundle based PDV technique has been developed by Nobes *et al* [9,10] at Cranfield University to make instantaneous or time-averaged three-component velocity measurements using only a single imaging head.

The single component measurement system described in chapter 5 was modified using an imaging fibre bundle to allow the measurement of multiple velocity components and then the calculation of the velocity vector. The system was first validated by measuring the velocity field of a rotating disc. Finally measurements were made on a seeded axis-symmetric air jet.

6.2 Modification of the MZI-PDV system to allow 3-component measurements

As described in chapter 5, a 35mm SLR camera lens was used to image a flow region as the input to the MZI in the MZI-PDV imaging head arrangement. This can only provide single velocity component measurements. Here, the camera lens was replaced using an imaging fibre bundle with matched camera lenses at each bundle channel end.

6.2.1 Imaging fibre bundles for 3-component image collecting

The imaging fibre bundle in use at Cranfield University is a coherent array of fibres that is split into four channels (Figure 6-1a). Each channel comprises 500×600 fibres and is 4m long. The bundle is constructed from 50μm 'multifibres' blocks, shown in Figure 6-1(c), of 5×5 fibres with 8μm cores at 10μm centres [11]. The fibre will allow a few

modes to transmit at a wavelength of 514.5nm because a fibre core of 4/5μm in diameter is required in order to keep single mode to transmit in the fibre for this wavelength. This possibly results in a noisy transmitted image that could be seen in the recorded images shown in section 6.4.2. One end of each channel received the image of the flow region using 35mm SLR camera lenses. The four channels were joined at the detector head, with each view occupying a quarter of the CCD image shown in Figure 6-1(b). The transmission through a bundle depends on the length and the wavelength. The loss through the bundle is ~40% for the 4m length at a wavelength of 514.5nm.

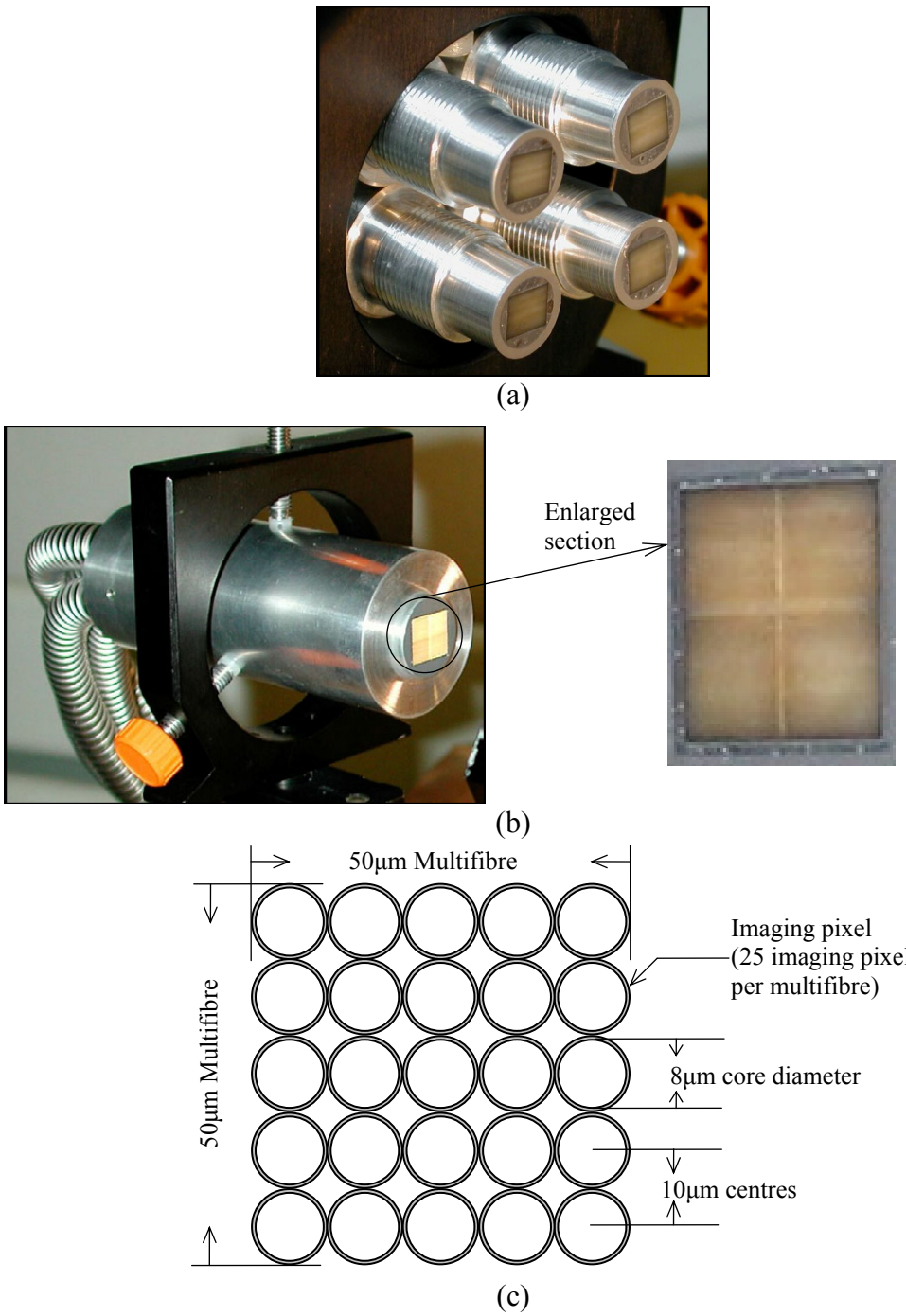

Figure 6-1 (a) Entry faces of the four-channel bundle without imaging lenses. (b) Combined exit face of the four channels. (c) The structure of one multifibre section of the bundle [11].

To demonstrate the combining of channels an example image from one camera of the combined four views is shown in Figure 6-2(a). This image shows a calibration dot card and the area viewed is ~60×75mm. The perspective distortion of the targets shows the different directions of the four views. Figure 6-2(b) is a magnified part of one view (top right) to highlight the patterns of the individuals fibres. It can be seen clearly that the dense packing of the fibres results in very minor edge effects. This can be removed by applying a smoothing filter. The black spots are imperfections in the imaging fibre bundle due to broken multifibres. Figure 6-3 shows the 'de-warped' view obtained from the four views of the calibration target using the de-warping processing method [12]. This will be discussed further in section 6.3.

By using the imaging fibre bundle it is possible to make three-component velocity measurements with only one PDV imaging head arrangement. This reduces the system complexity compared to those reported previously. The use of the fibre imaging bundle also provides more flexibility in viewing arrangements for flows with restricted optical access or unfriendly operating environments such as wind tunnels. This is of particular interest for MZI-PDV as the interferometer can be isolated from the flow environment. Another potential advantage of using the imaging fibre bundle approach is to measure the illumination laser frequency during measurements. This is realised by using the fourth channel to monitor the laser frequency in real-time by viewing the laser light scattering from a motionless screen [9].

6.2.2 Experimental arrangement

A schematic diagram of this new experimental arrangement is shown in Figure 6-4. As before the light source was a tuneable argon-ion laser (Spectra Physics BeamLok 2060-7S), incorporating a temperature-stabilised etalon to ensure single-mode operation at 514.5nm.

Light from the laser was coupled into an optical fibre through a Faraday isolator, and the output was formed into a light sheet using a prism-scanning device that the beam rapidly scanned across the measurement area. The scattered light from a flow region of interest was imaged using standard SLR camera lenses and ported to the MZI using the imaging fibre bundle. The MZI was constructed as in chapter 5 and the two complementary output images of the MZI were captured by the two CCD cameras (CCD1 and CCD2 as shown in Figure 6-4). The phase locking system described previously was used to compensate for the interferometer phase drift.

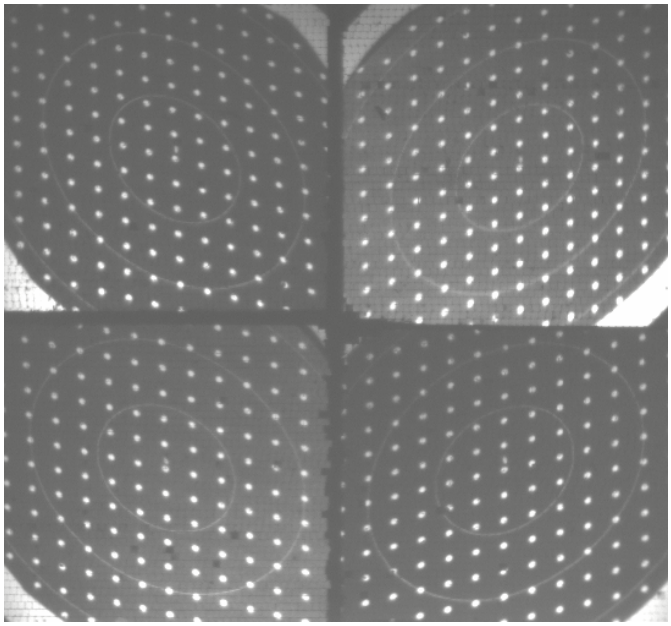

(a)

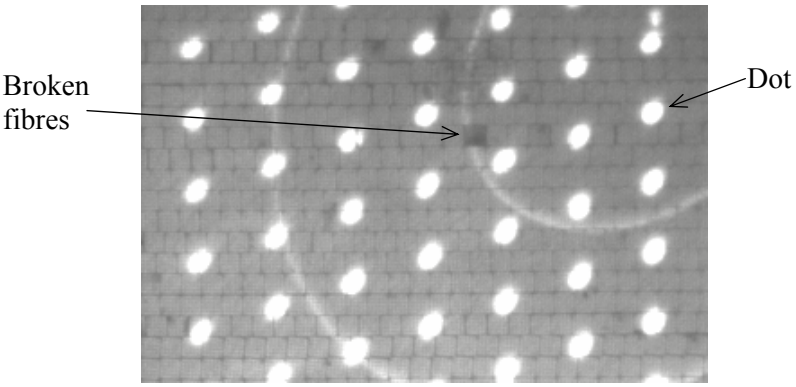

(b)

Figure 6-2 (a) An example camera image of a calibration dot card viewed by the imaging fibre bundle. The viewed area is ~60×75mm; the white dots are 2.5mm in diameter and spaced on a regular grid of 10mm. (b) A magnified part of one view (top right) in the image.

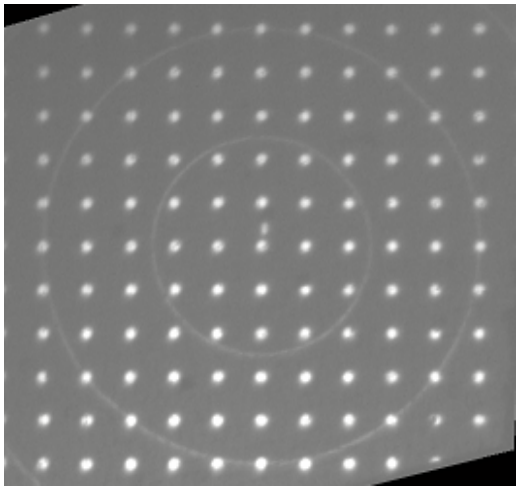

Figure 6-3 An example of the 'de-warped' views, showing all four views in Figure 6-2(a) overlaid.

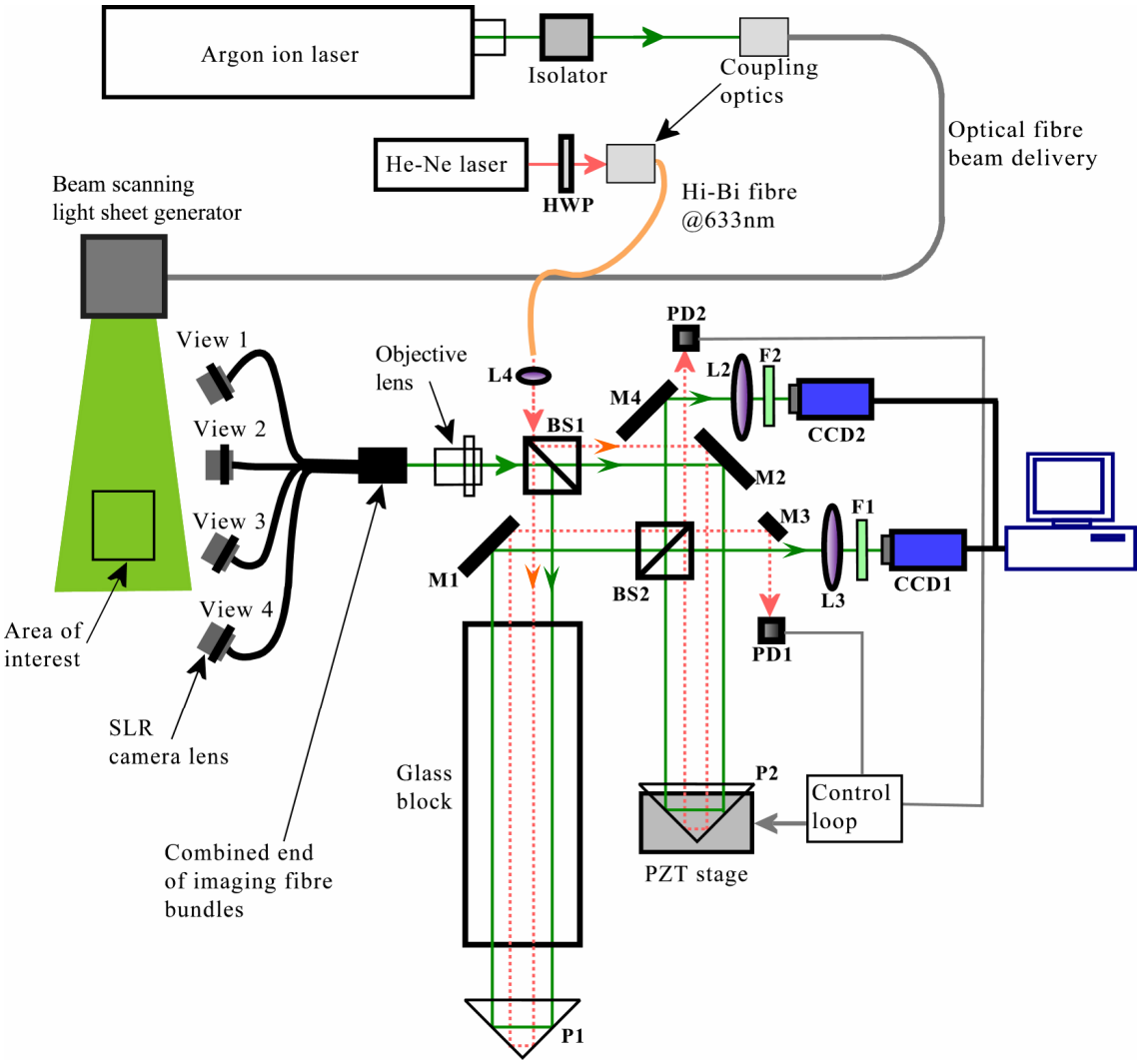

Figure 6-4 A schematic diagram of the experimental arrangement of the 3-component measurement MZI-PDV system using an imaging fibre bundle. HWP: half-wave plate; BS1, 2: non-polarisation beam splitters; L2, 3: tube lenses; L4: coupling lens; M1, 2, 3, 4: mirrors; F1, 2: green filters; P1, 2: right angle prisms. Beam path for measurement shown as solid line (green), beam path for locking system shown as a dotted line (red).

6.3 Processing scheme

Extra processing stages are required to calculate the 3-component velocity compared to a single component. The first step in the analysis of the recorded image data is to obtain the image de-warping coefficients that map the three obliquely viewed camera views onto a common grid. This is achieved by processing images of a common grid (dot pattern) placed into the light sheet plane prior to the measurement, also called the 'de-warping' process. The second is to calculate multiple velocity components, as in the single component MZI-PDV method (described in chapter 5). Then the orthogonal velocity components can be calculated using the non-orthogonal components. These steps are described in detail in the following sections.

6.3.1 Calculation of multiple velocity components

Figure 6-5 shows a flow diagram of the processing used in the calculation of each velocity component. The raw images have a background subtracted. This background is the noise accumulated in the exposure as well as the read out noise. The four separate views defined by the imaging fibre bundle channels are extracted from both images. These views are then de-warped and mapped onto a common grid. This means that each view has the same scale and is aligned with each other. The calibration of the image de-warping is performed before the flow measurements by using a target image of dots (Figure 6-2a). The calculated de-warping coefficients are then stored for each view.

The images obtained through the imaging fibre bundle are characterised by a significant degree of high-frequency modulation (Figure 6-2b), which is mainly due to the grid arrangement of the imaging fibres (Figure 6-1c). This intensity modulation can result in an additional signal in the normalised intensity images. Low-passing filtering, typically a 5×5 smoothing filter, is therefore applied to the image data to remove this effect.

Next, each view is processed individually by normalising the two images, as in single velocity component measurements, yielding the four phase map images.

The above processing is applied to the raw images captured when the flow is off and on. The calculated phase maps can then be used to calculate the Doppler shift images for each view, as shown in Figure 6-5(b).

The sensitivity vectors for each view can either be calculated directly from the de-warping calibration [13] or according to a pinhole camera model. These are then used to calculate the non-orthogonal velocity components of the flow.

It is worth noting that the data processing method based on the shift of the interference fringe pattern used in chapter 5 cannot be used here. Although velocity profiles in each view can be calculated as before, the profiles are not located in the same position when the four views are mapped onto a common grid using the de-warping process. The orthogonal velocity profiles therefore cannot be achieved. This is because the fringes and their locations are different in each view. Therefore, the data processing method for 3-component measurements is based on the normalised intensity calculated from the two outputs of the MZI (described in chapter 5).

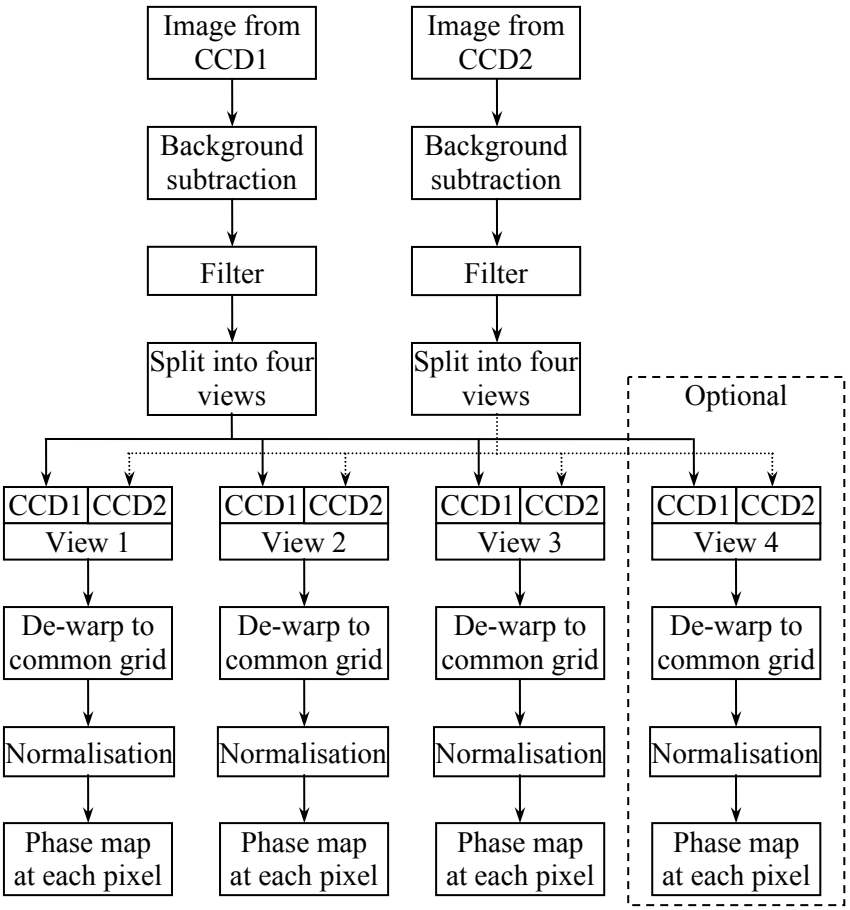

(a)

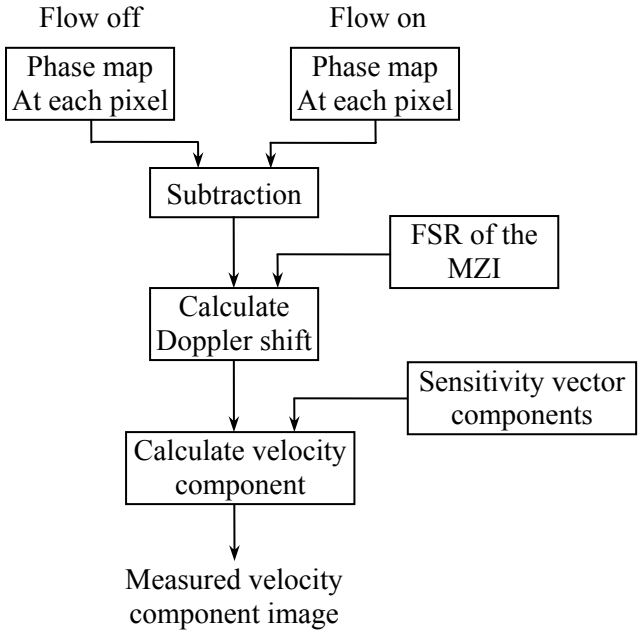

(b)

Figure 6-5 Flow diagram showing the processing used in the calculation of (a) each phase component and (b) each velocity component in the MZI-PDV technique.

6.3.2 Conversion to orthogonal velocity components

The final step is to convert from non-orthogonal to orthogonal velocity components that are aligned with the experiment.

In previous PDV work, there have been two methods for this. The first is using three measured components to calculate the orthogonal components in a co-ordinate system related to the measurement. This is used widely in PDV research groups. The transformation can be found in the work of Reinath [14] and has also been used in our research group [9,10].

The second is using multiple (more than three) measured components. The extra components are used to reduce errors. In Cranfield University, the use of the imaging fibre bundle with multiple channels has provided four measured velocity components, and the fourth can be used to reduce errors compared to that using three measured components. This has been investigated in detail by Charrett [15]. The key equations of the two methods are presented in the following.

Three component method (3C)

If $[U_m]$ represents the magnitudes of the measured non-orthogonal velocity components, written as a column vector, and $[V]$ is the required Cartesian components of velocity, then a transformation matrix [A] may be written as

$$[U_m] = [A] \times [V]. \qquad \textbf{Equation 6-1}$$

The three orthogonal velocity components can be given using the equations:

$$U = \frac{1}{\det([A])}\left[|U_1| \cdot (Y_2 Z_3 - Y_2 Z_3) - |U_2| \cdot (Y_1 Z_3 - Y_3 Z_1) + |U_3| \cdot (Y_1 Z_2 - Y_2 Z_1)\right]$$

$$V = \frac{1}{\det([A])}\left[-|U_1| \cdot (X_2 Z_3 - X_2 Z_3) + |U_2| \cdot (X_1 Z_3 - X_3 Z_1) + |U_3| \cdot (X_1 Z_2 - X_2 Z_1)\right]$$

$$W = \frac{1}{\det([A])}\left[|U_1| \cdot (X_2 Y_3 - X_2 Y_3) - |U_2| \cdot (X_1 Y_3 - X_3 Y_1) + |U_3| \cdot (X_1 Y_2 - X_2 Y_1)\right]$$

Equation 6-2

where:

$(\hat{o}_1 - \hat{\imath})$	Measured component from camera view 1 ($\hat{o}_1$)
$(\hat{o}_2 - \hat{\imath})$	Measured component from camera view 1 ($\hat{o}_2$)
$(\hat{o}_3 - \hat{\imath})$	Measured component from camera view 1 ($\hat{o}_3$)
$\|U_1\|$	Magnitude of the measured component from camera view 1
$\|U_2\|$	Magnitude of the measured component from camera view 2
$\|U_3\|$	Magnitude of the measured component from camera view 3
X_1, Y_1, Z_1	Unit vector components defining the direction of $(\hat{o}_1 - \hat{\imath})$
X_2, Y_2, Z_2	Unit vector components defining the direction of $(\hat{o}_2 - \hat{\imath})$
X_3, Y_3, Z_3	Unit vector components defining the direction of $(\hat{o}_3 - \hat{\imath})$
U, V, W	Orthogonal velocity components, horizontal, vertical and out-of-

plane respectively

$$\det([A]) = X_1Y_2Z_3 + Y_1Z_2X_3 + Z_1X_2Y_3 - Z_1Y_2X_3 - X_1Z_2Y_3 - Y_1X_2Z_3 .$$

Four component method (4C)

With four measured components, Equation 6-1 can be rewritten as

$$\begin{bmatrix} U_1 \\ U_2 \\ U_3 \\ U_4 \end{bmatrix} = \begin{bmatrix} X_1 & Y_1 & Z_1 \\ X_2 & Y_2 & Z_2 \\ X_3 & Y_3 & Z_3 \\ X_4 & Y_4 & Z4_1 \end{bmatrix} \times \begin{bmatrix} U \\ V \\ W \end{bmatrix} \text{ or}$$

$$[U_m] = [J] \times [V]. \qquad \textbf{Equation 6-3}$$

The general least squares solution for linear equations [16] is given by:

$$[V] = ([J]^T \times [w] \times [J])^{-1} \times [J]^T \times [w] \times [U_m]. \qquad \textbf{Equation 6-4}$$

Here w is the weighting matrix, which allows each equation to be ranked, with larger values indicating greater importance, and w_1 etc are the relative weightings. [w] has the form

$$[w] = \begin{bmatrix} w_1 & 0 & 0 & 0 \\ 0 & w_2 & 0 & 0 \\ 0 & 0 & w_3 & 0 \\ 0 & 0 & 0 & w_4 \end{bmatrix}. \qquad \textbf{Equation 6-5}$$

The approximate solutions of Equation 6-3 for the orthogonal velocity are

$$\begin{bmatrix} U_1 \\ U_2 \\ U_3 \\ U_4 \end{bmatrix} = \begin{bmatrix} X_1 & Y_1 & Z_1 \\ X_2 & Y_2 & Z_2 \\ X_3 & Y_3 & Z_3 \\ X_4 & Y_4 & Z4_1 \end{bmatrix} \times \begin{bmatrix} U \\ V \\ W \end{bmatrix} = L \begin{bmatrix} (df - ee)g + (ce - bf)h + (be - cd)j \\ (ce - bf)g + (af - cc)f + (bc - ae)j \\ (be - cd)g + (bc - ae)f + (ad - bb)j \end{bmatrix}$$

Equation 6-6

where:

$$a = \sum_n X_n^2 w_n , \qquad b = \sum_n X_n Y_n w_n , \qquad c = \sum_n X_n Z_n w_n , \qquad d = \sum_n Y_n^2 w_n ,$$

$$e = \sum_n Y_n Z_n w_n , \qquad f = \sum_n Z_n^2 w_n , \qquad g = \sum_n X_n w_n U_n , \qquad h = \sum_n Y_n w_n U_n ,$$

$$J = \sum_n Z_n w_n U_n , \qquad L = 1/a(df - ee) - b(bf - ce) - c(be - dc) .$$

6.4 Validation measurements on a rotating disc

A rotating disc was used as the first target to validate the 3-component MZI-PDV system providing a well-defined velocity field. This was also used in the single velocity component MZI-PDV system. The rotating disc is about 200mm in diameter giving a maximum velocity in the field of view of ~±30ms^{-1} at the disc edge that was measured independently using an optical tachometer.

6.4.1 Experimental arrangement

Figure 6-6 shows the viewing configuration used to make measurements on the rotating disc, along with the light sheet generator. XY plane is located in the surface of the disc in the used co-ordinate system, and the generated light sheet was propagating in the negative X direction located in the XY plane. The four camera lenses were located in the same plane in the positive Z space since only one side of the disc was illuminated. The illumination and observation unit vectors for the four views are given in Table 6-1. This arrangement gave relatively large Doppler sensitivity vectors, but led to unbalanced intensities collected in the four views because $\hat{o}_3$ and $\hat{o}_4$ were in forward scattering region while $\hat{o}_1$ and $\hat{o}_2$ in backward scattering region.

The four arms of the imaging fibre bundle were mounted onto a structure built with FlexLink structural components [17]. This provides a stable structure to mount the imaging lenses so that they are not affected by vibrations related to the running disc or flow, as shown in Figure 6-7. This also provides flexibility in mounting the views so as to obtain a well-conditioned viewing configuration.

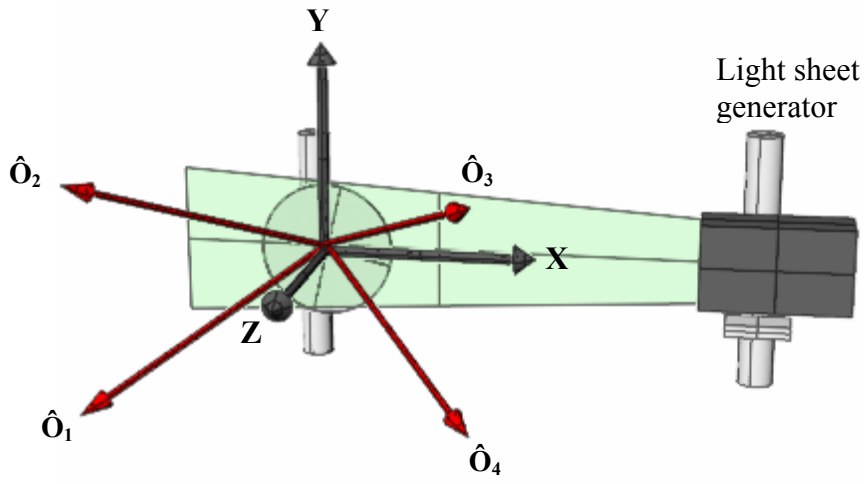

Figure 6-6 Diagram showing the viewing geometry used when making measurements on the rotating disc. $\hat{o}_1$, $\hat{o}_2$, $\hat{o}_3$, and $\hat{o}_4$ are the observation directions for each arm of the imaging fibre bundle.

Table 6-1 Illumination and observation unit vectors used for 3-component measurements on a rotating disc.

	Unit vectors	View location (cm)
Laser	[-1, 0, 0]	-
View 1	[-0.371, -0.557, 0.743]	[-60, -90, 120]
View 2	[-0.371, 0.557, 0.743]	[-60, 90, 120]
View 3	[0.371, 0.557, 0.743]	[60, 90, 120]
View 4	[0.371, -0.557, 0.743]	[60, -90, 120]

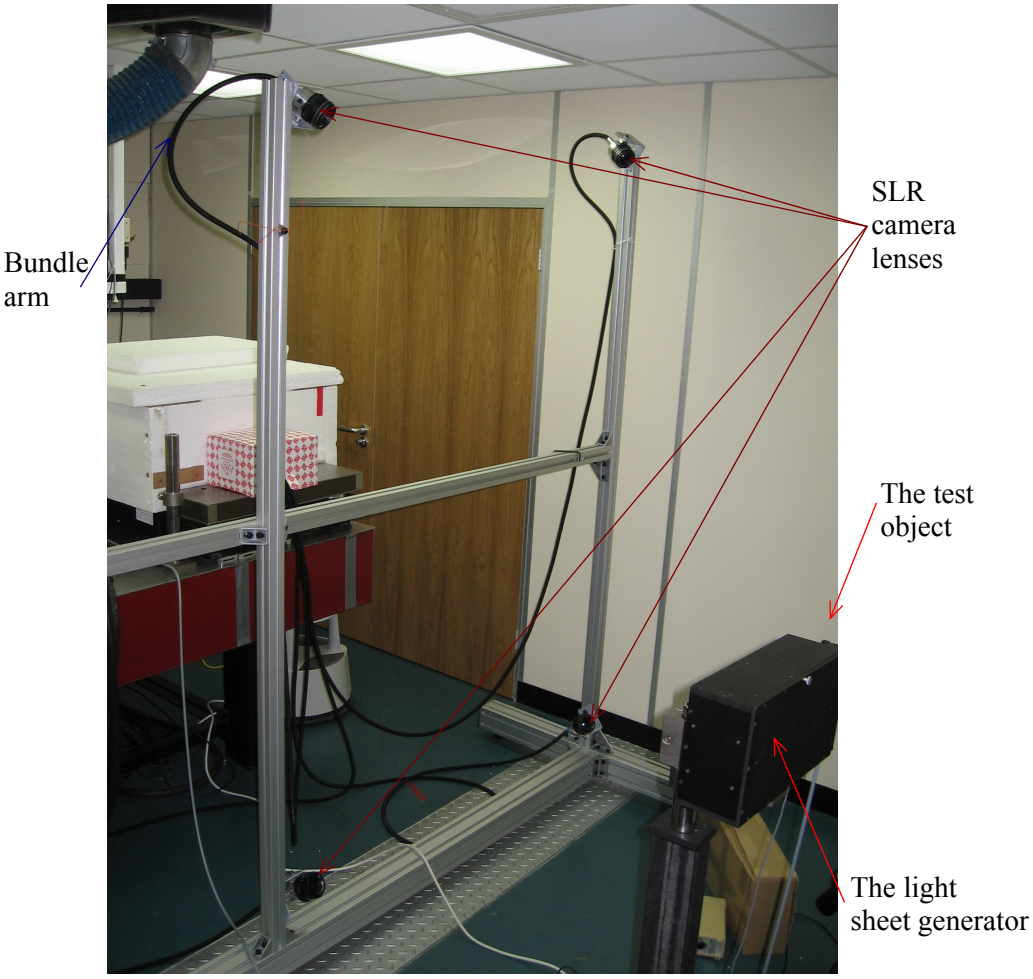

Figure 6-7 Photograph showing the fibre bundle mounted in the viewing configuration used to make 3-component measurements on the rotating disc.

6.4.2 Results

A pair of images were captured simultaneously (one on each CCD camera) with the disc motionless. The disc rotation was started and a second image pair captured. These are shown in Figure 6-8. The images with the disc stationary exhibit a speckled appearance as in the single component measurement and also some black spots are clearly seen due to broken fibres in the imaging fibre bundles. The invisible or poor-visibility edges of the images are due to the 'vignetting effect' in the imaging system. The optical power at the output of the optical fibre was ~200mW and the CCD camera integration time was set to be five seconds to obtain clear images.

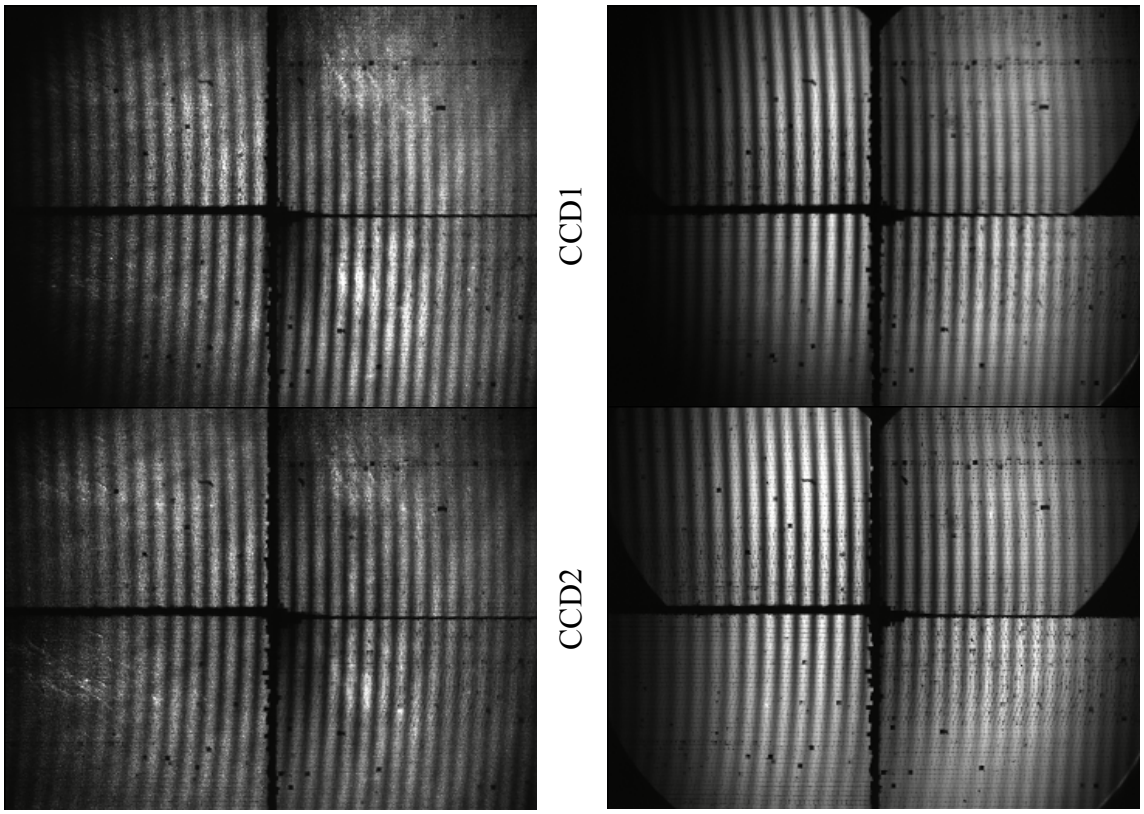

Figure 6-8 Two pairs of fringe images recorded by CCD1 (top) and CCD2 (bottom): for (a) the motionless and for (b) the rotating disc.

Figure 6-9 shows the positions of the dark fringes in the four split sub-images taken by CCD1 for the disc stationary and rotating. Here the shift in the fringe locations can be clearly seen. Similar images can be obtained using the second CCD with the dark fringes located between those found from CCD1 and are shown Figure 6-10. These fringe shift can be processed to give profiles of the velocity for each of the measured components, although as previously discussed the profiles for each component are not located at the same positions, so the orthogonal velocity components can be calculated using this method.

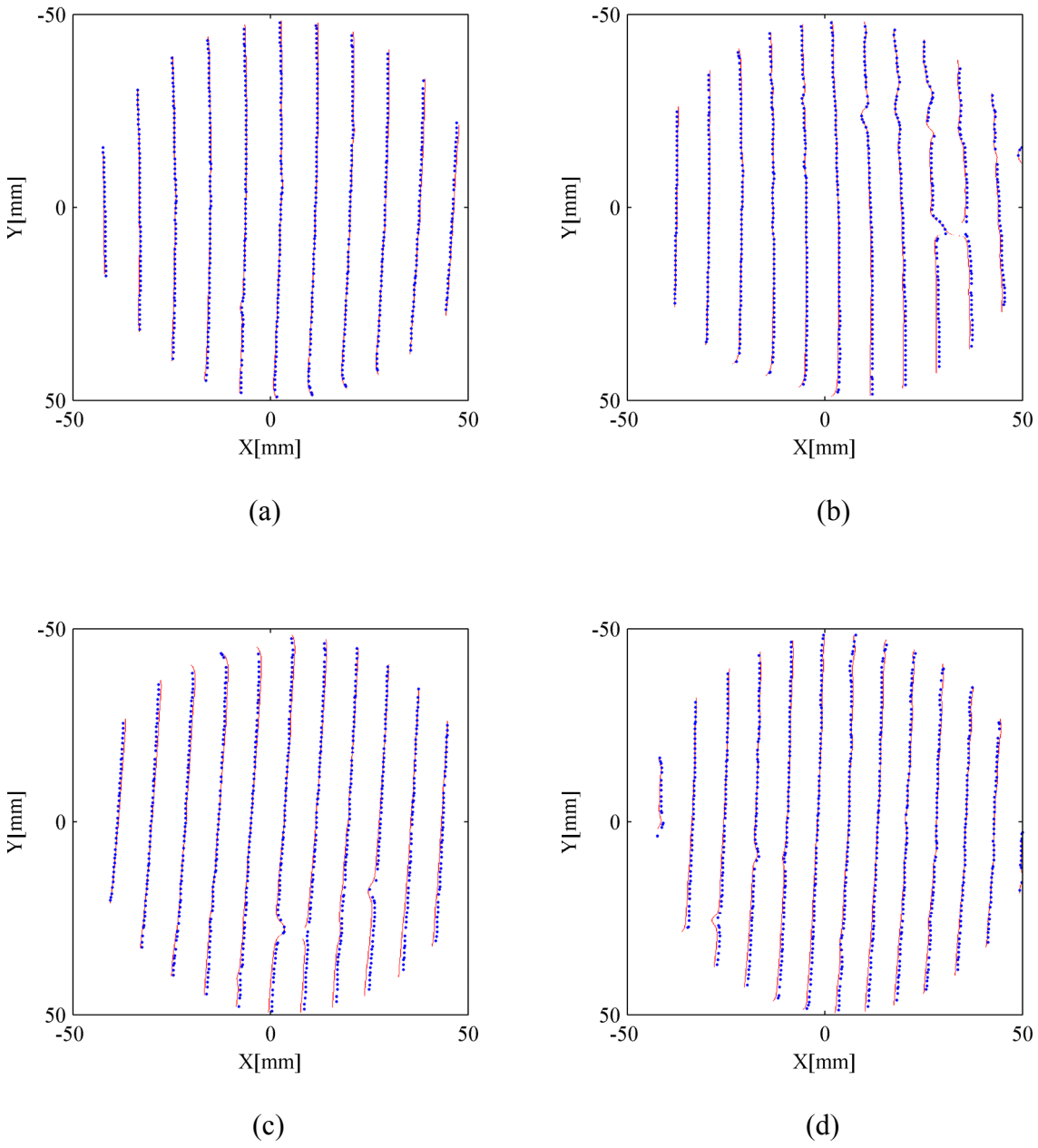

Figure 6-9 Dark fringes in images taken by CCD1 for the disc. Solid (red) lines: disc stationary; dashed (blue) lines: disc rotating.

(a) View 1; (b) View 2; (c) View 3; (d) View 4.

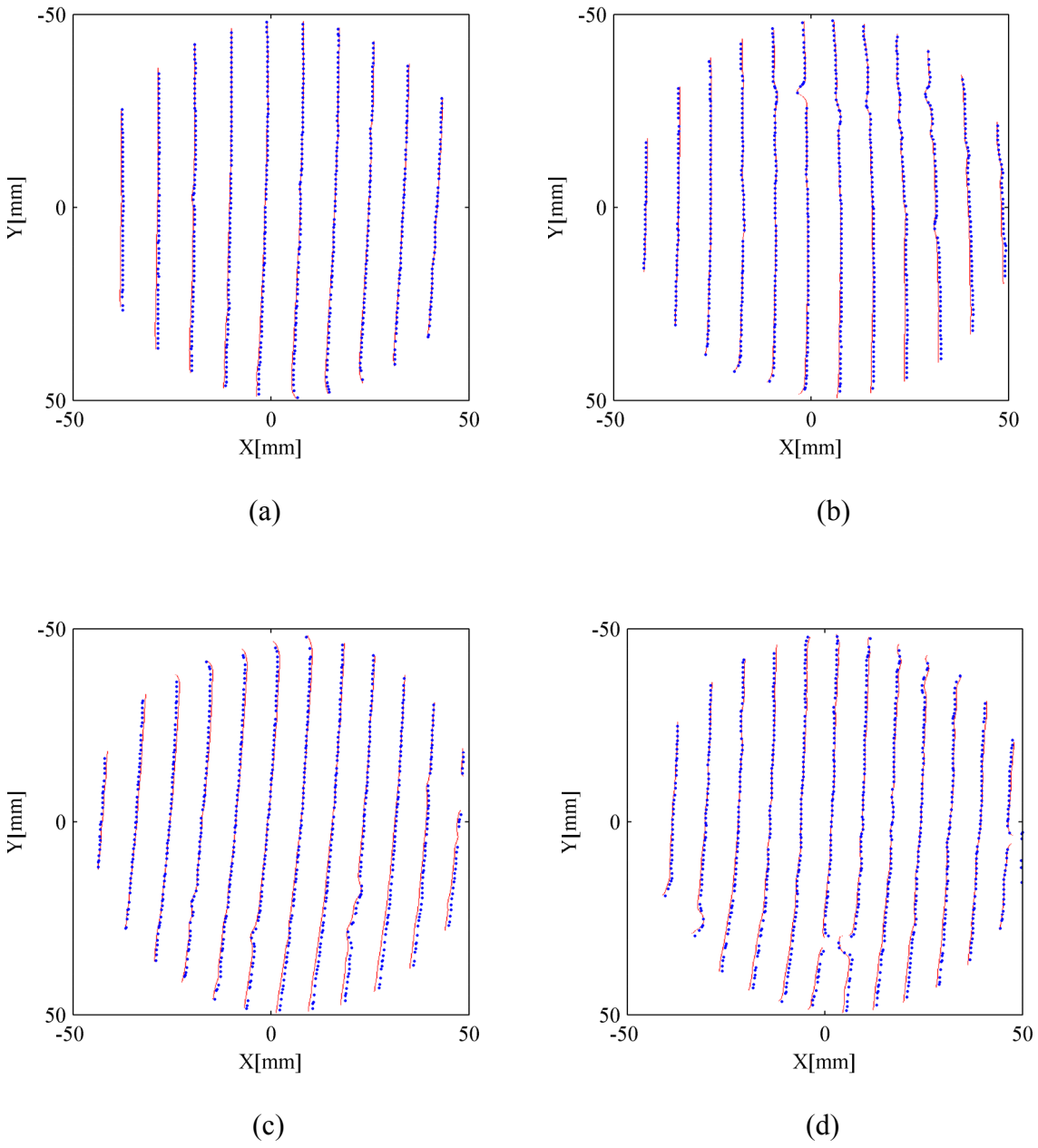

Figure 6-10 Dark fringes in images taken by CCD2 for the disc. Solid (red) lines: disc stationary; dashed (blue) lines: disc rotating.

(a) View 1; (b) View 2; (c) View 3; (d) View 4.

These images were then processed using the normalised intensity processing method. This method allows the velocity to be evaluated at each pixel in the collected images. The sensitivity vectors for the four views were determined for each view from measurements of the observation and illumination positions from which the variation of the sensitivity vector across the field of view can be calculated. The computed velocity components (non-orthogonal) for the four observation directions are shown in Figure 6-11(a)-(d) after five applications of a 9×9 smoothing filter. Compared to the single component measurement on the same rotating disc (described in chapter 5), here more filtering was applied to the raw images in order to locate the maxima and minima in the images. This comes from the worse image quality obtained through an imaging fibre bundle than a standard SLR camera lens due to the bundle manufacturing imperfections such as multifibre bounding edges and broken fibres as shown in Figure 6-2(a).

In order to assess the measurement accuracy in this system, a theoretical velocity component in the field of view was calculated for each observation direction. The theoretical velocity component for a rotating disc can be calculated from the computed sensitivity vectors for the four views and the rotation frequency of the disc that was measured by an optical tachometer. Therefore, at each point in the disc field of view, the measured velocity could be subtracted from the computed component. A histogram of this remaining error was then plotted, and the standard deviation was calculated. This method was used previously by Charrett [16] and is represented in Figure 6-12.

The histograms of the remaining error for each view are shown in Figure 6-11(a1)-(d1) respectively. The standard deviations for each of the four plots are shown in Table 6-2. These plots show that the remaining errors are not symmetrical distribution along the zero error. For example, the negative values are more than positive ones in the histogram of the remaining error for view 1, as shown in Figure 6-11(a1). This is possibly due to the difference in the interference fringe quality between the two measurement regions (top and bottom regions of the rotating disc) leading to the different velocity measurement errors. In the MZI-PDV technique, the measurement accuracy is directly related to the quality of the interference fringe image. This is also the reason why the standard deviation for view 1 is larger than those for the other three views, as shown in Table 6-2.

Table 6-2 Standard deviations of the variations of the measured and the theoretical velocity components for the rotating disc at each of the four views.

	View 1	View 2	View 3	View 4
Standard deviations	2.8 ms^{-1}	2.1 ms^{-1}	2.1 ms^{-1}	2.2 ms^{-1}

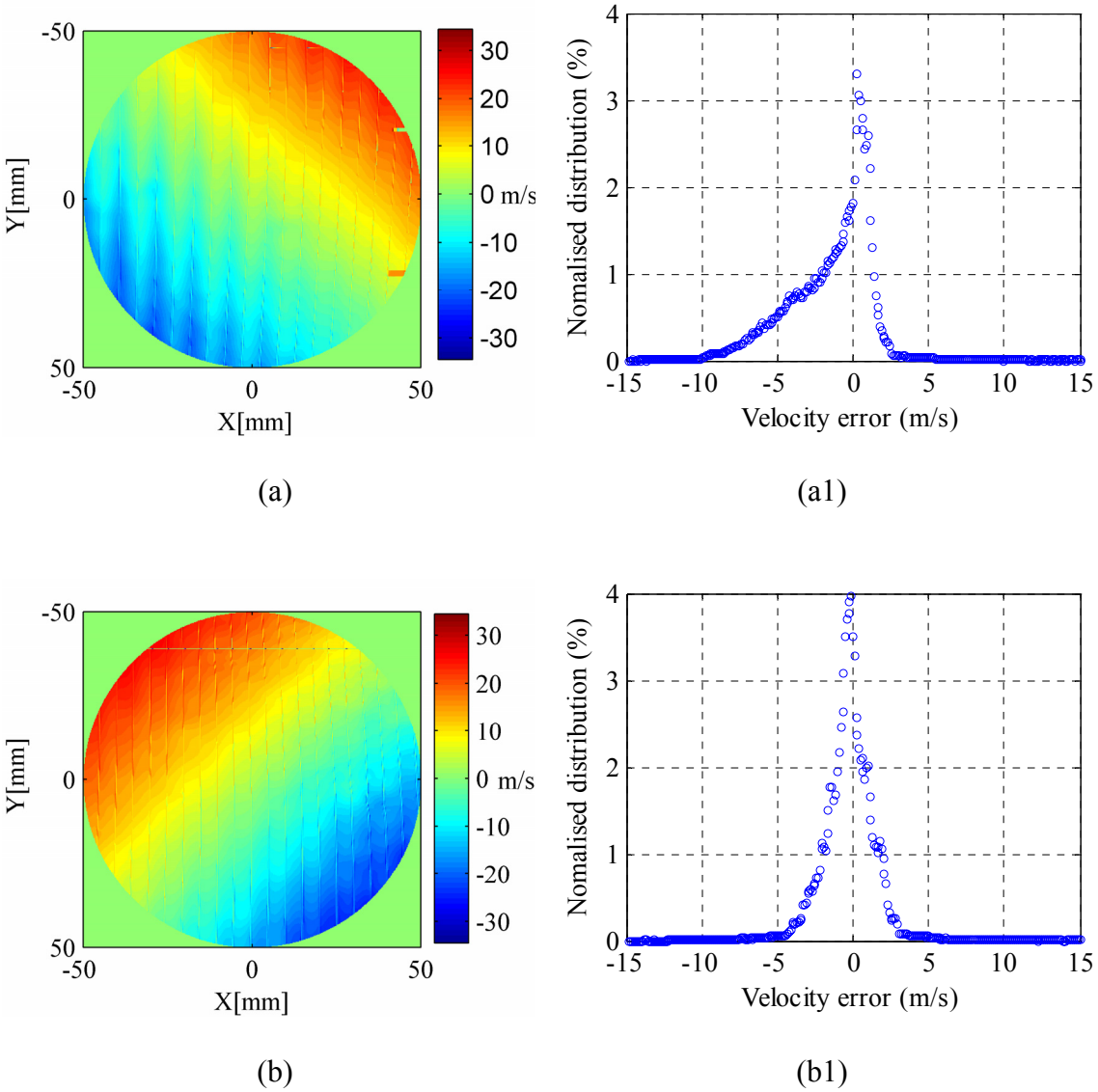

Figure 6-11 Computed measured velocity components using the normal MZI-PDV method: (a) for view 1; (b) for view 2.

(a1) and (b1) Histogram of the error residual that is difference between calculated and theoretical velocity component obtained independently by an optical tachometer for view 1 and view 2 respectively.

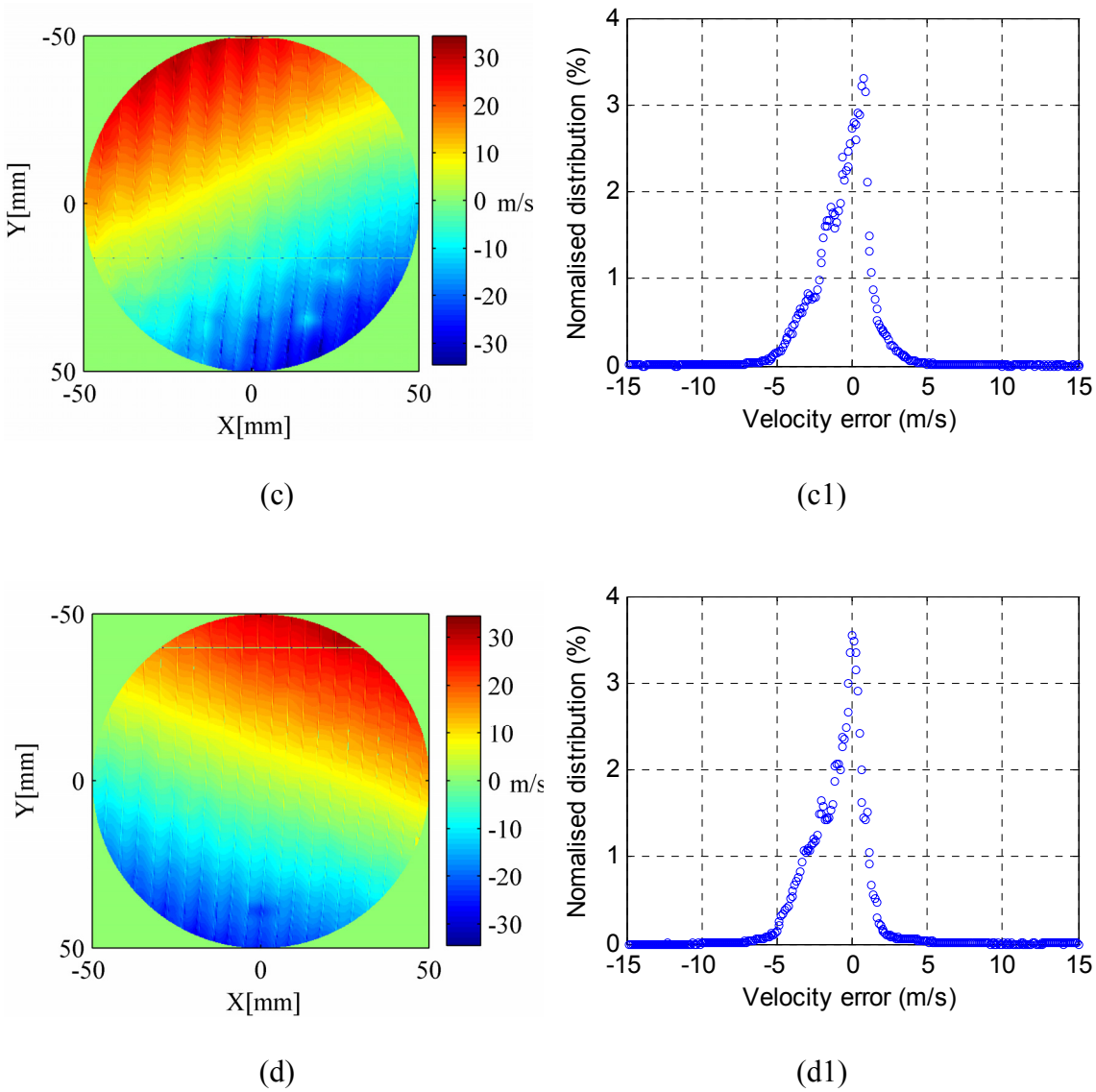

Figure 6-11 Computed measured velocity components using the normal MZI-PDV method: (c) for view 3; (d) for view 4.

(c1) and (d1) Histogram of the error residual that is difference between calculated and theoretical velocity component obtained independently by an optical tachometer for view 3 and view 4 respectively.

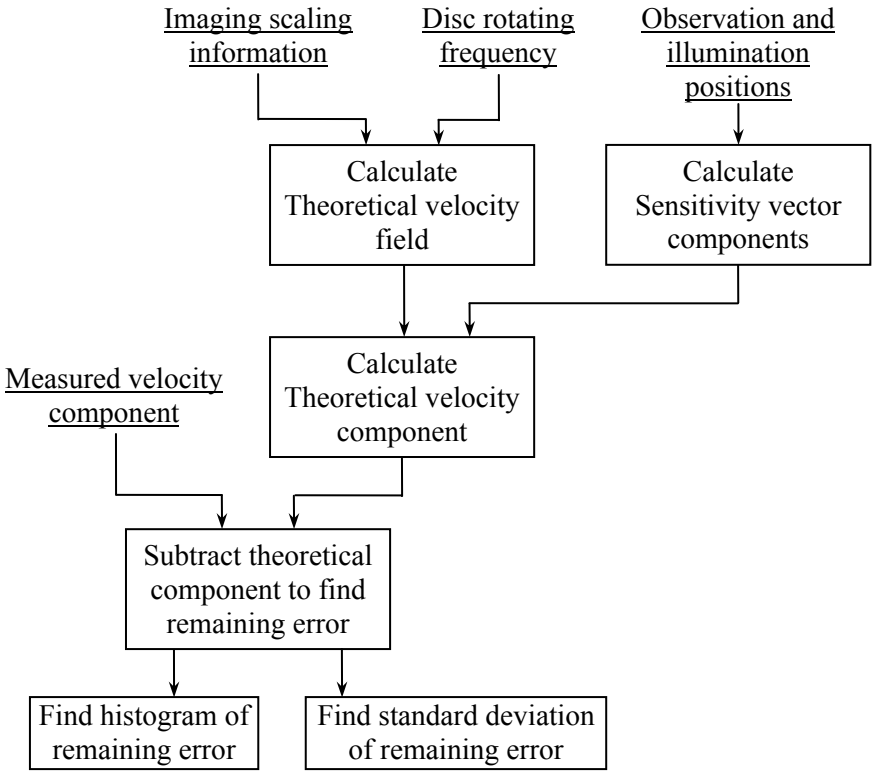

Figure 6-12 Diagram of the process used to calculate the error in experimental measurements on a rotating disc for a measured velocity component.

The measured velocity components are then converted to orthogonal velocity components U, V and W (the horizontal, vertical and out-of-plane components respectively). Figure 6-13, Figure 6-14 and Figure 6-15 show a comparison between the 3C and 4C methods (described in section 6.3.2) for calculating the orthogonal velocity components U, V and W respectively. The calculated orthogonal velocity components show the expected behaviour; horizontal velocity varies linearly across the height of the disc, and vertical velocity across the width. The out-of-plane component is, as would be expected, close to zero. The results computed by using the 4C method, shown in part (b), are visibly smoother that those computed by using the 3C method, shown in part (a).

The computed orthogonal velocity components were compared with the theoretical orthogonal velocity components for the rotating disc. The histograms of the remaining error in each component were plotted and these are shown as part (c) in Figure 6-13 to Figure 6-15. It can be seen clearly that calculating the orthogonal components using the 4C method makes an improvement of ~20% in the level of error. The standard deviations of the error were calculated and are shown in Table 6-3. Values agree well with those calculated from the optical tachometer measurement. The velocity standard deviation is about $\pm 3 ms^{-1}$ for the 4C method.

Table 6-3 Standard deviations of the variations between the calculated and theoretical orthogonal velocity components for the rotating disc.

Standard deviations	U	V	W
3C method	4.3 ms^{-1}	2.9 ms^{-1}	5.2 ms^{-1}
4C method	3.2 ms^{-1}	2.3 ms^{-1}	4.3 ms^{-1}
% difference between them	25%	20%	17%

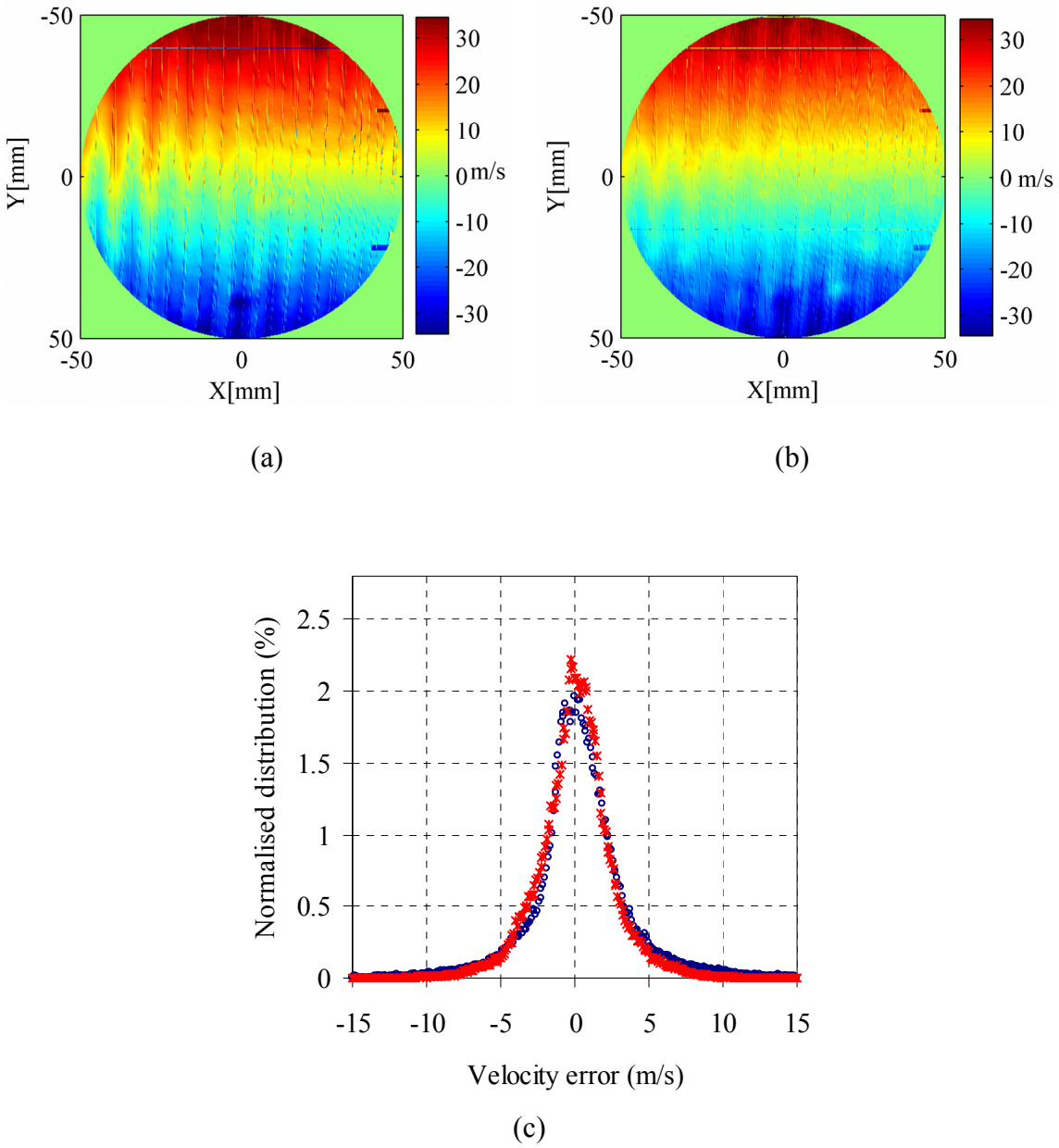

Figure 6-13 Computed U (horizontal) velocity components using different methods to convert measured components to an orthogonal co-ordinate system:

(a) 3C method; (b) 4C method. (c) Histogram of the error residual that is difference between calculated and theoretical velocity component obtained independently by an optical tachometer.

○ : 3C method

*** : 4C method.**

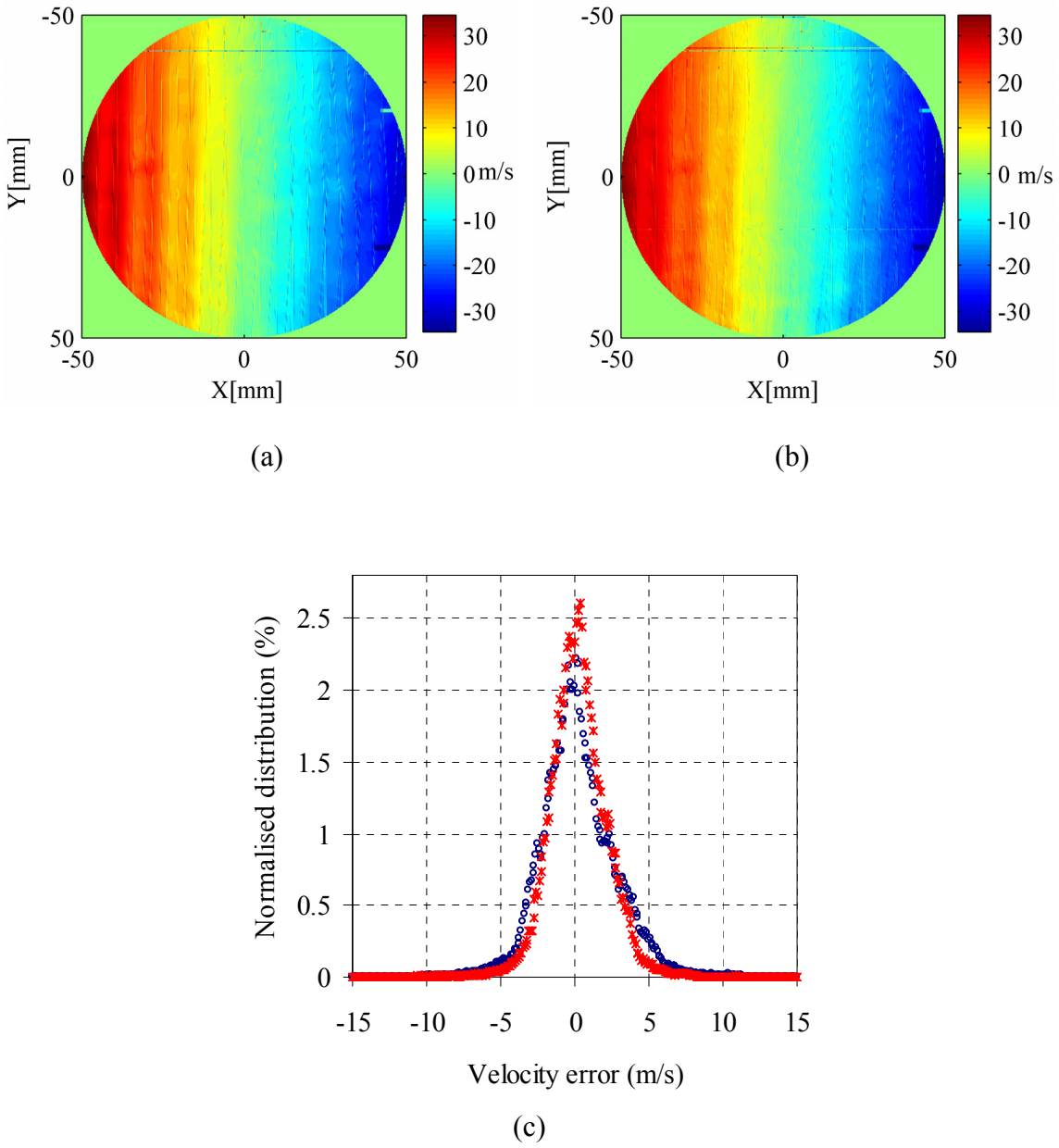

Figure 6-14 Computed V (vertical) velocity components using different methods to convert measured components to an orthogonal co-ordinate system:

(a) 3C method; (b) 4C method. (c) Histogram of the error residual that is difference between calculated and theoretical velocity component obtained independently by an optical tachometer.

○ : 3C method

*** : 4C method.**

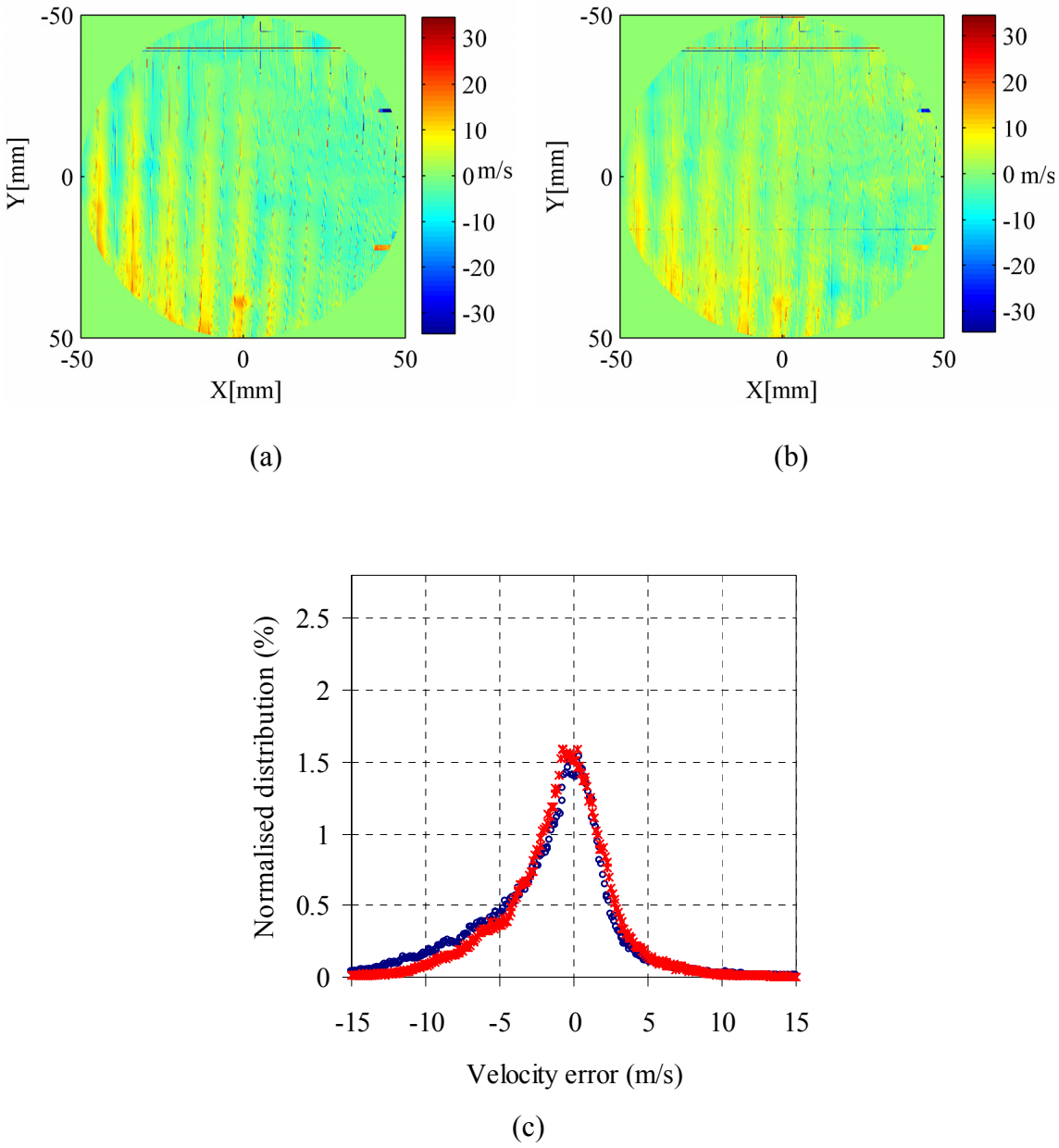

Figure 6-15 Computed W (out-of-plane) velocity components using different methods to convert measured components to an orthogonal co-ordinate system:

(a) 3C method; (b) 4C method. (c) Histogram of the error residual that is difference between calculated and theoretical velocity component obtained independently by an optical tachometer.

○ : 3C method

*** : 4C method.**

6.5 3-component velocity measurements on a seeded air jet

The system was then used to make measurements on a seeded air jet, with a 20mm diameter smooth contraction nozzle. The exit velocity of the jet was ~85ms^{-1}, which was calculated by measuring the nozzle pressure ratio in previous work [18].

The air intake to the jet, and the surrounding co-flow, were seeded using a Concept Engineering Vicount compact smoke generator operating at 37˚C with Nitrogen as the propellant gas. Dense and dry smoke particles in the 0.2-0.3μm diameter were produced by fine tuning of the generator. The observation directions were selected to be in the strong forward scattering so as to ensure sufficient signal on the CCD cameras.

6.5.1 Experimental arrangement

A symmetric experimental arrangement was used to make measurements on this air jet. The jet was positioned by using a stable support trestle with the main flow direction in the positive Y direction. The laser light sheet penetrated vertically through the flow field in the X-Y plane. The four imaging camera lenses at the arm ends of the fibre bundle were located symmetrically along the laser sheet in the Y-Z plane. This is shown in Figure 6-16 and the illumination and observation unit vectors for each view are given in Table 6-4. This arrangement was made in an attempt to optimise the positioning of the views, and make the collected intensities in the four views relatively balanced.

In addition, the performance of a three-component PDV system is influenced by the geometry of the experimental configuration, including the direction of the laser sheet and the choice of viewing angles. Errors can be introduced in the individual measured velocity components and the computed orthogonal velocity components. This was discussed in detail by Charrett *et al* [15].

Table 6-4 Illumination and observation unit vectors used for 3-component measurements on an axis-symmetric air jet.

	Unit vectors	View location (cm)
Laser	[1, 0, 0]	-
View 1	[0.208, -0.551, 0.808]	[17, -45, 66]
View 2	[0.105, 0.605, 0.789]	[8, 46, 60]
View 3	[0.106, 0.597, -0.795]	[8, 45, -60]
View 4	[0.208, -0.551, -0.808]	[17, -45, -66]

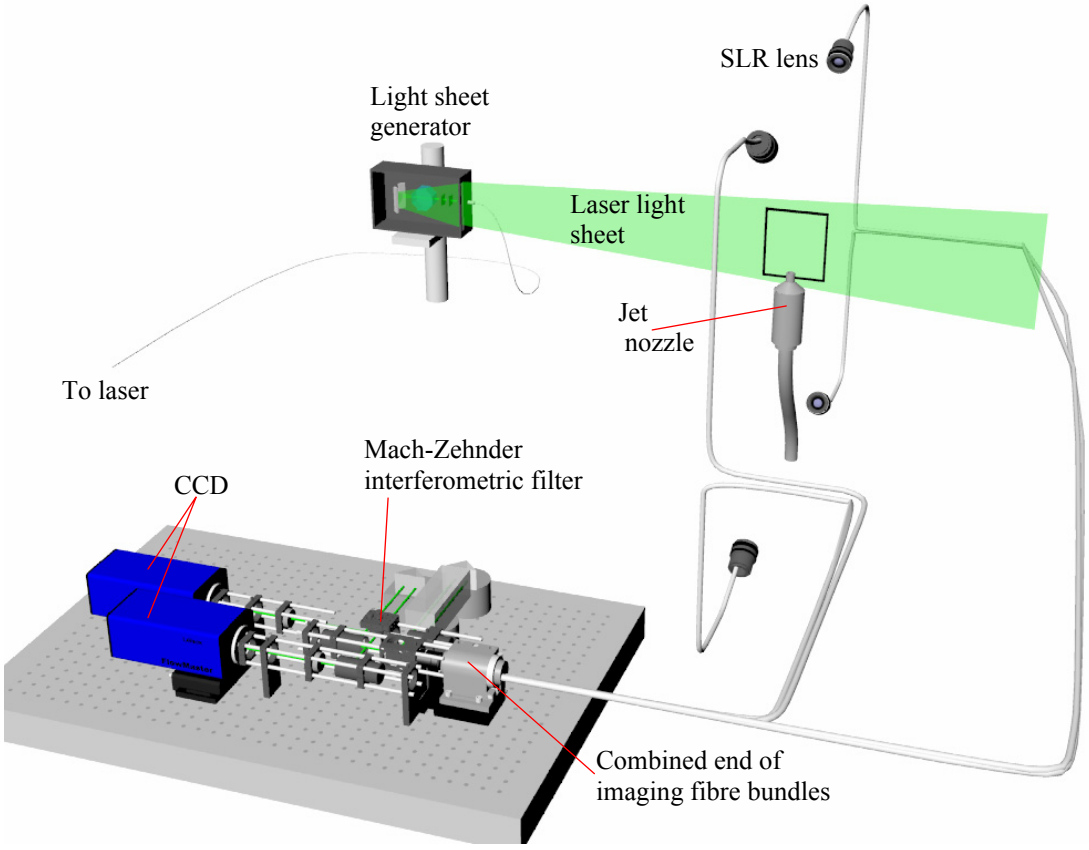

Figure 6-16 Diagram showing the experimental arrangement used for 3-component measurements made on an axis-symmetric air jet.

6.5.2 Results

When making single velocity component measurements on the seeded air jet (chapter 5) a smooth plate was positioned in the field of view and illuminated by the laser sheet to provide the 'flow-off' phase measurement. However, this did not work in 3-component measurements since both sides of the light sheet were viewed for better measurement performance in the comparison to theoretical velocity components. Instead, the seeded air jet flow was used to obtain the reference image (zero-velocity phase image) with the jet flow as slow as possible. This initial seeded flow field is still termed the 'flow off' field for convenience in the following text. The advantage in the method is that this will make the measurement plane defined by the laser sheet exactly the same for the reference image and the flow field image. However, a relative measurement error will be introduced that was estimated to be smaller than $1ms^{-1}$.

A raw photograph of the seeded air jet flow is shown in Figure 6-17 taken by a Canon digital camera. Two pairs of images were captured with the jet off and on, and are shown in Figure 6-18. The measured area was approximately 50×50mm and a camera exposure time of 10 seconds was used to obtain clear images.

These images were then processed using the normalised intensity processing method. Figure 6-19 shows the positions of the dark fringes in the four split sub-images taken by CCD1 for the jet flow off and on. Here the shift in the fringe locations can be seen

clearly. Similar images can be obtained using the second CCD with the dark fringes located between those found from CCD1, as shown in Figure 6-20.

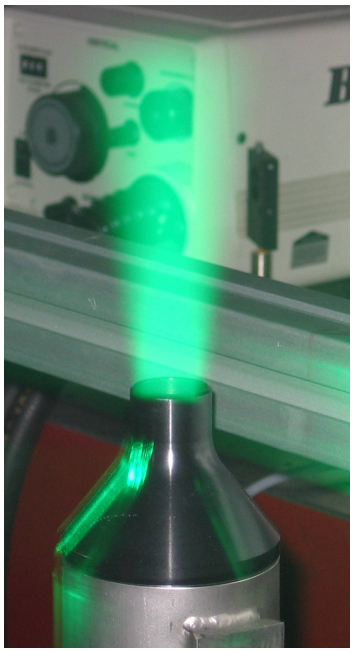

Figure 6-17 A photograph of the seeded air jet flow taken by a Canon digital camera.

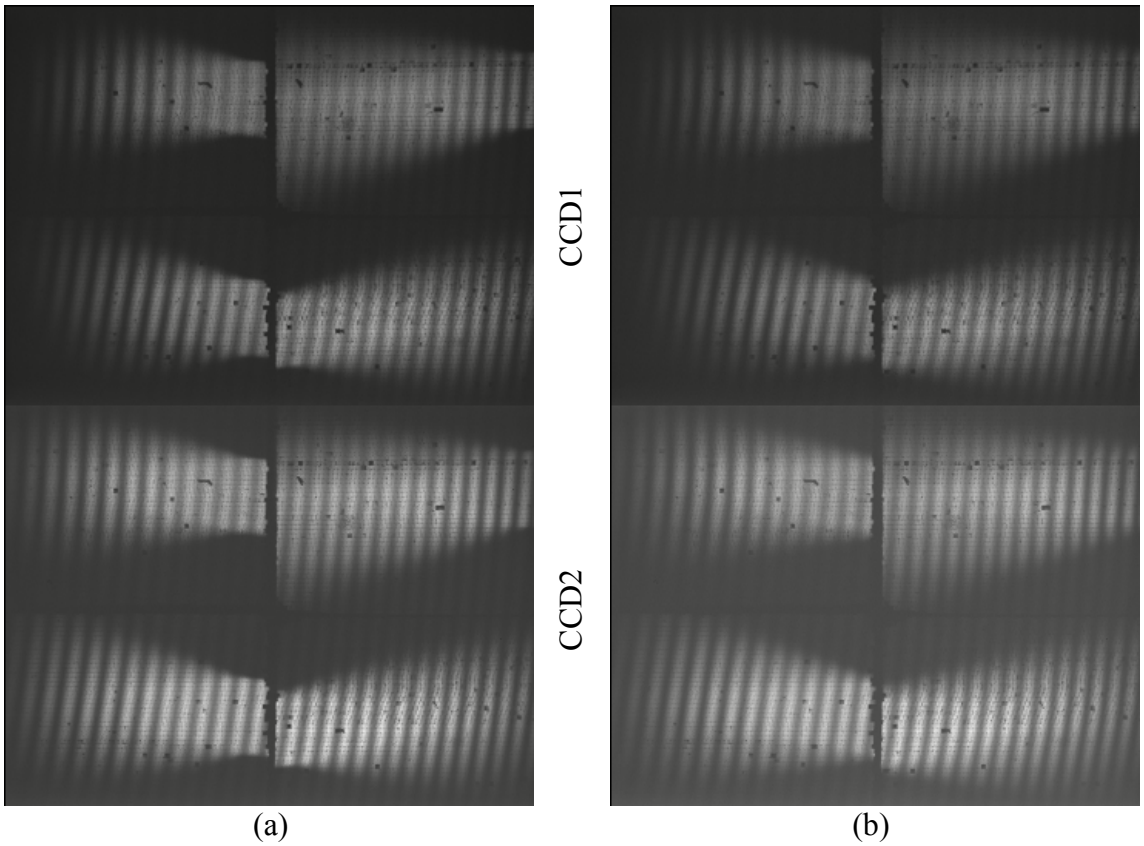

Figure 6-18 Two pairs of fringe images recorded by CCD1 (top) and CCD2 (bottom): for the jet flow off (a) and on (b) in the 3-component MZI-PDV system.

The computed velocity components (non-orthogonal) for the four observation directions are shown in Figure 6-21(a)-(d) after five applications of a 9×9 smoothing filter. The calculated velocity components are then converted to the orthogonal velocity components U, V and W, standing for the horizontal, vertical and out-of-plane components. Figure 6-22 and Figure 6-23 show the computed orthogonal velocity components U, V and W using the 3C and 4C methods respectively as described in section 6.3.2. These components show the expected behaviour in this experimental arrangement; horizontal velocity (U) is, as would be expected, close to zero, and vertical velocity varies along the air jet flow direction. The out-of-plane component (W) is close to zero.

The 'striping' effect in the images in Figure 6-21 to Figure 6-23 results from the image processing method used to calculate the velocity. Close to maxima and minima, the velocity sensitivity is lower than at the quadrature positions. Also, small deviations from a cosinusoidal form, resulting from smoothing, are largest close to maxima/minima, and can result in slight velocity errors.

Figure 6-24 shows a comparison between profiles, taken through the centre of the air jet at x/d = 1, 1.5, 2, 2.5 and 3 diameters downstream from the nozzle using the MZI-PDV system, and profiles calculated using empirical equations described by Rajaratnam [19], as shown in chapter 5. It can be seen that there is good agreement between them, in terms of the overall profile of the flow. The measured profiles are in better agreement with the theoretical profiles than those measured in single component experiments in chapter 5 on the same air jet. This is due to the improved seeding levels during the 3-component measurements providing higher seed density. The smoke generator was not adjusted to the optimal operation status during the single component measurements providing low seed density.

The measurements towards the outside of the jet flow vary more from the expected values possibly due to worse interference fringe quality in these regions, lower signal levels resulting from the 'vignetting effect' in the infinity-corrected optical system and lower seeding levels in these regions as well. This can be seen clearly in Figure 6-18.

Figure 6-25 shows an example of a measured velocity vector map computed using the 4C method for the field of view made on the air jet flow. Vectors indicate that the magnitude and the direction of the in-plane components of velocity while the colour map indicates the magnitude of the out-of-plane velocity component. Only every 40^{th} column and every 8^{th} point on each row are shown in this figure. Again it can be seen that the velocity field shown in Figure 6-25 is typical of what can be expected in the near field of the jet, a 'top-hat' velocity profile at the nozzle exit. This is similar to the velocity field measured on the same air jet by Charrett *et al* [20].

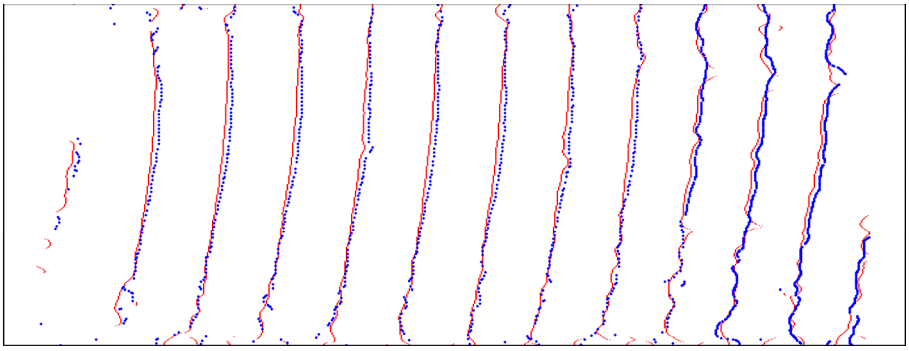

(a)

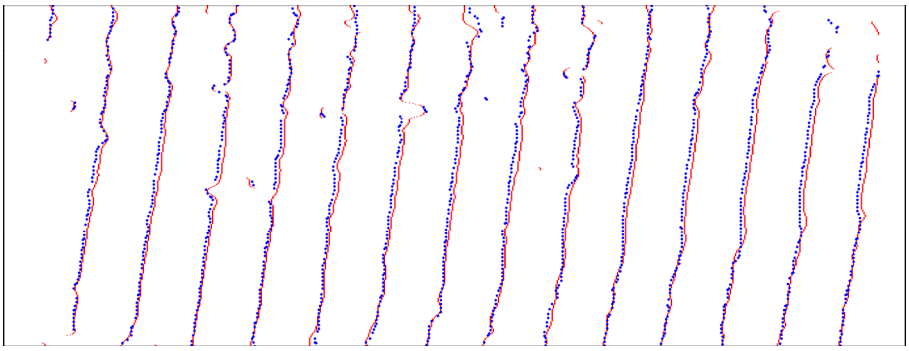

(b)

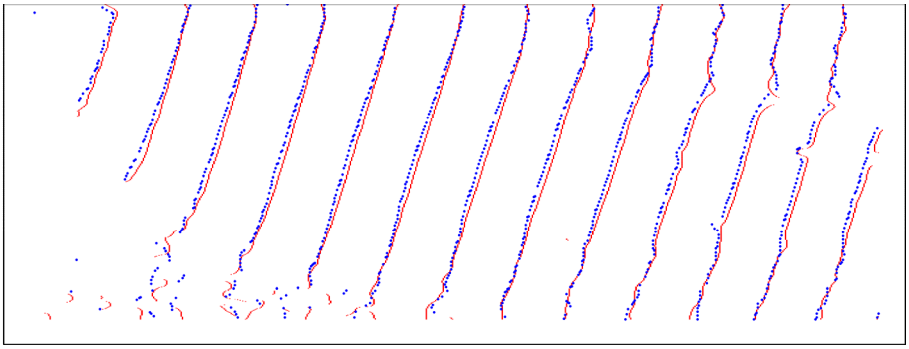

(c)

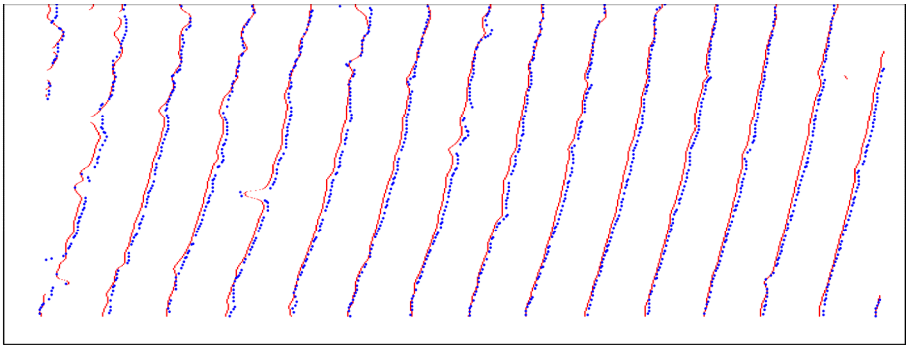

(d)

Figure 6-19 Dark fringes in images taken by CCD1. Red (solid lines): flow off; blue (dashed lines): flow on. (a): for view 1; (b): for view 2; (c): for view 3; (d): for view 4.

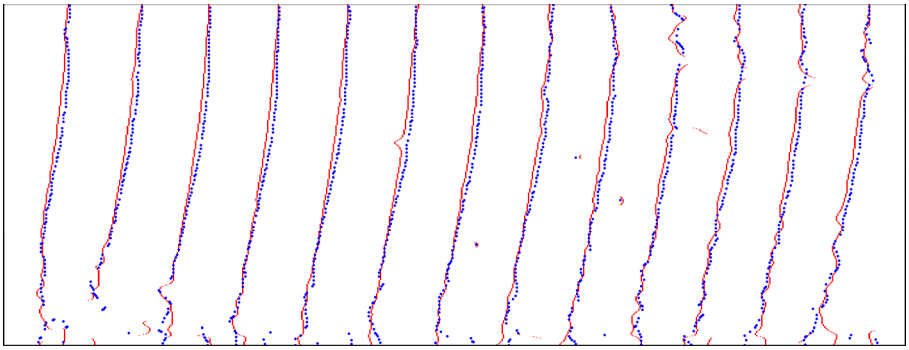

(a)

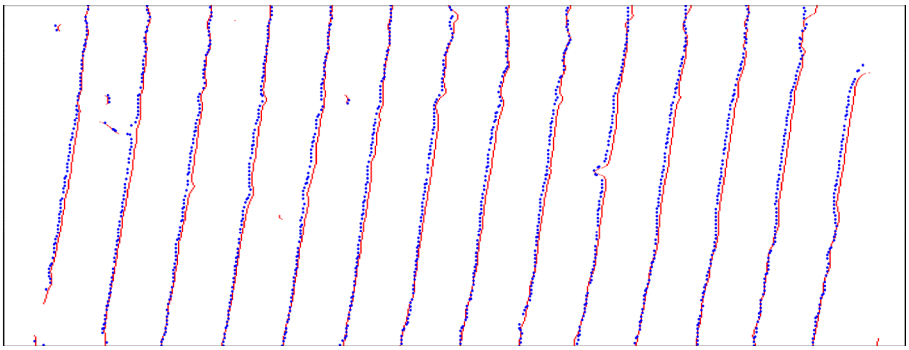

(b)

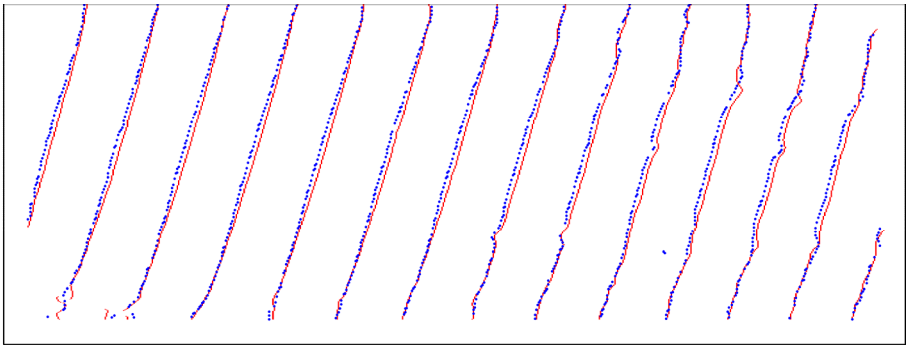

(c)

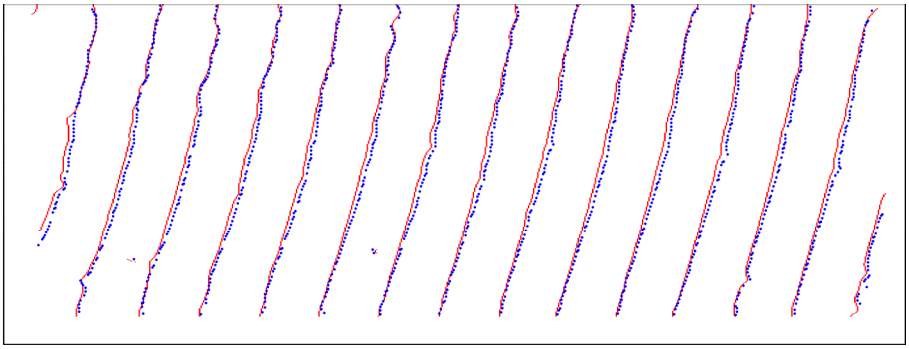

(d)

Figure 6-20 Dark fringes in images taken by CCD2. Red (solid lines): flow off; blue (dashed lines): flow on. (a): for view 1; (b): for view 2; (c): for view 3; (d): for view 4.

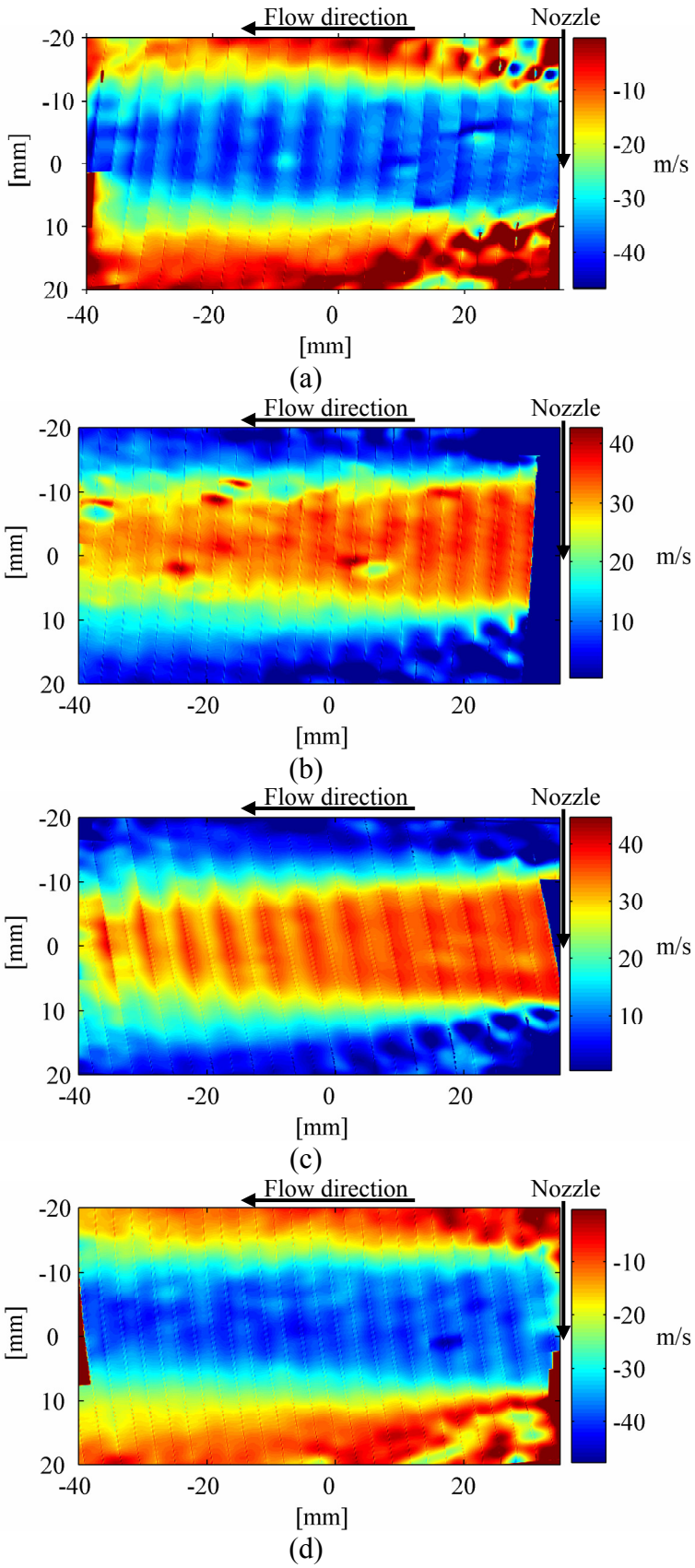

Figure 6-21 Computed measured velocity components using the MZI-PDV system. (a) For view 1; (b): for view 2; (c): for view 3; (d): for view 4.

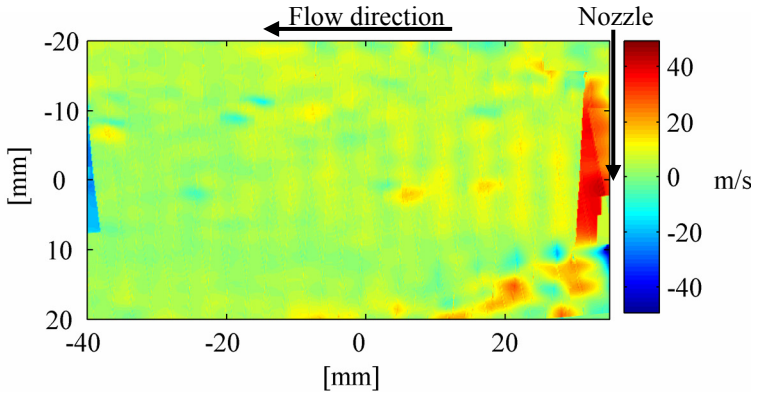

(a)

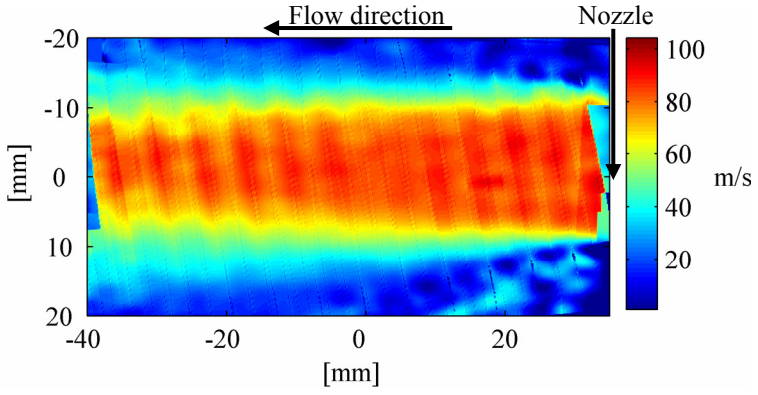

(b)

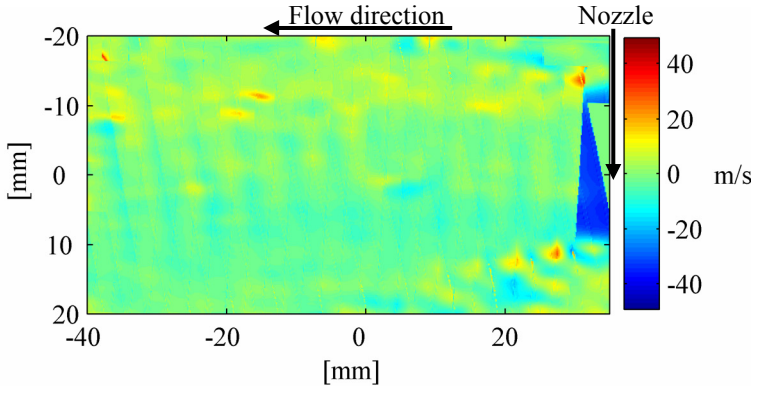

(c)

Figure 6-22 Computed orthogonal velocity components using 3C method to convert measured components to an orthogonal co-ordinate system. (a): U (horizontal); (b): V (vertical); (c): W (out-of-plane).

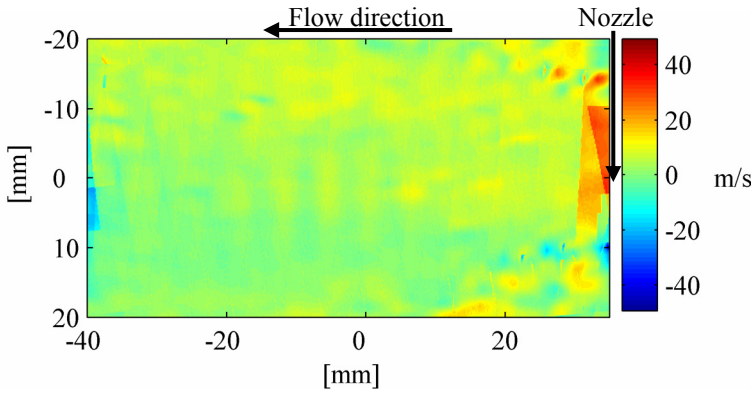

(a)

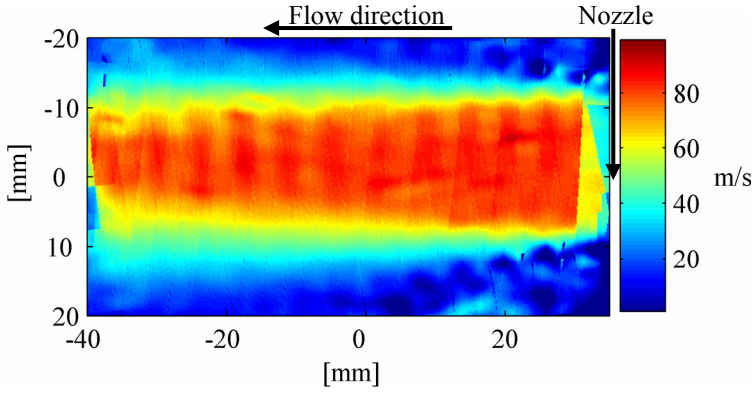

(b)

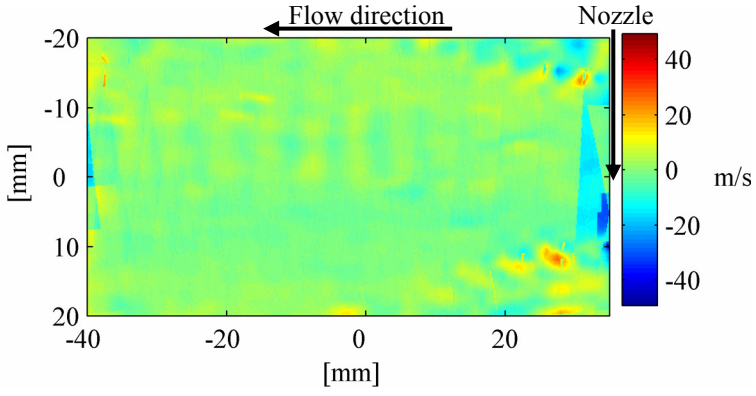

(c)

Figure 6-23 Computed orthogonal velocity components using 4C method to convert measured components to an orthogonal co-ordinate system. (a): U (horizontal); (b): V (vertical); (c): W (out-of-plane).

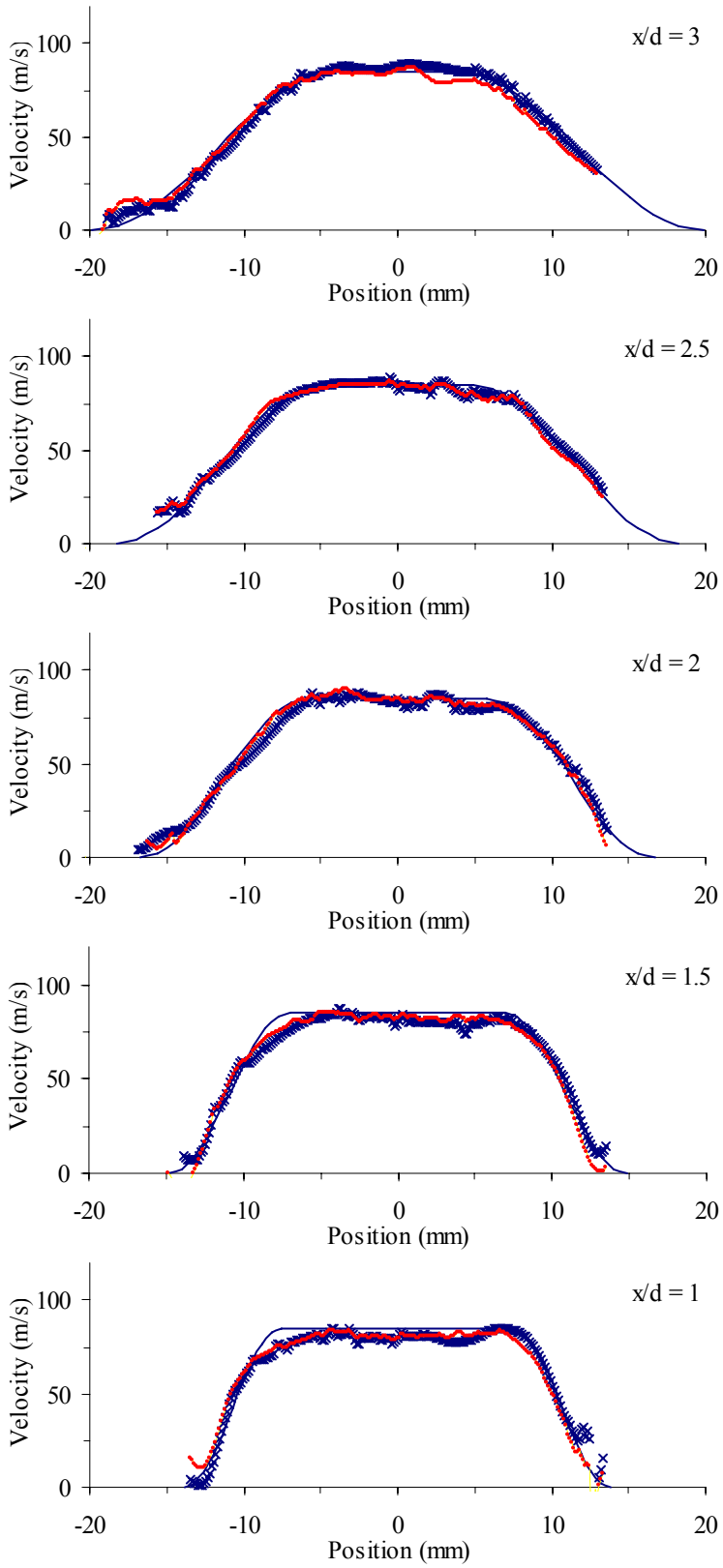

Figure 6-24 A comparison between computed velocity profiles, taken thorough the centre of the air jet at x/d = 1, 1.5, 2, 2.5 and 3 diameters downstream from the nozzle using the MZI-PDV system, and profiles calculated using empirical equations described by Rajaratnam [19].
— Theoretical values; × 3C method and ○ 4C method.

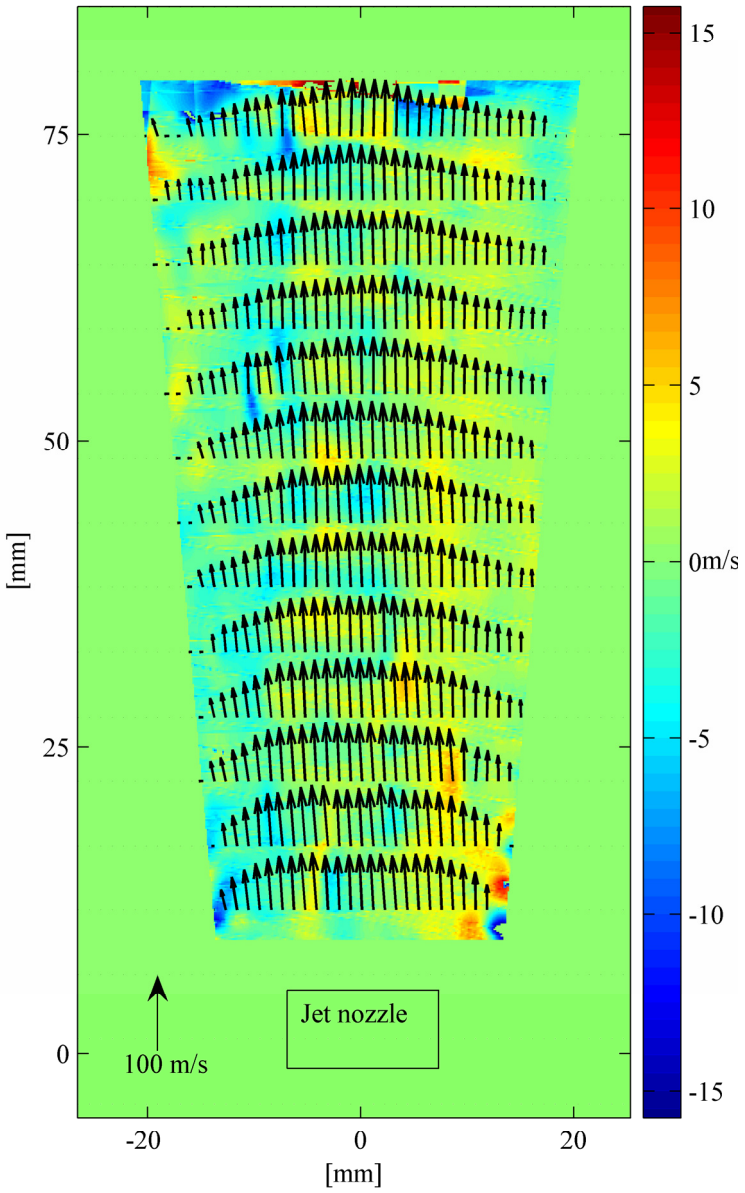

Figure 6-25 Example of a 3-component MZI-PDV measurement made on a seeded air jet. Vectors show the in plane velocities (every 8th and 40th vector show in the horizontal and vertical directions respectively and colour the out-of-plane velocity.

6.6 Summary

A 3-component MZI-PDV system was constructed by modifying the single velocity component MZI-PDV system (described in chapter 5) to allow 3-component measurements. This was realised by replacing the camera lens by an imaging fibre bundle with multiple channels, and at each bundle channel end matched camera lenses were located to image the field of view. The output of the combined end of these channels was used as the input to the MZI. This allows 3-component velocity measurements using only a singe imaging head.

The rotating disc used in validating the single component MZI-PDV system was again used to validate the 3-component MZI-PDV system. The calculated orthogonal velocity components show the expected behaviour; horizontal velocity varies linearly across the height of the disc, and vertical velocity across the width. The out-of-plane component is, as would be expected, close to zero. Values agree well with those calculated from the optical tachometer measurement. The standard deviation of the velocity error is about $\pm 3 ms^{-1}$ for a maximum velocity of $\sim 30 ms^{-1}$ in the field of view when comparing these velocities with the theoretical ones calculated from the optical tachometer measurement. It has been found that using the 4C method results in an improvement of ~20% in the level of measurement error over the 3C method when converting the measured non-orthogonal components to orthogonal components.

The system has also been demonstrated by making 3-component velocity measurements on a seeded air jet with a maximum exit velocity of $\sim 85 ms^{-1}$. The computed velocity field is typical of what can be expected in the near field of the jet.

6.7 References

[1] Roehle, I., Willert, C. and Schodl, R. (1998), "Recent applications of three-dimensional Doppler global velocimetry in turbo-machinery", *9th International Symposium on Applications of Laser Techniques to Fluid Mechanics,* Lisbon, Portugal, Paper 34-2.

[2] Samimy, M. and Wernet, M.P. (2000), "Review of planar multiple-component velocimetry in high-speed flows", *AIAA Journal,* Vol. 38, No. 4, pp. 553-74.

[3] Roehle, I. (1996), "Three-dimensional Doppler Global Velocimetry in the flow of a fuel spray nozzle and in the wake region of a car", *Flow Measurement and Instrumentation,* Vol. 7, No. 3-4, pp. 287-94.

[4] Meyers, J.F. (1995), "Development of Doppler global velocimetry as a flow diagnostics tool", *Measurement Science & Technology,* Vol. 6, No. 6, pp. 769-83.

[5] Clancy, P.S. and Samimy, M. (1999), "Planar Doppler velocimetry: 3-component velocimetry in supersonic jets", *AIAA Journal,* Vol. 37, No. 6, pp. 700-7.

[6] James, F.M. (1996), "Evolution of Doppler Global Velocimetry Data Processing", *8th International Symposium on Applications of Laser Techniques to Fluid Mechanics,* Lisbon, Portugal, NASA-96.

[7] McKenzie, R.L. (1996), "Measurement capabilities of planar Doppler velocimetry using pulsed lasers", *Applied Optics,* Vol. 35, No. 6, pp. 948-64.

[8] Arnette, S.A. , Elliott, G.S., Mosedale, A.D. and Carter, C.D. (2000), "Two-color planar Doppler velocimetry", *AIAA Journal,* Vol. 38, No. 11, pp. 2001-6.

[9] Nobes, D.S., Ford, H.D. and Tatam, R.P. (2004), "Instantaneous, three-component planar Doppler velocimetry using imaging fibre bundles", *Experiments in Fluids,* Vol. 36, No. 1, pp. 3-10.

[10] Charrett, T.O.H., Ford, H.D. and Tatam, R.P. (2005), "Single camera three component planar velocity measurements, using two frequency Planar Doppler Velocimetry (2*v*-PDV)", *Optical Diagnostics, International Society for Optical Engineering*, San Diego, CA, Vol. 5880, Paper 1-10.

[11] Schott, website (2007), http://www.schott.com.

[12] Nobes, D.S., Ford, H.D. and Tatam, R.P. (2001), "Instantaneous, two camera, three dimensional planar Doppler velocimetry using imaging fiber bundles", *Optical Diagnostics for Fluids, Solids, and Combustion, Proc. SPIE*, San Diego, CA, Vol. 4448, pp. 283-94.

[13] Nobes, D.S., Wieneke, B. and Tatam, R.P. (2004), "Determination of view vectors from image warping mapping functions", *Optical Engineering,* Vol. 43, No. 2, pp. 407-14.

[14] Reinath, M.S. (1997), "Doppler global velocimeter development for the large wind tunnels at Ames Research Center", *NASA,* Moffett Field, California, Technical Memorandum 112210.

[15] Charrett, T.O.H., Nobes, D.S. and Tatam, R.P. (2007), "Investigation into the selection of viewing configurations for three-component planar Doppler velocimetry measurements", *Applied Optics,* Vol. 46, No. 19, pp. 4102-16.

[16] Charrett, T. O. H. (2006), "Development of two-frequency planar Doppler velocimetry instrumentation", *PhD thesis,* Cranfield University, Cranfield, UK.

[17] FlexLink, website (2007), http://www.flexlink.com.

[18] Charrett, T.O.H., Ford, H.D., Nobes, D.S. and Tatam, R.P. (2004), "Two-frequency planar Doppler velocimetry (2*v*-PDV)", *Review of Scientific Instruments,* Vol. 75, No. 11, pp. 4487-96.

[19] Rajaratnam, N. (1976), "Turbulent jets", Elsevier, Amsterdam, Netherlands.

[20] Charrett, T.O.H., Ford, H.D. and Tatam, R.P. (2006), "Single camera 3D planar Doppler velocity measurements, using two frequency Planar Doppler Velocimetry (2*v*-PDV) and imaging fibre bundles", *44th AIAA Aerospace Sciences Meeting and Exhibit,* Reno, NV, AIAA 2006-47.

7 Conclusion and future work

7.1 Introduction

In this thesis a flow velocity measurement technique, Mach-Zehnder inteferometric filter based planar Doppler velocimetry (MZI-PDV), has been developed. The uncertainties associated with the technique have been investigated. The summary and the conclusion of the work are presented in the following sections. The final section gives the possible directions for further work.

7.2 Conclusions – Mach-Zehnder inteferometric filter based planar Doppler velocimetry (MZI-PDV)

In this work, an unbalanced Mach-Zehnder interferometer with a glass compensator block was used as a frequency-to-intensity converter for PDV to replace the iodine cell currently used. As an entirely new optical system, the use of an MZI provides several potential advantages compared to conventional molecular filters:

(1) The transfer function is well defined and constant over time, having the usual sinusoidal dependence on frequency of the interferometer.
(2) The path length imbalance of the interferometer can be selected by using different lengths of the glass block to correspond to the expected measurement range of velocities in a given flow situation.
(3) The illumination wavelength is no longer restricted to particular values. Any continuous wave or pulsed laser of sufficient power and narrow linewidth may be used to form the light sheet.

However, a disadvantage over molecular filters is that more high quality optical components are required (discussed in chapter 4). In addition, the inteferometric filter phase is sensitive to temperature variations and small mechanical vibrations because the components used to build the filter are discrete in free space. Some measures are therefore required to prevent the filter phase drift.

The use of an MZI also has advantages over the Michelson interferometer previously used for PDV [1]:

(1) No auxiliary optical component is required to allow the scattered light intensity to be normalised since an MZI provides normalised intensity automatically based on its two complementary outputs.
(2) The visibility of the transfer function (normalised intensity against frequency) is twice as large as for a Michelson interferometer under the same conditions, improving both the potential measurement accuracy and resolution.

However, the instrument based on a Michelson interferometer is more compact than an MZI, which helps reduce the sensitivity to environmental perturbations such as temperature variations and mechanical vibrations. However, the dominant

environmental disturbance in the developed MZI was the cooling fan of the CCD cameras used.

Two techniques can be used to process the interference fringe images to yield the velocity:

(1) Fringe shift method, described in 5.5.1, where the shift of the interference fringe pattern is used to calculate velocities along a profile.
(2) Normalised intensity method, described in 5.5.2, where the velocity can be evaluated at every point in the image by calculating the normalised intensity.

The first technique results in a discontinuous measurement of the measured velocity field, since the minimum recognizable fringe shifting distance is one pixel in the interference images. The technique therefore can not offer true planar velocity information. The second can provide pixel-by-pixel measurements. A successful marriage of them may be achieved where the fringe shifting processing technique is used for rapid velocity profile measurements, followed by a full-field measurement using the second processing technique since this will require more computation compared to the first technique.

In chapter 5, a single velocity component MZI-PDV system was described. The system was validated by making measurements on a rotating disc. The standard deviation of the measurement error was about 2.9ms^{-1} using the fringe shifting processing method and around 2ms^{-1} using the normalised intensity method, for a velocity range of ~±70ms^{-1}. The system was also demonstrated by making measurements of the flow component at an angle of ~45° from the main flow direction of an axisymmetric air jet with a maximum velocity of about 80ms^{-1}. The measurements show good agreement with the expected velocities calculated using empirical equations to describe the jet.

In chapter 6, a time-averaged 3-component MZI-PDV system was presented. The system measured multiple velocity components using an imaging fibre bundle with multiple channels, and then calculated the orthogonal velocity vectors using three or four observation directions. The rotating disc was again used to validate the system. The calculated orthogonal velocity components show the expected behaviour; horizontal velocity varies linearly across the height of the disc, and vertical velocity across the width. The out-of-plane component is, as would be expected, close to zero. Values agree well with those calculated from measurements obtained by an optical tachometer. The standard deviations of the remaining errors when computed velocities are compared to the theoretical values are ~4.3ms^{-1}, ~2.9ms^{-1} and ~5.2ms^{-1} for U, V and W components respectively when calculated using three observation directions/three measured components (3C method, described in 6.3). When calculated using four measured components (4C method, described in 6.3), an improvement of ~25%, ~20% and ~17% for U, V and W components respectively was obtained, giving standard deviations of ~3.2 ms^{-1}, ~2.3 ms^{-1} and ~4.3ms^{-1}.

The 3-component MZI-PDV system was also used to make measurements of the main flow component of the axis-symmetric air jet. The computed velocity components

showed good agreement with the expected velocities calculated using empirical equations to describe the jet.

The phase locking system designed to lock the MZI filter removed the low frequency component of the interferometer phase drift. This eliminated the effect of the noise from the interferometer phase drift on measurements. However, the operational efficiency depends on the frequency stability of the single frequency-stabilised He-Ne laser since a different light source (argon-ion laser) was used as the flow illumination source. Any frequency drift from this laser will be recorded as an additional Doppler shift, which will directly lead to measurement errors. A more efficient approach would be to use the same laser as the light source for both the flow illumination system and the phase locking system.

7.3 Conclusions – uncertainty analysis of MZI-PDV

In chapters 4 and 7, some uncertainty sources in the MZI-PDV system have been described and analysed. It has been found that the interferometric filter has the advantage of reducing the uncertainty due to polarisation sensitivity of the beam splitters used in the MZI-PDV system, compared to a conventional molecular absorption filter based PDV system. For example, the estimated maximum velocity error of about $\pm 1.5 ms^{-1}$ is caused from ±5% polarisation sensitivity of the two beam splitters used in the MZI-PDV system in this work, while it is $\sim \pm 7 ms^{-1}$ in a conventional PDV system using a beam splitter with a typical ±3% variation in the split ratio for S and P polarised light [2].

The transmittance of the glass block, inserted in the larger arm of the MZI, was found to have little effect on the amplitude of the normalised intensity in the interferometer since it will be larger than 0.8 for most commercially available glass blocks, which will cause a reduction of 0.6% in the amplitude of the normalised intensity in the MZI compared to an ideal transmittance of 1. The effect of the Fabry-Perot interference formed by the two surfaces of the block was also found to be negligible for small reflectances (<5%) in the surfaces.

The contrast of the interference fringes in the MZI was found to oscillate periodically at a frequency of $\sim 3\lambda$ when the flatness is increased in the interferometer and the oscillation amplitude decreases as the flatness increases. The flatness is therefore selected to be as small as possible in order to improve the interference fringe quality. In this work, an estimated flatness of $\sim 0.5\lambda$ leads to a contrast of 0.78 in the interference fringes.

The inclination angle from the optical axis in the imaging system used was found to have little effect on the contrast of the interference fringes since collimated light beams, rather than divergent ones, are used in the interferometer. However, this will lead to non-equidistant fringes in the collected image, which will increase the measurement error in the processing technique based on the fringe shift. Therefore the inclination angle should be made as small as possible. In this work, an inclination angle of $\sim 2.1^{\circ}$ determined by the infinity-corrected optical system was used, leading to an increase of 5% in the fringe space distance at the edge region compared with the centre region of

the measured area. A correction for the variable fringe space distances across the whole image is therefore required when the fringe shift processing method is used.

The optical path deviation, determined by the difference between the effective length of the glass block and the optical path difference within the MZI, was found to have little effect on the contrast of the interference fringes since collimated light beams, rather than divergent ones, are used in the interferometer.

The number of interference fringes in the images was found to affect the frequency sensitivity. Fewer fringes can improve the frequency sensitivity but increase the instrument sensitivity to environmental variations. Also it will lead to measurement errors by neglecting the optical path difference introduced by tilting the prism in one path of the interferometer, although this is relatively small (~<0.001%) in our present arrangement.

The use of filtering of the raw images introduces measurement errors when the image processing method based on the normalised intensity in the MZI, although this can remove the false minima and maxima, which is a key step in this image processing technique used in the MZI-PDV system. Therefore, as few applications of filtering as possible should be used. This requires an even power distribution in the illumination light sheet, high interference fringe visibility and even seeding.

7.4 Future work

7.4.1 Extension of the MZI-PDV technique to instantaneous measurements

The MZI-PDV system developed to date is only capable of making time-averaged velocity measurements of the flow. Using a pulsed laser source, typically a Q-switched frequency-doubled, injection-seeded Nd:YAG laser, it is possible to make instantaneous measurements using the technique since the flow field would be 'frozen' when the pulsed laser light illuminates a flow. A schematic of a proposed pulsed MZI-PDV system is shown in Figure 7-1. Here the output of a Nd:YAG laser beam is expanded to form a light sheet. This illuminates the flow and images are captured using the existing MZI imaging head and the exposure time of the CCD cameras is set to capture a single pulse.

This allows only relative velocity measurements because the MZI can not be locked to the high frequency component of the phase drift in the current phase locking system described in chapter 5. Generally the pulse width of the pulsed laser used to illuminate the flow is in the order of nanoseconds, typically 150ns. This problem will be discussed in section 7.4.2. This proposed system could be easily expanded to make 3-component measurements using the imaging fibre bundle described in chapter 6 using the existing MZI imaging head. A potential advantage in this 3-component technique is that the MZI phase drift and the pulse-to-pulse frequency instability of the laser could be eliminated/reduced by monitoring the interference pattern simultaneously using the fourth channel of the imaging fibre bundle to view a motionless screen illuminated by a small portion of each pulse as done by Nobes *et al* [3] for conventional PDV.

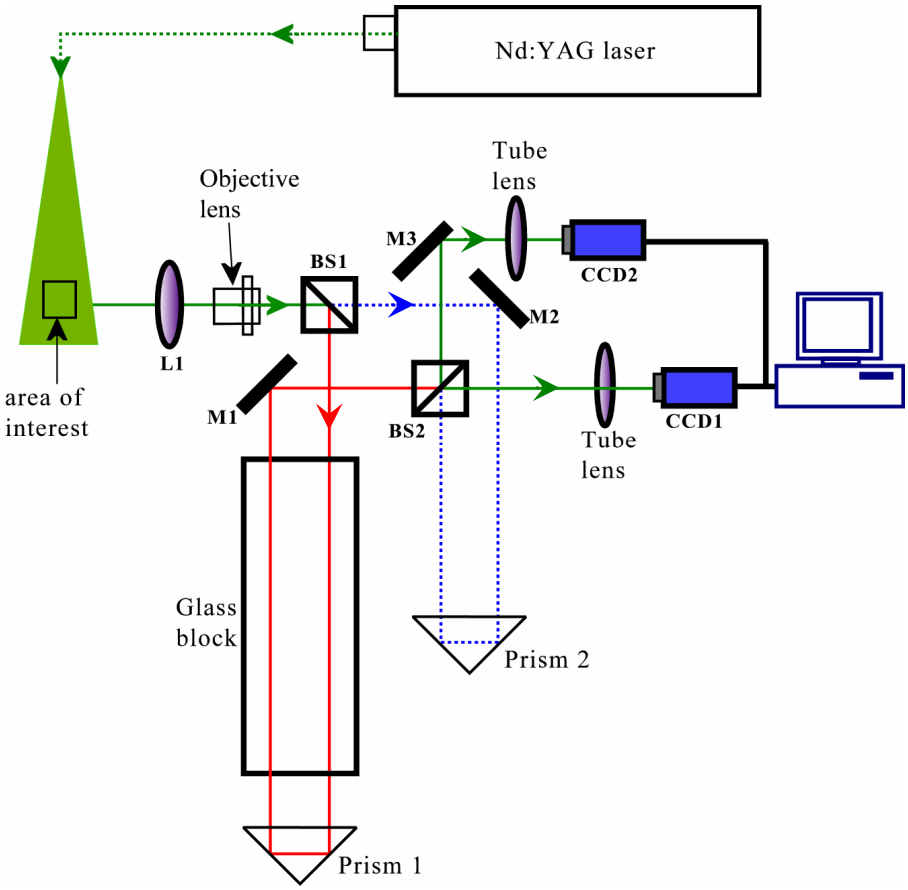

Figure 7-1 Schematic of the proposed pulsed MZI-PDV system. L1: camera lens; BS1, 2: 'non-polarising' beam splitters; M1, 2, 3: mirrors. Beam path for the Nd: YAG laser shown as solid line (green), beam paths for the two arms of the interferometer shown as a solid line (red) and a dotted line (blue) respectively.

7.4.2 Potential improvements to the phase locking system

One main problem in the existing phase locking system is that the operational stability depends mainly on the frequency stability of the single-frequency stabilised He-Ne laser used. Any frequency drift from this laser will be recorded as an additional Doppler shift, which will directly lead to measurement errors. Also the designed operation wavelength is 514.5nm rather than 632.8nm at which the He-Ne laser operates. This further reduces the operating efficiency of the locking system. To overcome this problem, two methods are possible. The first is to use two wavelength lines from the argon ion laser [4-6], for example, green (514.5nm) and blue (488.0nm) lines when the laser operates with an etalon to maintain the narrow linewidth of each line used. The system is shown in Figure 7-2. The green light would illuminate the flow region; the blue laser light would be the light source for the phase locking system. The laser frequency instability will be overcome due to the correlation of the two wavelength lines from the same laser cavity. Two green filters would be used to prevent the blue light beam being recorded by the cameras. The disadvantage of this approach is that the flow illumination power will be reduced.

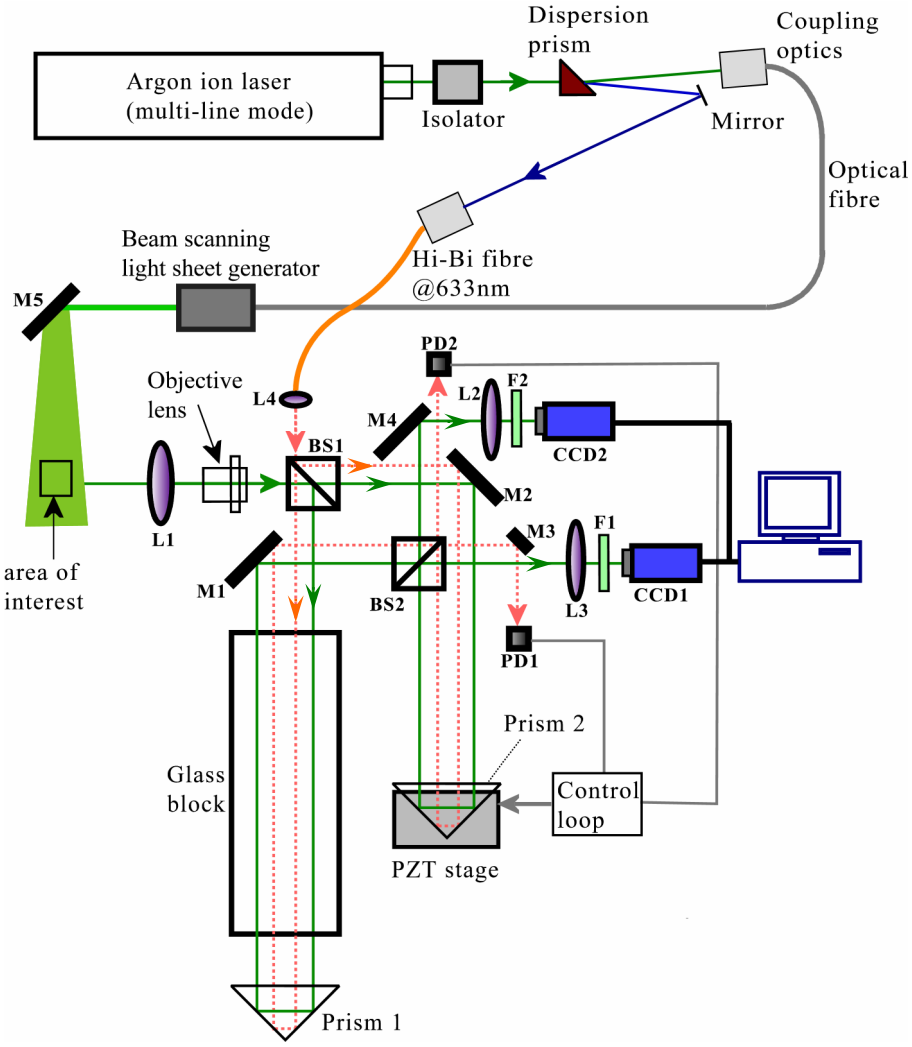

Figure 7-2 Schematic of the proposed MZI-PDV system where the illumination light and the light source for the phase locking system come from the same laser cavity. Beam path for measurement shown as solid line (green), beam path for locking system shown as a dotted line (red).

The second method is to use polarised light beams as shown in Figure 7-3. This idea is similar to the approach taken by Chehura *et al* [7] and Seiler *et al* [8]. The argon ion laser light is divided into two parts by a 'non-polarising' beam splitter BS. The main part is used to illuminate the flow and the other as the light source for the phase locking system described in chapter 5. The scattered light from flow particles is polarised as horizontal linear polarised light by P1 and enters the interferometer and its two complementary interference images (Doppler shifted) are captured by cameras CCD1 and CCD2. The small part of the laser light that is vertically polarised also enters the interferometer and its two interference outputs (un-shifted) are monitored using two photodiodes PD1 and PD2 with the aid of two polarisation beam splitters PBS3 and PBS4. In this approach, a possible problem is the interference between the two polarised beams located at PBS3 and PBS4, also termed 'polarisation cross-talk'. Another problem is that only one polarisation state of the scattered light from a flow is collected, leading to the reduction of the collected power.

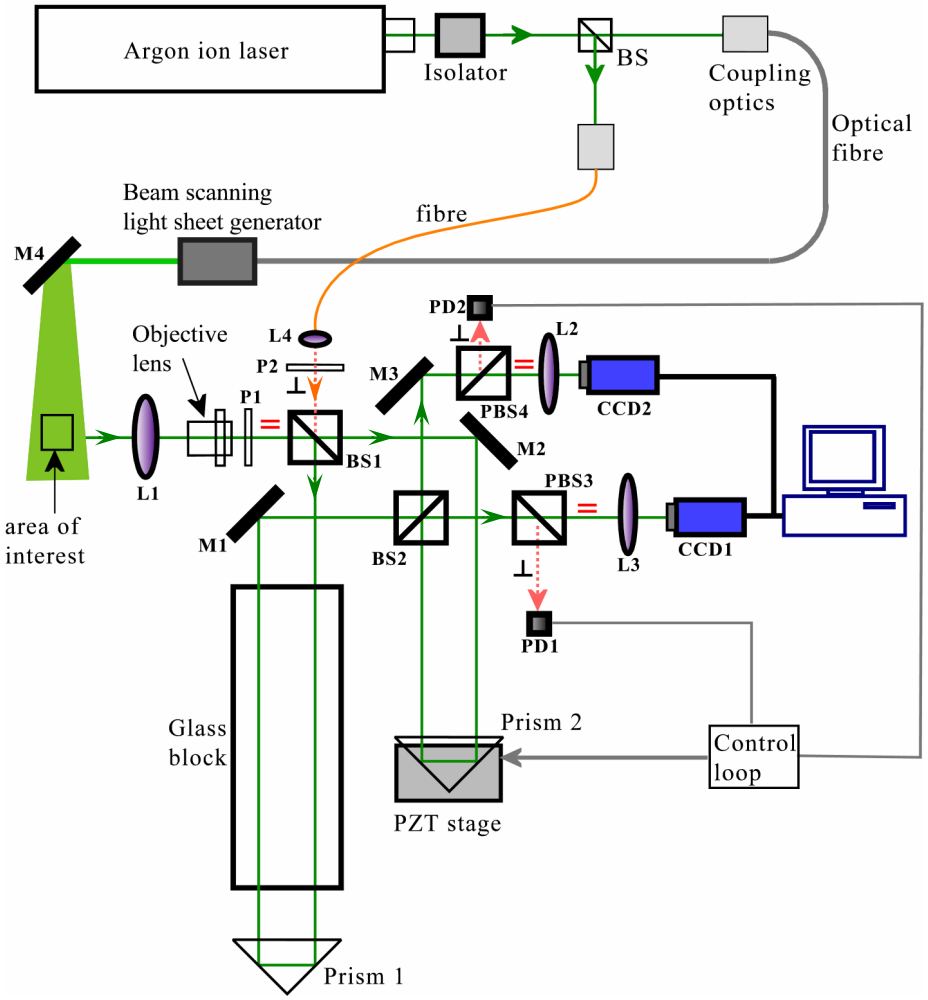

Figure 7-3 Schematic of the proposed MZI-PDV system where the polarised laser beams are used. BS, BS1, BS2: 'non-polarising' beam splitters; PBS3, 4: polarisation beam splitters; P1: linearly polariser (horizontal); P2: linearly polariser (vertical); L1: camera lens; L2, 3: tube lenses; L4: coupling lens. M1, 2, 3: mirrors; PD1, 2: photodiodes. Beam path for measurement shown as solid line (green), beam path for locking system shown as a dotted line (red).

A further modification would be to monitor the laser frequency and the interferometer phase drifts during a measurement by using a third CCD camera (CCD3 in Figure 7-4). This would view a motionless screen illuminated by a small part of the laser light. This would allow the removal of the phase locking system. However, this would only work on the cases where the interferometer phase drift is slow. Fast drifting in the interferometer phase would cause the 'wash-out' effect in the interference fringe pattern and the reference camera is not enough without the locking system.

As shown in chapter 5, the camera's cooling fans caused a large contribution to the interferometer phase drift. Therefore to reduce the AC component of the interferometer phase drift due to the fans vibration, the cameras fans should either be turned off (not advisable when using cooled CCD chips) or isolated from the interferometer components. This could be realised by mounting the fans outside of the camera body or mounting the cameras separate from the interferometer.

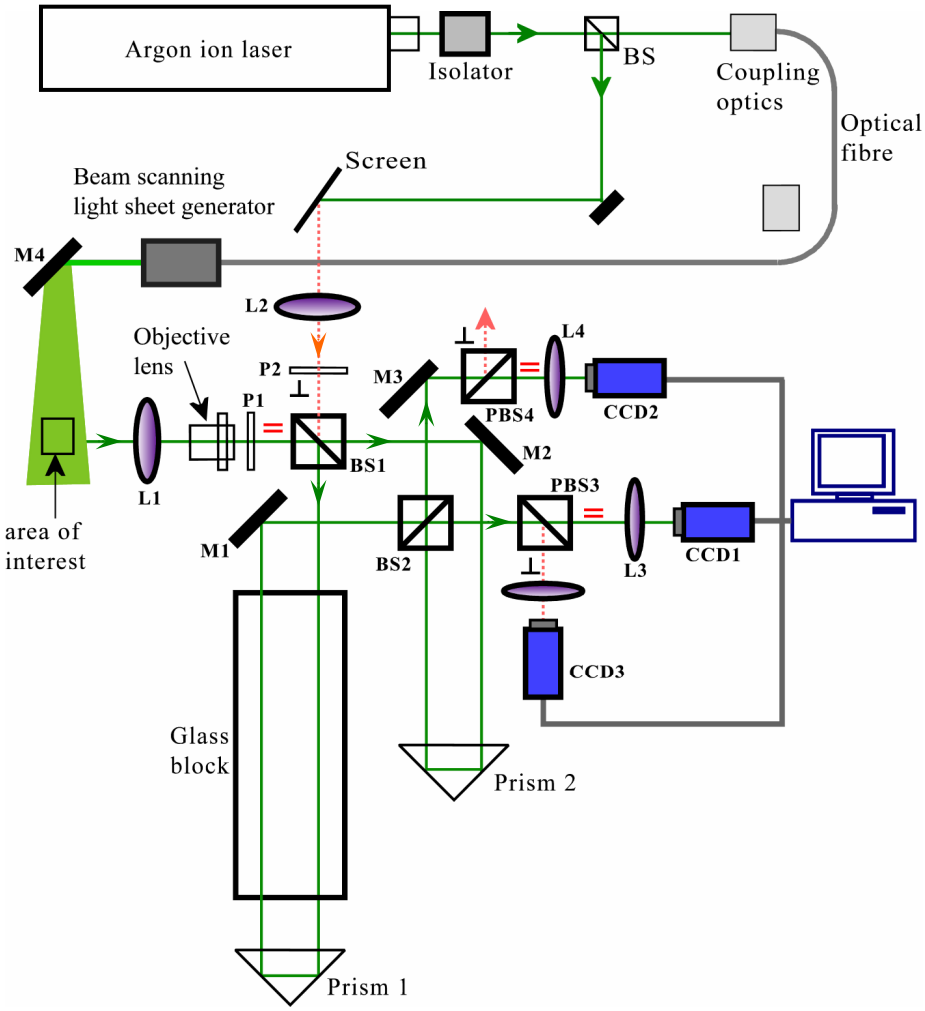

Figure 7-4 Schematic of the proposed MZI-PDV system using three cameras where the polarised laser beams are used. BS, BS1, BS2: 'non-polarising' beam splitters; PBS3, 4: polarisation beam splitters; P1: linearly polariser (horizontal); P2: linearly polariser (vertical); L1: camera lens; L2: coupling lens; L3, 4: tube lenses; M1, 2, 3: mirrors. Beam path for measurement shown as solid line (green), beam path for locking system shown as a dotted line (red).

7.4.3 Potential improvements to the single camera MZI-PDV technique

In the single camera MZI-PDV technique (described in chapter 4.2), the images were shifted by a few pixels in order to map the maxima in the first images (before application of the π phase change) to the minima in the second set of images taken after the phase change for the flow. This shift is necessary to correct for the interferometer phase drift between frames, since the phase locking system can not be operated during the π phase change. This is because the locking system stabilises the phase around the quadrature position at the locking system wavelength. A potential solution to this problem is to use the dispersion of the interferometer to calculate the displacement, Δd, of prism 2 (Figure 7-3) required to keep the locking system locked at quadrature position whilst still providing the necessary phase change at the illumination wavelength. The distance can be found from:

$$\Delta d = \left(m + \frac{1}{2} \right) \cdot \lambda_0 = \frac{n}{2} \cdot \lambda_1 , \qquad m, n = 0,1,2... \qquad \textbf{Equation 7-1}$$

where λ_0 is the flow illumination wavelength (argon ion laser, 514.5nm) and λ_1 is the locking system wavelength (He-Ne laser, 633nm). This indicates that for a certain displacement a ($m \cdot 2\pi + \pi$) phase change at the illumination wavelength can be achieved, while the locking system will still stabilise to a quadrature position after a phase change of $n \cdot 2\pi$ at the locking wavelength.

Figure 7-5 shows the calculated phase change for the displacement. To achieve the equivalent of π phase change at the illumination wavelength (argon ion laser) would require Δd = ~ 24.7, 83.6, 143.1μm …, as shown in Figure 7-5, but the PZT stage currently used has a displacement of ≤20μm, so this is not currently possible. Therefore, a displacement of ~1.3μm could be selected, which corresponds to the condition at m = 2 and n = 4. This would lead to a π phase change for the argon ion laser with an error of ~8%, which could be eliminated by resetting the working point of the locking system, although this would lead to a reduction of the sensitivity in the phase locking system. This is because the locking system would not stabilise to a quadrature position that is at 50% point of the transfer function of the filter.

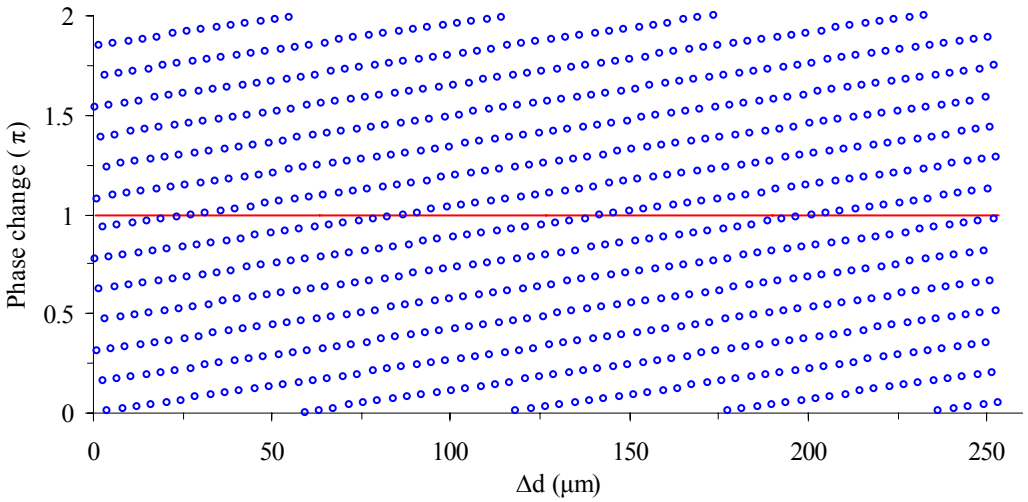

Figure 7-5 Calculated phase change at the illumination wavelength for the displacement while the locking system will still stabilise to a quadrature position.

7.4.4 Potential improvements in MZI-PDV processing

In the existing normalised intensity processing method (described in 5.5.2), an approximation has been used to find the local fringe amplitude maximum and minimum. This was done by finding the nearest max/min to each pixel. A possible approach to remove this approximation is to calibrate the intefereometric filter at each pixel before any measurement. This can be realised by taking several images when the fringe pattern is shifted. The fringe pattern can be shifted by modulating the laser frequency or the optical path imbalance of the interferometer. The latter is much quicker but the phase drift of the interferometer could be a problem due to the phase locking system needing to be turned off.

In this way, the maximal $I_{N\max}$ and minimal $I_{N\min}$ values for the normalised intensity at each pixel can be established. So the value for each pixel can be expressed as

$$I_N(i,j) = \frac{I_1(i,j) - I_2(i,j)}{I_1(i,j) + I_2(i,j)} = \left(\frac{I_{N\max}(i,j) + I_{N\min}(i,j)}{2}\right) + \left(\frac{I_{N\max}(i,j) - I_{N\min}(i,j)}{2}\right)\cos(\Delta\varphi(i,j))$$

Equation 7-2

where the indices (i,j) give the pixel position in the images. The phase difference, $\Delta\varphi(i,j)$, for each pixel, can then be found by rearranging Equation 5-5, which removes the approximation used in current data processing techniques.

$$\Delta\varphi(i,j) = \arccos\left(\frac{2\cdot I_N(i,j) - \left(I_{N\max}(i,j) + I_{N\min}(i,j)\right)}{I_{N\max}(i,j) - I_{N\min}(i,j)}\right) \pm n\pi \qquad n = 0,1,2,3...$$

Equation 7-3

7.4.5 Possible experiments for different measurement ranges

In the existing MZI-PDV system, a 15cm glass block was used to correct for the difference in magnification in the two arms of the MZI and provide a free spectral range (FSR) of ~1.2GHz. This is similar to the width of the iodine absorption line (of the order of 1GHz) used in conventional PDV systems. Other block lengths are available, e.g. 8cm and 23cm. This would provide a FSR of ~2.2GHz for high velocities or ~756MHz for low velocities.

7.4.6 Possible improvement in the experimental arrangement

In the existing MZI-PDV system, an infinity-corrected microscope optical system consisting of a matched objective and a tube lens with an infinity-space distance of around 600mm was used to fit the MZI optical components. This results in a ~35% reduction in average image intensity and a reduction in the usable image area of ~40% when compared to the infinity-space distance of 200mm recommended by the manufacturer. Therefore, reducing this infinity-space distance could improve the light efficiency and enlarge the field of view. A possible approach is shown in Figure 7-6.

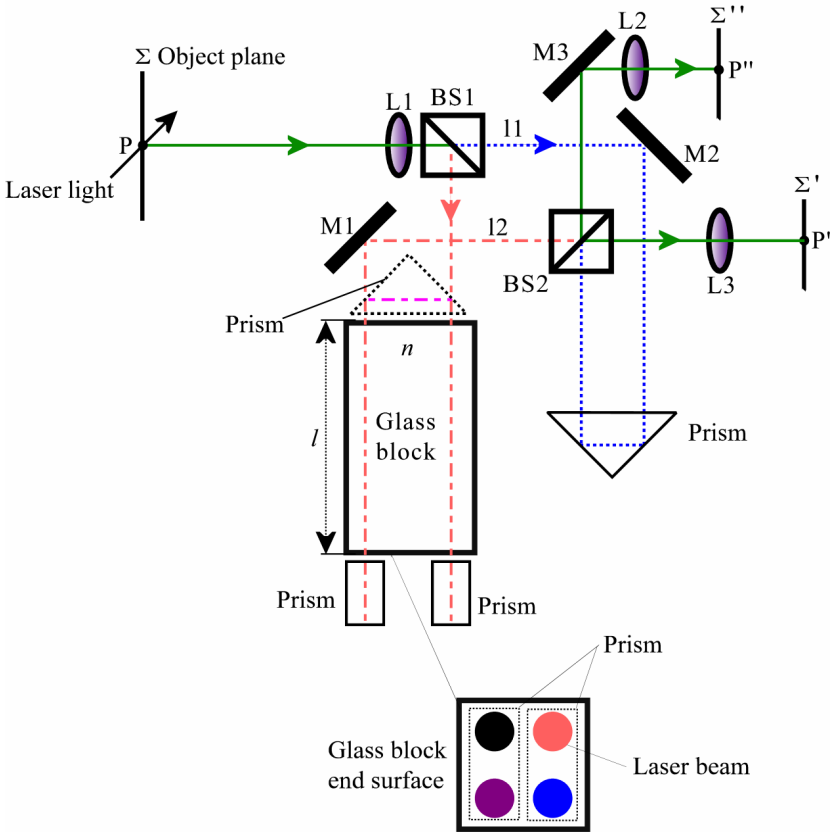

Figure 7-6 Schematic of the proposed MZI-PDV system using three cameras where the polarised laser beams are used. BS1, BS2: 'non-polarising' beam splitters; L1: objective; L2, 3: tube lenses; M1, 2, 3: mirrors. *l*: length of glass block; *n*: refractive index of glass block. Beam path for measurement shown as solid line (green), beam paths for the two arms of the interferometer shown as a dashed line (red) and a dotted line (blue) respectively. In the glass block end surface, the laser beams in different paths shown as different colours (black, orange, violet and blue).

In this arrangement, the laser beam passes through the glass block four times with the aid of three prisms located near the two end surfaces of the glass block (see glass block end surface in Figure 7-6). This reduces the length of the glass block used by a factor of 2 compared to the current experimental arrangement used in chapter 5 and 6 leading to a more compact structure. The infinity-space distance could be reduced from ~600mm (currently used) to ~300mm. this could improve the working performance (image quality) as shown in Table 4-1. However, a possible problem is the increased sensitivity to environmental variations especially for mechanical vibrations due to more prisms used.

Table 7-1 Comparison of the working performance of the infinity space with different distances.

		Average intensity	Maximum intensity	Usable image area	Image magnification
Infinity-space distance (mm)	200	1	1	1	1.25
	300	0.95	0.97	0.90	1.26
	600	0.75	0.82	0.60	1.31
% improvement (300 over 600mm)		20%	15%	30%	4%

7.5 References

[1] Seiler, F. and Oertel, H. (1985), "Visualization of velocity fields with Doppler-pictures", *Flow Visualization III, Proceedings of the Third International Symposium on Flow Visualization,* Ann Arbor, MI, pp. 454-9.

[2] Meyers, J.F., Lee, J.W. and Schwartz, R.J. (2001), "Characterization of measurement error sources in Doppler global velocimetry", *Measurement Science and Technology,* Vol. 12, No. 4, pp. 357-68.

[3] Nobes, D.S., Ford, H.D. and Tatam, R.P. (2004), "Instantaneous, three-component planar Doppler velocimetry using imaging fibre bundles", *Experiments in Fluids,* Vol. 36, No. 1, pp. 3-10.

[4] Butefisch, K.A. (1989), "Three component laser Doppler anemometry in large wind tunnels", *Progress in Aerospace Sciences,* Vol. 26, No. 1, pp. 79-113.

[5] Schodl, R. (1999), "Capabilities of optical point measurement techniques with respect to aero engine application", *Planar Optical Measurement Methods for Gas Turbine Components, RTO Lecture Series 217,* Cranfield, UK/Cleveland, USA.

[6] Ivanchenko, O., Esirgemez, E. and Olcmen, S. (2007), "A miniature three-component LDV probe", *Measurement Science and Technology,* Vol. 18, No. 7, pp. 2014-20.

[7] Chehura, E., Ye, C.-C. and Tatam, R.P. (2003), "In-line laser Doppler velocimeter using fibre-optic Bragg grating interferometric filters", *Measurement Science and Technology,* Vol. 14, No. 6, pp. 724-35.

[8] Seiler, F., George, A., Havermann, M. and Srulijes, J. (2004), "Doppler picture velovimetry (DPV) applied to high-speed shock tunnel flows", *11th International Symposium on Flow Visualization,* Notre Dame, Indiana.

Publications

Journal paper

Lu, Z.H., Charrett, T.O.H., Ford, H.D. and Tatam, R.P. (2007), "Mach-Zehnder interferometric filter based planar Doppler velocimetry", *Journal of Optics A: Pure and Applied Optics,* Vol. 9, pp.1-12.

Conference papers

Lu, Z.H., Charrett, T.O.H., Ford, H.D. and Tatam, R.P. (2007), "Planar Doppler velocimetry using a Mach-Zehnder interferometric filter", *3rd International Conference in the series of Optical and Laser Diagnostics (ICOLAD)*, City University, London, UK, published in *Journal of Physics: conference series* 85 012011.

Lu, Z.H., Charrett, T.O.H., Ford, H.D. and Tatam, R.P. (2007), "Frequency-to-intensity transduction methods for planar Doppler velocimetry (PDV)", *Optical Techniques and Applications in Fluid Mechanics*, Photonex, Coventry, UK.

Lu, Z.H., Charrett, T.O.H., Ford, H.D. and Tatam, R.P. (2007), "Mach-Zehnder interferometric filter based planar Doppler velocimetry", *14th International Symposium on Applications of Laser Techniques to Fluid Mechanics*, Lisbon, Portugal [accepted].

Lu, Z.H., Charrett, T.O.H., Ford, H.D. and Tatam, R.P. (2007), "3D planar velocity measurements, using Mach-Zehnder interferometric-filter-based planar Doppler velocimetry (MZI-PDV) and imaging fibre bundles", *19th Conference on Optical Fibre Sensors (OFS)*, Australia [accepted].

APPENDIX A: Electronic Control Circuit for Phase locking and control system in the MZI-PDV

This appendix discusses the electronic circuits that were designed for phase locking and control of the Mach-Zehnder interferometer. The electronic circuit desgns and formulations presented here, follows the analysis published by Chehura [1]. The circuits were designed with operational amplifiers, resistors, and capacitors, all chosen to offer minimum drift or noise. The working principle is shown in Figure A-1.

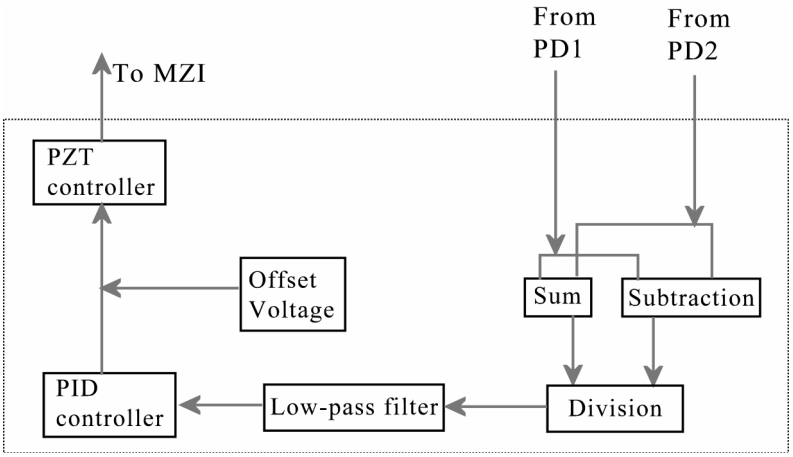

Figure A-1 The diagram of the control loop.

Two photodiodes PD1 and PD2 were used to monitor the complementary interferometric outputs in the phase locking system. The signals from PD1 and PD2 were normalised through an electrical circuit comprises sum, subtraction and division units. The circuit is one part of the PID control loop shown in Figure A-1.

Through a low-pass filter, this output was connected to a custom-designed PID electronic circuit. The circuit then generated an error signal relating to the interferometer phase drift. The error voltage was then fed back onto the piezoelectrically controlled stage supporting the right-angle prism, to modify the interferometer path difference.

The operational amplifier used here was OP-177FP manufactured by Anolog Devices and its parameters are listed below [2].

Table A-1 Analog Devices OP-177 parameters.

Parameters	OP-177FP
Input offset voltage	10μV
Average voltage drift	0.1 μV/ºC
Input offset current	0.5nA
Input bias current	2.4nA
Input bias current drift	8pA/ºC

Analogue division was carried out using an AD734 chip from Analog Devices [2]. This chip provides the function

$$W = \frac{(X_1 - X_2)\cdot(Y_1 - Y_2)}{(U_1 - U_2)} + Z_2 \qquad \textbf{Equation A-1}$$

where $X = X_1 - X_2$, $Y = Y_1 - Y_2$ and $U = U_1 - U_2$ are inputs; Z_2 is the supply; W is the output. The X, Y, and Z signals may all be positive or negative, but U must be positive and in the range +10mV to +10V. The X input must have a magnitude of less than $1.25U$. From Y, the amplified coefficient can be adjusted.

The whole circuit for the signal detection, summation, subtraction and analogue division [3,4,5] is shown in Figure A-2. The division voltage signal (normalised output) was connected to the circuits of Figure A-3, through a low-pass filter with a cut-off frequency of ~6Hz for the generation of the feedback control signal. More details about the low pass filter can be found in section 5.4.4 in chapter 5. The control signal was used to control the PZT stage attaching the prism that modulates the path difference of the interferometer.

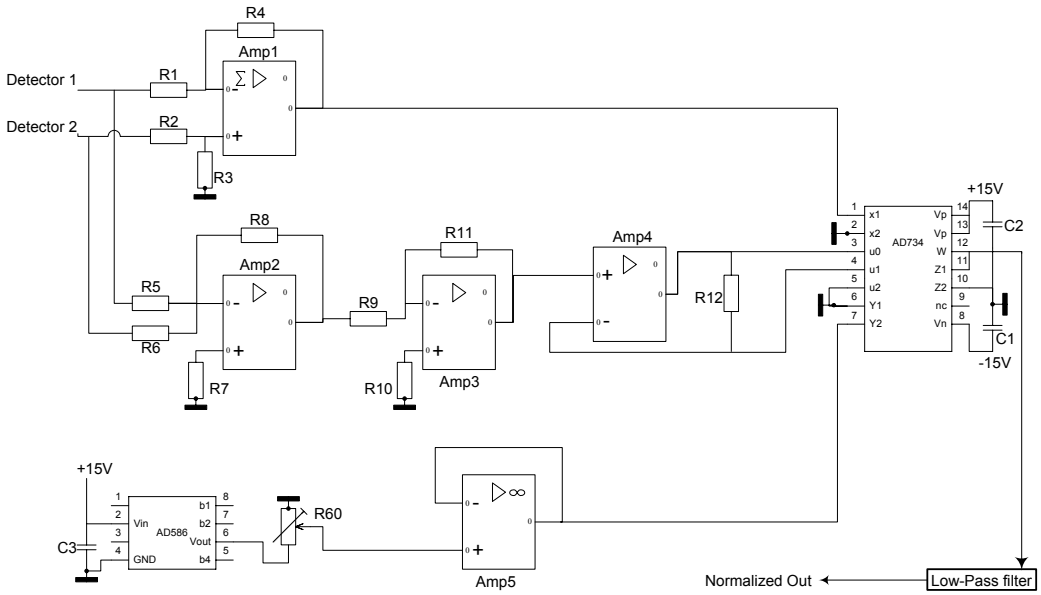

Figure A-2 Signal detection, summation, subtraction and division circuits.

Based on the normalised output signal $V_{normalised-out}$ of circuits A-2, and a constant voltage source $V_{set-point}$ from an AD586 chip used as the set point for the control system, the amplifier (Amp7) was used as a comparator to generate the error voltage

$$V_{error} = V_{normalized-out} - V_{set-point} \qquad \textbf{Equation A-2}$$

The following relation gives the proportional signal $V_{proportional}$:

$$V_{proportional} = \frac{R_{19}}{R_{17}} \cdot \frac{R_{22}}{R_{20}} \cdot V_{error} \cdot \qquad \textbf{Equation A-3}$$

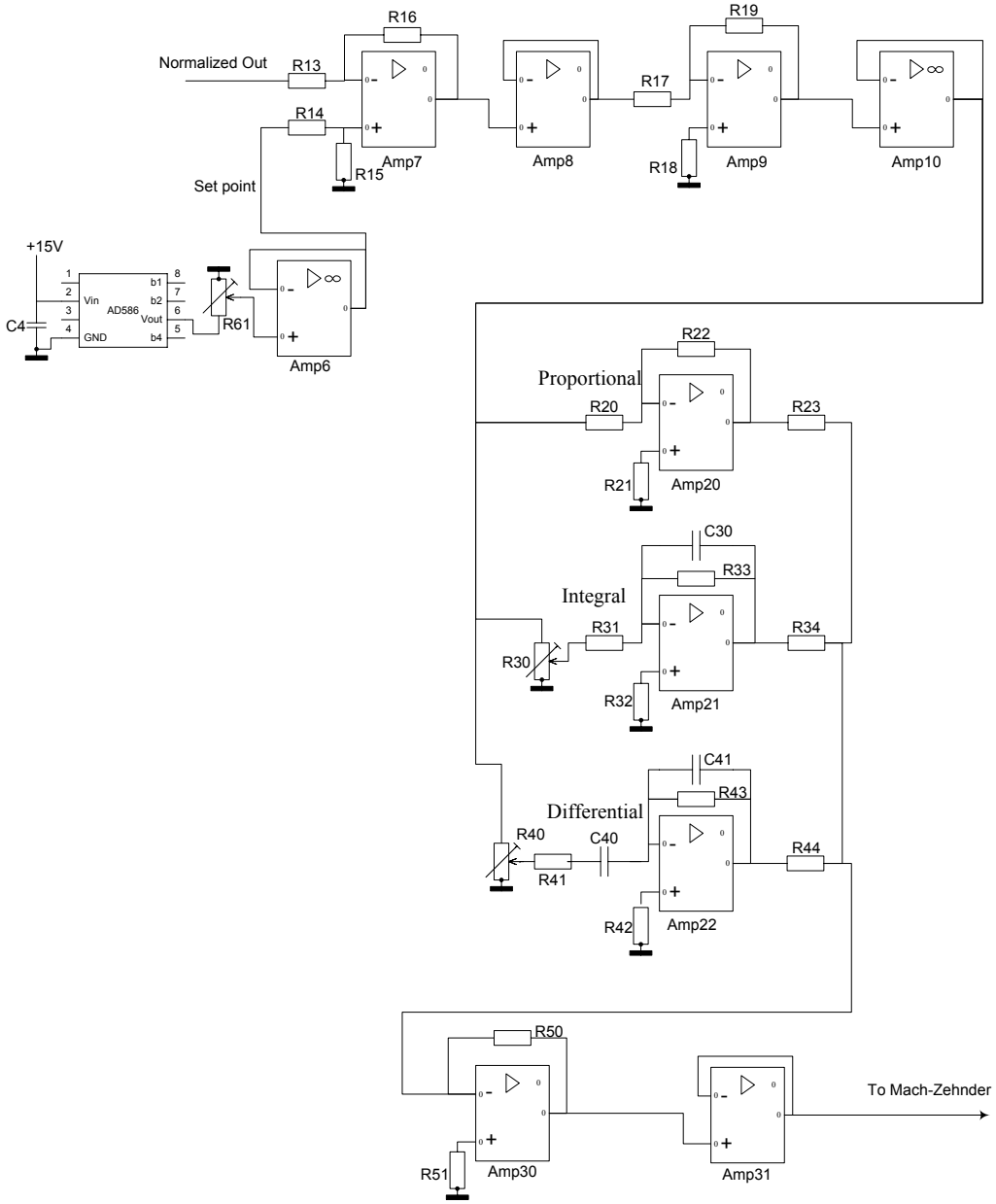

Figure A-3 PID feedback signal generation circuits.

The integral signal is given by

$$V_{\text{int}egral} = \frac{R_{19}}{R_{17}} \cdot \frac{R_x}{R_{30}} \cdot \frac{1}{R_{31} \cdot C_{30}} \cdot \frac{\omega C_1 R_{33}}{\left(1 + \omega^2 C_{30}^2 R_{33}^2\right)^{\frac{1}{2}}} \int V_{error} \cdot dt \qquad \textbf{Equation A-4}$$

where ω represents the frequency. R_{33} is an integral excursion leaking resistor to avoid saturation and cut-off of the integrator, which is normally $\geq 10R_{31}$. R_x is the resistance at the potentiometer with total resistance R_{30}.

The derivative signal is given by

$$V_{derivative} = \frac{R_{19}}{R_{17}} \cdot \frac{R_y}{R_{40}} \cdot R_{43} \cdot C_{40} \cdot \frac{dV_{error}}{dt} \qquad \textbf{Equation A-5}$$

where R_y is the resistance at the potentiometer with total resistance R_{40}. R_{41} and C_{41} were added to limit high frequency gain. And the relations are required.

$$R_{43} \cdot C_{40} = R_{41} \cdot C_{41}. \qquad \textbf{Equation A-6}$$

Then the maximum frequency of the differentiator and corresponding maximum gain are given by [5]

$$f = \frac{1}{2\pi \cdot R_{43} \cdot C_{40}}$$

$$G_{\max} = \frac{R_{43}}{R_{41}}. \qquad \textbf{Equation A-7}$$

The PID control signal [1,6] was obtained by

$$V_{pid} = -\left[\frac{R_{50}}{R_{23}} \cdot V_{proportional} + \frac{R_{50}}{R_{34}} \cdot V_{integral} + \frac{R_{50}}{R_{44}} \cdot V_{derivative} \right] \qquad \textbf{Equation A-8}$$

The gain $G_{proportional}$, $G_{integral}$ and $G_{derivative}$ on P, I, and D actions respectively were set according to the following relations.

$$G_{proportional} = \frac{R_{19} \cdot R_{22} \cdot R_{50}}{R_{17} \cdot R_{20} \cdot R_{23}}$$

$$G_{integral} = \frac{R_{19} \cdot R_x \cdot R_{50}}{R_{17} \cdot R_{30} \cdot R_{34}}$$

$$G_{derivative} = \frac{R_{19} \cdot R_y \cdot R_{50}}{R_{17} \cdot R_{40} \cdot R_{44}}. \qquad \textbf{Equation A-9}$$

The electronic elements used are listed below.

100k	R1, R2, R3, R4, R5, R6, R7, R8, R9, R10, R11, R13, R14, R15, R16,R17, R20, R22, R31, R32, R42, R43
2M	R12
51k	R21
4.64k	R23, R50
20k	R30, R40
1M	R33
10k	R34, R44
62k	R19
37k	R18
50k	R60, R61
2k	R41
1.6k	R51
0.1μ	C1, C2, C3, C4
2.2 μ	C30
0.33 μ	C2
2n	C41

References

[1] Edmon C. (2002), "In-line using fibre-optic laser Doppler velocimeter using Bragg grating interferometric filters as frequency to intensity transducers", PhD thesis, Cranfield University, Cranfield, UK.

[2] Analog Devices, Inc. (2007), www.analog.com.

[3] Jiirbi, D. (1981), “Operational Amplifiers”, Elsevier Scientific Pub. Co. Ltd.

[4] David, F.S. (1976), “Handbook of operational amplifier circuit design”, McGraw-Hill.

[5] Robert G.I. (1981), “Operational amplifier characteristics and applications”, Prentice-Hall.

[6] Kevin W. (1963), “An introduction to control systems”, World Scientific Publishing Co. Ltd.

APPENDIX B: A low-pass filter

This appendix describes a low-pass filter designed to remove high frequency components of the normalised output of the Mach-Zehnder interferometer. The circuits were designed with operational amplifiers, resistors, and capacitors as shown in Figure B-1.

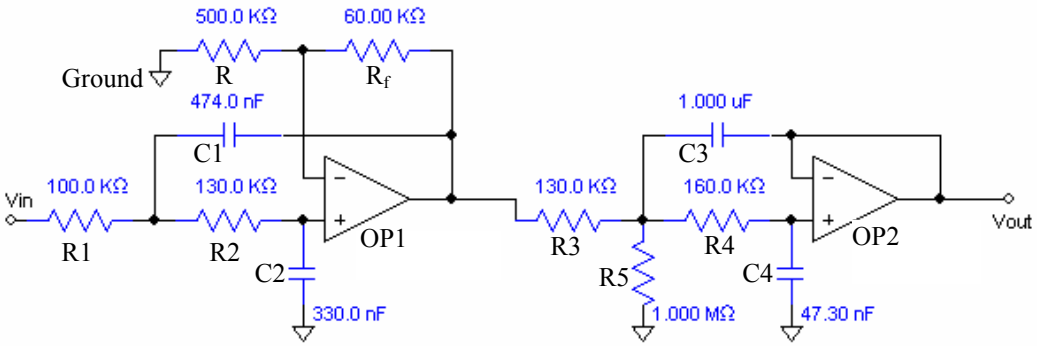

Figure B-1 Low-pass filter circuits. The cut-off frequency is ~6Hz. OP: operational amplifier.

The circuits of Figure B-1 are for a 4th order low-pass filter design using four capacitors (C1-4). The first stage is the RC filter composed of the resistor R1 and capacitor C1 with a cut-off frequency of $1/(2\pi \cdot R1 \cdot C1)$. The second, third and fourth stages are RC filters composed of R2 and C2, R3 and C3 and R4 and C4 respectively. The resister R5 is used to adjust the gain of the circuits.

Finally the 4th order Chebyshev low-pass filter of offers a pass band frequency of ~5Hz, a cut-off frequency of ~6Hz, and a band ripple of ~0.2dB, which is obtained using the filter-solutions software [1]. The circuit frequency response from 0 to 200Hz is shown in Figure B-2. The frequency and phase responses from 0 to 20Hz are shown in Figure B-3.

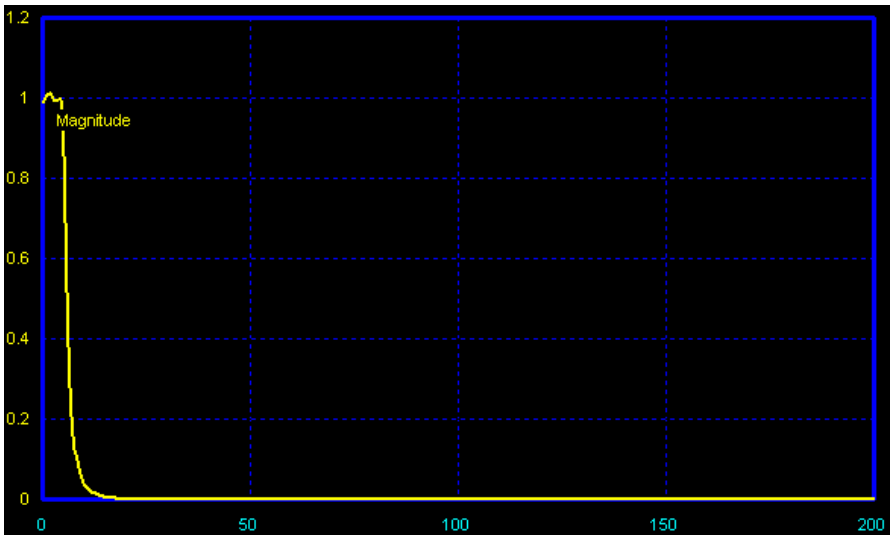

Figure B-2 Circuit frequency response curve under 200Hz.

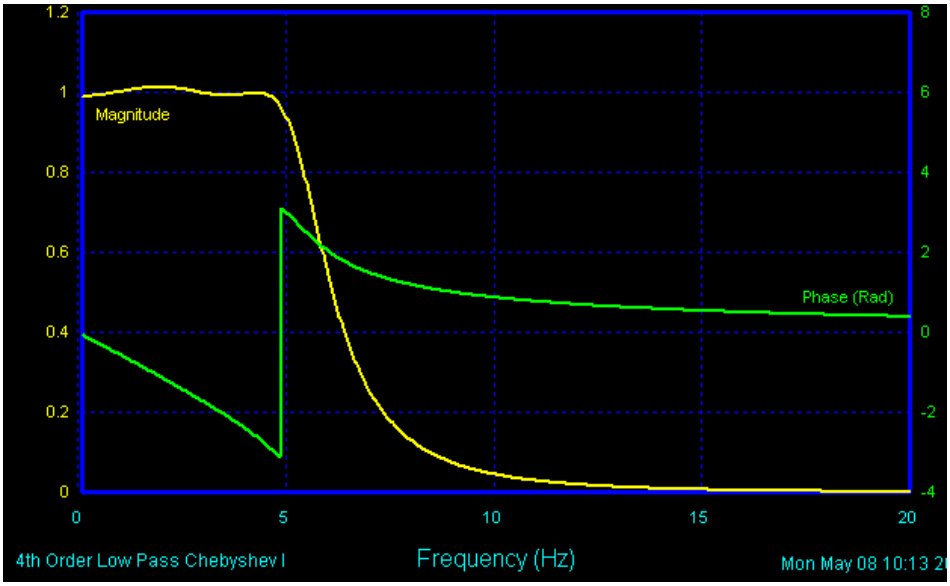

Figure B-3 Circuit frequency and phase response curves under 20Hz.

References

[1] Nuhertz Technologies, LLC, (2007), www.filter-solutions.com.

APPENDIX C: Contrast of the interference image in a Mach-Zehnder interferometer (MZI)

1. Relation between the block length and physical path length imbalance in a MZI

An unbalanced MZI used for planar Doppler velocimetry (PDV) in this work is shown in Figure C-1. The physical path length difference in the two arms of the interferometer is $(l_2 - l_1)$. This will lead to an increase of $2\Delta h$ in diameter for the light beam following path l2 compared to the beam following path l1 for a beam inclination angle of θ before the two beams combine at a beam splitter BS2. Δh is given by Equation C-1 and this is shown in Figure C-2(a).

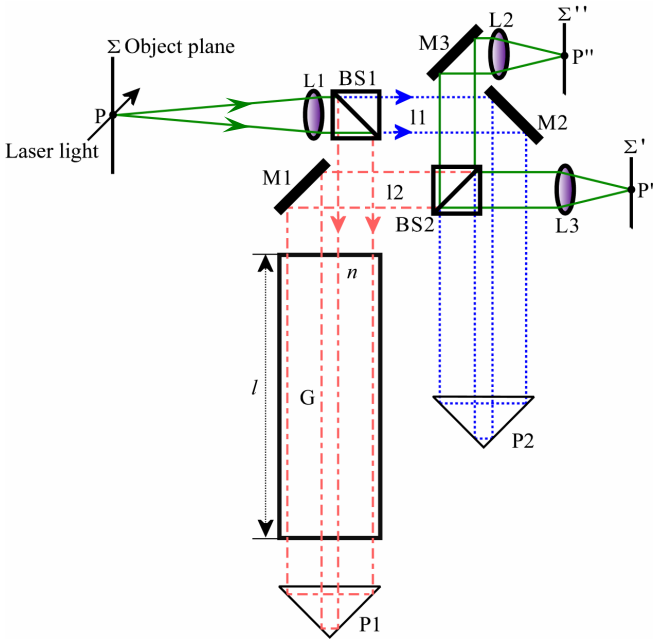

Figure C-1 An unbalanced Mach-Zehnder interferometer for PDV used in this work. The beam paths are shown in different styles and colours: path l1 is dashed (blue), path l2 is dot-dashed (red) and combined path is solid (green). BS1, 2: 'non-polarising' beam splitters; M1, 2, 3: mirrors; G: glass block with a length of *l* and a refractive index of *n*; P1, 2: right angle prisms; L1: camera lens; L2, 3: tube lens; P: particle.

$$\Delta h = (l_2 - l_1) \cdot \tan\theta \,. \qquad \textbf{Equation C-1}$$

A glass block can be inserted into the larger arm (l2) to correct for the difference in magnification and focal distance in the two arms. The function of the glass block is illuminated in Figure C-2(b). Here the light beam inclination angle of θ was enlarged in order for the demonstration compared to that in Figure C-2(a). It can be clearly seen that the block can reduce the beam diameter and the reduction $2\Delta h_c$ is calculated using Equation C-2 resulting from the geometry.

$$\Delta h_c = l \cdot (\tan\theta - \tan\gamma) \,. \qquad \textbf{Equation C-2}$$

In order to completely correct for the difference in magnification in the two arms of the MZI the relation between the block length (l) and physical path length imbalance (l_2–l_1) is written from Equations C-1 and C-2 as:

$$(l_2 - l_1)\cdot \tan\theta = 2l\cdot(\tan\theta - \tan\gamma) \qquad \textbf{Equation C-3}$$

where $\dfrac{\sin\theta}{\sin\lambda} = n$ computed by using the Snell's law of refraction. The block length is $2l$ because the light beam passes the block for two times.

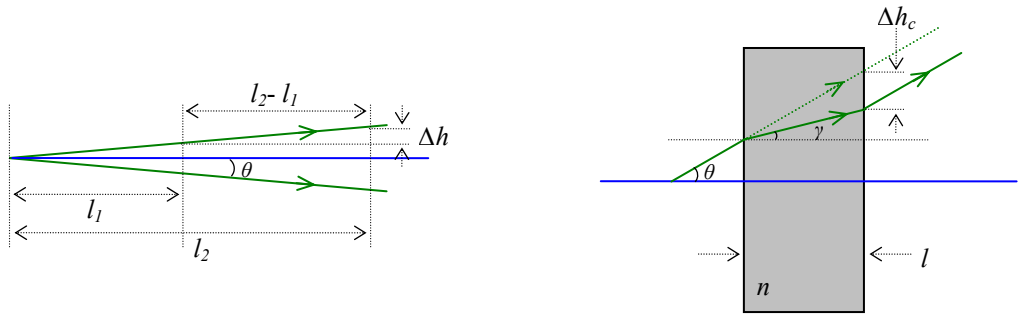

(a) (b)

Figure C-2 (a) An increase of $2\Delta h$ in diameter for the light beam following path l2 compared to the beam following path l1 for a beam inclination angle of θ. (b) Demonstration of the function of the block. Optical axis as shown in blue line, light beam shown in green lines. γ: the refractive angle in the block with a length l and refractive index of n.

Equation C-3 can be rewritten as

$$2l = \frac{(l_2 - l_1)\cdot\sqrt{n^2 - \sin^2(\theta)}}{\sqrt{n^2 - \sin^2(\theta)} - \cos(\theta)}. \qquad \textbf{Equation C-4}$$

This means that, ideally, different block lengths are necessary to correct for the different magnifications in the two arms of the MZI, for different light beam inclination angles. When the inclination angle of θ is equal to zero, i.e. light beams are parallel to the optical axis as shown in Figure C-2, Equation C-4 can be simplified as

$$2l = (l_2 - l_1)\cdot\frac{n}{n-1}. \qquad \textbf{Equation C-5}$$

2. Contrast of the interference image in a MZI

The contrast of the interference image in the MZI can be expressed as:

$$C = \frac{I_{\max} - I_{\min}}{I_{\max}} \qquad \textbf{Equation C-6}$$

where $I_{\max}$, $I_{\min}$ are the maximum and minimum intensities respectively in the image.

As discussed in section 1, when the inclination angle θ is equal to zero, the light beams in the two arms in the MZI are parallel to the optical axis leading to a contrast of unity.

This is due to the complete overlap between the two beams in the interfering plane with a beam size of r in diameter as shown in Figure C-3(a).

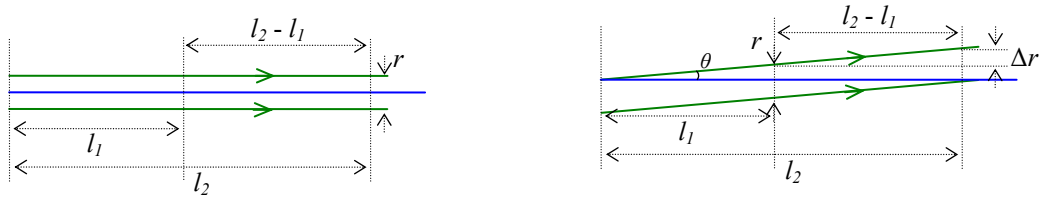

(a) (b)

Figure C-3 (a) The complete alignment between the two beams in the interfering plane with a beam size of r in diameter. (b) A misalignment (Δr) between the two interfering beams for the light beam inclination angle of θ in the interfering plane located at beam splitter BS2 (Figure C-1) although the two beams have the same diameter.

When the inclination angle θ is not equal to zero, there will be a misalignment (Δr) between the two interfering beams in the interfering plane located at beam splitter BS2 (Figure C-1) although the two beams have the same diameter as shown in Figure C-3(b). This will reduce the contrast of the interference image and the reduction is expressed in Equation C-7.

$$C = \frac{[(r-\Delta r)\cdot 1+\frac{2\Delta r}{4}]-[(r-\Delta r)\cdot 0+\frac{2\Delta r}{4}]}{(r-\Delta r)\cdot 1+\frac{2\Delta r}{4}} = \frac{r-\Delta r}{r-\Delta r/2} \qquad \textbf{Equation C-7}$$

where the beam diameter r is limited by the dimension of beam splitter BS1 used in the ZMI (Figure C-1). r can be expressed in Equation C-8, where r_0 is the dimension of BS1 that is around 20mm in this work as shown in Figure C-4.

$$r = r_0(1-\tan\theta)\,. \qquad \textbf{Equation C-8}$$

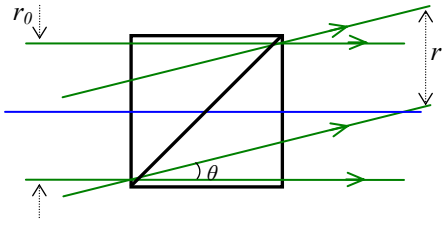

Figure C-4 The beam diameter r is limited by the dimension r_0 of beam splitter BS1 used in the ZMI.

From Equation C-3, the misalignment (Δr) between the two interfering beams in the MZI can be expressed as

$$\Delta r = 2l \cdot (\tan\theta - \tan\gamma) - (l_2 - l_1) \cdot \tan\theta$$
$$= (l_2 - l_1 - 2l) \cdot \tan\theta + \frac{2l \cdot \sin\theta}{\sqrt{n^2 - \sin^2\theta}}. \qquad \textbf{Equation C-9}$$

Combining Equations C-7-9 the contrast of the interference image in the MZI can be rewritten as

$$C = \frac{r_0 \cdot (1 - \tan\theta) - (l_2 - l_1 - 2l) \cdot \tan\theta - \dfrac{2l \cdot \sin\theta}{\sqrt{n^2 - \sin^2\theta}}}{r_0 \cdot (1 - \tan\theta) - \dfrac{1}{2}(l_2 - l_1 - 2l) \cdot \tan\theta - \dfrac{2l \cdot \sin\theta}{2 \cdot \sqrt{n^2 - \sin^2\theta}}}. \qquad \textbf{Equation C-10}$$